EXPERIMENTAL AND NUMERICAL INVESTIGATIONS OF SAND-EPOXY COATING EFFECTS ON SAND-GFRP INTERFACIAL SHEAR BEHAVIOUR

BIDUR PATHAK

PhD

The Hong Kong Polytechnic University

This programme is jointly offered by
The Hong Kong Polytechnic University
and
Southern University of Science and Technology

2025

The Hong Kong Polytechnic University

Department of Civil and Environmental Engineering

Southern University of Science and Technology

Department of Ocean Science and Engineering

Experimental and Numerical Investigations of Sand-Epoxy Coating Effects on Sand-GFRP Interfacial Shear Behaviour

PATHAK Bidur

A thesis submitted in partial fulfilment of the requirements for the degree of Doctor of Philosophy

April 2025

CERTIFICATE OF ORIGINALITY

I hereby declare that this thesis is my own work and that, to the best of my knowledge and belief, it reproduces no material previously published or written, nor material that has been accepted for the award of any other degree or diploma, except where due acknowledgement has been made in the text.

Signature:
Name: Bidur Pathak

ABSTRACT

Glass fibre-reinforced polymer (GFRP) composites have been widely used in engineering applications, including offshore structures, owing to their high strength-to-weight ratio and inherent corrosion resistance. However, their smooth surfaces and relatively low hardness can limit shear performance at the soil-GFRP interface. Surface modifications, such as sand-epoxy coatings, have been proposed to enhance surface roughness and hardness, thereby promoting mechanical interlocking and improving interface friction. This study aims to develop a comprehensive understanding of the shear mechanism at the sand-GFRP interface by systematically investigating the effects of GFRP surface type and roughness on shear and volumetric behaviour, as well as the evolution of surface roughness under cyclic shearing.

A series of interface direct shear tests was conducted under both monotonic and cyclic shearing conditions. Air-dried standard silica sand was employed as the test material, in conjunction with uncoated GFRP plates and sand-epoxied GFRP plates featuring different concentrations and grades of epoxied sand. Three distinct GFRP surface types (i.e., smooth finish, rough finish, and sand-epoxied surfaces with differing sand concentrations) were examined to evaluate their performance under varying particle sizes, initial relative densities, sand proportions, and normal stresses. The optimal sand coating configuration was identified through monotonic testing, while long-term performance was assessed via cyclic testing. The frictional characteristics of the interfaces were analysed to elucidate variations in shear stress mobilisation, vertical deformation, and roughness evolution mechanisms under moderate to high normal stresses (200 kPa to 800 kPa). A discrete element method (DEM) simulation was performed to provide micromechanical insights into the sand-GFRP interface behaviour under constant normal stresses up to 200 kPa, focusing on contact evolution and roughness changes. Additionally, a finite element method (FEM) analysis using an enhanced hyperbolic constitutive model was implemented within ABAQUS,

integrating user-defined subroutines to validate the experimental results. Model parameters were calibrated through a covariance matrix adaptation evolution strategy (CMA-ES), leveraging data from both monotonic and cyclic shearing tests.

The results indicate that increasing the dosage of epoxied sand enhances the surface roughness of GFRP, thereby improving interlocking mechanisms and resulting in higher interface shear strength. Under cyclic shearing conditions, both mobilised shear stress and vertical deformation increased with cycle number, normal stress, and interface roughness. GFRP degradation and particle breakage became more pronounced as the median particle size increased. The evolution of roughness was attributed to mass sliding and rotation in smooth interfaces, whereas rotational effects and bonding-debonding mechanisms governed in rough surfaces. The application of sand-epoxy coating significantly enhanced surface hardness and relative roughness while effectively mitigating long-term degradation. Cyclic shearing exhibited higher interfacial friction angles than monotonic shearing due to the combined effects of surface degradation, particle breakage, interlocking, and stress redistribution at the interface under elevated normal stress. DEM simulations revealed that sand-epoxy coatings can increase peak friction angles by up to 37% and 98% for fine and medium sands, respectively, with force chain concentration being more evident in dense specimens. Interface slip decreased with increasing normalised roughness, and the roughest interfaces promoted diagonal force chain alignment, particularly under high normal stresses. FEM simulations demonstrated that the model effectively captured hardening behaviour and contraction but exhibited limitations in predicting softening and dilation under large deformations. Further refinements are needed to enhance the model's predictability.

This research advances the characterisation of the sand-GFRP interface and informs the practical design of sand-epoxy coatings by integrating experimental investigations with numerical analyses, encompassing micromechanical and macromechanical modelling. The findings provide fundamental insights into interface contact mechanics and shear behaviour, forming a foundation for future

developments in geotechnical applications involving GFRP composites and granular materials under diverse loading conditions, with potential for subsequent validation under environmental scenarios.

Keywords: sand-GFRP interface; sand-epoxied GFRP; monotonic and cyclic shearing; roughness; micromechanics

RESUME AND ACADEMIC ACHIEVEMENTS

Resume

Bidur Pathak was born in 1992 in Dolakha District/Bagmati Province, Nepal. He began his bachelor's study in Civil Engineering at the National College of Engineering, Tribhuvan University (TU) in November 2011 and obtained a Bachelor of Civil Engineering degree in April 2016. He then pursued a master's study at the School of Civil Engineering and Mechanics, Huazhong University of Science and Technology (HUST), starting in September 2018, and obtained a Master of Engineering in Geotechnical Engineering in August 2020.

He has been pursuing a '*Joint PhD leading to a dual-award degree*' in Geotechnical Engineering at the Department of Civil and Environmental Engineering, The Hong Kong Polytechnic University (PolyU) since September 2020, and in Mechanics at the Department of Ocean Science and Engineering, Southern University of Science and Technology (SUSTech) since October 2020.

Academic Achievements during the Study

Wang H-L, **Pathak B**, and Yin Z-Y*. Investigation on the micro-structure, unconfined compressive strength, and thermal conductivity of compacted CDG soil by MICP treatment during curing[J]. Journal of Materials in Civil Engineering, 2023, 35(6): 04023131.

Pathak B, Yin Z-Y, Wang P, and Fu Y*. DEM investigation of the impact of sand-epoxy coating on the shear behaviour of sand-GFRP interface[J]. Computers and Geotechnics, 2025, 188: 107513.

Pathak B, Yin Z-Y, Fu Y*, and Luo Z, Impact of sand coating on the shear behavior of sand-GFRP interface: an experimental investigation[J]. Acta Geotechnica, 2025 (Accepted).

Pathak B, Yin Z-Y, Fu Y*, and Luo, Z. Evolution of surface roughness and particle breakage with interface shear behaviour of sand-epoxied GFRP against sand under elevated normal stress [J], Canadian Geotechnical Journal, 2025 (Accepted).

ACKNOWLEDGEMENTS

I am profoundly grateful to my chief supervisors, Professor Zhen-Yu Yin from the Department of Civil and Environmental Engineering at The Hong Kong Polytechnic University (PolyU) and Assistant Professor Yong Fu from the Department of Ocean Science and Engineering at the Southern University of Science and Technology (SUSTech), for their invaluable guidance, patience, motivation, and unwavering support throughout my doctoral journey. Their mentorship has been instrumental in shaping my academic and professional development. I extend my heartfelt appreciation to Professor Jun-Jie Zheng for encouraging me to pursue higher education and for recommending me to Professor Zhen-Yu Yin, thereby providing me with this invaluable platform for learning and career advancement. Their guidance will remain a lifelong inspiration.

I am equally indebted to my co-supervisors, Professor Han-Lin Wang, Professor Pei Wang, Dr Zhibin Luo, and Professor Jie Yang, for their continuous guidance and support in experiments, modelling, and manuscript preparation.

I sincerely thank the Board of Examiners (BoE), Professor Tao Yu as Chairman of the BoE, Professor Anthony Kwan Leung from The Hong Kong University of Science and Technology, and Professor Stefano Utili from Newcastle University, United Kingdom, for their time and constructive feedback in reviewing my thesis.

I extend my special thanks to Associate Professor Shaolin Xu, Assistant Professor Wei-Qiang Feng, Professor Wen-Bo Chen, Professor Yin-Fu Jin, and Professor Jian-Hua Yin for their encouragement during challenging times. I also express my gratitude to Dr Mei-Po Ho (Mabel), Mr David Leung, Mr C.K. Leung, Ms Fion Cheng, and Mr Raymond Leung for their invaluable assistance in my experimental work.

I would also like to acknowledge Ms Du-Jiao Guo, Ms Fuli Wang, and all

the faculty members and laboratory staff for their generous support. Special thanks go to my seniors, Dr Tuo Wang, Dr Ning Zhang, Dr Tahir Fazal, Dr Meysam Bayat, Dr Cui Xie, Dr Ding-Bao Song, Dr Jing-Cheng Teng, Dr Yu Pan, Dr Kai Lou, and Dr Chang He, as well as the Geo-Invention group, for their guidance and encouragement. I am further grateful to my friends and colleagues, Mr Min-Hao Zhang, Mr Hai-Lin Wang, Mr Kamal Al-Zaoari, Mr Rui Liang, Mr Jun Li, and Mr Dongze Li, for their camaraderie and assistance.

My sincere appreciation goes to The Hong Kong Polytechnic University and the Southern University of Science and Technology for offering me the opportunity to undertake a Joint PhD leading to a dual-award programme, along with full financial support throughout my four years of study. I am also grateful to the Education Bureau of the Hong Kong Special Administrative Region of the People's Republic of China, Ministry of Education of the People's Republic of China, the Ministry of Education of Nepal, and the strong bilateral relations between Nepal and Hong Kong as well as Nepal and China, which facilitated my pursuit of higher education.

Finally, my deepest gratitude goes to my parents, siblings, brother-in-law, sister-in-law, and especially my fiancée, whose unwavering love, patience, and encouragement have been my greatest source of strength. I am also thankful to my extended family for their unconditional support.

TABLE OF CONTENTS

LIST OF FIGURES

LIST OF TABLES

CHAPTER 1: INTRODUCTION

1.1 Background

In geotechnical, underground, and ocean engineering, soil-structure interface contact problems are prevalent. However, under complex loading such as vertical, lateral, and dynamic loading, the mechanical response at the interface between soil and structure is the field of concern for soil-to-soil and different for various structural materials. Due to the inclusion of nonlinear, large deformation, local discontinuity, and global volumetric variation, contact surface research becomes extremely difficult. The application of Glass Fiber Reinforced Polymer (GFRP) in structural, ocean, and geotechnical engineering has grown significantly due to its high strength-to-weight ratio, corrosion resistance, and versatility in structural design (Frost and Han, 1999; Bakis et al., 2002; Bai, 2023). GFRP materials are particularly favoured for use in environments where traditional materials like steel, reinforced concrete (RC), and timber are prone to degradation, such as in coastal or harsh soil conditions (Iskander and Hassan, 1998; Frost and Han, 1999). However, despite their advantages, GFRP's long-term performance is heavily influenced by the interface between the GFRP surface and the surrounding medium, such as soil or sand, particularly under the action of both static and dynamic loading conditions. A critical area of research lies in understanding and improving the frictional properties, surface roughness, and shear strength of the sand-GFRP interface, as these factors directly affect the stability, durability, and load-bearing capacity of GFRP-based structures.

Sand, mainly silica sand, is a commonly used material in geotechnical research for studying the behaviour of material interfaces, owing to its predictable characteristics and its role as a fundamental granular material in soil mechanics (e.g., Al-Douri and Poulos, 1992; Westgate and DeJong, 2023). Silica sand, with varying particle size distributions and shapes, provides valuable insights into particle interlocking, sliding, and rotational movement at interfaces

(DeJong and Westgate, 2009; Lashkari and Jamali, 2021). Previous research has extensively studied the shear behaviour of sand-fibre reinforced polymers (FRPs) interfaces under static, monotonic loading conditions (Frost and Han, 1999; Sakr et al., 2005; Almallah et al., 2020a; Namjoo et al., 2022). These studies have shown that factors such as particle gradation, shape, and surface roughness play pivotal roles in the frictional response of sand-FRP interfaces (Namjoo et al., 2022; Westgate and DeJong, 2023). However, limited work has explored the cyclic shear behaviour of these interfaces, which is vital for understanding long-term performance, particularly under repeated loading, which is typical in geotechnical applications. However, these studies can be explored in relation to several structural materials such as steel, geosynthetic, and epoxy. The critical concern on these materials should be provided basically in cyclic or dynamic loading conditions to analyse the wearing behaviour of surfaces on the range of applied normal stress and corresponding effects on shear behaviour (e.g., Shooter and Tabor, 1952; Dove and Frost, 1999; Ho et al., 2011; Rui et al., 2021; Feng et al., 2022).

One of the challenges in improving GFRP durability arises from its reduced surface hardness, while the low surface roughness leads to poor interfacial frictional properties. These factors together become critical under cyclic or dynamic loading. GFRP laminates and bars are increasingly adopted in marine geotechnics for structural elements. However, their long-term durability under repetitive shear loading and environmental stressors (e.g., ultraviolet radiation and alkaline conditions) remains an area of concern. Degradation of resin matrix, fibre-matrix debonding, and surface wear pose significant risks to performance (Teng et al., 2024; Yue et al., 2024; Smoleń et al., 2024; Cao et al., 2025). These degradation mechanisms critically impact bond behaviour and interface shear strength, especially under cyclic shear loading representative of offshore and coastal environments.

The effectiveness of GFRPs in geotechnical systems (e.g., foundations, pipelines, and sea walls) heavily depends on their interface behaviour with soil, which governs the mobilised shear resistance during loading events (Frost and

Han, 1999; Pando et al., 2002; Giraldo and Rayhani, 2014). Sand coatings on FRP surfaces have been proposed to enhance the friction properties of the interface and surface roughness of FRP laminates (Toufigh et al., 2016; Xiong et al., 2019). Sand-coated FRP has been shown to increase the surface hardness of FRP, thereby reducing the wear and tear of the material over time. These coatings can also help improve interface friction by increasing the roughness of the FRP surface, which in turn enhances particle interlocking and shear strength (Almallah et al., 2020a; Namjoo et al., 2022). In the context of GFRP bars, surface treatment and bar geometry, such as sand coating, ribbing, and wrapping finishes, promote mechanical interlocking and bond performance (Morales Arias et al., 2012; Shakiba et al., 2022). However, there is a lack of comprehensive studies that examine the combined impact of sand gradation, particle shape, and sand-epoxy coatings on the interface shear behaviour of sand-GFRP interface, particularly under both monotonic and cyclic shearing conditions covering a varying normal stress range (50 kPa to 800 kPa), useful for moderate to large-scale constructions. Understanding the mechanical behaviour of sand-GFRP interfaces under such loading conditions is essential for developing more effective and durable GFRP-based applications. Several factors, including normal stress, particle size, surface roughness, and particle breakage, influence the interface shear strength of sand-GFRP systems. Studies by White (2002) and White et al. (2013) have emphasised the importance of particle shape, particle size, and crushing strength in influencing sand-based foundations' load-bearing capacity and settlement behaviour. However, the impact of cyclic loading on the volumetric behaviour and long-term stability of the interface remains underexplored in the sand-GFRP interface.

Direct and simple shear apparatuses are commonly used in laboratory testing of soil-structure interfaces (e.g., Zhang and Zhang, 2009; Zohra et al., 2022). However, the direct shear apparatus has several limitations, including a fixed shear plane and a relatively small shearing area. The simple shear apparatus mitigates some of these deficiencies, but persistent issues with uneven stress and strain distributions can still compromise measurement precision and validity. To

improve experimental accuracy and better investigate soil-structure interface behaviour, direct shear tests can be complemented with model pile or pullout tests. When physical testing is impractical, numerical simulations provide comparable insights and analytical depth. Consequently, advanced numerical methods such as the discrete element method (DEM) and finite element method (FEM) have been employed to simulate particle-scale interactions and interface responses (e.g., Yin et al., 2018b, Wang and Yin, 2022; Wang et al., 2022b). DEM models provide a deeper understanding of the micromechanical mechanisms, particularly in terms of force chain formation and contact dynamics (Wang and Yin, 2022; Song et al., 2024). DEM has been increasingly used to study the evolution of surface roughness and interface degradation at interface shearing (Feng et al., 2020; Chen et al., 2021; Feng et al., 2022), revealing important insights into the role of particle shape, force chain anisotropy, and local roughness variations in driving interface stability (e.g., Chen et al., 2021; Wang et al., 2022a; Su et al., 2025).

The shearing behaviour of the soil-structure interface (SSI) depends on the soil constitutive model, which is used to capture interface behaviour, capabilities of numerical platforms such as the finite element method and the finite difference method (FDM), and corresponding software such as ABAQUS, PLAXIS, and FLAC. These capabilities also depend on the numerical approach chosen to implement the simulation. The unrealistic predictions of the behaviour of soil-structure interface systems lead to severe damage to properties and are prone to damage to the community. The classical models, such as the Mohr-Coulomb model, Modified Cam-Clay model, and Hyperbolic model, may not be singly effective to account for all these essential behaviours of the soil-structure interface (e.g., Lade, 2005a; Kok et al., 2009). In history, failure was evidenced due to the wrong choice of constitutive models. For example, to study the pile-soil interface systems, a simple interface model coupled with a comprehensive soil constitutive model is unrealistic and not from an economic engineering viewpoint. However, a proper interface coupled with a simple constitutive model could result in accurate and reasonable predictions. The importance of

sophisticated interface models is to justify the experimental testing by including various parameters such as critical state, breakage, and shear reversal in cyclic shearing. The enhancement of classical models with essential parameters is always promoted to better build the proper interface model rather than completely forming a new one. Studies evaluated that enhanced non-linear models are capable of predicting soil-structure interface shear behaviour can be utilised to validate the experiments (Yang and Yin, 2021; Wang et al., 2024b; Wang et al., 2024c) and evaluation of the existing constitutive models for sand-GFRP interfaces, helps reinforce the studies and improvement in models by the identification of necessary improvement required.

In recent years, advancements in material modification techniques, particularly the application of sand coating and tailored sand gradation, have shown promise in enhancing interface friction. However, these modifications also raise concerns about surface stability due to the removal of coated particles during shearing (e.g., Toufigh et al., 2016; Almallah et al., 2020b; Namjoo et al., 2022). However, the long-term performance of these modified surfaces under cyclic loading and the better approach of sand coatings in mitigating surface roughness degradation over time require further investigation. The integration of experimental testing and numerical modelling in this study aims to provide a holistic approach to understanding the sand-GFRP interface and improving interface durability, especially under the influence of cyclic shearing.

This study seeks to fill these gaps by investigating the shear behaviour of sand-GFRP interfaces under monotonic and cyclic shear conditions. It aims to evaluate the impact of sand-epoxy coatings, particle shape, and gradation on the interface friction properties, surface roughness evolution, and long-term performance. The study will also utilise DEM and FEM simulations to model and quantify the micromechanical interactions at the sand-GFRP interface, thereby improving the predictive capabilities for interface behaviour in real-world applications. Ultimately, this research will provide a comprehensive understanding of the factors influencing the durability and load-bearing capacity of sand-GFRP systems, contributing to the design of more resilient and

sustainable GFRP-based structures in the field of geotechnical engineering.

The sand-GFRP interface can be studied through the laboratory test method, which focuses on the failure and deformation mechanism stress-displacement relationship, and then finds the rule of stress distribution and interface displacement along with local and global soil response in critical failure criteria. After that, the experimental findings will be validated using the appropriate constitutive models, and finally, numerical simulation and verification can be done according to practical engineering needs. Therefore, this research aims to investigate the sand-GFRP interface behaviour via experimental testing and numerical approach (FEM and DEM) to expedite the study of the application of GFRP in design and construction. By exploring the effectiveness of sand coating, the performance of sand-epoxied GFRP in application areas such as GFRP sea walls, GFRP piles, and GFRP anchorage in slope reinforcement will be enhanced. Thus, several objectives are set up to achieve the research aims as presented below.

1.2 Statement of the research problem

The shear behaviour of sand-GFRP interfaces remains a critical concern in geotechnical applications, particularly under cyclic loading conditions. While sand coatings and tailored gradation have shown the potential to enhance interface friction, their long-term stability and effectiveness in mitigating surface roughness degradation remain unclear. The detachment of coated particles during shearing raises concerns about interface durability, necessitating further investigation into the impact of sand-epoxy coatings, particle morphology, and stress conditions on shear resistance. Additionally, existing studies have yet to explore sand-GFRP systems through numerical modelling or accurately capture the micromechanical interactions and the evolving surface roughness at the interface. A comprehensive experimental and numerical approach is required to evaluate shear behaviour, optimise coating techniques, and improve predictive models for practical applications such as GFRP sea walls, piles, and slope reinforcement. This study addresses these gaps by integrating laboratory testing

with DEM and FEM simulations to enhance the understanding and durability of sand-GFRP interfaces in real-world engineering scenarios.

1.3 Objectives and significance of the research

Several objectives are made to achieve the proposed study. The objectives of this study are:

1) To investigate the interface shear behaviour of sand-GFRP systems under varying normal stresses, ranging from moderate to large, through monotonic and cyclic shearing tests.
2) To examine the impact of sand-epoxy coatings on the friction properties and surface roughness of GFRP and to assess how these modifications influence the interface shear stress and long-term durability of sand-GFRP interfaces.
3) To evaluate the effect of particle size, particle shape, and roughness on the shear stress and volumetric behaviour of sand-GFRP interfaces under controlled laboratory conditions, considering both loose and dense sand specimens.
4) To identify optimal coating concentrations and sand grades that enhance interface friction property while mitigating excessive roughness fluctuations and interface degradation during cyclic shearing.
5) To utilise the discrete element method (DEM) to simulate the micromechanical behaviour of sand-GFRP interfaces, providing deeper insights into the particle interactions, force chain formation, and surface roughness evolution under different loading conditions.
6) To validate the experimental investigation, evaluate existing constitutive models via the finite element method (FEM) for sand-GFRP interfaces, and identify necessary refinements, particularly in incorporating the effects of particle size and evolving surface roughness in order to enhance the accuracy of numerical predictions for practical engineering applications in future studies.

After completion of this study in both experimental testing and numerical

approach (DEM and FEM), this study will be the basis for the advanced study of the sand-FRP interface shear behaviour, such as model tests and field tests in the future. This study provides a detailed investigation of the effect of several influencing factors, such as particle size and sand mixtures, the impact of normal loadings, and the effect of roughness, which enhance the design constraint. This research holds significant value for both theoretical and practical applications in the field of material interfaces and composite technology. The sand-GFRP interface is crucial in understanding the mechanical properties of GFRP used in various structural applications, especially in environments where frictional resistance plays a pivotal role, such as in geotechnical, ocean, and construction engineering. The following five key points highlight the significance of this research.

1) **Advancing understanding of contact mechanisms:** This study provides critical insights into the complex contact mechanisms at the sand-GFRP interface, contributing to a deeper understanding of particle interlocking, sliding, and rotational effects. This is essential for improving the design and performance of GFRP-based composite structures subjected to varying loading conditions.
2) **Improving GFRP durability and performance:** The incorporation of sand-epoxy coatings to enhance interface friction properties and surface hardness contributes significantly to improving the stability and long-term durability of GFRP in cyclic or dynamic environments, which is essential for the sustainability and reliability of GFRP-based applications in infrastructure and construction.
3) **Material selection and engineering design:** This study's optimisation of sand gradation and coating concentrations provides a framework for designing sand-GFRP interfaces with tailored frictional properties, enhancing load-bearing capacity and reliable long-term performance. The developed design charts offer guidance for material selection and design parameters in geotechnical structures, including foundations and retaining walls.

4) **Contribution to numerical modelling:** The DEM and the FEM simulations of interface shear behaviour provide a robust numerical framework for improving the predictive accuracy of models simulating geotechnical materials. By accounting for evolving surface roughness, micromechanical interactions, and continuum-scale behaviour, this research integrates particle-scale insights to capture global interface response, establishing a foundation for future studies on sand-GFRP systems, offering valuable guidance for design and analysis.
5) **Future research and development:** This study establishes a framework for subsequent experimental and numerical investigations by highlighting gaps in current modelling techniques. Such advancements are expected to deepen the understanding of interface degradation, supporting the development of more resilient and efficient composite materials.

1.4 Structure of the thesis

This thesis is composed of seven chapters. The description of the structure of this thesis is organised below (Figure 1-1).

Chapter 1 is the introduction of the whole research work. This chapter establishes the foundation of the research by delineating the background, statement of the problem, objectives, significance, and organisation of the thesis.

Chapter 2 provides a detailed literature review. A comprehensive review of existing studies on soil-structure interfaces, with a particular focus on sand as the soil medium, is presented. The chapter reviews the macromechanical and micromechanical interaction between sand and structural materials, including steel, geomembranes, and fibre-reinforced polymers. Emphasis is placed on sand-GFRP interfaces, identifying key parameters that influence shear behaviour, which are critical for subsequent experimental and numerical analyses.

Chapter 3 details the experimental procedures and findings related to the monotonic shearing behaviour of sand-GFRP interfaces, considering the effects of sand-epoxy coatings. It explores the impact of variables such as specimen relative density, epoxy-coated sand concentration, and sand mixtures on interface

shear behaviour.

Chapter 4 presents the experimental investigation of sand-GFRP interface behaviour under moderate to large normal stress. Focusing on the evolution of surface roughness in sand-epoxied GFRP and its influence on interface behaviour under monotonic and cyclic shearing, this chapter investigates the long-term durability and performance of sand-epoxy coatings. Factors such as particle size effects, epoxy-coated sand grade (roughness) effects, and normal stress effects are analysed.

Chapter 5 presents DEM simulations to examine the impact of sand-epoxy coatings on sand-GFRP interface shear behaviour at macroscopic and microscopic levels. It emphasises particle interactions at interfaces and the evolution of surface roughness, correlating these findings with the experimental results from Chapter 3.

Chapter 6 presents FEM validation of experimental investigations. The experimental observations are validated through FEM simulations utilising an enhanced hyperbolic model as the constitutive model for sand-GFRP interfaces. The chapter discusses the predictive accuracy of the simulations in replicating observed behaviours.

Chapter 7 provides conclusion by synthesising the main findings of the study and offers recommendations for future research directions.

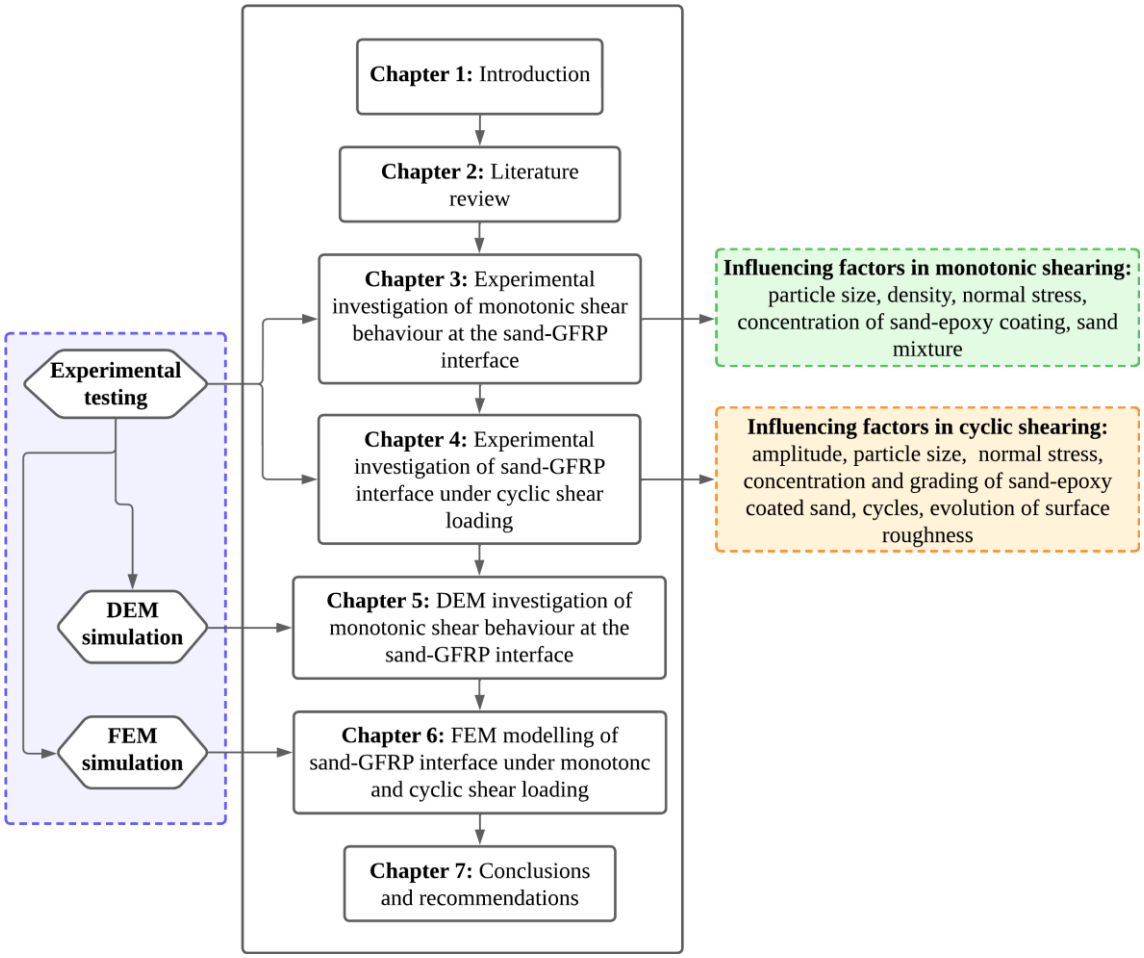

Figure 1-1 Flowchart of the thesis structure

CHAPTER 2: LITERATURE REVIEW

2.1 Introduction

This chapter begins with a comprehensive overview of sand, fibre-reinforced polymer (FRP) composites, and the sand-structure interface to establish a solid understanding of the fundamental material properties and their contact mechanism. This foundational knowledge is critical for analysing the shear behaviour of the interface under both monotonic and cyclic shear loading conditions. The chapter then explores the key factors influencing the soil-structure interface (SSI), specifically focusing on the sand-FRP interface. The discussion then shifts to the application of sand-epoxy coatings on FRP surfaces and their impact on shear behaviour, with particular attention to the evolution of surface roughness based on the latest developments in the field. Finally, a review of numerical methods, including the discrete element method (DEM) and finite element method (FEM), is provided. These methods are essential for investigating the microscopic mechanisms and constitutive modelling of shear behaviour at the sand-FRP interface.

2.2 Classification and morphology of sand

Sand is classified based on particle size, morphology, origin, and mineral composition (ASTM D2487-17e1, 2017). Based on size, it is categorised into fine (0.075-0.425 mm), medium (0.425-2 mm), and coarse (2-4.75 mm) sand. Morphologically, sand particles range from angular to rounded, influencing their mechanical behaviour. Wadell (1932) and Wang et al. (2023) characterised particle morphology using circularity (C_{irc}), which describes proximity to a perfect circle, and roundness (R_{rd}), indicating three-dimensional smoothness. The circularity and the roundness are defined as:

$$\mathrm{C_{irc}} = \frac{4\pi A}{\left(P_{\mathrm{p}}\right)^2} \tag{2-1}$$

$$\mathrm{R_{rd}} = \frac{4A}{\pi a^2} \tag{2-2}$$

where A is the two-dimensional projected area of a particle, P_{p} is the corresponding perimeter of a particle obtained from the projection, and a is the major axis of the ellipse fitting in the projection. Additionally, Janoo (1998) defined the roughness factor (R.F.) to present the texture of particles, which is evaluated by:

$$\mathrm{R.F.} = \left(\frac{P_p}{P_c}\right) \tag{2-3}$$

where P_{c} refers to the convex perimeter of the particle. R.F. equal to 1 indicates a smooth particle.

In recent years, more comprehensive morphological descriptors have been developed to consider a wider range of parameters for detailed particle analysis. Altuhafi et al. (2016) combined sphericity (degree to which a particle's three-dimensional shape approximates a sphere), convexity (ratio of the particle's actual projected area to its convex hull area, indicating surface irregularity), and aspect ratio (ratio of particle length to its intermediate dimension) into a composite morphology index, which showed strong correlation with packing density and angularity. Sphericity, as defined by Vangla and Latha (2015), quantifies the closeness of a particle's shape to a perfect sphere, while circularity, introduced by Wadell (1932) and refined by Liu et al. (2019), is given as the ratio of the diameter of the largest inscribed circle to that of the smallest circumscribed circle in a two-dimensional projection, reflecting 2D shape regularity. Angelidakis et al. (2022) proposed elongation (ratio of particle length to width), flatness (ratio of particle thickness to width), and compactness (degree to which a particle's form approaches an equidimensional shape), offering improved classification between particle forms, particularly for grains with extreme aspect ratios. Dynamic image analysis (DIA) now enables high-resolution and high-throughput quantification of these descriptors, capturing particle form, angularity,

and surface texture with nanometre-scale precision.

Origin-based classifications include river sand (water-rounded), marine sand (deposited by marine processes), desert sand (wind-rounded), glacial sand (mechanically ground by glaciers), volcanic sand (ash-based), and manufactured sand (crushed granite alternative to river sand). Mineralogically, sand may be composed of quartz (silica), feldspar, lithic fragments, carbonate minerals, or iron-rich compounds (e.g., hematite).

The crushing strength and compressibility of sand are strongly influenced by both particle morphology and mineralogy. Morphologically, angular particles are more prone to crushing and promote greater densification under load, as their elongated and irregular shapes concentrate stress at asperities and induce earlier fracture relative to equant or rounded particles. From a mineralogical perspective, carbonate sands generally exhibit lower crush resistance than silica sands. Silica sand, known for its high quartz content, is widely used in interface direct shear tests under normal stresses of 50-800 kPa due to its well-documented contact performance (Frost and Han, 1999; DeJong and Westgate, 2009; Ho et al., 2011; Rui et al., 2021; Westgate and DeJong, 2023). Its consistent properties enable direct comparisons with existing research, improving the reliability of interface shear behaviour studies. Additionally, particle shape, size distribution, and intergranular friction properties are critical factors in evaluating foundation load-bearing capacity, settlement behaviour, and failure mechanisms (e.g., White et al., 2013; Wu et al., 2020).

2.3 Fibre-reinforced polymer composites

2.3.1 Applications of FRP composites

Fibre-reinforced polymer (FRP) composites consist of continuous fibres, such as glass, carbon, or aramid, embedded in a polymer resin matrix (e.g., epoxy, polyester, vinylester). The fibres are the primary load-bearing component, making their type and volume fraction critical to performance, while the resin matrix ensures fibre alignment, force transfer, and supports compressive loads.

Key FRP materials include glass fibre-reinforced polymer (GFRP), carbon fibre-reinforced polymer (CFRP), and aramid fibre-reinforced polymer (AFRP) (e.g., Alnatit, 2011; Qureshi, 2022). A tensile test comparison of CFRP, GFRP, AFRP, and steel bars (Figure 2-1) demonstrated superior tensile strength and stiffness for CFRP, with GFRP offering excellent ductility and AFRP a balanced performance across loading conditions (Alnatit, 2011). Steel, however, exhibited the highest ultimate strength in the plastic state.

FRP composites are manufactured using methods such as pultrusion for high-quality composites, wet lay-up with woven fabric sheets for flexibility, and prepreg for convenient application and research purposes (Qureshi, 2022). Orthophthalic and isophthalic epoxy resins are commonly used, with thixotropic epoxy also employed in CFRP and large rupture strain FRP (LRS-FRP) composites (Teng et al., 2024). Teng et al. (2024) used these resins to prepare GFRP plates via wet lay-up (Figures 2-2(a) to 2-2(c)), while Figures 2-2(d) and 2-2(e) illustrate CFRP and GFRP sheets used in Giraldo and Rayhani (2013).

FRPs offer advantages over traditional materials like reinforced concrete and timber, including a high strength-to-weight ratio, exceptional corrosion resistance, and electrical non-conductivity (Frost and Han, 1999; Bakis et al., 2002; Bai, 2023a). GFRPs are also transparent to radio frequencies and more cost-effective than CFRPs in structural and underground applications (Qureshi, 2022). However, limitations include the lack of yielding before rupture and the lower modulus of elasticity of GFRP compared to steel (Alnatit, 2011; Bai, 2023b). Despite these drawbacks, FRPs are widely used in construction, including structural strengthening, hybrid reinforcement, and applications in bridges, parking structures, underwater installations, and tunnels (e.g., Frost and Han, 1999; Bakis et al., 2002; Bai, 2023a). The interaction between soil and FRP, particularly in terms of shear resistance and soil deformation at the interface, is crucial for evaluating the performance of FRP-reinforced geotechnical systems (Archard, 1957; Frost and Han, 1999).

2.3.2 Methods for enhancing surface properties of FRP

FRP composites exhibit characteristics such as anisotropy, reduced stiffness, lower surface hardness, and diminished surface roughness, distinguishing them from steel and reinforced concrete (Iskander and Hassan, 1998; Frost and Han, 1999; Pando et al., 2002; Sakr et al., 2005). To address challenges related to low surface hardness and reduced friction at the soil-FRP interface, a sand-coating technique was introduced to enhance the performance of CFRP (Toufigh et al., 2016). Almallah et al. (2020a) applied sand coatings to GFRP sheets using silica sand concentrations ranging from 500 g/m^2 to 2500 g/m^2, while Namjoo et al. (2022) produced sand-coated CFRP surfaces with particle sizes between 0.23 mm and 1.59 mm, creating textures from smooth to highly rough, as shown in Figure 2-3. These studies consistently demonstrated that sand coatings improve friction properties at interfaces and surface roughness (Namjoo et al., 2022).

2.3.3 Surface roughness measurement parameters

Introducing the structural surface measurement parameters, Yoshimi and Kishida (1981) introduced the maximum height of surface asperities as a parameter for quantifying steel roughness, which they termed the maximum roughness ($R_{\max}$). This parameter quantifies the vertical distance between the highest peak and the lowest valley within a defined sampling length on a surface. Later, Uesugi and Kishida (1986b) used average maximum roughness ($R_{\max,\text{avg}}$) parameter to define interface roughness as presented in Equation (2-4):

$$R_{\max,\text{avg}} = \frac{1}{n}\sum_{i=1}^{n}\left(R_{\text{z,max,}}\right)_i \tag{2-4}$$

where $\left(R_{\text{z,max,}}\right)_i$ refers to the maximum roughness in each sampling length for i =1, …, n samples. Similarly, DeJong and Westgate (2009) introduced the arithmetic average roughness parameter based on Thomas's mean line (1998), as presented in Equation (2-5a).

$$R_{\mathrm{a}} = \frac{1}{l}\int_{0}^{l} |z| dx \tag{2-5a}$$

Where $|z|$ refers to the absolute height of the surface profile from the mean line. R_{a} can be obtained for structural surfaces using instruments such as Profilometers and Laser Scanning Microscopes. ISO 4287 (1997) defines the standard parameters for surface texture characterisation (Equations (2-5b) to (2-5e)). These parameters are derived from the roughness profile in accordance with the standard methodology, as illustrated in Figure 2-4(a). Surface texture characteristics considering varieties of parameters such as maximum height of profile (R_{z}), total height of profile (R_{t}), mean height of profile (R_{c}) have purpose-specific uses in measuring roughness on regular surface textures.

$$R_{\mathrm{z}} = R_{\mathrm{p}} + R_{\mathrm{v}} \tag{2-5b}$$

$$R_{\mathrm{t}} = \max\left(R_{\mathrm{p}(i)}\right) + \max(R_{\mathrm{v}(i)}) \tag{2-5c}$$

$$R_{\mathrm{c}} = \left(\frac{1}{m}\right)\sum_{i=1}^{m} R_{t(i)} \tag{2-5d}$$

$$R_{\mathrm{q}} = \sqrt{\frac{1}{l}\int_{0}^{l} z^2(x) dx} \tag{2-5e}$$

Although R_{z} and R_{max} may appear similar, but their concepts differ. R_{z} computes the average of the five highest peaks along the sampling length, whereas R_{max} represents the maximum value within the entire sampling length ($R_{\mathrm{z,max}}$). Additionally, an average amplitude in height direction can be obtained by root mean square roughness (R_{q}). The three-dimensional evaluation method analyses the entire surface rather than multiple individual profiles. This approach reduces the risk of missing areas with the highest peaks or deepest valleys. Key 3D parameters, such as maximum peak height (S_{p}), maximum valley depth (S_{v}), and maximum height ($S_{\mathrm{z}} = S_{\mathrm{p}} + S_{\mathrm{v}}$), are comparable to their 2D counterparts (Araújo et al., 2022). Additionally, mean height parameters, including the arithmetical mean height (S_{a}) and root mean square height (S_{q}), correspond to the 2D R_{a} and R_{q} values, respectively, reflecting surface topography. Other

parameters, such as peak material volume (V_{mp}), core material volume (V_{mc}), core void volume (V_{vc}), and dale void volume (V_{vv}), can be derived from the material ratio curve, which represents the cumulative surface distribution with areal material ratio (m_r) on the horizontal axis and surface height or depth on the vertical axis. Two intermediate values, 'p' and 'q', are related to V_{vv} and V_{mp} linked to the lowest valley and the highest peaks (Figure 2-4(b); Araújo et al., 2022). For example, recent studies (Vangla and Gali, 2016; Teng et al., 2024) have employed a 3D approach to illustrate the topography of geomembranes and GFRPs. Overall, Araújo et al. (2022) suggested that, among several widely used parameters. S_a is a reliable parameter to investigate the evolution of surface roughness.

$$S_a = \frac{1}{M.N} \int_0^N \int_0^M |z(x,y)| dxdy \tag{2-6a}$$

$$S_q = \frac{1}{M.N} \int_0^N \int_0^M z^2(x,y) dxdy \tag{2-6b}$$

Where *M* and *N* are length and breadth of the area field.

2.4 Shear behaviour at the soil-FRP interface

2.4.1 Experimental devices for interface shear testing

The shear behaviour of soil-structure interfaces has been studied using various laboratory testing devices. These include the interface direct shear apparatus (Potyondy, 1961; Desai et al., 1985; Al-Douri and Poulos, 1992; Hu and Pu, 2004; Sakr et al., 2005; DeJong and Westgate, 2009; Wang et al., 2019; Teng et al., 2024), ring shear apparatus (Yoshimi and Kishida, 1981; Ho et al., 2011; Zhou et al., 2020), two-dimensional simple shear apparatus (Uesugi and Kishida, 1986a, 1986b; Tsubakihara and Kishida, 1993), and three-dimensional simple shear apparatus (Evgin and Fakharian, 1998). Large-scale methods such as the large-scale shear apparatus (Zhang and Zhang, 2006; Feng et al., 2018), pull-out tests

(Zhang et al., 2015), and model-scale tests (Sakr et al., 2005; Giraldo and Rayhani, 2014) have also been used to examine interface shear behaviour.

Among these, the ring shear apparatus is particularly effective for measuring the full shear strength envelope, including post-peak behaviour and large displacements, without constraints from the apparatus' movement (Rui et al., 2021; Zohra et al., 2022). While direct shear tests can suffer from stress concentration near the edges, their simplicity, cost-effectiveness, and ability to focus on interface-specific parameters such as stress-displacement behaviour, friction angles, and adhesion make them ideal for studying interfaces like soil-geosynthetic and soil-steel boundaries. As a result, the interface direct shear apparatus is commonly used to research sand-FRP interface shear behaviour (Frost and Han, 1999; Sakr et al., 2005; Almallah et al., 2020a; Teng et al., 2024).

2.4.2 Influence of boundary conditions

Boulon (1989) proposed a novel interpretation of interface behaviour in direct shear tests, identifying two distinct zones during shearing: (a) the active zone, where tangential deformations occur, corresponding to the shear zone thickness, extending from the structural contact point to several times the mean particle size, and (b) the passive zone, adjacent to the shear zone, where only vertical deformations occur, resembling oedometric conditions. Three boundary conditions have been considered for studying soil-structure interfaces: constant volume (CV), constant normal load (CNL), and constant normal stiffness (CNS) (e.g., Fioravante et al., 1999; Porcino et al., 2003; Di Donna et al., 2015; Maghsoodi et al., 2020a; Maghsoodi et al., 2020b; Yang and Yin, 2021; Figure 2-5). The CNL condition predicts a higher volumetric response, while the CV condition predicts a lower response. The CNS condition is recommended for studying actual stress-displacement and volumetric behaviour, as it more accurately represents real-world stress changes during interface shearing (e.g., Porcino et al., 2003; Di Donna et al., 2015). Although CNS better reflects field conditions, most sand-FRP interface studies use CNL due to its simplicity, cost-effectiveness, and alignment with standard geotechnical testing protocols. CNL

tests require less specialised equipment and provide straightforward results, making them more accessible for foundational studies (e.g., Frost and Han, 1999; Namjoo et al., 2022).

2.4.3 Overview of soil-structure interface behaviour

Understanding the behaviour of sand-structure interfaces is crucial in geotechnical applications, as failure modes are highly dependent on the density of the sand. General shear failure occurs in dense sand, punching shear failure in loose sand, and local shear failure represents an intermediate case (Yin et al., 2020). The performance of sand-structure interfaces under various loading conditions is commonly evaluated through critical design parameters such as peak, critical state, and ultimate friction angles. However, mobilised interface shear strength is typically lower than that of pure soil, particularly under long-term or repeated loading conditions (e.g., Bishop, 1966; Ponce and Bell, 1971; Yoshimi and Kishida, 1981; Jewell, 1989; Al-Douri and Poulos, 1992; Paikowsky et al., 1995; Evgin and Fakharian, 1998; Frost and Han, 1999; Feng et al., 2018; Liu et al., 2021).

2.4.3.1 Shear mechanisms and behaviour at sand-structure interfaces

Direct shear tests are widely employed to investigate sand-structure interactions, particularly for evaluating residual or ultimate shear strength, defined as the state in which additional horizontal displacement produces no further changes in shear stress. These tests provide valuable insight into both local and global responses during shearing (DeJong and Westgate, 2009). The behaviour of sand during shearing is primarily influenced by density. Dense sand experiences outward particle movement from the shear zone, resulting in dilation and volumetric expansion, which contributes to peak shear strength and a strain-softening response (Figure 2-6). Loose sand exhibits inward particle movement, leading to contraction and volumetric compression, which results in a residual shear strength and a strain-hardening response (Figure 2-6; Hu and Pu, 2004).

The peak internal friction angle (ϕ_p) and ultimate internal friction angle

(ϕ_{ult}) in the direct shear tests for pure sand shearing, can be obtained from the Mohr-Coulomb stress envelope:

$$\phi_p = \tan^{-1}\left(\frac{\tau_p}{\sigma_n}\right) \quad (2\text{-}7a)$$

$$\phi_{ult} = \tan^{-1}\left(\frac{\tau_{ult}}{\sigma_n}\right) \quad (2\text{-}7b)$$

where τ_p is the peak shear strength of sand and τ_{ult} is the ultimate shear strength, which represents the post-peak stable shear stress state of sand, and σ_n is the applied normal stress on the shearing plane of the sand specimen. Similarly, the peak interface friction angle (δ_p) and ultimate interface friction angle (δ_{ult}) for sand-FRP interfaces can be determined from:

$$\delta_p = \tan^{-1}\left(\frac{\tau_p}{\sigma_n}\right) \quad (2\text{-}8a)$$

$$\delta_{ult} = \tan^{-1}\left(\frac{\tau_{ult}}{\sigma_n}\right) \quad (2\text{-}8b)$$

herein τ_p is the peak shear stress and τ_{ult} is the ultimate shear stress at the interface.

Throughout the shearing process, sand particles undergo translation, rotation, slip, rearrangement, and crushing, which collectively influence shear strength and interface friction (e.g., DeJong and Westgate, 2009; Ho et al., 2011; Lashkari and Jamali, 2021). Slip at the sand-structure interface is primarily due to insufficient interlocking between particles, leading to reduced friction properties. For rough interfaces, bulk dilatancy and strain localisation are prominent, whereas smooth interfaces tend to experience slipping with minor dilation (Hu and Pu, 2004). Several strategies have been proposed to mitigate slips and enhance shear strength at sand-FRP interfaces. These include increasing surface roughness and applying sand coatings, which improve interface friction and adhesion (e.g., Sakr et al., 2005; Almallah et al., 2020a). Additionally, optimising particle size, particle shape, and increasing normal stress enhances shear resistance, thereby further minimising slip (e.g., Westgate and DeJong, 2023). Higher normal loads contribute to greater shear resistance and a narrower shear

zone, especially in dense sand, while intense shearing influences volumetric strain variations and shear band formation (DeJong and Westgate, 2009).

2.4.3.2 Shear zone thickness and particle interlocking

The thickness of the shear zone varies based on material properties and loading conditions. Previous studies on sand-steel interfaces (e.g., Uesugi et al., 1988; Hu and Jia, 2003; Hu and Pu, 2004; DeJong and Westgate, 2009; Pra-ai and Boulon, 2017) reported shear zone thicknesses ranging between $5D_{50}$ and $12D_{50}$, whereas for geotextiles and geomembranes, the shear zone thickness was typically between $2D_{50}$ and $10D_{50}$ (e.g., Frost et al., 2002; Frost et al., 2012; Lashkari and Jamali, 2021).

Particle shape and gradation significantly affect shear behaviour. Angular particles tend to increase shear zone thickness and dilation, as they provide greater interlocking during shear. The shear zone thickness is influenced by several factors, including particle size, particle shape, initial density, and surface roughness (David Suits et al., 2003; Tiwari and Al-Adhadh, 2013). The coefficient of uniformity is often used to represent particle size distribution. Studies have shown that well-graded gravel exhibits higher interface friction with CFRP composites compared to poorly graded gravel (Lavanya et al., 2014). Specimens with a smaller void ratio enhance particle interlocking, improving interface friction with CFRP materials. However, for sands, a lower coefficient of uniformity results in higher interface friction when sheared against grooved steel plates (Wang et al., 2019).

2.4.3.3 Recent practices for enhancing FRP surface properties in soil-structure interfaces

The primary challenges of FRP applications in geotechnical engineering are its inherently low hardness, surface roughness, and interface friction properties. Various techniques have been explored to address these limitations, mainly through surface finishing and sand-coating methods.

(1) Surface finishing techniques

Sakr et al. (2005) investigated the use of rough surface finish GFRP to enhance interface shear strength. Their experimental findings indicated that rough-surfaced FRP increased interface friction angles and promoted strain-softening behaviour in dense sand-FRP interfaces. Similarly, Giraldo and Rayhani (2013) observed that protruded fibres enhanced resistance by improving interlocking at the shearing surface. The importance of epoxy type and surface treatment in achieving optimal surface hardness and interface friction was also highlighted (Teng et al., 2024).

(2) Sand-coating methods

Toufigh et al. (2016) introduced a sand-coating technique to enhance FRP roughness, significantly improving interface shear strength. The interlocking between soil particles and sand-coated GFRP plates resulted in an increased interface friction angle, as reported by Almallah et al. (2020a). Studies suggest that the optimal ratio of coating sands varies with the surrounding soil type. For instance, silty sand and sandy lean clay exhibited the highest interface friction angle at 2000 g/m^2 sand-coated GFRP, while sand achieved maximum friction at 1500 g/m^2 (Almallah et al., 2020a).

Further research by Namjoo et al. (2020) demonstrated that shearing fine and medium sands against sand-coated CFRP increased the peak friction angle by 15% to 37% compared to uncoated CFRP. Similarly, Almallah et al. (2020b) reported that 1500 g/m^2 silica sand-coated GFRP improved peak friction angles by 28% relative to uncoated GFRP. For GFRP piles, sand coating enhanced the ultimate pile capacity by 30% over steel piles (Almallah et al., 2020b). However, after testing, sand particle detachment from coated piles indicates a need for improved coating durability in future applications. Additionally, the normalised roughness ($R_{\text{max.avg}}/D_{50}$) for sand-coated CFRP ranged between 0.2 and 0.5, with variations depending on mean particle size (Namjoo et al., 2022). For instance, the mean particle size of 0.45 mm of the sand-coated surface was critical for 0.45 and 0.23 mm of the mean particle sizes of sand specimens. However, 0.89 mm of the sand-coated surface was critical for 2.18, 1.59, and 0.89 mm of mean particle sizes of sand specimens (Namjoo et al., 2022). While previous studies reported negligible

roughness changes under normal stresses up to 100 kPa, its behaviour at higher stress levels common in engineering applications remains uncertain, highlighting the need for further research (e.g., Frost and Han, 1999; Pando et al., 2002; Sakr et al., 2005; Toufigh et al., 2016; Almallah et al., 2020b; Namjoo et al., 2020; Namjoo et al., 2022).

2.4.4 Factors influencing monotonic shearing

The primary focus of this section is to review the previous studies on soil-FRP interface shear behaviour, influencing factors, and interface roughness-enhancing mechanisms to improve the friction of the soil-FRP interface. Several studies were conducted in the soil-FRP structure interface, mostly in the direct shear box test and a few in the soil-FRP pile model test. Iskander and Hassan (1998) performed a test on the pile using conventional material and FRP. Their study found that the FRP pile's performance was better than steel and concrete piles in terms of durability and corrosion resistance (Iskander and Hassan, 1998).

2.4.4.1 Particle characteristics and soil density

Frost and Han (1999) conducted the direct shear test to study sand-FRP interface behaviour with subrounded to rounded shape of silica-enriched Ottawa sand, subangular to angular shape of blasting sand, and rounded shape of glass beads as granular material, and steel and FRP as structural material. They found that the interface friction angle decreases with an increase in mean particle size in the identical roughness of FRP, which indicates less contact of larger particles with the FRP. Angularity promotes interface contact and interlocking at the interface (e.g., Frost and Han, 1999; Namjoo et al., 2022). Furthermore, they reported that larger particle sizes having relatively angular shapes enhance interface friction (e.g., Namjoo et al., 2020; Namjoo et al., 2022). Thus, the interlocking mechanism becomes more pronounced, and the contact area expands, leading to stronger resistance. A dry sand-FRP interface exhibited higher interlocking than a glass bead-FRP interface (Frost and Han, 1999).

The denser the specimen, the higher the contact between specimen particles

and the surface, which contributes to more significant shear strength and promotes strain-softening (e.g., Frost and Han, 1999; Tiwari and Al-Adhadh, 2013). Namjoo et al. (2020) investigated the shear behaviour of sand-geosynthetic and sand-CFRP interfaces. Sand samples with three different particle sizes (D_{50}: 0.247 mm, 0.726 mm, and 1.22 mm) were prepared at a relative density of 70% for a modified interface direct shear test. The results showed no softening behaviour in the sand-CFRP interface, while CFRP with low surface roughness was employed; however, increased surface roughness led to a slight strain-softening.

2.4.4.2 Effect of shearing rate

Unlike the shear behaviour of clay-structure interfaces, where drainage conditions and viscosity are influenced by the shearing rate (Martinez and Stutz, 2019), sand-FRP interfaces quickly attain the ultimate state due to the drained conditions and the non-cohesive nature of the sand particles. This results in minimal or no significant effect on interface shear strength within the range from 0.25 to 5.08 mm/min of shearing rate (Frost and Han, 1999; Toufigh et al., 2016). However, most studies on the shearing rate in sand-FRP interfaces focused on rates between 0.2 mm/min and 1.0 mm/min (e.g., Pando et al., 2002; Sakr et al., 2005; Almallah et al., 2020a; Teng et al., 2024), ensuring an adequate length of interface shearing to reach the ultimate state provided with a minimum of 10 minutes of shearing in accordance with ASTM D3080-11 (2011).

2.4.4.3 Effect of normal stress

Previous studies have consistently demonstrated that normal stress significantly influences interface shear strength (e.g., Potyondy, 1961; Desai et al., 1985; Paikowsky et al., 1995; Frost and Han, 1999; Zettler et al., 2000; Fleming et al., 2006; Lashkari and Jamali, 2021). Investigations into the shear behaviour of sand and sand-FRP interfaces (e.g., Frost and Han, 1999; Pando et al., 2002; Sakr et al., 2005; Almallah et al., 2020a; Namjoo et al., 2020) have consistently shown that increasing normal stress enhances interface shear strength by suppressing

particle rearrangement and surface contact, thereby reducing the friction coefficient.

Higher normal stress promotes particle penetration into softer FRP surfaces, leading to scar and trench formation (Pando et al., 2002; Sakr et al., 2005). Stress hardening predominates on smooth surfaces, while post-peak behaviour emerges on rougher interfaces (Sakr et al., 2005). Trenching of polymers during shearing, termed the ploughing effect, results in increased abrasion of FRP or polymer materials (Shooter and Tabor, 1952; Frost and Han, 1999; Fleming et al., 2006; O'Rourke et al., 1990; Han, 1997; Dove and Frost, 1999). Three distinct interface responses under increasing normal stress have been identified (Figure 2-7):

Case I (Semi-hard to hard surfaces): Minimal roughness evolution; friction coefficient decreases with stress, stabilising at higher stresses (Archard, 1957; Frost and Han, 1999).

Case II (Semi-hard surfaces): Surface roughness facilitates particle slipping; polymers transition from elastic to plastic deformation, gradually reducing friction (Archard, 1953, 1957).

Case III (Soft to semi-hard surfaces): Indentation and trenching cause initial friction reduction, followed by an abrupt increase due to ploughing, common in softer geomaterials (Dove and Frost, 1999; Vangla and Latha, 2015; Chen et al., 2021).

Dove and Frost (1999) further noted that friction initially declines as stress per particle decreases with more contact. However, beyond a critical stress threshold, increased stress transmission induces particle ploughing, thereby enhancing interface friction, particularly in softer materials.

2.4.4.4 Effect of surface roughness and interface roughness

The surface characteristics of structures, including texture type and asperity height/angle, significantly influence soil-structure interaction (SSI) behaviour (Chen et al., 2015; Feligha et al., 2015; Martinez and Frost, 2017). Surface roughness is crucial in enhancing interface friction, as increased roughness improves the interface friction angle (Tsubakihara et al., 1993; Feligha et al.,

2015; Chen et al., 2015; Su et al., 2018; Zhang et al., 2021). Rough surfaces promote strain-softening and dilation in dense specimens, whereas, in loose specimens, they induce strain-hardening and contraction (Tiwari and Al-Adhadh, 2013; DeJong and Westgate, 2009). Tsubakihara et al. (1993) identified three idealised failure modes for soil-structure interfaces (Figure 2-8):

(1) **Rough surface-induced shear failure:** Granular soils like sand experience shear failure due to interlocking with asperities, leading to higher shear resistance than clay.

(2) **Smooth surface-induced shear failure:** Minimal roughness reduces friction, promoting particle sliding, particularly in sand, whereas clay retains some cohesion-induced resistance.

(3) **Intermediate roughness-induced failure:** A combination of particle shearing and sliding occurs, with sand undergoing partial interlocking and clay experiencing dominant displacement sliding.

The interface peak strength is governed by surface roughness, initial relative density, and particle irregularities (Lashkari and Jamali, 2021). Increased particle irregularity enhances penetration into soft geosynthetics, promoting rolling and sliding (Ari and Akbulut, 2022; Feng and Wang, 2023). On smooth interfaces (R_n < 0.03), sliding dominates as sand particles exceed asperity dimensions (Martinez and Frost, 2017). Higher relative density and particle regularity increase interface slip, whereas increased normal stress and mean particle size reduce it, particularly against softer structural materials (Lashkari and Jamali, 2021).

Roughness quantification is essential, with parameters such as arithmetic average roughness, profile height, and maximum height aiding local and global assessments (Araújo et al., 2022). FRP surfaces exhibit minimal roughness, balancing slip resistance with adequate interlocking (Frost and Han, 1999). Therefore, understanding surface roughness evolution is critical in evaluating sand-FRP interface shear behaviour, with further discussions addressing friction enhancement strategies.

2.4.4.5 Evolution of surface roughness under monotonic shearing

FRP deterioration in ocean environments arises from continuous wave-induced granular material thrust, where angular particles exacerbate groove and trench formation as normal stress exceeds a critical threshold (Dove and Frost, 1999; Vangla and Latha, 2015). Degradation intensifies with increasing particle size, leading to enhanced penetration, rolling, and sliding of particles in soft materials like geosynthetics (Zettler et al., 2000; Frost et al., 2012; Vangla and Latha, 2015; Xu et al., 2023; Ari and Akbulut, 2022; Feng and Wang, 2023).

Unlike geomembrane surfaces, which experience ploughing or indentation, semi-hard surfaces like GFRP undergo abrasion primarily due to mass sliding and rotational particle interactions rather than direct indentation (Pando et al., 2002; He et al., 2021). Mass sliding at the sand-FRP interface, driven by normal stress, leads to epoxy degradation, forming linear scars and shallow grooves, as shown in Figure 2-9 (Pando et al., 2002; Sakr et al., 2005; Giraldo and Rayhani, 2013; Vangla and Latha, 2015; He et al., 2021). Meanwhile, rotational effects, where sand particles twist and spin due to surface roughness, generate mechanical interlocking, increasing friction and resistance to movement (Lashkari and Jamali, 2021; Chen et al., 2021). When shear stress surpasses interlock resistance, surface degradation accelerates, leading to deeper grooves and epoxy breakdown (Vangla and Latha, 2015; Vangla and Gali, 2016; Chen et al., 2021; He et al., 2021). These effects intensify with increasing particle size and angularity, and their coupling further accelerates FRP surface wear and damage.

The surface roughness evolution in FRP differs from geomembranes due to distinct mechanical properties, though some mechanistic similarities may exist. Understanding sand-FRP interface roughness evolution is essential for evaluating wear characteristics, durability, and performance under monotonic and cyclic shearing conditions. A detailed investigation into this process is crucial for assessing FRP longevity in harsh environments.

2.4.5 Factors influencing cyclic shearing

Foundation elements such as piers, piles, and anchors endure static, periodic, and

cyclic loads from traffic, waves, earthquakes, and machinery. Differential settlement due to cyclic loading critically affects structural stability, as repeated loading deteriorates structural capacity, particularly pile shaft resistance, by inducing cumulative soil contraction in the shear zone, leading to residual deformation (Figure 2-10; Wichtmann, 2016; Maghsoodi, 2020). Assessing mobilised shear stress and deformation at sand-FRP interfaces under cyclic shearing is crucial for foundation design. Cyclic loading effects are investigated through laboratory element tests, model tests, centrifuge tests, and field tests. Among these, direct shear tests remain fundamental, with two primary approaches: (a) stress-controlled cyclic shearing, commonly applied in geotechnical engineering for studying soil behaviour under cyclic loading (e.g., earthquakes, traffic loads) and (b) displacement-controlled cyclic shearing, frequently used in laboratory settings to evaluate material deformation and stress-strain responses (DeJong et al., 2003). Displacement-controlled testing is preferred in controlled environments, offering valuable insights into material cyclic responses. Key factors affecting sand-FRP interface behaviour under cyclic loading include particle characteristics, loading amplitude, normal stress, and cycle numbers. Reviewing interface behaviour with steel, concrete, and geosynthetics aids in understanding. And clarify how the sand-FRP interface will perform under repeated loading conditions.

2.4.5.1 Particle characteristics and soil density

The cyclic shear response and volumetric behaviour at the sand-structure interface are influenced by particle shape, size, and specimen density (Uesugi et al., 1989; Al-Douri and Poulos, 1992; Westgate and DeJong, 2023). Angularity enhances interlocking, increasing cyclic shear stress, whilst larger particle sizes contribute to higher interface friction due to increased contact area and particle fragmentation (Uesugi et al., 1989; Westgate and DeJong, 2023). However, this mechanism relies on effective particle-interface contact.

Denser specimens with angular particles exhibit pronounced strain-softening, whereas smaller, angular particles in looser specimens facilitate earlier

contraction under cyclic shearing due to easier particle rearrangement (Westgate and DeJong, 2023). Global and local soil-structure interaction (SSI) behaviour, analysed via particle image velocimetry (PIV) (White, 2002; DeJong et al., 2003; Westgate and DeJong, 2023), highlights the interplay between particle angularity, size, densification, and surface roughness in shear zone formation and particle translation, rotation, and interlocking.

For instance, dense subrounded silica sand (D_{50} = 0.74 mm) against smooth surfaces favours mass sliding, whereas rougher surfaces promote interlocking and shear zone formation (~7 mm thick) (Westgate and DeJong, 2023). Conversely, larger particles against smooth surfaces experience minimal interlocking, leading to interface slippage (Rui et al., 2021). Understanding these mechanisms is essential for evaluating sand-FRP cyclic shear behaviour in geotechnical applications.

2.4.5.2 Effect of amplitudes and cycle numbers

Displacement-controlled cyclic shearing primarily depends on tangential displacement amplitude, with most studies conducted within a range of ±0.4 mm to ±5.0 mm (Desai et al., 1985; Al-Douri and Poulos, 1992; Shahrour and Rezaie, 1997; Oumarou and Evgin, 2005; Rui et al., 2021). Larger amplitudes increase displacement reversal zones, facilitating more significant particle movement and rearrangement (Oumarou and Evgin, 2005; Rui et al., 2021). The greatest vertical compression in calcareous and silica sand specimens was observed at ±5.0 mm within this range (Al-Douri and Poulos, 1992). At small amplitudes (< ±1.0 mm), particle movement is restricted when the mean particle size is comparable to or exceeds the semi-amplitude, necessitating a higher number of cycles to reach a stable mobilised shear stress state. Increasing tangential displacement amplitude and cycle count degrades interface strength and stiffness (Poulos, 1989; Cen et al., 2018), though prolonged cycling induces densification, stabilising strength degradation (Zhou et al., 2020). Rui et al. (2021) found that cumulative cyclic displacements of 0.5 m and 1.0 m were required to reach stability for fine (0.1-0.25 mm) and medium (0.5-1.0 mm) sand, respectively, against steel surfaces.

The number of cycles required for stable mobilised shear stress depends on mineralogy, particle characteristics, and surface degradation under given tangential cyclic amplitude and normal stress (Rui et al., 2021; Westgate and DeJong, 2023). Asymmetric hysteresis loops may form due to the anisotropy of FRP materials, leading to differences in interface shear strength during forward and backward shearing. This anisotropy was observed by Vieira et al. (2013) and Wang et al. (2016) in cyclic testing of sand-geotextile and soil-geogrid interfaces, respectively. To account for anisotropy in FRP, the maximum shear strength in each cycle of cyclic shearing can be determined by the maximum cyclic shear stress during forward shearing ($\tau_{\mathrm{m}}^{\mathrm{a}}$) and reverse shearing ($\tau_{\mathrm{m}}^{\mathrm{b}}$). This value represents the mobilised cyclic shear stress (τ_{m}) (Desai et al., 1985). No anisotropy is present if the forward and reverse mobilised shear stresses are equal (Equation (2-9a)). Otherwise, both forward and reverse mobilised shear stresses must be considered separately to assess the anisotropy effect (Equation (2-9b)). In practice, the forward mobilised shear stress typically serves as the representative measure of shear strength, reflecting the primary loading direction. The stiffness and damping ratio of cyclic tests can be determined using secant shear stiffness (K) and damping ratio (D) definitions (Desai et al., 1985; Vieira et al., 2013; Wang et al., 2016; Figure 2-11).

$$\tau_{\mathrm{m}} = |\tau_{\mathrm{m}}^{\mathrm{a}}|, \qquad \text{if } |\tau_{\mathrm{m}}^{\mathrm{a}}| \geq |\tau_{\mathrm{m}}^{\mathrm{b}}| \tag{2-9a}$$

$$\tau_{\mathrm{m}} = \{|\tau_{\mathrm{m}}^{\mathrm{a}}|, |\tau_{\mathrm{m}}^{\mathrm{b}}|\}, \qquad \text{if } |\tau_{\mathrm{m}}^{\mathrm{b}}| \gg |\tau_{\mathrm{m}}^{\mathrm{a}}| \tag{2-9b}$$

$$K = \frac{|\tau_{\mathrm{m}}^{\mathrm{a}}| + |\tau_{\mathrm{m}}^{\mathrm{b}}|}{2\Delta_{\mathrm{a}}} \tag{2-10}$$

$$D = \frac{D_1 + D_2}{2} = \frac{1}{2}\left(\frac{A}{4\pi A_1} + \frac{A}{4\pi A_2}\right) = \frac{A}{4\pi\Delta_{\mathrm{a}}}\left(\frac{1}{|\tau_{\mathrm{m}}^{\mathrm{a}}|} + \frac{1}{|\tau_{\mathrm{m}}^{\mathrm{b}}|}\right) \tag{2-11}$$

where Δ_{a} is the displacement semi-amplitude, D_1 and D_2 are the damping ratios for the first and second half-cycles; A is the total area of the loop, and A_1 and A_2 are the dashed regions as presented in Figure 2-11.

2.4.5.3 Effect of surface roughness

Rough surfaces in cyclic shearing facilitate greater particle rearrangement at the interface compared to monotonic shearing, significantly affecting material behaviour (Shahrour and Rezaie, 1997; Rui et al., 2021). Surface roughness plays a crucial role in enhancing interfacial shear strength, influencing deformation mechanisms, and inducing volume changes such as dilation or contraction as particles interlock and adjust under repeated loading cycles (Uesugi et al., 1989). Shahrour and Rezaie (1997) examined the effects of surface roughness on loose and dense specimens, using polished steel surfaces to create a smooth interface and glued sand particles on steel blocks for a rough interface. Smooth surfaces exhibited lower interfacial shear strength due to reduced interlocking, often leading to strain-hardening or hysteresis deterioration, where shear strength increases with cyclic loading (Chiang, 1999; Figure 2-12a). Conversely, rough surfaces enhanced interlocking between particles and surface materials, promoting dilation in dense specimens during initial cycles, followed by particle rearrangement, resulting in volume expansion and strain-softening (DeJong et al., 2003; Westgate and DeJong, 2023; Figure 2-12b).

Normal displacement analysis of dense sand specimens further illustrates dilation on stress reversal (Figure 2-13; DeJong et al., 2003). Over successive cycles, greater contraction was observed on rough surfaces compared to smooth ones (Shahrour and Rezaie, 1997). Additionally, the effect of particle size necessitates further investigation into relative roughness and its role in cyclic shearing behaviour. Notably, the impact of sand-coated FRP on cyclic shearing remains underexplored in the literature, highlighting the need for further research into sand-FRP interface shear behaviour.

2.4.5.4 Effect of normal stress

Most cyclic shearing studies have been conducted under ≤ 400 kPa normal stress (Desai et al., 1985; Al-Douri and Poulos, 1992; Shahrour and Rezaie, 1997; Oumarou and Evgin, 2005; Mortara et al., 2007; Rui et al., 2021), with limited research at higher stresses (e.g., Westgate and DeJong, 2023). Using a ring shear device, Rui et al. (2021) investigated silica and carbonate sand against steel

surfaces (average roughness = 3.25 μm and 5.25 μm). Their findings indicated that for fine sand (0.1-0.25 mm), a 3.25 μm roughness of surface yielded a higher interface-mobilised friction angle under 50 kPa, whereas, for medium sand (0.5-1.0 mm), higher friction occurred under 200 kPa. Interface friction evolves after extensive cyclic displacement (≥ 2 m), with higher normal stress enhancing bonding between sand particles and hard surfaces. Concurrently, particle breakage reduces mean particle size, improving interface roughness (Westgate and DeJong, 2023). In contrast, softer surfaces degrade under particle indentation and grooving, leading to increased strength (Vangla and Latha, 2015; Dove and Frost, 1999).

Under higher normal stress, limited particle rearrangement may lead to particle breakage or gradual reconfiguration, influencing interface stability (Al-Douri and Poulos, 1992; Rui et al., 2021). Notably, cyclic shearing exhibited a 2° to 4° higher interface friction angle compared to monotonic shearing (Brumund and Leonards, 1973; Uesugi et al., 1989; Rui et al., 2021). The mobilised cyclic friction angle (ϕ_{limit}) for pure sand and the mobilised cyclic interface friction angle (δ_{limit}) for sand-structure interfaces, corresponding to the limit number of cycles at which the mobilised shear stress stabilises, can be determined from the mobilised cyclic shear stress (τ_{m}). This is achieved by analysing the cyclic stress envelope under at least three normal stress levels and is calculated following established methods (e.g., Desai et al., 1985):

$$\phi_{\text{limit}} = \tan^{-1}\left(\frac{\tau_{\text{limit}}}{\sigma_{\text{n}}}\right) \tag{2-12a}$$

$$\delta_{\text{limit}} = \tan^{-1}\left(\frac{\tau_{\text{limit}}}{\sigma_{\text{n}}}\right) \tag{2-12b}$$

where τ_{limit} is the mobilised cyclic shear stress at the n^{th} cycle as a limit number.

2.4.5.5 Evolution of particle breakage

Figure 2-14 illustrates the interface shearing zone for carbonate and silica sand against a steel pile in a model test (White, 2002). Studies have consistently shown that the mechanical behaviour of the interface zone differs notably from the

surrounding soil, leading to greater deformation and an increased tendency for particle breakage. The extent of particle breakage is strongly governed by mineralogy, morphology, and gradation (Al-Douri and Poulos, 1992; Ho et al., 2011; Rui et al., 2021; Westgate and DeJong, 2023).

Carbonate and calcareous sands, characterised by their angularity, exhibit greater breakage and volumetric change than silica or quartz sands (Al-Douri and Poulos, 1992; Ho et al., 2011; Zhou et al., 2020). Zhou et al. (2020) investigated shear-induced breakage under large displacements (10 m), revealing distinct breakage modes: quartz sand experiences local contact damage, increasing surface irregularity and concavity, whereas carbonate sand undergoes global splitting and asperity abrasion, resulting in smoother, rounder particles. Consequently, quartz particles retain their angularity, whereas carbonate grains progressively lose concavities.

Particle breakage and deformation intensify with increasing median particle size, normal stress, cycle number, and surface roughness (Liu et al., 2019; Zhou et al., 2020; Rui et al., 2021). As breakage progresses, the interface zone evolves, influenced by surface roughness variations. However, the breakage mechanisms at the semi-hard surface of FRP and sand-coated FRP remain unexplored. Investigating bonding and debonding mechanisms during cyclic shearing is crucial to understanding their impact on interface shear strength.

2.4.5.6 Evolution of surface roughness under cyclic shearing

Several studies have investigated cyclic shearing of structural materials such as steel and geosynthetics, with some also examining the effects of gluing or coating sand onto steel blocks to enhance interface characteristics (e.g., Shahrour and Rezaie, 1997; Westgate and DeJong, 2023). However, the extent of surface roughness variation after cyclic interface shearing and its influence on interface friction remains largely unexplored. Thus, the increasing use of fibre-reinforced polymers demands a comprehensive investigation into surface roughness evolution and its implications for interface friction.

The abovementioned studies on structural materials such as steel,

geosynthetics, and geomembranes underscore particle characteristics, surface roughness, and progressive shearing cycles in governing interfacial mechanical behaviour. In moderate to large-scale engineering applications, assessing interface shear behaviour under high normal stress conditions, i.e., ≥ 400 kPa and large displacements or cyclic shearing, is essential to understand the performance and durability of sand-coated surface (Shahrour and Rezaie, 1997; Ho et al., 2011; Chen et al., 2015; Rui et al., 2021; Westgate and DeJong, 2023).

2.5 Micromechanical shear behaviour at the sand-FRP interface

2.5.1 DEM investigation for sand-structure interfaces

The micromechanical behaviour of sand-structure interfaces is fundamental to the stability and performance of geotechnical structures such as foundations and retaining walls. The DEM serves as a powerful tool for simulating particle-scale interactions (Cundall and Strack, 1979), modelling granular materials as spheres, clumps, ellipsoids, or polygons to capture particle movements, contact forces, and moments (Necochea et al., 2024).

DEM facilitates the analysis of particle rearrangement, force chains, shear band formation, and nonlinear soil-structure interactions (Grabowski et al., 2021a; Nitka and Grabowski, 2021; Hou et al., 2021; Zhang and Huang, 2022). It provides insights into interface behaviour, influenced by particle shape, size, distribution, surface roughness, and material properties, aiding in accurate predictions and safer geotechnical designs (Wang and Yin, 2022; Wang et al., 2022a; Wang et al., 2022b; Necochea et al., 2024). Commonly used DEM software includes open-source options such as YADE and ESyS-Particle and commercial software like Particle Flow Code (PFC). Laboratory constraints have limited the in-depth study of sand-FRP interface mechanisms, making DEM a valuable alternative. While DEM has been extensively applied to sand-steel (Jing et al., 2018; Wang and Yin, 2022), sand-geotextile (Feng et al., 2018; Feng et al., 2022; Jia et al., 2024), and sand-geomembrane interfaces (Feng et al., 2018), its potential in sand-FRP interactions remains underexplored.

Surface roughness characterisation is central to sand-structure interactions. , As shown in Figure 2-15, materials such as steel are modelled using grooves or sawtooth profiles (Jing et al., 2018; Grabowski et al., 2021a; Wang and Yin, 2022), while flexible materials like geomembranes and geotextiles utilise overlapping ball patterns (Feng et al., 2018; Feng et al., 2022). Unlike rigid materials, flexible materials deform and wear, affecting roughness evolution, influenced by normal stress, shearing duration, and material properties (O'Rourke et al., 1990; Ho et al., 2011; Feng et al., 2022). DEM simulations highlight the impact of model size, particle size, and computational costs (Jing et al., 2018). Jacobson et al. (2007) determined that $L/D_{50} \geq 33$ ensures well-defined shear bands in DEM direct shear tests, while sand-geomembrane interface studies suggest a sand specimen length of $35D_{50}$ and height of $10D_{50}$ results in shear band thicknesses of $2.7D_{50}$-$4.4D_{50}$ (Figure 2-15(b); Feng et al., 2018). Additionally, Grabowski et al. (2021a) modelled IDST with 80,000 unscaled particles, aligning with experimental setups.

Most SSI 3D models employ linear contact models (Frost et al., 2002; Feng et al., 2018; Feng et al., 2020; Zhao et al., 2021; Ari and Akbulut, 2022) or linear rolling resistance models (Jing et al., 2018; Hou et al., 2021; Wang and Yin, 2022; Grabowski et al., 2021a; Grabowski et al., 2021b; Feng et al., 2022), incorporating interactions between sand particles, walls, and loading plates. Normal and shear stiffness values typically range from 10^5 to 10^{10} N/m, with normal-to-shear stiffness ratios spanning various studies (Chen et al., 2023). The particle friction coefficient usually falls between 0.4 and 0.8, while rolling resistance friction coefficients range from 0.05 to 0.2. Boundary conditions primarily include CNL and CNS, with some studies utilising CV boundary conditions to capture interface shear response (Chen et al., 2023).

2.5.2 Macromechanical and micromechanical perspectives for interface shear behaviour

2.5.2.1 Macromechanical behaviour

Jing et al. (2018) conducted a numerical study on spherical particles (D_{50} = 3.48

mm) shearing against steel plates with varying roughness, revealing two failure patterns: (1) elastic-perfectly plastic for $R_n < 0.375$, and (2) strain-softening for $R_n \geq 0.375$ (Figure 2-16(a)). Increased roughness enhanced interlocking resistance, with softening occurring at $R_n \geq 0.375$ due to strong interlocking. Dilation was also more pronounced at $R_n \geq 0.375$ (Figure 2-16(b)), while smooth interfaces ($R_n < 0.375$) showed negligible dilation. $R_n = 0.75$ marked the critical interface roughness, beyond which shear stress no longer increased.

In Gu et al.'s (2017) study, dense specimens exhibited softening, while loose specimens showed hardening, with shear stress increasing with normal stress (Figure 2-16(c)). Regardless of initial density, specimens exhibited dilation (Figure 2-16(d)), which could be a limitation of the DEM approach, where friction parameters alone are considered, unlike experimental setups that account for particle morphology. Recent studies have incorporated various particle asphericities, including quasi-spherical, polyhedral, elongated, and ellipsoidal shapes, to enhance the accuracy and realism of simulations (Zhao et al., 2015; Martinez and Frost, 2016; Danesh et al., 2020; Necochea et al., 2024; Su et al., 2025).

2.5.2.2 Micromechanical behaviour

The micromechanical behaviour of soils has been characterised by the formation of localised bands, commonly referred to as shear zones, contact distribution, and fabric evolutions (Chen et al., 2023). The thickness of shear zones can be estimated using various parameters, including void ratio distribution, tangential particle displacement, particle rotation velocity, average velocity, and vertical deformation. As illustrated in Figure 2-17, the shear band is typically arc-shaped, with two thinner edges at its ends due to boundary effects (Jing et al., 2018; Wang and Yin, 2022). Previous studies observed that the shear zone thickness for spherical particles ranges from $4D_{50}$ to $8D_{50}$ when in contact with grooved steel (e.g., Jing et al., 2018; Wang and Yin, 2022; Chen et al., 2023), while it was typically between $2D_{50}$ to $5D_{50}$ when interacting with geomembranes and geotextiles (Feng et al., 2018; Feng et al., 2020). This suggests a greater

susceptibility to slip at sphere-polymer interfaces. Additionally, an increase in the normalised roughness and particle irregularity tends to enhance displacement localisation, leading to an increase in shear zone thickness (Su et al., 2025).

Theoretically, the distribution of force chains is in the direction of maximum compressive stress to overcome the deformation. Wang and Yin's (2022) findings illustrated that the force chain distribution initially oriented vertically, as the tangential displacement approached towards steady state, it rotated to 49° and concentrated at the bottom, i.e.,, at the interface (Figure 2-18). Similarly, the polar mean contact force distribution at the beginning of interface shearing was oriented vertically (black line). Later, at the residual state, it changed to a diagonal orientation (red line) (Figure 2-19). The orientation to the horizontal and magnitude of forces increased with normalised roughness (Grabowski et al., 2021a; Grabowski et al., 2021b). For example, with increasing R_{n} from 0.5 to 2.0, the orientation of the mean contact force at the residual state changes from 145° to 135°, as illustrated in Figure 2-19.

2.5.3 Surface roughness evolution using DEM

Over the past decades, the evolution of surface roughness on polymeric materials, such as geomembranes and geotextiles, has been extensively investigated through experimental studies. However, Chen et al. (2021) utilised CFD-DEM coupling to model smooth geomembranes and examine roughness evolution. Their findings revealed the variation in roughness after testing, which was closely linked to material hardness and the applied critical normal stress, as Dove and Frost (1999) suggested. These results were also consistent with the experimental study by Vangla and Latha (2015). However, the sand-FRP interface shear behaviour in DEM and its contact mechanism have yet to be fully explored. While DEM alone presents challenges in simulating FRP mechanisms, the integration of the Edinburgh-Elasto-Plastic-Adhesion (EEPA) contact model, developed by Morrisey (2013), within overlapped layers of spherical particles as shown in Figure 2-20 with a minimum of two layers may provide a meaningful model to simulate the sand-FRP interface along with roughness evolution due to their

contact mechanism. The contact force ($\mathrm{F_c}$) and moment ($\mathrm{M_c}$) in the EEPA model can be obtained as:

$$\mathrm{F_c} = \mathrm{F}^{\mathrm{EEPA}} + \mathrm{F}^{\mathrm{d}}, \qquad \mathrm{M_c} = M^{\mathrm{r}} \tag{2-13}$$

where $\mathrm{F}^{\mathrm{EEPA}}$ is a non-linear force, and F^{d} is the dashpot force, and M^{r} is the rolling resistance moment. The non-linear force can be obtained as,

$$\mathrm{F}^{\mathrm{EEPA}} = F_{\mathrm{n}}^{\mathrm{EEPA}} \hat{n}_{\mathrm{c}} + F_{\mathrm{s}}^{\mathrm{EEPA}} \tag{2-14}$$

An extension of the linear hysteretic model (Walton and Braun, 1986), which allows tensile force, and a non-linear force-displacement behaviour can be adopted. The force-displacement law in the normal direction can be obtained for the normal force F^{EEPA} as:

$$F_{\mathrm{n}}^{\mathrm{EEPA}} = \begin{cases} F_0 + k_1 \delta_n^{\mathrm{m}} & \text{if } k_2\left(\delta_{\mathrm{n}}^{\mathrm{m}} - \delta_{\mathrm{p}}^{\mathrm{m}}\right) \geq k_1 \delta_n^{\mathrm{m}} \\ F_0 + k_2\left(\delta_{\mathrm{n}}^{\mathrm{m}} - \delta_{\mathrm{p}}^{\mathrm{m}}\right) & \text{if } k_1 \delta_n^{\mathrm{m}} > k_2\left(\delta_{\mathrm{n}}^{\mathrm{m}} - \delta_{\mathrm{p}}^{\mathrm{m}}\right) > -k_{\mathrm{a}} \delta_{\mathrm{n}}^{\chi} \\ F_0 - k_{\mathrm{a}} \delta_{\mathrm{n}}^{\chi} & \text{if } -k_{\mathrm{a}} \delta_{\mathrm{n}}^{\chi} \geq k_2\left(\delta_{\mathrm{n}}^{\mathrm{m}} - \delta_{\mathrm{p}}^{\mathrm{m}}\right) \end{cases} \tag{2-15}$$

where F_0 refers pull-off force, k_1 refers to virgin loading branch stiffness, k_2 refers loading-unloading stiffness with plastic overlap $\delta_{\mathrm{p}}^{\mathrm{m}}$, k_{a} refers to the adhesion branch stiffness, δ_n^{m} refers to normal overlap with exponent m = 1.5 by default. The contact is activated at zero normal overlap and the stiffness can be obtained as:

$$k_1 = \frac{4}{3} E^* \bar{R}\,, \quad k_2 = \frac{k_1}{1 - \lambda_{\mathrm{p}}}, \text{and } k_{\mathrm{a}} = \frac{F_{\min} - F_0}{\delta_{\min}^{\chi}} \tag{2-16}$$

where E^* refers to effective Young's modulus, $\bar{R}$ refers to the effective radius of contacting pieces, λ_{p} refers to the plasticity ratio. When the overlap force in k_2 branch equals to pull-off force, plastic overlap δ_{p} can be obtained by utilising the corresponding maximum overlap $\delta_{\max}$ and plasticity ratio, $\delta_{\mathrm{p}} = \lambda_{\mathrm{p}}^{1/\mathrm{m}} \delta_{\max}$; Unloading leads to a tensile force development, which is considered as contact surface adhesion energy (γ^*, based on Johnson-Kendall-Roberts (JKR) model Johnson et al. (1971)) for adhesive forces, and when tensile force equals minimum force ($F_{\min}$),

$$F_{\min} = F_0 - \frac{3}{2}\pi\gamma^* a \tag{2-17}$$

where $a = \sqrt{2\delta_p \bar{R}}$.

When unloading is allowed to continue until zero overlap, a minimum limit force ($F_{min}^{\text{limit}} = F_0 - k_2\delta_{\text{n}}^{\text{m}}$) is obtained. To obtain a real solution of minimum force when the adhesion surface energy is very large, it can be modified as an average of the pull-off force and the limit force.

$$F_{\min} = \begin{cases} F_0 - \frac{3}{2}\pi\gamma^* a & \text{if } F_{\min} > F_{min}^{\text{limit}} \\ \frac{1}{2}\left(F_0 + F_{min}^{\text{limit}}\right) & \text{otherwise} \end{cases} \tag{2-18}$$

Shear force ($F_{\text{s}}^{EEPA^*}$) can be obtained based on a trial shear force ($(F_{\text{s}}^{EEPA})_0$) with timestep update in relative shear-displacement increment ($\Delta\delta_{\text{s}}$) as,

$$F_{\text{s}}^{EEPA^*} = (F_{\text{s}}^{EEPA})_0 + k_{\text{s}}^t \Delta\delta_{\text{s}} \tag{2-19}$$

where k_{s}^t refers to tangent shear stiffness, which is a function of the normal overlap as presented below,

$$k_{\text{s}}^t = k_{\text{sf}} 8G^* + \sqrt{\bar{R}\delta_{\text{n}}} \tag{2-20}$$

where G^* refers to the effective shear modulus and k_{sf} refers to the scaling factor. This shear stiffness is based on Hertz's theory. When two pieces consist of the same material,

$$E^* = \frac{G}{1-\nu} \quad \text{and} \quad G = 2(2-\nu)G^* \tag{2-21}$$

where ν is poissons' ratio. Furthermore, JKR and Hertz's theories can be updated for the calculation of shear force,

$$F_{\text{s}}^{\text{EEPA}} = \begin{cases} F_{\text{s}}^{EEPA^*} & \text{if } \left|F_{\text{s}}^{EEPA^*}\right| \le \mu(F_{\text{n}}^{\text{EEPA}} - F_{\min}) \\ \mu(F_{\text{n}}^{\text{EEPA}} - F_{\min})\left(\frac{F_{\text{s}}^{EEPA^*}}{|F_{\text{s}}^{EEPA^*}|}\right) & \text{otherwise} \end{cases} \tag{2-22}$$

where μ refers to the friction coefficient and reference force. '$(F_{\text{n}}^{\text{EEPA}} - F_{\min})$' cannot be negative. Ultimately, the damping force (F^{d}) which is also called a

dashpot or viscous, is given by,

$$\mathrm{F}^{\mathrm{d}} = -F_{\mathrm{n}}^{\mathrm{d}}\hat{\mathrm{n}}_{\mathrm{c}} + F_{\mathrm{s}}^{\mathrm{d}} \tag{2-23}$$

herein $F_{\mathrm{n}}^{\mathrm{d}}$ refers to the damping force in the normal direction and $F_{\mathrm{s}}^{\mathrm{d}}$ refers to the damping force in the shear direction. The details of the EEPA contact model can be found in the manual of the PFC 7.0 version by Itasca. To utilise this model in layers of FRP, shear modulus, effective surface adhesion energy, pull-off force, damping, and plasticity ratio need to be defined and calibrated.

2.6 Constitutive modelling of sand-FRP interface shear behaviour

The previous sections provided a comprehensive review of experimental interface behaviour, highlighting how various factors influence SSI behaviour and their relevance to the soil-FRP interface. Following this, the micromechanical aspects of sand-FRP modelling were discussed. The next step in the experimental study is to conduct verification based on theoretical frameworks, governing equations, and modelling using commercial FEM software.

2.6.1 Classical and commonly used soil models

Over the past decades, a wide range of constitutive models have been developed to describe the stress-strain and failure behaviour of soils under various loading conditions. Among the most commonly adopted are Hooke's Law, Mohr-Coulomb, Drucker-Prager, Duncan-Chang (hyperbolic), Modified Cam-Clay, and Hardening Soil models (Brinkgreve, 2005; Kok et al., 2009; Lade, 2005a). However, the selection of a suitable model depends on both the nature of the soil and the intended application. For this study, particular emphasis is placed on Mohr-Coulomb and Duncan-Chang, as they are highly relevant to sand-structure interface behaviour.

The Mohr-Coulomb (M-C) model is a linearly elastic, perfectly plastic model, which follows Hooke's law and defines shear stress at failure (τ_{f}) as:

$$\tau_{\mathrm{f}} = c + \sigma_{\mathrm{f}}^{'} \tan\phi^{'} \tag{2-24}$$

Elastic parameters include Young's modulus of elasticity (E) and Poisson's ratio (ν), while plastic deformation is governed by friction angle (ϕ) and cohesion (c), with dilatancy angle (ψ) often introduced via a non-associated flow rule. The M-C model is widely used due to its simplicity and effectiveness in capturing peak strength behaviour in granular materials (e.g., sand). However, its assumptions of perfect plasticity and constant stiffness limit its ability to model strain softening, stiffness degradation, and progressive failure under complex stress paths (Kok et al., 2009).

To improve on stiffness representation and stress-dependency, the Duncan-Chang (hyperbolic) model was introduced for drained triaxial conditions in sands and clays. The stress–strain behaviour is expressed using the hyperbolic relationship:

$$q = \frac{\varepsilon}{a + b\varepsilon} \tag{2-25}$$

where a is the reciprocal of the initial tangent modulus (E_i), $\frac{1}{a} = E_i = KP_{\text{at}}\left(\frac{\sigma_3}{P_{\text{at}}}\right)^n$ and b relates to the asymptotic deviatoric stress, $\frac{1}{b} = (\sigma_1 - \sigma_3)_{\text{ult}}$. This empirical model allows better representation of nonlinearity and stress dependency, making it especially suitable for interface studies under varying stress levels. However, its lack of a formal plasticity framework limits its applicability in modelling irreversible volumetric strain or dilatancy under cyclic or complex loading (Duncan and Chang, 1970).

More advanced model like Modified Cam-Clay (MCC), developed by Roscoe and Burland (1968) based on critical state theory (Roscoe et al., 1963; Schofield and Wroth, 1968), provide improved predictions of undrained shear strength estimation over Mohr-Coulomb, However, its associated flow rule overestimates failure stress on the 'dry side' and fails to capture dilatancy and strain softening in normally consolidated soils or loose sands. The Hardening Soil model, proposed by Brinkgreve and Vermeer (1997) and Schanz (1998), extends applicability to both soft and stiff soils (Schanz et al., 1999). It incorporates stress-dependent stiffness, shear, and volumetric hardening, and allows for associated or non-associated flow rules with cap yield surfaces

(Vermeer et al., 1991; Schanz et al., 2019). While it offers enhanced deformation prediction, its lack of creep and anisotropic formulations, along with high calibration demands in terms of cost and data requirements, limit its practicality for granular soil-structure interface modelling (Kok et al., 2009). In summary, soil constitutive models are developed for specific applications, with their suitability governed by both theoretical formulation and practical constraints. An appropriate model should meet three criteria (Brinkgreve, 2005; Kok et al., 2009): (1) establish consistent, stable, and unique theoretical requirements based on continuum mechanics; (2) reproduce experimental behaviour with minimal parameters; and (3) support implementation in numerical methods such as FEM. However, practical use is often constrained by the cost and complexity of parameter calibration. Even well-established models may yield unreliable results if constitutive parameters are not determined with adequate precision.

2.6.2 Constitutive modelling of soil-structure interfaces

Soil behaviour is typically characterised by non-linear stress-strain relationships, stress-dilatancy, strain-dependent stiffness, and time-dependent effects like consolidation and creep (Lashkari, 2012; Le et al., 2012; Yin and Chang, 2013). In response, various interface constitutive models have been developed over the years. Early models, such as the zero-thickness element model by Goodman et al. (1968), Duncan and Chang's (1970) hyperbolic model, and Zaman et al.'s (1984) cyclic model, used the Mohr-Coulomb failure criterion and stress-dependent models. Desai et al. (1986) introduced nonlinear soil behaviour to model the interaction between grouted anchors and soil, highlighting the importance of normal stress and roughness in interface stress-deformation. Later, Desai and Ma (1992) proposed the disturbed-state concept (DSC) to describe frictional hardening and softening behaviour in joints, with satisfactory back predictions from CNL and CNS test data. Fakharian and Evgin (2000) developed a model for monotonic and cyclic loading based on a single-surface elasto-plastic model. Ghionna and Mortara (2002) extended this with a plastic potential and yield surface for sand-structure interfaces, verified through CNS and CNL tests.

Gennaro and Frank (2002) introduced an elasto-plastic model with 14 parameters to describe phase transformation and the ultimate state of granular interfaces under all boundary conditions. D'Aguiar et al. (2011) presented an elasto-plastic model for both monotonic and cyclic loading using the Terzaghi effective stress principle, though it was limited in its ability to model features like critical state stress-dilatancy response. Hu and Pu (2004) proposed a constitutive damage model for rough interfaces, which was later enhanced with the DSC concept and charge-coupled device (CCD) cameras.

Liu et al. (2006) and Liu et al. (2014) extended the model with the inclusion of critical state to rough interfaces and pile interactions, leading to a generalised plasticity model with 16 parameters. Nonlinear models like the hyperbolic soil model (Gómez et al., 2003; Bian et al., 2020) were further developed to include stress-path dependence and hysteretic behaviour, though they remain limited to monotonic loading. In cases involving granular materials, particle crushing and degradation may significantly affect interface shearing under cyclic loading. Models incorporating breakage (Daouadji and Hicher, 2010) and stress-dilatancy (Yin et al., 2018b) have been developed to address these effects. Yang and Yin (2021) advanced the exponential model with breakage parameters, showing its applicability for both sand and clay, with satisfactory FEM simulations using 12 parameters. On advancing to these models, an evaluation performed by Wang et al. (2024b) and Wang et al. (2024a) utilised six different models, including three nonlinear incremental models, i.e., exponential, hyperbolic, and hypoplastic, and three elasto-plastic models (MCC, SANISAND, SIMSAND) to compare monotonic and cyclic shearing performance, respectively. In the global comparison of these models considering relative density, interface stiffness, and shearing rate nonlinear incremental model dominated the overall performance compared to the elasto-plastic model (Wang et al., 2024c). However, the model performance in cyclic shearing was compared considering the effects of amplitude, accumulated normal displacement, and stress degradation. A satisfactory performance to replicate experimental results by all six models was reported (Wang et al., 2024b). In addition to this evaluation, the importance of

particle breakage parameters for the modelling of reversible and irreversible normal displacement during cyclic shearing in all models except MCC was highlighted by Wang et al. (2024b).

Understanding existing soil models is crucial for studying soil-structure interface behaviour. Choosing an appropriate model requires coupling mechanism of soil and interface materials and modelling with proper boundary conditions. A simple, robust constitutive model with fewer parameters and strong simulation capabilities remains an area for future development. While the above models vary in complexity, their practical applicability is strongly influenced by the effort required to determine their constitutive parameters. Many advanced models demand extensive laboratory or in-situ testing under specific boundary conditions, which can incur significant monetary and time costs. Furthermore, parameter calibration often involves multiple interdependent variables, where small measurement errors can propagate and result in substantial uncertainty in predicted interface behaviour. Consequently, even theoretically robust models may yield unreliable predictions if parameter estimation is subject to imprecision. This limitation underlines the importance of developing models that balance physical realism with practical feasibility, ideally using a reduced but representative set of parameters that can be reliably obtained from routine tests.

2.6.3 Enhanced nonlinear hyperbolic model

A simple nonlinear elastic stress-dependent Duncan-Chang soil model (an enhancement to the Mohr-Coulomb model) (Duncan and Chang, 1970) can be considered to model the sand-FRP interface shear behaviour, which could be enhanced to account for nonlinear shear modulus, incremental stress-dilatancy, critical void ratio, breakage, and stress reversal as demonstrated by Yang and Yin (2021) in the exponential model. The asymptotic relationship for the hyperbolic function is,

$$\eta = \frac{b\gamma}{a + \gamma} \tag{2-26}$$

The Equation (2-26) can be devised as,

$$\frac{\tau}{\sigma_n + \sigma_a} = \tan(\phi_p)\frac{\gamma}{a+\gamma} \tag{2-27}$$

where, $\tau = \sqrt{\tau_x^2 + \tau_y^2}$ and $\gamma = \sqrt{\gamma_x^2 + \gamma_y^2}$. Nonlinear shear modulus can be calculated by the ratio of change in shear stress to shear displacement,

$$\begin{aligned} G = \frac{d\tau}{d\gamma} = (\sigma_n + \sigma_a)\tan(\phi_p)\left[\frac{1}{(a+\gamma)} - \frac{\gamma}{(a+\gamma)^2}\right] \\ \Rightarrow \frac{\tau}{\sigma_n + \sigma_a} = \tan(\phi_p)\frac{a}{(a+\gamma)^2} \end{aligned} \tag{2-28}$$

Initially, $\gamma = 0$

$$G = \frac{\tan(\phi_p)(\sigma_n + \sigma_a)}{a} \Rightarrow a = \frac{\tan(\phi_p)(\sigma_n + \sigma_a)}{G} \tag{2-29}$$

After load application, shear stress increases; thus, incremental shear stress is,

$$\begin{aligned} d\tau &= \left[\frac{\partial\tau}{\partial\gamma}d\gamma + \frac{\partial\tau}{\partial\sigma_n}d\sigma_n\right]d\sigma_n \\ d\tau &= G\left(\frac{a}{a+\gamma}\right)\left(1 - \frac{\eta}{\tan(\phi_p)}\right)d\gamma + \eta\left(1 - \frac{a}{a+\gamma}\right)d\sigma_n \end{aligned} \tag{2-30}$$

Normal displacement induced during shearing is,

$$du_n^{in} = A_d(\tan(\phi_{pt}) - \eta)d\gamma \tag{2-31}$$

where, A_d is the dilatancy parameter, and ϕ_{pt} refers to the phase transformation friction angle. An increase in normal stress during shearing can be obtained by

$$d\sigma_n = K_n(du_n - du_n^{in}) = K_n(du_n - [A_d(\tan(\phi_{pt}) - \eta)d\gamma]) \tag{2-32}$$

where, $K_n = G * R$ is the bulk modulus of the soil specimen, and R is the material constant. It is expected that the surrounding soil mass of the shearing zone provides confinement during shearing, which is represented by the elastic element (spring; soil shows elastic behaviour at the isotropic stress state or low stress level, which is immediately after changes in stress state (Lade, 2005a, 2005b). Based on Hooke's law, a spring element having stiffness K in the normal direction of the interface is assumed,

$$d\sigma_n = -Kdu_n \Rightarrow du_n = -\frac{K}{d\sigma_n} \tag{2-33}$$

Considering, three different boundary conditions to describe the soil-structure interface shear modes: (1) constant volume (CV) test: representative of undrained condition $(du_n = 0, d\sigma_n \neq 0 \text{ at } K = \infty)$; (2) constant normal load (CNL) test: representative of drained condition $(du_n \neq 0, d\sigma_n = 0 \text{ at } K = 0)$; (3) constant normal stiffness (CNS) test: representative of partially drained condition $(du_n \neq 0, d\sigma_n \neq 0, \text{at } K = \text{constant})$.Substituting Equation (2-33) in Equation (2-32),

$$d\sigma_n = -\frac{K_n K}{K_n + K} A_d \left(\tan(\phi_{pt}) - \eta\right) d\gamma \tag{2-34}$$

$$du_n = \frac{K_n}{K_n + K} A_d \left(\tan(\phi_{pt}) - \eta\right) d\gamma \tag{2-35}$$

Substituting Equations (2-34) and (2-35) in Equation (2-30) we get,

$$d\tau = \left[G\left(\frac{a}{a+\gamma}\right)\left(1 - \frac{\eta}{\tan(\phi_p)}\right) - \frac{K_n K}{K_n + K} A_d \tan(\phi_{pt} - \eta)\eta \left(1 - \frac{a}{a+\gamma}\right)\right] d\gamma \tag{2-36}$$

Finally, the basic model is obtained from Equations (2-34), (2-35), and (2-36). The hyperbolic model can be enhanced by including the nonlinear shear modulus, the critical state concept, and the breakage effect in the basic model. The following relation can obtain **the** nonlinear shear modulus,

$$G = G_0 \frac{(2.97 - e)^2}{1 + e} \left(\frac{\sigma_n + \sigma_a}{P_{at}}\right)^{n_g} \tag{2-37}$$

where, G_0 is initial shear modulus, P_{at} is the atmospheric pressure at mean sea level (101.325 kPa at MSLP) can be considered for reference stress state, and power index n_g = 0.6 is adopted based on the many test results.

Based on the critical state concept suggested by Yin et al. (2018b), the ultimate state can be defined (stress state and shear zone thickness remain constant while increasing shear displacement),

$$e_c = e_{ref} exp\left[-\lambda\left(\frac{\sigma_n}{P_{at}}\right)^{\xi}\right] \tag{2-38}$$

where e_c refers to the critical void ratio, which can be determined based on the reference critical void ratio e_{ref}, atmospheric pressure P_{at}, and nonlinearity parameters λ and ξ. Based on the critical state concept, the ratio of critical void ratio (e_c) to the current void ratio (e) define three different modes of soil packing: (1) loose packing ($e_c/e < 1$); (2) dense packing ($e_c/e > 1$); and (3) intermediate or critical state, where the initial state lies on CSL ($e_c/e = 1$). This different condition of void ratio according to soil packing can be stated by the density effect study of Biarez and Hicher (1994) and can be adopted in the model.

$$\begin{aligned} \tan(\phi_p) &= \left(\frac{e_c}{e}\right)^{n_p} \tan(\phi_\mu) \\ \tan(\phi_{pt}) &= \left(\frac{e}{e_c}\right)^{n_d} \tan(\phi_\mu) \end{aligned} \tag{2-39}$$

Where ϕ_μ is the critical frictional angle, which is smaller than ϕ_p in dense packing and bigger than the initial mobilised peak frictional angle ϕ_p in loose packing. During shearing, dense packing particles (higher interlocking) dissipate energy at the phase transformation to reach a looser state called dilative behaviour, and loose soil accumulates energy to reach a dense state. Hence, the mobilised phase transformation angle ϕ_{pt} is bigger in loose packing (contractive) and smaller in dense packing (dilative) compared to the critical frictional angle (Equation (2-39)).

The breakage effect can be studied to obtain e_{ref} by translating CSL downwards in the $e - \sigma_n$ a plane based on Liu et al. (2014) approach, similar to Yin and Yang (2021) on the nonlinear incremental approach for an exponential function.

$$e_{ref} = e_{refu} + \left(e_{ref0} - e_{refu}\right) \exp(-\rho B_r^*) \tag{2-40}$$

where e_{ref0} and e_{refu} are the initial and ultimate reference critical void ratios corresponding to virgin soil without particle breakage and crushed soil, respectively; ρ is the material constant that controls the decreasing rate of CSL

due to particle breakage.

$$F(d) = (1 - B_r^*)F_0(d) + B_r^* F_u(d) \tag{2-41}$$

where $F_0(d)$ and $F_u(d)$ are initial and ultimate (fractal) particle size distributions (GSDs), respectively, and $F_u(d) = (d/d_{max})^{0.3}$ (d and d_{max} are particle size and maximum particle size, respectively) defined by Coop et al.(2004). A modified energy approach (Daouadji et al., 2001; Daouadji and Hicher, 2010; Hu et al., 2011) can be adapted to calculate B_r^*:

$$B_r^* = \frac{W}{b + W}, \qquad W = \int (\langle \sigma_n du_n \rangle + \tau d\gamma) \tag{2-42}$$

where $\langle\rangle$ is the Macaulay brackets; b is a material constant (kPa·mm) controlling the evolution rate of the particle breakage index B_r^* it could be calibrated according to the particle size distributions before and after shearing. However, it is not always possible to get two different particle size distributions for each set of experiments, thus in that case maximum void ratio (at very high uniformity (d_{60}/d_{10}) of granular materials) can be adopted as e_{refu} (Biarez and Hicher, 1994). To better approximate the normal displacement behaviour as mentioned in Wang et al. (2024a) and Wang et al. (2024b) modified breakage parameter of Equation (2-42) can be adopted:

$$B_r^* = \frac{\mathrm{W}^{n_w}}{b + \mathrm{W}^{n_w}} \tag{2-43}$$

where n_w refers to the power term for energy produced during particle breakage, which assists in fitting and controlling the breakage at the CSL.

Finally, an update in the void ratio can be done based on the variation in normal displacement.

$$e = e_i - du_n(1 + e_0) \Rightarrow \Delta e = -du_n(1 + e_0) \tag{2-44}$$

In the cyclic shear loading, the direction of shear stress changes, and hence, the corresponding shear displacement will have different values due to changes in shearing direction and particle orientation, changes in the coefficient of friction and material energy, which ultimately affect shear stress. Shear stress reversal is adapted to define this behaviour, as defined by Manning's rule in

hysteretic stress-strain behaviour (Tatsuoka et al., 2003).

$$\eta^* = |\eta - \eta^R| = tan(\phi_p)^* \left(\frac{|\gamma - \gamma^R|}{a + |\gamma - \gamma^R|}\right) \quad (2\text{-}45)$$

The corresponding incremental normal displacement can be obtained by,

$$du_n^{in} = A_d(\tan(\phi_{pt})^* - |\eta - \eta^R|)|d\gamma| \quad (2\text{-}46)$$

where, $\tan(\phi_p)^* = |\tan(\phi_p)n - \eta^R|$ and $\tan(\phi_{pt})^* = |\tan(\phi_{pt})n - \eta^R|$ with a given value of $n = (\tau - \tau^R)/|\tau - \tau^R|$. Also, the moment of shear reversal can be obtained by the product of shear displacement of the last loading cycle step to the current loading cycle step, with a negative sign convention in two-dimensional loading ($\sigma_n - \tau$). A similar approach can be implemented for three-dimensional loading ($\sigma_n - \tau_x - \tau_y$) where both sign conventions are considered based on the stress ratio value of the last and current steps.

The formulation of the enhanced nonlinear hyperbolic model in this study also considers the practical challenges associated with parameter determination. While the model aims to capture key nonlinear and cyclic interface behaviours, the selection of parameters has been guided by the need to minimise calibration complexity. Parameters are chosen to be either directly measurable from standard interface shear tests or inferred with minimal additional testing, thereby reducing both cost and time requirements. By limiting reliance on parameters with high uncertainty in estimation, the proposed approach seeks to improve the reliability of simulations in real-world engineering applications, addressing a common limitation of many existing constitutive models.

2.6.4 Numerical modelling approaches

Finite element methods supported by commercial software like ABAQUS and PLAXIS are widely used in geotechnical engineering for soil-structure interface modelling (Ali et al., 2016; Saberi et al., 2019; Liu et al., 2020). FEM is particularly suited for continuum materials and requires two-node elements, node-to-node elements with finer meshing, or zero-thickness/thin-layer elements (Zohra et al., 2022). Conventional continuum meshing may struggle to capture

failure distinctly and can result in weak meshes requiring caution. Goodman et al. (1968) introduced the zero-thickness interface model, which consists of four nodes and is ideal for joint and fracture modelling. However, this approach faces ill-conditioning due to off-diagonal stiffness matrix terms (Schellekens and De Borst, 1993), which can be addressed by the Newton-Cotes quadrature scheme. Zero-thickness element extensions have been applied in offshore interface modelling (Cerfontaine et al., 2015). Desai et al. (1984) introduced a thin-layer element with penalty methods for soil-structure interfaces, while surface-to-surface modelling with master-slave algorithms is effective for large deformation problems (Khishvand and Nazem, 2016). ABAQUS supports surface-to-surface modelling with various contact constraints, including ties, embedded regions, and rigid bodies. Using implicit solution algorithms, Saberi et al. (2019) successfully simulated sand-structure interface behaviour under monotonic and cyclic shearing conditions, linking user-defined subroutines in FORTRAN to define the SSI model for FEM simulations in ABAQUS (Saberi et al., 2019; Dassault Systèmes, 2020).

In practical applications, FEM modelling of interfaces can encounter mesh-dependent solutions, particularly in problems involving strain localisation, softening behaviour, or highly nonlinear constitutive models (Liu et al., 2021; Liu et al., 2022). Such mesh sensitivity typically arises when the finite element size becomes comparable to or larger than the localisation zone, leading to artificial stiffness or unrealistic energy dissipation. Remedies include mesh refinement, regularisation techniques, or adopting constitutive models formulated with an internal length scale to mitigate localisation effects. Another practical consideration is the availability of constitutive models within the chosen FEM code. Although a theoretically superior model may exist, it is often not implemented in commercial software, requiring either the selection of a different model or the development of a user-defined material subroutine considering the independent rotation of grains linking to mesh independent solutions (Liu et al., 2021). This introduces trade-offs between model accuracy, numerical stability, computational cost, and ease of implementation. Therefore, model selection in

FEM studies is not solely a theoretical exercise but must balance the physics of the problem with the computational and software constraints.

2.7 Summary

A comprehensive literature review was conducted in this chapter. The experimental investigation, DEM investigation, and FEM investigation of SSI, including various influencing factors in sand-structure interface relevance to the sand-FRP interface, were detailed and discussed based on the available studies. The following key investigation is essential to enhance the understanding of the impact of sand-coating on sand-FRP interface shear behaviour.

Most of the studies conducted sand-coating without a surface finish, which undermines the removal of coated sand. Thus, an improvement in the sand-coating approach must be considered. Various influencing factors, such as particle size effect, roughness effect, and normal stress effect in monotonic shearing, while these effects incorporate cycle numbers in cyclic shearing, are crucial to exploring the sand-FRP interface shear behaviour. Investigating surface roughness variation and its influence on corresponding shear behaviour is crucial for evaluating the sand-coating method. The micromechanical investigation related to sand particles, their interaction in the contact mechanism, and corresponding roughness evolution on FRP surfaces due to interface contact will strengthen the study from specimens and structural aspects. Finally, incorporating a theoretical framework supported by FEM modelling by utilising a nonlinear hyperbolic model will verify the entire investigation of the sand-FRP interface.

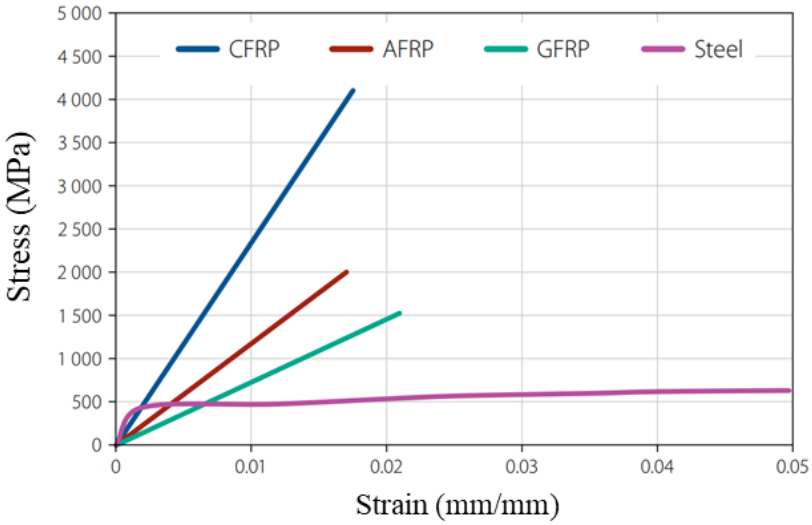

Figure 2-1 A comparative tensile test of CFRP, GFRP, AFRP, and steel bars in terms of stress-strain relationship (Alnatit, 2011)

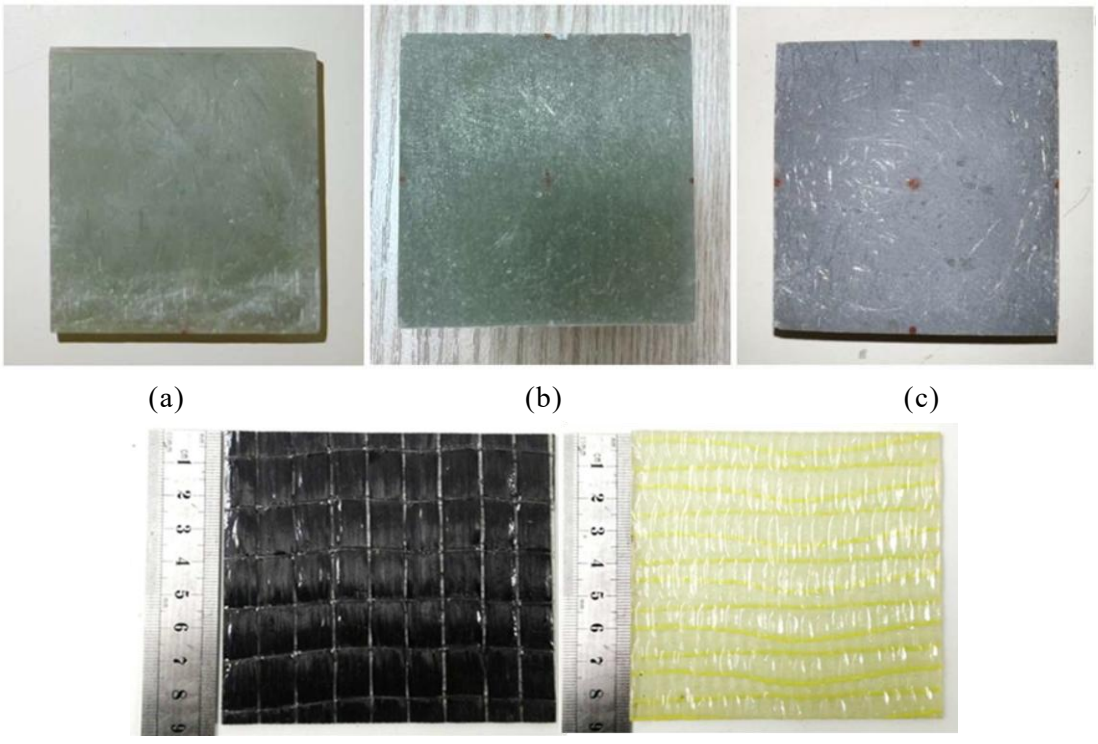

(a) (b) (c)

(d) (e)

Figure 2-2 Vacuum-assisted wet lay-up GFRP plates with varieties of epoxy: (a) orthophthalic epoxy resin, (b) isophthalic epoxy resin, and (c) thixotropic epoxy resin (Teng et al., 2024); wet lay-up FRP sheets of (d) CFRP and (e) GFRP (Giraldo and Rayhani, 2013)

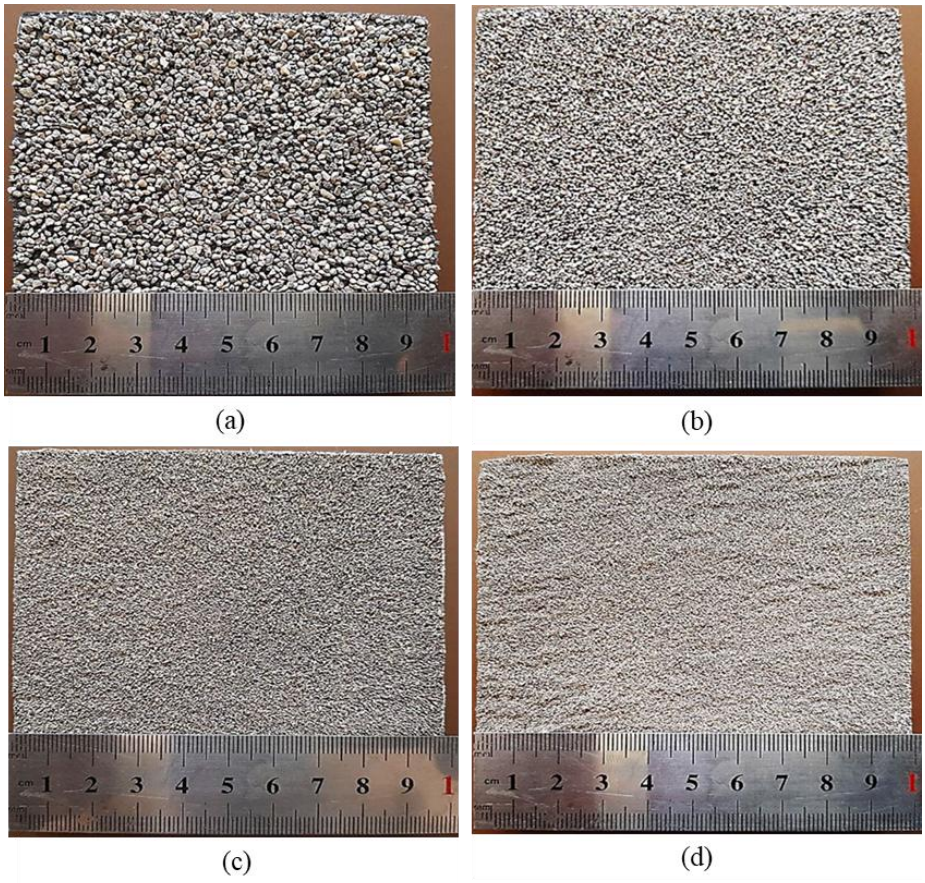

Figure 2-3 Sand-coated CFRP sheets with different mean particle size (grade designation) of (a)1.59 mm (sand 10-16), (b) 0.89 mm (sand 16-30), (c) 0.45 mm (sand 30-50), and (d) 0.23 mm (sand 50-100) (Namjoo et al., 2022)

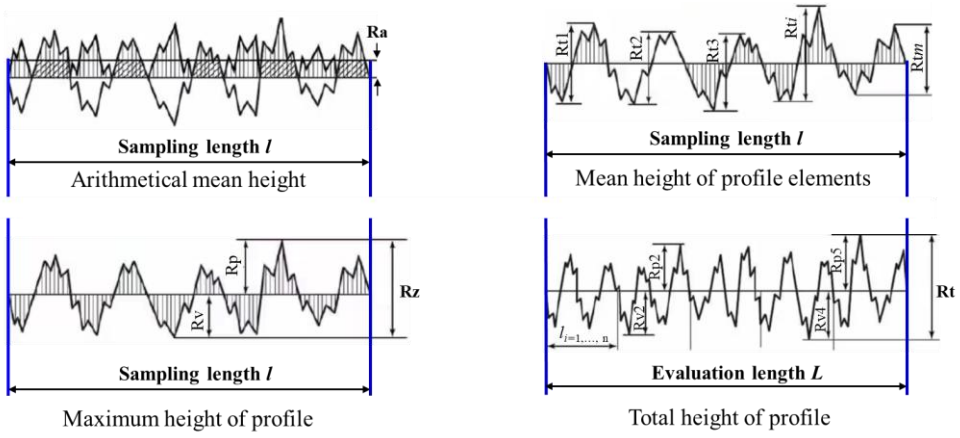

(a)

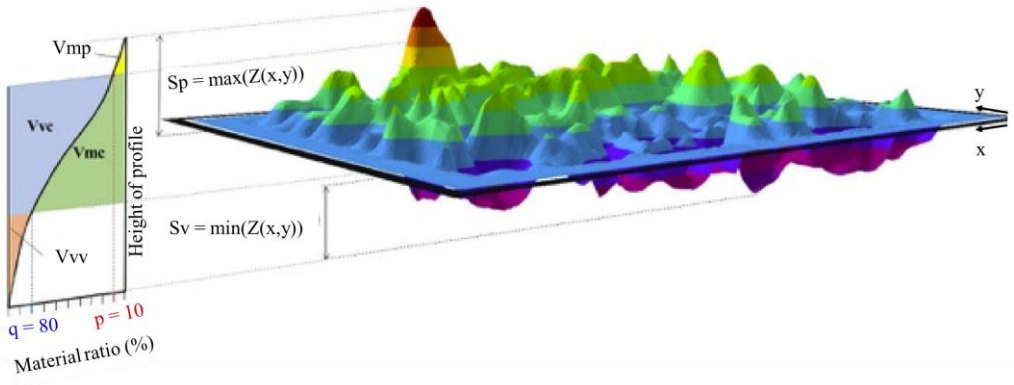

(b)

Figure 2-4 (a) Two-dimensional roughness parameters (ISO 4287, 1997) and (b) three-dimensional roughness parameters (Araújo et al., 2022; ISO 25178-2, 2012)

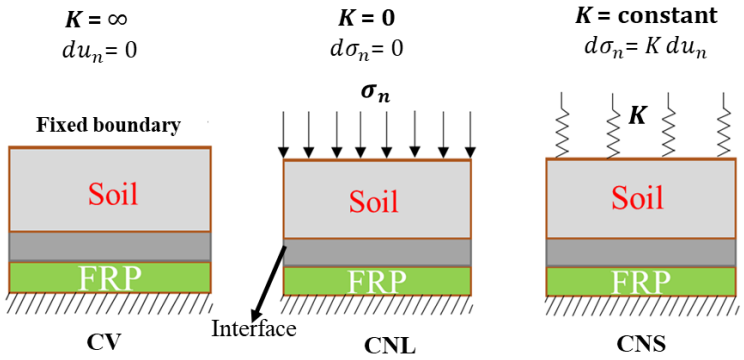

Figure 2-5 Schematic representations for soil-FRP interface in three conditions: CV, CNL, and CNS condition (adapted from Boulon, 1986)

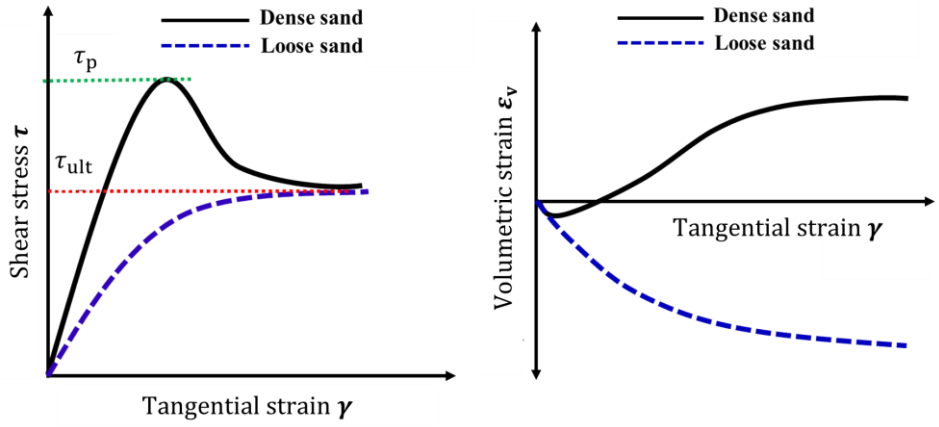

Figure 2-6 Theoretical trends of shear stress and volumetric behaviour with tangential strain for loose and dense sands

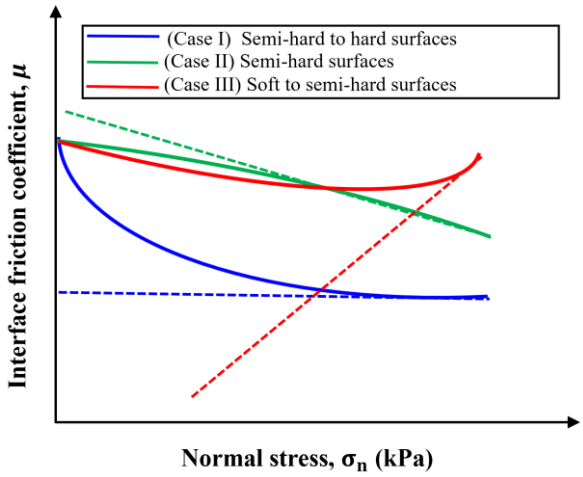

Figure 2-7 Generalised plot of interface friction coefficient versus normal stress

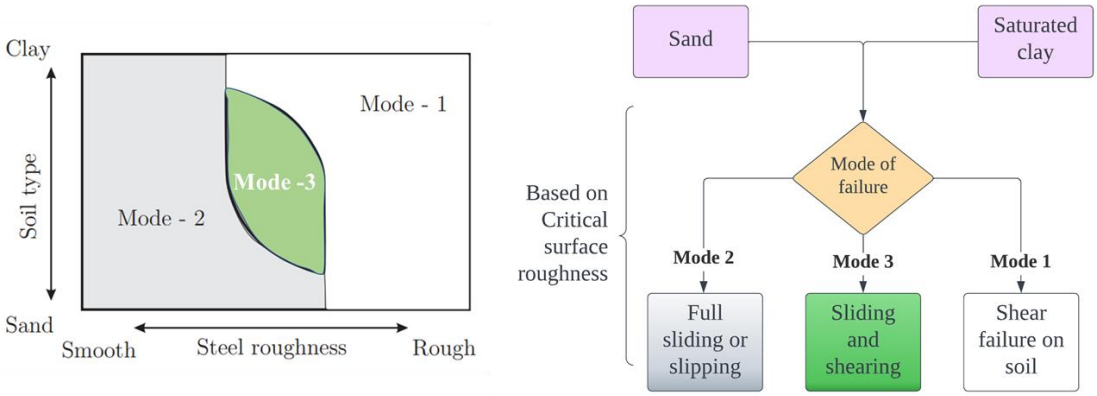

Figure 2-8 Idealised failure modes based on soil type and structure roughness (Tsubakihara et al., 1993)

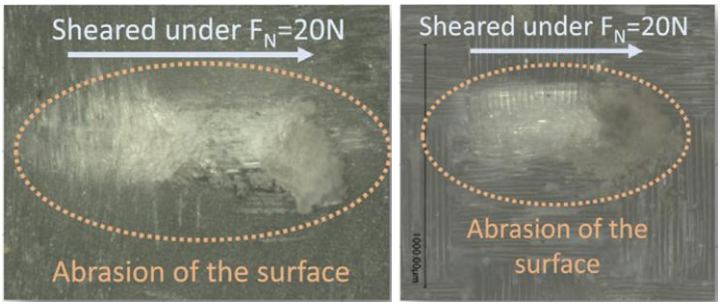

(a) (b)

Figure 2-9 Abrasion of the GFRP surfaces: (a) smooth surface and (b) rough surface (He et al., 2021)

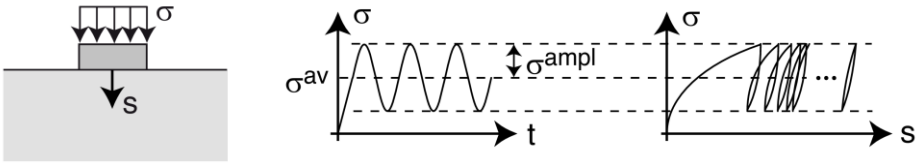

Figure 2-10 Foundation settlement under cyclic loading (Wichtmann, 2016)

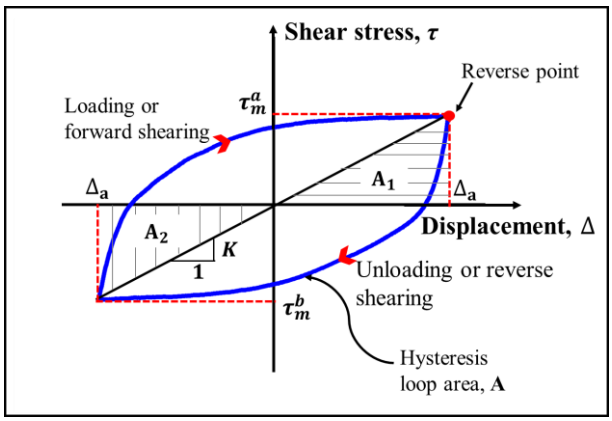

Figure 2-11 Hysteresis loop to calculate mobilised shear stress, secant shear stiffness, and damping ratio

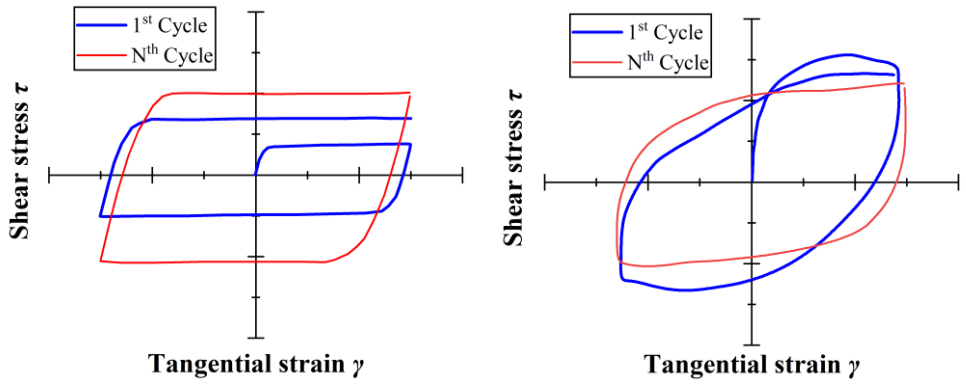

Figure 2-12 Generalised plot of (a) cyclic strain-hardening behaviour and (b) cyclic strain-softening behaviour

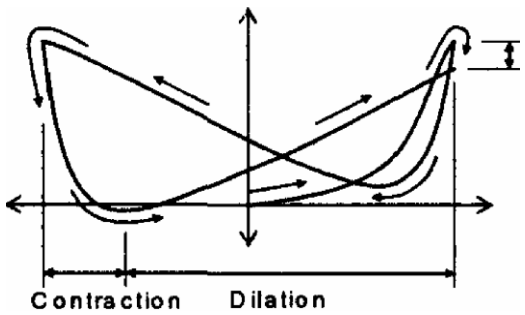

Figure 2-13 Generalised plot of normal displacement response of sand specimen against the rough surface for the first cycle (DeJong et al., 2003)

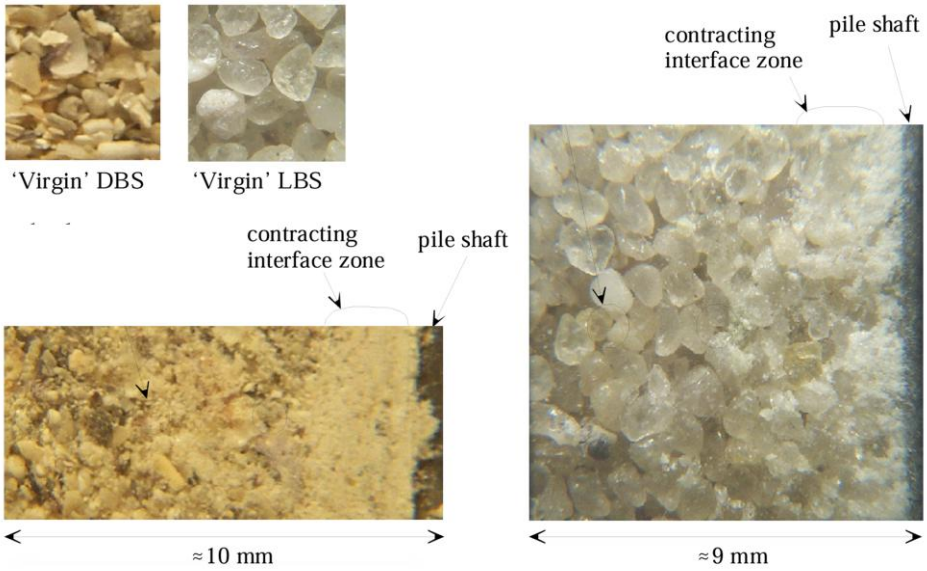

Figure 2-14 Particle breakage at interface shearing zone for carbonate sand (DBS) and silica sand (LBS) (White, 2002)

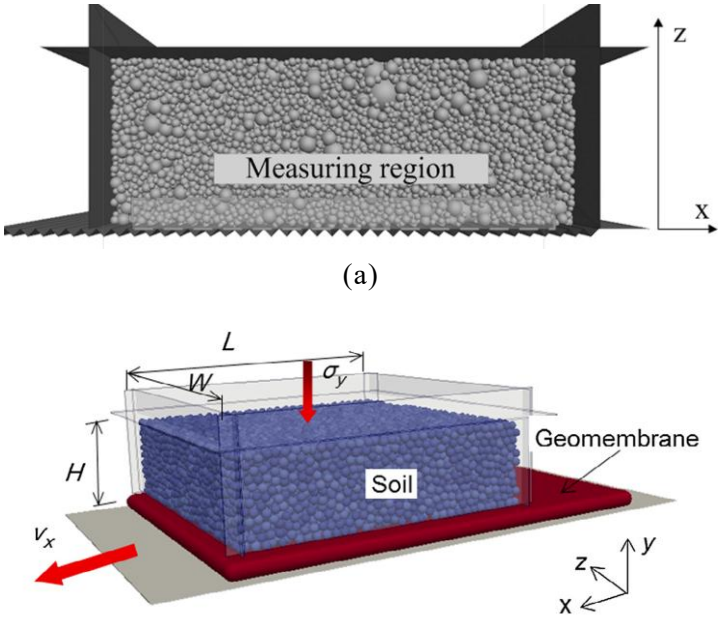

Figure 2-15 (a) Sand-groove steel plate interface model (Jing et al., 2018) and (b) sand-geomembrane interface model (Feng et al., 2018)

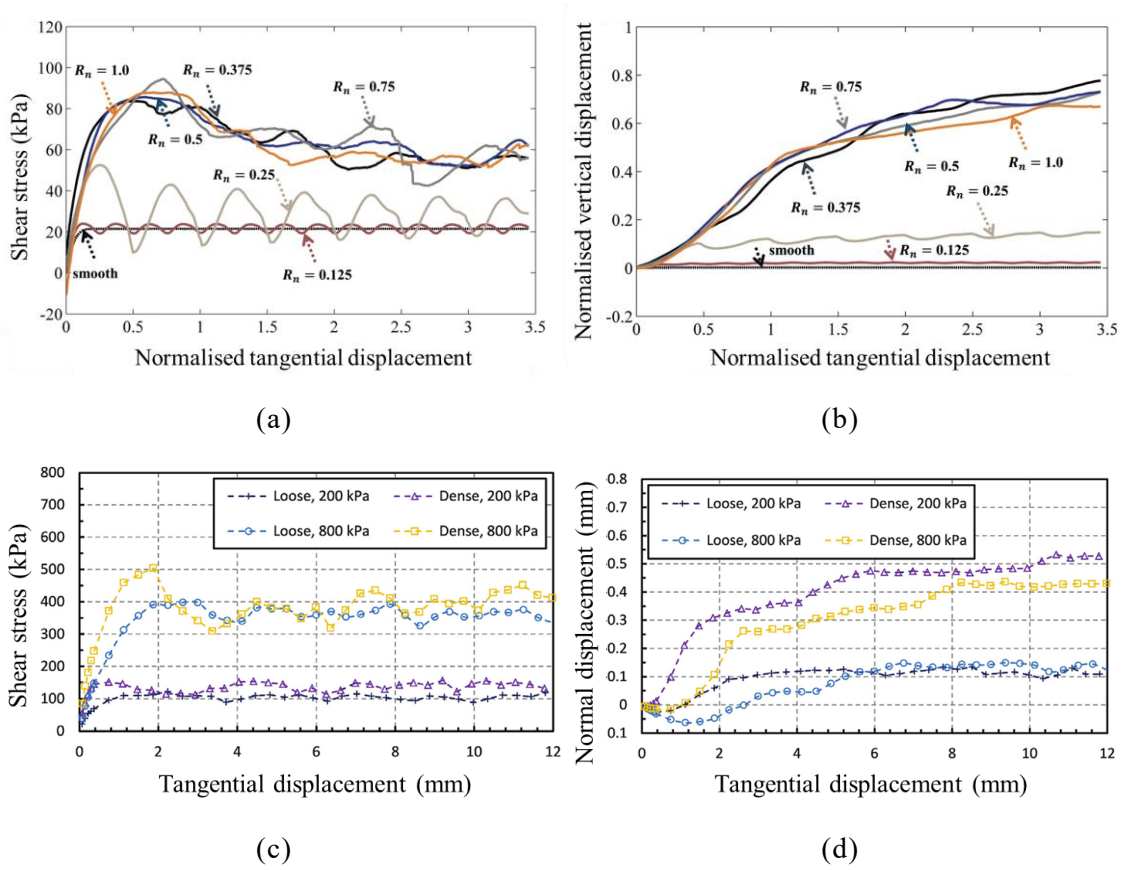

Figure 2-16 Typical macroscopic interface shearing behaviour: (a) shear stress versus tangential displacement and (b) normalised vertical displacement response under different R_n and 80 kPa normal stress (Jing et al., 2018); (c) shear stress versus tangential displacement for loose and dense specimens, and (d) normal displacement response under 200 and 800 kPa normal stress (Gu et al., 2017)

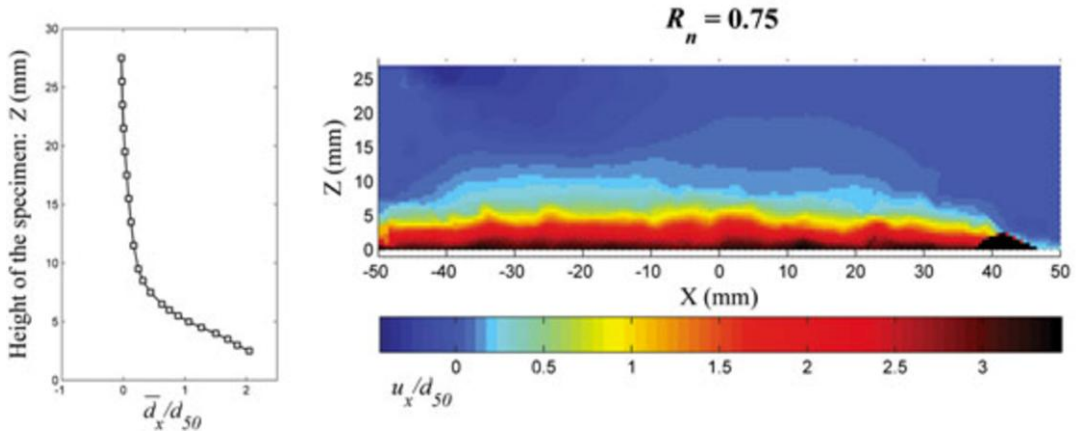

Figure 2-17 Shear band based on normalised shear displacement under 80 kPa normal stress (Jing et al., 2018)

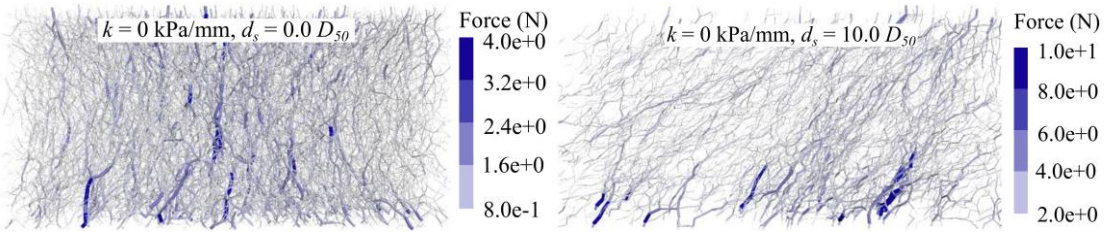

Figure 2-18 Force chains of specimens in interface shear tests (Wang and Yin, 2022)

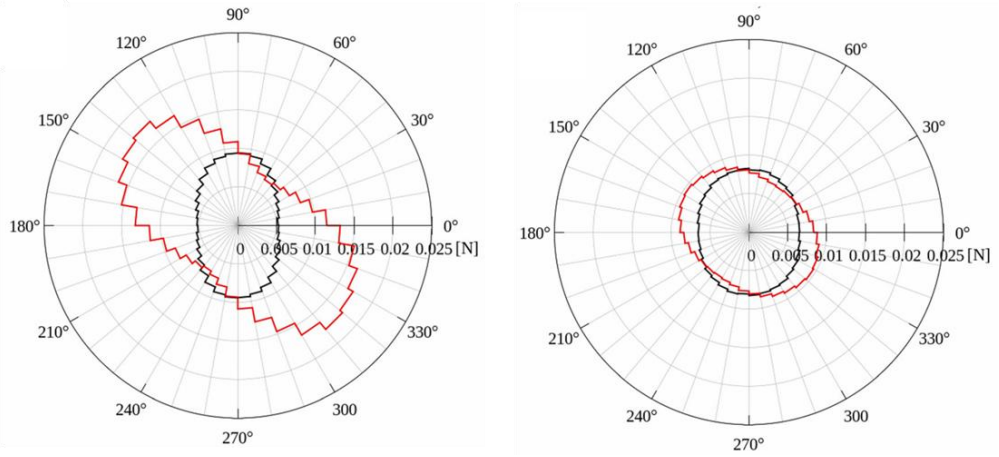

(a) (b)

Figure 2-19 Polar mean contact force distribution for clumps at the beginning of the test (black line) and at residual state (red line) under 100 kPa: (a) R_n=2.0 and (b) R_n = 0.5 (Grabowski et al., 2021b)s

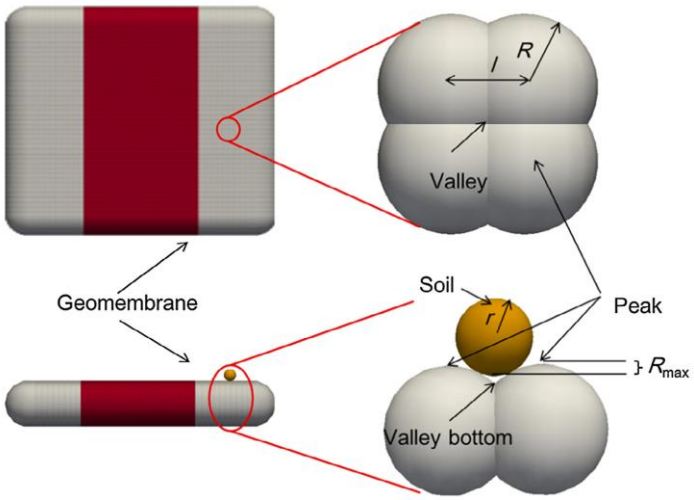

Figure 2-20 Modelling of geomembrane by overlapped assembly of balls (Feng et al., 2018)

CHAPTER 3: EXPERIMENTAL INVESTIGATION OF MONOTONIC SHEAR BEHAVIOUR AT THE SAND-GFRP INTERFACE

3.1 Introduction

A comprehensive understanding of the interface shearing mechanism between sand-coated FRP and sand remains incomplete, although significant research has been conducted to examine the effects of soil properties, stress conditions, FRP types, and their material properties on the shear behaviour of the sand-FRP interface. Notably, previous studies have not sufficiently accounted for variations in the roughness of sand-coated FRP and the volumetric behaviour of sand specimens at the sand-GFRP interface. Investigating the evolution of GFRP roughness under different tensile loads offers a practical approach to understanding the contact phenomena of sand-GFRP interactions under field conditions. Additionally, sequential testing allows for a more in-depth analysis of the influence of normal stress on interface shearing.

This study aims to elucidate the shearing mechanism of the sand-GFRP interface by evaluating the effects of GFRP surface texture and roughness on shear behaviour. Three types of GFRP surfaces are considered: (1) smooth-surface GFRP, (2) sand-epoxied GFRP with varying silica sand coating ratios, and (3) rough-surface GFRP. Furthermore, the study examines the effectiveness of different GFRP surface treatments under diverse conditions by analysing the impact of initial relative density and sand mixture composition on the interface shear behaviour. Experimental results from interface shear tests are systematically interpreted, providing a rational discussion of the underlying deformation mechanisms involved in interface shearing. Based on relative roughness and interface friction angle criteria, interface roughness classifications are established, and simplified design charts are proposed to support

performance-based interface design by estimating friction angles and guiding the optimisation of sand-epoxy coatings.

3.2 Materials and experimental methods

3.2.1 Material properties

Two types of Fujian standard sand were used to prepare testing specimens. The sands have particle size distributions of 0.15 to 0.3 mm and 0.85 to 1.18 mm, which are designated as fine (F) and medium (M) sands, respectively, as shown in Figure 3-1. Based on the presented morphology of fine and medium sand particles, as shown in Figure 3-1(d), particle shapes have been quantified by using circularity (C_{irc}) and roundness (R_{rd}) parameters (Wadell, 1932; Wang et al., 2023). The estimated mean C_{irc} and R_{rd} values for fine sand are 0.726 and 0.596, whereas for medium sand are 0.855 and 0.678. Based on the mean C_{irc} and R_{rd} values and morphology photos, fine sand is more angular and has a rougher texture than medium sand, which can be classified as subangular to subrounded, and medium sand as subrounded. Furthermore, silica sand with a particle size of 0.1–0.8 mm was used to obtain roughness varieties in GFRP plates, as shown in Figure 3-1(c), and the corresponding morphology can be observed in Figure 3-1(d).

Square GFRP plates measuring 20 cm × 20 cm with a thickness of 2 cm were fabricated by cutting from a pultruded GFRP panel manufactured using a 450 g/m^2 fiberglass strand mat embedded at 28% by weight in ATLAC 430 epoxy resin. These plates are representative of medium-strength FRP products commonly used in industrial applications. To create varying surface roughness, smooth and rough finishes were produced by pressing the plates against smooth or machine-finished stainless-steel plates, respectively. For sand-epoxied specimens, the GFRP surfaces were first mechanically roughened, then a fresh epoxy resin binder was applied. Silica sand was uniformly distributed onto the wet epoxy at dosages of 500, 1000, and 1500 g/m^2 to achieve varying surface roughness. The sand-epoxy coatings with concentrations of 500, 1000, and

1500 g/m^2 were selected to represent a practical range of sand application intensities based on fabrication feasibility, preliminary trials, and consistency with values reported in a previous study (e.g., Almallah et al., 2020a). A dead load of 6 kPa was applied via a stainless-steel cover plate during curing of the sand-epoxy coating (Toufigh et al., 2016). Finally, any exposed sand surfaces were sealed with a thin epoxy coat to ensure proper bonding, resulting in enhanced surface roughness and hardness. To validate the uniformity of the surface coating, weight measurements were conducted to confirm the targeted sand concentration rates (500-1500 g/m^2), and visual inspection was performed to assess the consistency of sand distribution and epoxy coverage across the GFRP surfaces.

3.2.2 Mixture proportions and GFRP composition

In order to investigate the effects of particle size, density of sand, and roughness of GFRP, seven types of sand mixtures, including pure fine sand and pure medium sand, two relative densities, and three categories of GFRP plates were used in this study. Detailed mix designs for the sand specimens and GFRP types are presented in Tables 3-1 and 3-2. Table 3-1 shows the soil properties of fine sand, medium sand, and sand mixtures at five different proportions of fine (F) and medium (M) sands. Figure 3-2(a) shows the particle size distribution of the sand mixture, while the first and the last rows of Table 3-1 show the soil properties of 100% fine sand and 100% medium sand. The nomination of samples S1, S2, S3, S4, and S5 between F and M denotes 5, 10, 20, 30, and 50% of fine sand content in the fine and medium sand mixture. Meanwhile, the mixture criteria are based on the median particle size of medium sand (d_{50} = 1.001), almost 4.7 times the fine sand (d_{50} = 0.212) and the approach is filler or admixture bonding of fine sand in medium sand as a main component, and how this behaviour alters with increasing fine sand content in the gap-graded mixture. Additionally, the elevation of the shear strength could be expected due to the enhancement of density and lowering of the inter-particle void simultaneously with various proportions of fine sand within the gap-graded mixture.

This kind of concept was extracted from the fines (<0.075 mm) effect in the sand mixture and several useful findings related to this (e.g., Thevanayagam, 2007; Cabalar, 2010; Minh and Cheng, 2016). For each type of sand mixture, both loose ($D_r = 35\%$) and dense ($D_r = 90\%$) specimens were prepared to simulate loose and dense field conditions. The relationship between the index void ratio (maximum index void ratio 'e_{max}' and minimum index void ratio 'e_{min}') of the sand mixture and the fine sand content is shown in Figure 3-2(b). The increase in fine sand content decreases the index void ratio until the minimum index void ratio of the S4 mixture (30% fine sand content) increases again, and a similar scenario can be observed for the maximum index void ratio.

3.2.3 Specimens preparation and testing methods

Three categories of GFRP plates were used in this study: smooth surface finish plain GFRP, sand-epoxied GFRP with varying concentrations of silica sand coatings (i.e., 500–1500 g/m^2), and rough surface finish plain GFRP, were used in the study. All three categories of GFRP were prepared from five batches of production, including three batches of sand-epoxied GFRP with different amounts of epoxied silica sand from 500 to 1500 g/m^2. Figure 3-3(a) shows photographic views of these GFRP plates, while Figure 3-3(b) presents their corresponding surface profiles. A 3D Laser Scanning Microscope with a 10× objective lens is used to measure the surface roughness of the GFRP specimen. GFRP plates of Figure 3-3(a) were measured in 4 sampling locations to evaluate the average roughness. The arithmetic average roughness of each sampling location was measured along the shearing direction, taking the surface size 3×3 pitch (3925×2875 μm) directly above each mark (referencing the mark as the bottom-middle of the pitch). Then, the average of the arithmetic average roughness at the four sampling locations was calculated to determine the average roughness (R_a) for each GFRP plate in the initial state and after interface shearing. In addition to measuring the average roughness on four sampling locations using 3×3 pitch size, seven additional sampling locations were measured using a larger 5×5 pitch size (6405×4625 μm; Figure 3-3(c)). This was done to assess the impact

of both sampling locations and size on the average roughness measurement, and to investigate how surface roughness evolves on PFRP(R) plates following interface shearing, particularly in relation to the inherent weave pattern and directional irregularities of the rough surface finish GFRP.

The degree of roughness variation can affect interface shear strength (Stark et al., 1996; Fleming et al., 2006; Xu et al., 2023) at the sand-GFRP interface. Furthermore, the term 'representative average roughness' (R_{ra}) can be introduced to address roughness variation quantitatively as,

$$R_{\mathrm{ra}} = \frac{\sum_{i=0}^{n-1}(R_{\mathrm{a}})_i}{n} \tag{3-1}$$

where n refers to the total number of average roughness measurements for a particular structural unit of FRP at a specific location before $((R_{\mathrm{a}})_{i=0})$ and after $((R_{\mathrm{a}})_{i=1,2,\dots,n-1})$ interface shear testing. A relative roughness (R) parameter based on the R_{a} can be implemented (Paikwosky et al., 1995; Subba Rao et al., 1998) to evaluate the interface alternatively. Subba Rao et al. (1998) introduced the weighted average diameter of sand particles as a denominator to evaluate relative roughness, a broader term for sand mixture. It can represent the particle size between the gap of the sand mixture, i.e., particle sizes that are not even present in the gap-graded sand mixture. Thus, relative roughness can be modified as,

$$R = \frac{R_{ra}}{d_{50}} \tag{3-2}$$

where d_{50} is the median particle size, which can be obtained from the particle size distribution curve.

The testing of surface hardness is necessary in the study of the alteration in roughness of GFRP plates during shearing under different normal stresses (Pando et al., 2002). Hardness is defined as a material's resistance to localised plastic deformation, commonly measured by indentation tests such as the Vickers hardness test, which reports hardness in units of gf/mm^2 (HV). Unlike stiffness or modulus, which quantify elastic deformation, hardness characterises surface resistance to permanent deformation or scratching. Micro indentation was performed with the standard Vickers diamond pyramid at an angle of 136°

between the apex by using the Digital Micro-Hardness Tester-SCTMC. A test force of 100 gf (0.981 N) was applied through the micro indenter in force-controlled mode, and 21 tests were performed on each batch of GFRP plates used in this study to determine the Vickers hardness (HV) value (Table 3-2; Pando et al., 2002; He et al., 2021; ASTM E384-22, 2022).

Two categories of sand specimens with different compositions were prepared. Category 1 used pure fine and medium sand for shear tests, while Category 2 involved using fine sand, medium sand, and sand mixtures against GFRP for interface shear tests. Air-dried sand of predetermined mass was used to prepare the Category 1 specimen with dimensions of 60 mm (length) × 60 mm (width) × 28 mm (thickness). In Category 2, the lower half of the shear box was filled with a GFRP composite plate, and the upper half was filled with sand with dimensions of 60 mm (length) × 60 mm (width) × 18 mm (thickness). The dense sand specimens were prepared as a homogeneous mixture by levelling and compacting in three layers, whereas the loose sand specimens were prepared as a homogeneous single layer by filling and levelling without compression, ensuring uniform particle packing in both cases. The normal loads applied in the direct shear tests were 50, 100, and 200 kPa. All tests were conducted at a controlled laboratory temperature of 20 ± 2 ºC. A constant shear displacement rate of 0.6 mm/min was applied to minimize rate effects, and shearing was continued in the lower half of the shear box until a displacement of 10 mm was reached, capturing the ultimate state of the soil in accordance with ASTM D3080 (2011).

3.2.4 Testing programme and repeatability tests

A total of 28 sets of tests were conducted, including four sets of direct shear tests on pure sands and 24 sets of interface direct shear tests on different types of sand and GFRP plates. The testing program of the interface direct shear test is presented in Table 3-3 with specific specimen ID nomination. For example, specimen ID “F-L-PFRP(S)” denotes the fine sand type of loose sand specimen sheared against smooth surface finish plain GFRP, and specimen ID “S3-D-PFRP(R)” denotes the 20% fine sand and 80% medium sand mixtures type of

dense sand specimen sheared against rough surface finish plain GFRP.

To assess the reliability of the preparation process and to study the repeatability of the sand specimens during interface shearing, interface direct shear tests were performed on loose specimens of medium sand against 1500FRP and fine sand against PFRP(R) under 50 kPa and 100 kPa. Figure 3-5 shows good repeatability between batches of samples with similar shear strength, stiffness, and stress-displacement response.

3.3 Analysis and interpretation of shear behaviour at the sand-GFRP interface

3.3.1 Pure sand shearing

The strain-softening behaviour was observed for dense specimens, with peak shear stresses occurring at the tangential displacement of around 1.5 mm, 2 mm, and 2.5 mm for fine and medium sand, as shown in Figures 3-6(a) and 3-6(c). With the slight strain-hardening, the loose specimen continues to deform plastically after tangential displacement of 3.5 mm, 4 mm, and 4.5 mm under normal stress of 50 kPa, 100 kPa, and 200 kPa. The loose and dense specimens appeared to be approaching identical shear stress at around 5 mm of tangential displacement for fine sand, whereas this occurred at a higher displacement for medium sand. In the case of medium sand, the shear stress approached the ultimate shear stress after 6 mm for loose specimens, and it was observed after 8 mm tangential displacement under normal stress of 50 kPa, 100 kPa, and 200 kPa for dense specimens. Fine sand exhibited higher shear strength than medium sand, primarily due to its relatively subangular particle shape and rough surface texture. As shown in Figures 3-6(b) and 3-6(d), all the dense sand specimens show a slight contraction followed by shear dilatancy under 50 and 100 kPa normal stress, but significant contraction was observed under 200 kPa normal stress. Both dilative and contractive behaviour follow the expected theoretical trend for dense and loose specimens. Medium sand exhibited larger deformation than fine sand due

to the larger particle size.

The shear stress response of medium sand is similar to the case of glass beads (D_{50} = 0.65) in the previous study (Lashkari and Jamali, 2021). The behaviour of fine sand can be related to subangular particles (D_{50} = 0.32) of their study. Even though the specimens were medium dense in the Lashkari and Jamali (2021) study, the angularity and minimum void ratios prevailed to acquire larger shear stress and dilative behaviour. In loose specimens of fine sand, a slight dilation was observed along the contractive behaviour at 3 to 6 mm of tangential displacement, which might be the effect of angularity, and this mechanism is in agreement with Lashkari and Jamali's (2021) findings.

Given the stable shear stress ratios and normal displacement of both loose and dense specimens corresponding to fine and medium sand, the ultimate state was achieved after 9 mm of tangential displacement, regardless of the reasonable contraction trend of loose specimens. Figure 3-6(e) illustrates the peak and ultimate shear stresses of fine and medium sands, showing that fine sand has a steeper failure envelope, indicative of higher internal friction due to greater interparticle interlocking. Figure 3-6(f) presents the variation in maximum normal displacement, highlighting that dilation decreases linearly with increasing normal stress, while contraction increases. Medium sand exhibits more pronounced volumetric changes than fine sand, owing to its coarser particle size. In summary, the dilation angles for fine sand decreased from 12.7° to 8.8°, and for medium sand from 10.9° to 7.8°, as confining pressure increased from 50 to 200 kPa, consistent with the observed linear reduction in dilation. Fine sand exhibited higher peak (40.6°) and ultimate (28°) friction angles for dense specimens compared to medium sand, which showed peak and ultimate friction angles of 31.6° and 24.5°, respectively, as summarised in Table 3-4. In contrast, loose specimens exhibited ultimate friction angles of 29.7° for fine sand and 23.4° for medium sand. These results confirm that finer particles with relatively angular particle shape and higher density contribute to increased shear strength through enhanced interparticle friction and dilation, while increased confinement suppresses dilative behaviour.

3.3.2 Effect of GFRP surface roughness

Figure 3-7 shows the mechanical responses of loose sand-GFRP and dense sand-GFRP interfaces under the normal stress of 50 kPa. All the loose specimens exhibited strain-hardening with elastic deformation occurring first until plastic deformation occurred after 1 mm tangential displacement (Figure 3-7(a)). The dense specimens exhibited elastic deformation earlier than 1 mm tangential displacement and then continued plastic deformation (Figure 3-7(c)). For both medium and fine sands, the peak and ultimate shear stresses increased with higher roughness levels of GFRP plates. The maximum interface shear strength was observed in the fine sand-1500FRP interface as 32.8 kPa and 25.5 kPa for the peak and ultimate state of the dense specimen, and 26.5 kPa at the ultimate state of the loose specimen. Figure 3-7(b) illustrates that the contraction behaviour of loose specimens of fine and medium sand increases with increasing roughness of GFRP plates.

The medium sand sheared against 1500FRP exhibited the maximum contraction, even more than the pure shearing of medium sand, followed by PFRP(R) with a linear increase in normal displacement beyond 3 mm of tangential displacement. This might be due to the slipping of particles under the 50 kPa normal stress, and maybe a few sub-rounded particles moved outward of the shear box through the interface under this stress state. In contrast, the maximum dilation in dense specimens of medium sand while shearing against 1500FRP is the expected behaviour for the medium sand in a rough surface interface due to higher interlocking. The dilative behaviour of fine sand showing higher dilation in the F-D-1000FRP interface compared to the F-D-1500FRP interface is possibly due to slight surface waviness. In fact, shear stress remained unaffected by this waviness (Figure 3-3(a), Figure 3-7(d)).

It is assumed that the measured peak shear stress and the ultimate shear stress (at 9–10 mm displacement) accurately reflect the interface strength. Figure 3-8 shows the variations in peak and ultimate shear stress of fine sand-GFRP interfaces with the average roughness of GFRP under 50 to 200 kPa normal stress. The shear stress increased linearly with a higher average roughness of GFRP,

which is consistent with those of Frost and Han (1999) for blasting sand and glass beads-FRP interface in the peak interface friction coefficient versus normalised roughness plot. The increase in roughness significantly affects the peak shear stress for dense sand under 200 kPa normal stress compared to 50 kPa normal stress with respect to ultimate shear stress. These phenomena are consistent with the interpretation of DeJong and Westgate (2009). In summary, higher normal stress enhances the particle confinement and interlocking with the rough surface, thereby increasing resistance to particle rearrangement and ultimately resulting in higher peak shear stress.

3.3.3 Influence of normal stress

Figure 3-9 illustrates the influence of normal stress on the interface friction coefficient, along with comparisons to literature. As shown in Figures 3-9(a) and 3-9(b), all three interfaces, i.e., F-PFRP(S), F-1500FRP, and M-1500FRP, exhibit a clear decrease in friction coefficient with increasing normal stress, following logarithmic trend consistent with Archard's (1957) theory and previous findings, e.g., Frost and Han (1999) and Zettler et al. (2000). Frost and Han (1999) similarly reported a reduction in peak interface friction coefficient with increasing normal stress at the sand-GFRP interface, whereas Uesugi and Kishida (1986b) observed a weaker dependency for sand-steel interfaces. Despite similar initial roughness of 1500FRPs, fine sand consistently yields higher peak and ultimate interface friction coefficients than medium sand, attributed to its higher internal friction angle and enhanced interparticle and interface interlocking (Figure 3-9). Although the ultimate friction coefficient for loose and dense specimens is essentially the same, differences in particle rearrangement process, dilative behaviour in dense and contractive behaviour in loose sand, become less pronounced at higher normal stress (e.g., O'Rourke et al., 1990; DeJong and Westgate, 2009). Notably, the initial roughness of 1500FRP is nearly six times greater than PFRP(S), contributing to a 50% increase in peak interface friction and over 20% gain in ultimate friction for the fine sand-GFRP interface.

Figures 3-9(c) and 3-9(d) compare the interface friction coefficients at peak

(Figure 3-9(c)) and ultimate (Figure 3-9(d)) states from this study, using fine and medium sands sheared against plain GFRP (i.e., both smooth-surfaced (S) and rough-surfaced (R)) and sand-epoxied GFRP, with relevant literature involving sand sheared against uncoated and sand-coated FRP (Frost and Han, 1999; Sakr et al., 2005; Toufigh et al., 2016; Almallah et al., 2020a; Namjoo et al., 2022). Detailed descriptions of interface materials and test conditions are provided in Appendix A (Table A-1). The present study yielded peak and ultimate friction coefficients comparable to those reported by Frost and Han (1999) (pultruded GFRP) and Sakr et al. (2005) (filament-wound), respectively. In contrast, Almallah et al. (2020a) recorded substantially the highest peak values for sand-coated GFRP (~0.8–1.15), even for uncoated GFRP (~0.75–1.05), attributed to their use of a broader particle size distribution (0.075–4.75 mm) and coarser coating grade (1.18–2.36 mm). The present study employed finer and more narrowly graded sand (0.15–0.3 mm and 0.85–1.18 mm), which inherently limits the degree of particle interlocking and shear resistance. However, both this study and Almallah et al.'s (2020a) investigation show consistent improvements of over 30% at peak and over 20% at ultimate states due to sand-epoxy coating. While studies such as Toufigh et al (2016) and Namjoo et al. (2022) also used coarser and exposed coatings, the current findings reflect a more conservative frictional response with finer coatings (0.1–0.8 mm). This difference stems from the controlled particle gradation, morphology, and sand-epoxy non-exposed coating methodology employed here, allowing for clearer isolation of the effects of interface roughness. Consequently, although lower in absolute values, the findings offer a robust and reproducible reference for evaluating sand-GFRP interaction under well-defined conditions.

3.3.4 Variations in average roughness of GFRP plates and rotation effects

Figure 3-10 shows the initial and after testing 3D surface profiles of GFRP plates. As shown in Figure 3-10, the number of small patches of hills and valleys increases as the amount of epoxied sand rises from 500 to 1500 g/m^2. This

corresponds to a progressive roughening of the GFRP surface. With the progression of interface testing, roughness evolves, accompanied by the development of surface degradation characterised by scar formation for smooth surfaces, whereas scars and impression or groove-like degradation patterns for rougher surfaces (e.g., 1000FRP and 1500FRP). These features of roughness evolution, particularly the widening of scars and grooves, intensify with increasing normal stress and initial roughness order when sheared against fine sand specimens. At the M-1500FRP interface, groove formation and surface smoothing become more pronounced as normal stress increases. Overall, surface degradation increases with normal stress. Notably, the heavily deteriorated 1500FRP batch of GFRP plates significantly contributes to interlocking and resistance force generation, as evidenced by the pronounced softening effect observed in the F-D-1500FRP specimen (Figure 3-7(c)). Beyond 6 mm of tangential displacement, a slight post-peak hardening effect was noted for the F-1500FRP interface, whereas the M-1500FRP demonstrated a sudden drop, likely due to localised smoothing and asperity collapse. The near-perfect coefficient of determination ($R^2 \approx 1$) obtained from the linear fitting of peak and ultimate shear stresses under varying normal stresses (50, 100, and 200 kPa) (Figure A-1), further validates the consistency of the degradation-induced mechanical response, which will be discussed in the next section.

The variation in average roughness of plain and sand-epoxied GFRP surfaces is quantitatively illustrated in Figure 3-11. For the 1000FRP and 1500FRP sheared against fine sand, roughness increases progressively with successive tests under normal stresses ranging from 50 to 200 kPa. In contrast, the roughness of PFRP(S), 500FRP, and PFRP(R) decreases under similar conditions. Specifically, at 200 kPa, the average roughness of 1000FRP and 1500FRP increases by 10.5% and 7.0%, respectively, relative to their initial states. Conversely, the roughness reduction for F-PFRP(S), F-500FRP, M-PFRP(R), and M-1500FRP, are 6.3%, 2.9%, 13.1%, and 23.4%, respectively.

The shearing surfaces of sand-epoxied GFRP specimens (≥ 48 HV; except for 500FRP) are notably harder than the plain GFRP (~27.5 HV), with initial

average roughness for PFRP(S) and 1500FRP ranging between 8 μm and 52 μm. In specimens like 500FRP, 1000FRP, and 1500FRP, the presence of epoxied sand contributes to higher initial roughness and increased interlocking during interface shearing, particularly against fine sand. This roughness and associated shear strength are attributed to the progressive removal of epoxy and epoxied sand particles under stress (Figure 3-10). Fine sand particles promote groove formation on the rougher GFRP surface, enhancing sliding resistance and inducing particle rotation. This process leads to the formation of impressions and trenches on the testing surface, consistent with previous studies (e.g., O'Rourke et al., 1990; Sakr et al., 2005), thereby increasing the average roughness of 1000FRP and 1500FRP. In contrast, 500FRP exhibits fine linear scars along the shear direction at higher normal stresses, indicating greater slip and limited particle rotation. This mechanism leads to superficial deterioration of the epoxied layer, thereby reducing the average roughness through surface smoothing.

For the M-1500FRP interface, roughness decreases as thicker epoxy layers are eroded by rolling subrounded particles of medium sand. Moreover, due to the lower hardness of the coating epoxy layer, sandwiched between the specimen sand and bonded sand, and its removal at higher normal stresses, surface smoothing occurs, leading to reduced surface roughness.

3.3.5 Effect of mixture proportion

Figure 3-12 shows the peak and ultimate shear stress envelopes for dense and loose specimens of the sand mixture in the sand mixture-PFRP(R) interface. Among the four different mixtures, the largest slope of the stress envelope was exhibited by the S4 specimen, especially in the dense specimens, while the failure envelopes of S2, S3, and S4 loose specimens coincide with each other. Relatively subangular particles of fine sand enhance the interlocking between fine and medium sand with an increase in fine sand content. The significant effect of fine sand content can be observed in the S4 mixture, mainly for the peak state. Moreover, the fine sand content causes a very small change in median particle size, coefficient of uniformity, and initial void ratio from one mixture

combination to another (Table 3-1). Therefore, the S2, S3, and S4 mixture may not exhibit distinct behaviour at the ultimate state due to the combined influence of these factors.

Figure 3-13 shows the variations in peak and ultimate shear stress with fine sand content in sand mixture sheared against rough surface finish plain GFRP interfaces under 50, 100, and 200 kPa normal stress. A third-degree polynomial provides a good fit to the data, despite the absence of intermediate points between 50% and 100% fine sand content. Similar nonlinear effects of fines content on shear strength have been reported in other granular mixtures. For example, Yilmaz et al. (2021) investigated the strength-dilatancy and critical state behaviour of binary mixtures of graded sands and found that variations in fines content and particle-size ratio led to significant, nonlinear changes in peak friction angle and dilation. Although their analysis did not employ a cubic polynomial fit, the reported trends support the nonlinear behaviour captured in the present model across the tested fine contents of 0%, 5%, 10%, 20%, 30%, 50%, and 100%. In the current study, both peak and ultimate shear stress exhibited a non-monotonic trend with increasing fine sand content, rising, then falling, and rising again, reaching maxima at approximately 30 % and 100 % fine sand. The initial enhancement in interface shear strength is attributed to fine sand content acting as a filler for the medium sand, producing maximum interlocking bonds. The subsequent reduction in strength with further fine sand addition is likely due to the reduced volume of medium sand particles, where fine sand content in the mixture behaves as a main component, and medium sand behaves as an admixture featuring a lower internal friction angle, which weakens interlocking. At high fines content, the fine sand becomes the dominant structural component, with medium sand acting as an admixture, aligning with the concept of transitional fines content, which denotes the shift from coarse-particle-dominated to fine-particle-dominated behaviour in binary mixtures. Previous studies report this threshold to typically lie between 20% and 50%, depending on the soil property considered (Thevanayagam et al., 2002; Yang et al., 2006; Zuo and Baudet, 2015). The findings are contrary to the graded sand of Wang et al.'s

(2019) study. The difference between the ultimate shear stress of the dense and loose specimens that appear under 200 kPa normal stress and the ultimate shear stress that appears at 50 kPa normal stress is caused by the higher potential for filler movement in loose specimens (Frost and Han, 1999) and the movement of fine sand in the mixture during the processing of the shear box after specimen preparation and before shearing.

As shown in Figure 3-14(a), the surface profiles are unique for all seven sampling locations, and alterations in the maximum height of the surface profile after each normal stress shearing can be qualitatively visualised. A detailed pictorial description for the S4-PFRP(R) interface at mark 1 of PFRP(R), including height profiles and laser images, is presented in Figure 3-14(b). The images reveal that, with increasing normal stress, the surface undergoes notable evolution characterised by the formation of scars, impressions, and a combination of impression development and surface smoothing. This trend reflects the mixed influence of the sand composition, 30% fine and 70% medium particles. Fine sand primarily causes scars due to its ability to penetrate and abrade the GFRP surface, enhancing local surface roughness. Meanwhile, the dominant medium sand particles, which are larger and relatively subrounded, contribute to impression formation and surface smoothing by rolling, thereby eroding and flattening asperities. Most of the sharp edges of the crest along the shearing surface disappear under 200 kPa normal stress.

As shown in Figure 3-15, the trend of variation in average roughness for the seven sampling locations is fairly straight and stable compared to that of the four sampling locations. Furthermore, during shearing under three normal stress levels for the S1 to S5 mixture against the PFRP(R) plates, the proportions of sand mixtures had minimal effect on the variation in average roughness, an observation consistent with the visual findings reported by O'Rourke et al. (1990). Additionally, the consistent roughness measurements under varying normal stresses highlight the effectiveness and stability of the plain rough surface finish GFRP as an alternative to sand-epoxy coatings, though long-term durability requires further investigation beyond the present monotonic testing.

The average roughness of the seven sampling locations exceeds that of the four sampling locations by more than 11 μm, due to the surface inclination along the length, broader surface coverage, and the inherent irregularities in GFRP surface texture. While measuring the average roughness of the PFRP(R), a 3×3 pitch size in at least four locations is sufficient if the selected sampling location represents approximately the entire structural roughness; otherwise, the selection of a larger surface area is suggested. Specifically, the 5×5 pitch size is more representative of the PFRP(R) surface.

3.3.6 Comparison of friction angles and maximum normal displacement variations

Figure 3-16(a) presents the stress envelopes used to determine friction angles for loose and dense specimens of fine sand a the F-PFRP(S) interface, demonstrating a reliable linear fitting approach with a coefficient of determination (R^2) close to 1 (see Appendix A for other interfaces). Figure 3-16(b) presents a bar chart comparing the internal friction angles with the interface friction angles for both dense and loose specimens of fine sand and medium sand. PFRP(S) and 500FRP contribute less to the peak friction angle compared to 1000FRP and 1500FRP when sheared against fine sand. The F-1500FRP interface exhibits the highest interface friction angle among the tested interface configurations, exceeding that of the F-PFRP(S) interface by more than 40% at the peak state, 20.4% at the ultimate state for dense sand, and 25.3% at the ultimate state for loose sand (Figure 3-16(b)). Variations in ultimate friction angles between dense and loose specimens are primarily attributed to differences in packing conditions, particle rearrangement during shearing, and their proximity to the reference critical state. Error bars shown at the ultimate state represent deviations of ±0.5° to ±1° for various interfaces, and up to ±2° for pure sand.

Similarly, for medium sand, M-1500FRP interface shows a notable increase in friction angle compared to M-PFRP(R), with an enhancement of 9.4% at the peak state and 7.5% at the ultimate state for dense specimens, and 7.2% at the ultimate state for loose specimens. The findings are consistent with the previous

study (Almallah et al., 2020a), where an increasing amount of coated sand enhances the interlocking in the interface until 1500 g/m^2 of sand coating in GFRP when sheared against poorly graded sand, but a lower interface friction angle was obtained in the present study of sand-epoxied GFRP. This is because the sand-epoxied surface of the GFRP in the present study is sealed with a thin epoxy layer. However, the interface surface is an open surface of coated sand in the Almallah et al. (2020a) investigation. Overall, the peak friction angle ratios (the ratio of the interface friction angle to the internal friction angle of pure sand) for F-1500FRP and M-1500FRP are approximately 0.72 and 0.76, respectively, indicating effective interface performance and suggesting potential for further enhancement through interface optimization. Figure 3-16(c) shows that the interface friction angle increases linearly with an increase in representative average roughness of GFRP. This trend is even more significant for the peak state. The results indicate that the soil failure in the interface shear test occurs at the interface. In short, the larger the roughness of GFRP plates, the greater the interlocking and interface friction angle, followed by significant strain-softening for dense specimens and strain-hardening for loose specimens.

Figures 3-17(a) and 3-17(b) show the variation in the peak and ultimate interface friction angle of dense and loose specimens of fine and medium sand against GFRP plates and sand mixture against the PFRP(R) interface with respect to relative roughness. Fine sand-GFRP interfaces show the linearly increasing trend of interface friction angles with an increase in relative roughness. However, within the small range of relative roughness variation in sand mixture compared to fine and medium sand, sand mixture shows the quadratic curvilinear trend with the optimum interface friction angles of approximately 28° and 25° for peak and ultimate states, respectively, in dense specimens at a relative roughness value of 0.031, closely matching that of the S4 mixture. It can be interpreted that increasing the fine sand proportion in medium sand up to 30% improves the interface shear strength by increasing the internal friction angle and interlocking between fine and medium sand particles, while simultaneously reducing the mixture's median particle size.

Five literatures (Subba Rao et al., 1998; Dietz and Lings, 2006; Han et al., 2018; Su et al., 2018; Wang et al., 2023) are considered to understand the effect of relative roughness on peak and ultimate interface friction angle. The details of the interface materials and testing setup are summarised in Table 3-5. The $R_{\max}$ roughness of regular sawtooth plates having right-angle grooves (isosceles triangle) used in Wang et al. (2023) and Su et al. (2018) studies is approximated in average roughness by dividing by 4. Relative roughness is obtained by using Equation (2-10), where $R_{ra} = R_{\mathrm{a}}$ for stainless steel. Based on the varieties of plotted data in Figures 3-17(c) and 3-17(d), a dashed line can be drawn that represents the interface roughness in three categories: smooth ($R \leq 0.001$), intermediate ($0.001 \leq R \leq 0.2$), and rough ($R \geq 0.2$). The representative trend line was plotted in a similar concept to Paikowsky et al. (1995). The internal friction angle of fine sand is assumed to be the margin for the critical interface for the rough category, and the interface is categorised based on the interface friction angles with respect to relative roughness. All the interface friction angles of this study are relevant to the intermediate category, except for the fine sand-1500FRP interface. Even though all these results of the present study remain below the trend line, they are closer to the findings of Su et al. (2018) and Wang et al. (2023). Sand particles used by Dietz and Lings (2006) and Han et al. (2018) are relatively angular to subangular compared to the present study, as well as other literature related to Fujian sand. Hence, higher interlocking is expected, resulting in a greater friction angle compared to the present study in an intermediate interface. Even though the sand particles used by Subba Rao et al. (1998) were well-rounded, within a small range of relative roughness values (0.005 to 0.057), both peak and ultimate interface friction angles exceeded those obtained in the present study as well as those reported in other literature. This might be due to the overprediction of the interface friction angle in the interface shear test type B apparatus of Subba Rao et al.'s (1998) study.

As shown in Figures 3-17(c) and 3-17(d), the variation trends of the peak and ultimate interface friction angles indicate that the friction angle initially increases with increasing relative roughness. This increment continues until

reaching the transition zone between the intermediate and rough zones, after which it stabilises or slightly declines. This transition zone is also called critical interface roughness. Moreover, as the rough zone of the interface is encountered, the interface shear resistance becomes similar to internal soil strength; thereby, the failure plane shifts upward, i.e., within the soil mass.

Figures 3-17(e) and 3-17(f) present simplified design charts for estimating peak and ultimate interface friction angles at the sand GFRP interface. These charts incorporate surface roughness, sand particle size, and morphology (subangular to subrounded, i.e., $R_{rd} = 0.4 - 0.68$), and sand-epoxy coating configurations under normal stresses ranging from 50–200 kPa. The shaded zones are derived from a consolidated dataset comprising the present study and supporting literature. The optimal boundary lines reflect the representative trends observed in Figures 3-17(c) and 3-17(d) and correspond to the critical frictional criteria of sand particles interacting with rough interfaces. In contrast, the lower bounds of the shaded region are derived from the current interface experimental data. In the peak state, the shaded zone spans 5° to 15°, and in the ultimate state, 4° to 8°; both ranges correspond to increasing relative roughness. A material and design tolerance of ±1° is considered. With the present dataset, the proposed design charts offer an empirically grounded reference for estimating interface friction angles of sand-epoxied GFRP surfaces and optimising the application of sand-epoxy coatings for targeted interface behaviour, where optimisation refers to tailoring sand particle size, coating grade, and surface morphology to achieve desired frictional performance while maintaining surface stability. However, they are not yet suitable for direct field application. To develop design-ready tools, these charts should be expanded using broader, field-representative datasets that encompass a wider range of sand types, particle sizes, epoxied sand grades, and full-scale boundary conditions. Such enhancements will improve accuracy and reliability, enabling safer and performance-based interface design for real-world applications. An economical design zone to support performance-based and safe design is recommended, specifically near the transition from intermediate to rough interface, where failure is more likely to occur at the interface rather than

the surrounding soil. This approach aligns with geotechnical safety principles aimed at minimising soil instability. Additionally, the charts support a reverse design approach: by specifying a target interface friction angle along with known particle size and morphology and expected surface characteristics (e.g., sand-epoxy coating grade and surface roughness), engineers can estimate the required relative roughness within the economical design zone. This approach enables the selection or engineering of a suitable sand-epoxied GFRP surface to meet defined performance and safety criteria.

Figures 3-18(a) and 3-18(b) show the variations in maximum normal displacement of fine sand with relative roughness. For loose specimens under 50 kPa, maximum normal displacement increases linearly with roughness, reaching a maximum contraction of about 0.15 mm for 1500FRP ($R > 0.2$). In contrast, specimens sheared against smoother surfaces (e.g., PFRP(S) and 500FRP) exhibit sharp increases in contraction with increasing normal stress (100 to 200 kPa), indicating particles slip along the interface. In dense specimens, normal displacement generally decreases with increasing stress, especially under smoother interfaces. As shown in Figure 3-18(b), the largest reduction (about -0.3 mm) occurs for dense sand specimens against PFRP(S) at 200 kPa normal stress, whereas displacement remains minimal against rougher surfaces like 1500FRP. High normal stress narrows the shear zone and enhances interlocking, particularly in dense sand. However, at smoother interfaces, the narrow zone promotes surface smoothing and particle slip (e.g., -0.025 mm at 200 kPa for PFRP(S)). Although PFRP(R) and 1500FRP have higher roughness, their relative roughness remains close to that of PFRP(S) in fine sand, limiting the interfacial strength gain. Minor strain softening in medium sand-GFRP interfaces is attributed to its lower internal frictional angle compared to fine sand, allowing more particle slip and rolling. These trends are consistent with prior findings on sand-geomembrane (Frost et al., 2012; Lashkari and Jamali, 2021) and soil-FRP interface (Almallah et al., 2020a).

Figure 3-18(c) shows an almost horizontal trend in maximum normal displacement for loose sand mixture across normal stresses from 50 to 200 kPa.

This behaviour likely results from the narrow range of relative roughness (0.028 and 0.033), minimising its effect. Notably, the interface corresponding to the S1 specimen (5% fine sand) exhibits localised particle movement under 50 kPa normal stress, suggesting that fine sand tends to migrate toward the interface during shearing. This mechanism leads to a non-homogeneous mixture and promotes interface slip. In contrast, Figure 3-18(d) reveals a linearly decreasing dilative response in dense sand mixtures with increasing normal stress (100 to 200 kPa), correlating with increasing relative roughness. Specimens S1 (extreme left in Figure 18d) and S5 (extreme right in Figure 18d) exhibit the sharpest reduction in dilation at 200 kPa, highlighting the influence of fine sand content. Post-strain softening, fine particles migrate through voids among medium sand particles, diminishing dilative behaviour, particularly in specimens S4 and S5. This particle migration may also contribute to subtle changes in the effective roughness of the GFRP surface, affecting interfacial behaviour. Although the 1500FRP sand-epoxied plate exhibits the highest shear strength among all tested interfaces, its roughness variation remains unstable due to weakened bonding between the epoxied sand layer, GFRP base, and the binder, primarily caused by rotation of sand particles and grooving during shearing. In contrast, the rough surface finish plain GFRP (PFRP(R)) demonstrates more stable roughness, with a slight reduction when sheared against medium sand, and minimal variation against sand mixtures (Figure 3-15).

While sand-epoxy coating enhances the interface friction, the long-term field performance ultimately depends on maintaining stability of the surface roughness and hardness under potential scouring, within the constraints of economical design. Thus, further research is essential to stabilise roughness variation for sand-epoxied GFRP. Until such improvements are achieved, the rough surface plain GFRP may serve as a temporary yet practical alternative, though the focus remains on advancing sand-epoxy coating technologies for reliable, high-performance interface design.

3.4 Design implications and broader application of sand-epoxied GFRP

This study provides valuable insights into the shear performance of sand GFRP interfaces with and without sand epoxy coating. The findings demonstrate that sand-epoxy coatings can significantly enhance surface hardness, nearly doubling it, and increase interface friction up to 40% at peak state and 25% at ultimate state compared to uncoated GFRP. These improvements offer an effective approach for increasing surface roughness and interface strength within the studied normal stress range (50–200 kPa). These results have direct implications for the design of geotechnical systems such as retaining structures, seawalls, and shallow-embedded anchors, where optimised interface behaviour can improve structural performance and durability. However, the observed roughness variation during shearing, particularly under elevated normal stress, underscores the need for future research to incorporate more robust coating strategies and to systematically quantify surface degradation. This will be essential to ensure the long-term effectiveness of sand-epoxy coatings is fully understood and can be reliably integrated into the design of geotechnical systems. While the present study focused on monotonic interface shear testing of GFRP laminates, the enhanced bond performance of sand-coated GFRP bars under marine conditions, as reported by (Morales Arias et al., 2012; Shakiba et al., 2022), supports the broader applicability of the sand-epoxy coating technique. Although the current research was conducted under controlled laboratory conditions, it exclusively examined interface shear behaviour using air-dried sand specimens against a single gradation (0.1–0.8 mm) epoxied sand bonded with ATLAC 430 epoxy resin, a vinyl ester-based epoxy resin known for its chemical stability and long-term durability in marine environments (Zhao et al., 2024).

Despite the promising results, the scope of Chapter 3 remains limited. The testing conditions do not account for moisture effects, cyclic or dynamic loading, varying particle size distributions, or alternative epoxy formulations,

which are common in real-world geotechnical applications. Moreover, the exclusive focus on a single sand gradation of sand-epoxy coating and dry state restricts the generalisability of the findings across diverse environmental and loading conditions encountered in practice. These limitations highlight the need for caution when directly applying the results to design without further validation. To support practical implementation, a simplified design chart has been developed (Figures 3-17(e) and 3-17(f)), summarising key findings such as interface friction angles and interface roughness classifications for both plain GFRP and sand-epoxied GFRP. These charts, based on data from direct shear tests at sand-GFRP interfaces, serve as a foundational reference for engineers and researchers engaged in the design of geotechnical systems incorporating composite materials. The next chapter will extend the interface direct shear testing program to achieve greater practical relevance and ensure robust application. Emphasis will be placed on advancing experimental conditions and parameter ranges, including:

- Conducting cyclic shearing under elevated normal stresses to assess long-term interface stability and performance, employing larger specimen sizes for improved representativeness.
- Evaluating an expanded set of variables such as particle size distribution, epoxy-coated sand gradations, epoxy resin formulations, and surface roughness treatments to optimise interface shear behaviour.

3.5 Summary

Chapter 3 experimentally investigated the shear behaviour of the sand-GFRP interface, focusing on the influence of GFRP surface type and roughness. Three types of GFRP were utilised: smooth surface finish plain GFRP, sand-epoxied GFRP with varying silica sand coating ratios, and rough surface finish plain GFRP. Air-dried fine and medium sands were used in monotonic direct shear tests under normal stresses ranging from 50 to 200 kPa. The study examined the effectiveness of these GFRP types by considering key factors such as initial

relative density and mix proportion of sand, to understand their impact on the interface shear behaviour. The main findings are summarised as follows:

1) The interface shear response of sand-GFRP is influenced by factors such as particle size, mix proportion, GFRP surface roughness, and normal stress level. Enhanced shear strength was observed for fine sand, dense specimens, higher normal stress, and increased interface roughness. For a given condition, an increase in particle size leads to more pronounced dilation and contraction during shearing. Notably, loose specimens exhibit amplified contraction under progressing shear, primarily due to higher applied normal stresses in successive tests. Additionally, the shear strength of sand mixtures improves with the inclusion of fine sand (subangular to subrounded), reaching a maximum at approximately 30% fine sand content. Beyond this, a reduction occurs due to the diminishing proportion of relatively subrounded medium sand particles, which reduces interparticle interlock.
2) At lower silica sand coating ratios (i.e., smoother surfaces), the interface exhibits a greater extent of slipping and lesser particle rotation. Conversely, fine sand specimens display a higher tendency of rotational behaviour and reduced bulk sliding, attributed to stronger interlocking with the sand-epoxied GFRP interface.
3) While increasing the concentration of epoxied sand enhances shear strength, it also introduces instability in surface roughness during shearing. Substantial fluctuations in roughness were observed along the length of the interface, particularly under high concentrations of epoxied sand. In contrast, rough surface finish plain GFRPs yield more stable roughness variation during shearing, while still providing a notable enhancement in interface shear strength. Therefore, further refinement of sand-epoxied GFRP is essential to stabilise roughness variation, particularly by improving surface morphology quality for long-term performance.
4) The relative roughness, defined as the ratio of representative average

surface roughness to median particle size, serves as a key parameter in interpreting interface behaviour. Fine sand-GFRP interfaces show a linear increase in interface friction angle with increasing relative roughness, whereas sand mixture-GFRP follows a quadratic trend. Based on present results and supporting literature, interface roughness has been categorised as smooth ($R \leq 0.001$), intermediate ($0.001 \leq R \leq 0.2$), and rough ($R \geq 0.2$). All interfaces examined in this study fall within the intermediate category, except for the fine sand-1500FRP interface, which qualifies as rough.

5) Simplified design charts have been proposed as empirical tools to estimate interface friction angles of sand-epoxied GFRP surfaces and serve as a basis for optimising sand-epoxy coatings considering particle size, morphology, and surface roughness. Though currently limited to laboratory-scale applicability, the proposed design charts offer a foundation for performance-based interface design and support reverse design by linking target friction angles to required surface roughness.

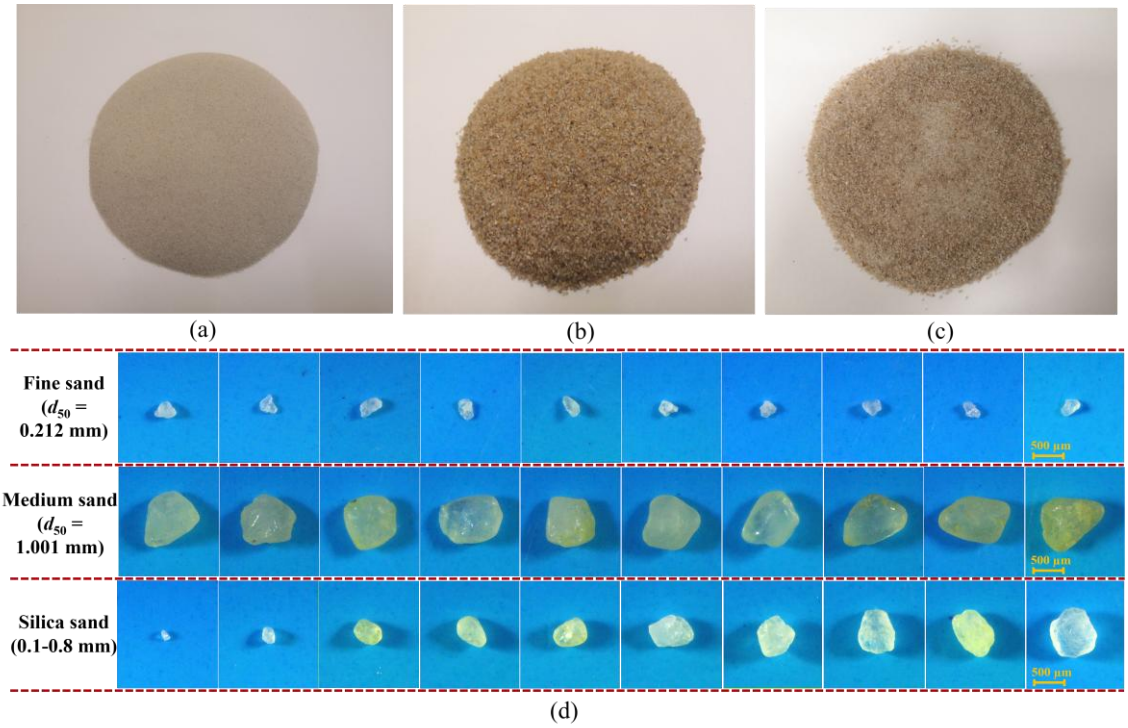

Figure 3-1 Photo view of sands: (a) fine sand, (b) medium sand, (c) silica sand for sand-epoxy coating, and (d) morphology of fine sand, medium sand, and silica sand particles

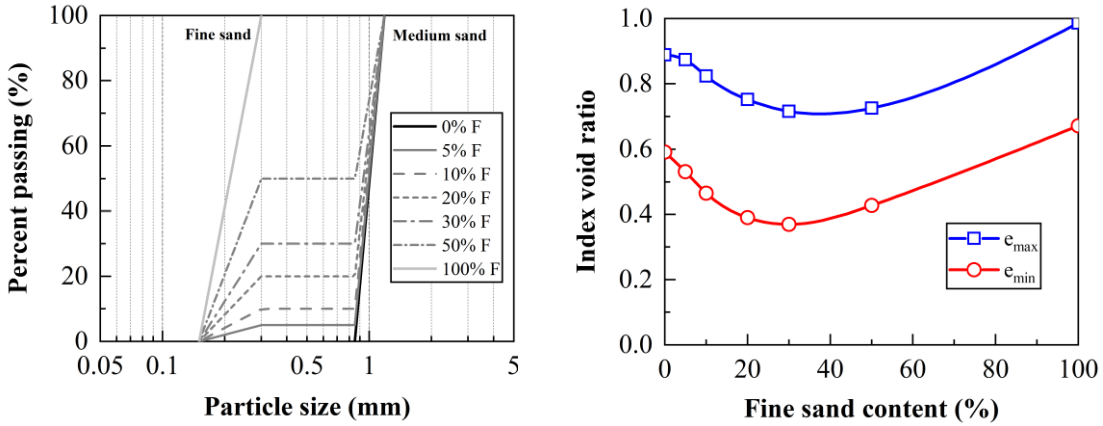

Figure 3-2 (a) Particle size distribution of sand mixture; (b) index void ratio of sand mixture versus fine sand content

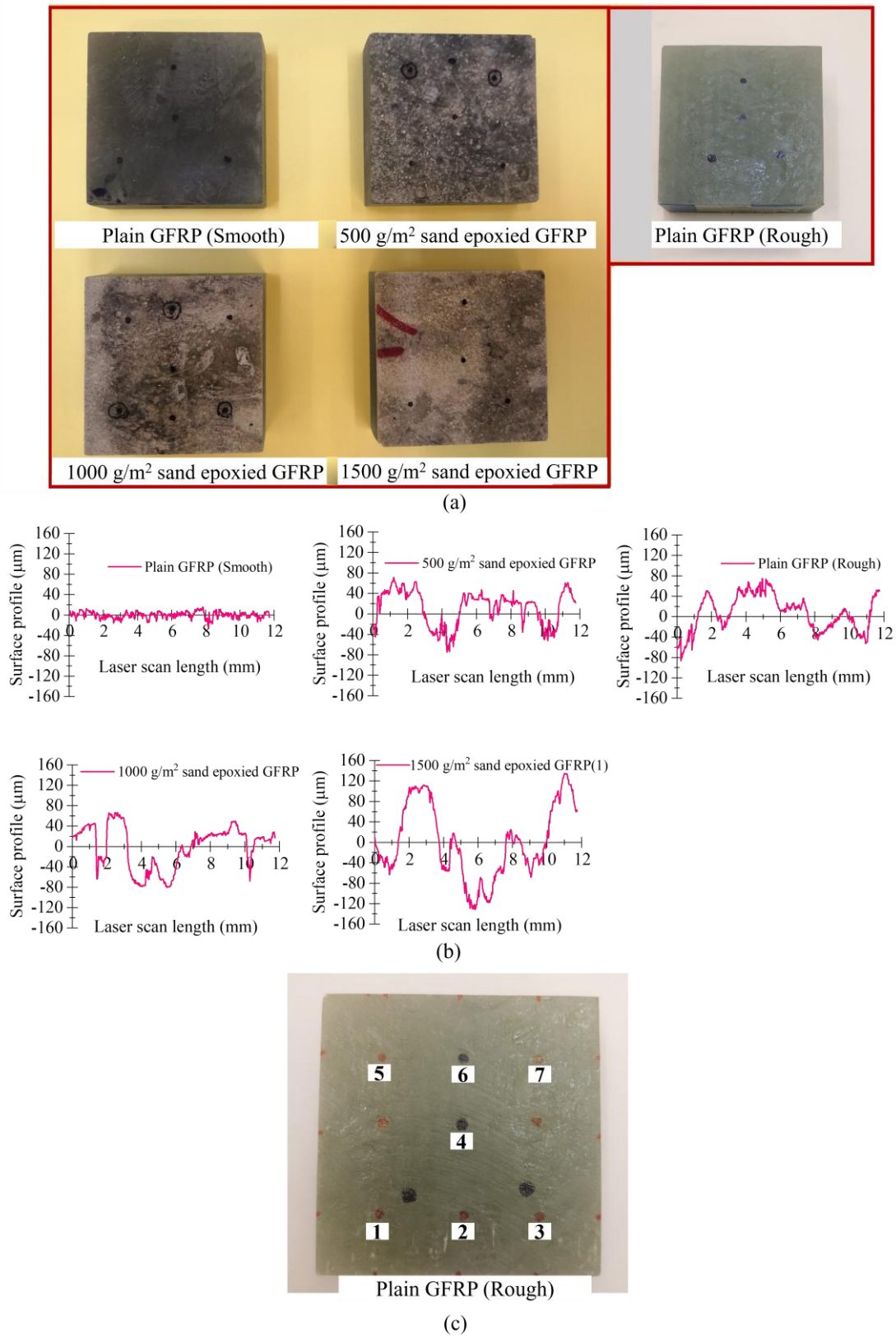

Figure 3-3 Photo view and surface roughness profiles of GFRP plates: (a) GFRP plates

with varying amounts of epoxied silica sand; (b) profiles of surface roughness of plain and sand-epoxied GFRP plates; and (c) seven measurement points marked on the rough surface finish plain GFRP for average roughness evaluation

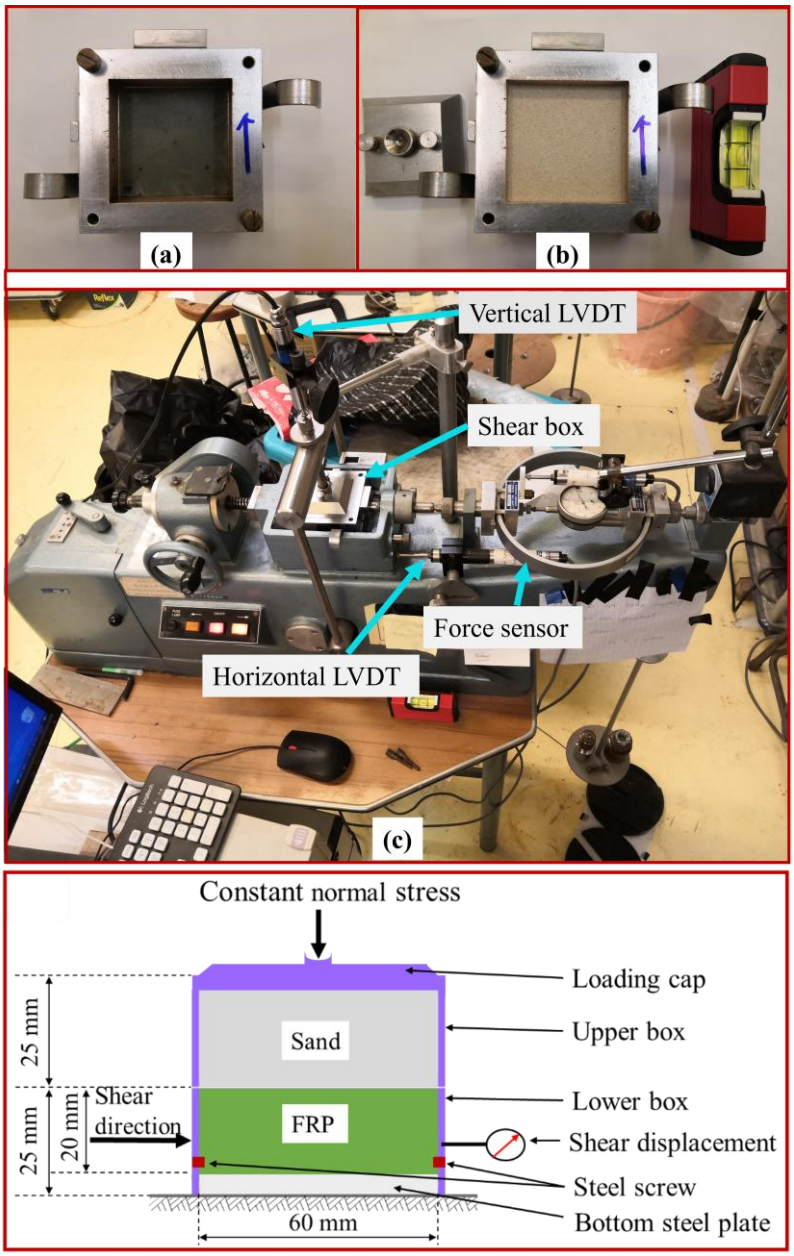

(d)

Figure 3-4 Testing preparation and apparatus: (a) shear box with plain GFRP plate; (b) loose sample of fine sand prepared for the testing; (c) modified direct shear testing apparatus; and (d) schematic diagram of the modified shear box testing setup

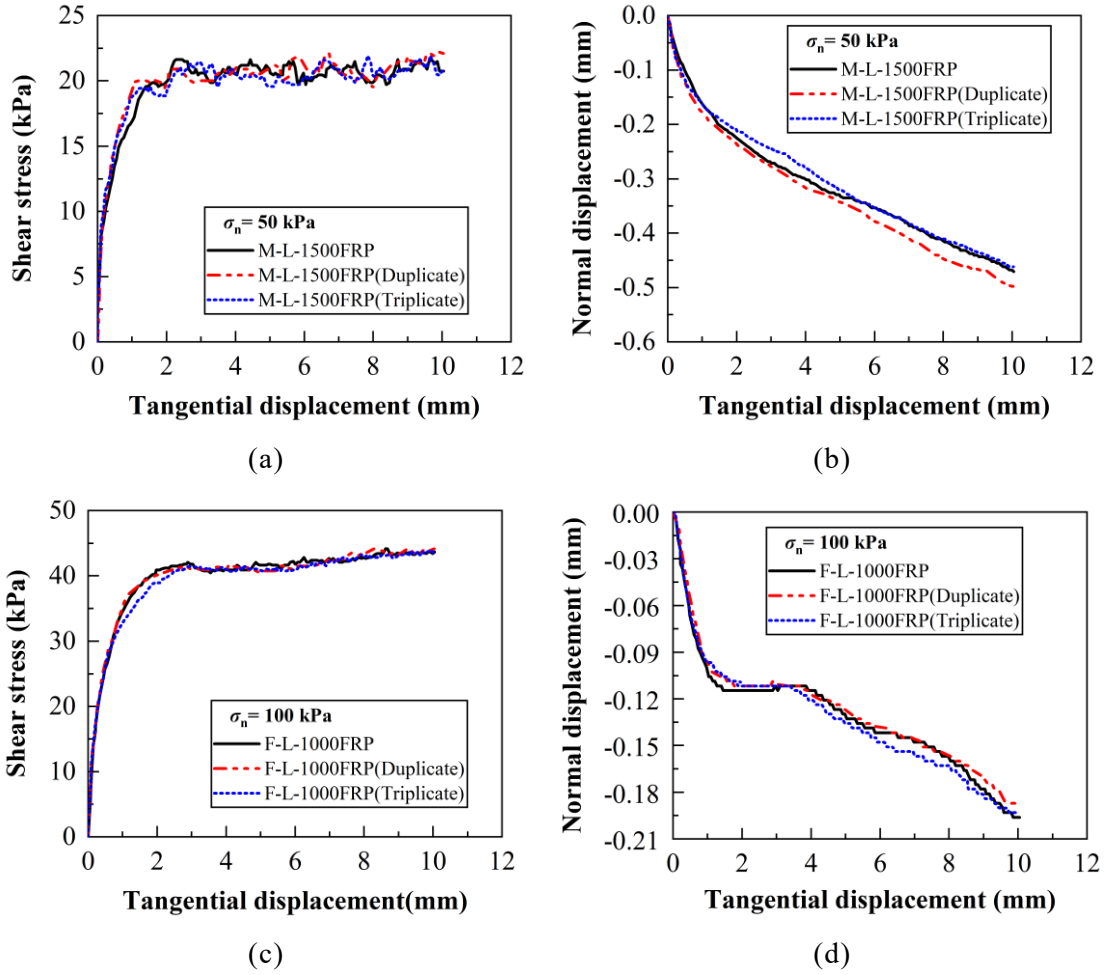

Figure 3-5 Repeatability of testing results under different normal stress: (a) shear stress versus tangential displacement and (b) normal displacement versus tangential displacement for medium sand-1500FRP interface under 50 kPa normal stress; (c) shear stress versus tangential displacement and (d) normal displacement versus tangential displacement for fine sand-1000FRP interface under 100 kPa normal stress

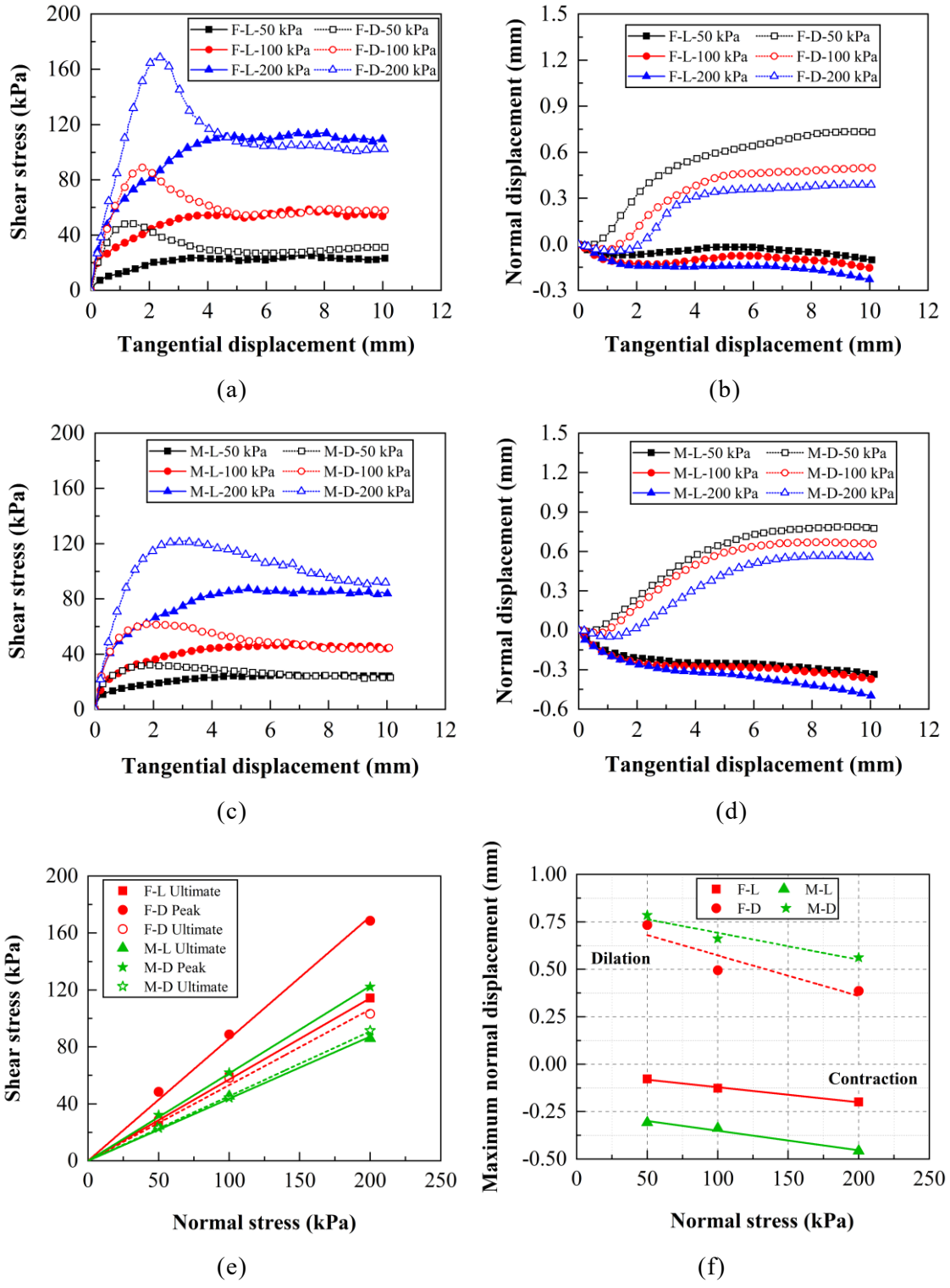

Figure 3-6 Mechanical responses of loose and dense specimens: (a) shear stress versus tangential displacement and (b) normal displacement versus tangential displacement for fine sand; (c) shear stress versus tangential displacement and (d) normal displacement versus tangential displacement for medium sand; (e) peak shear stress and failure envelopes for fine sand and medium sand; (f) variation in maximum

normal displacement with respect to normal stress

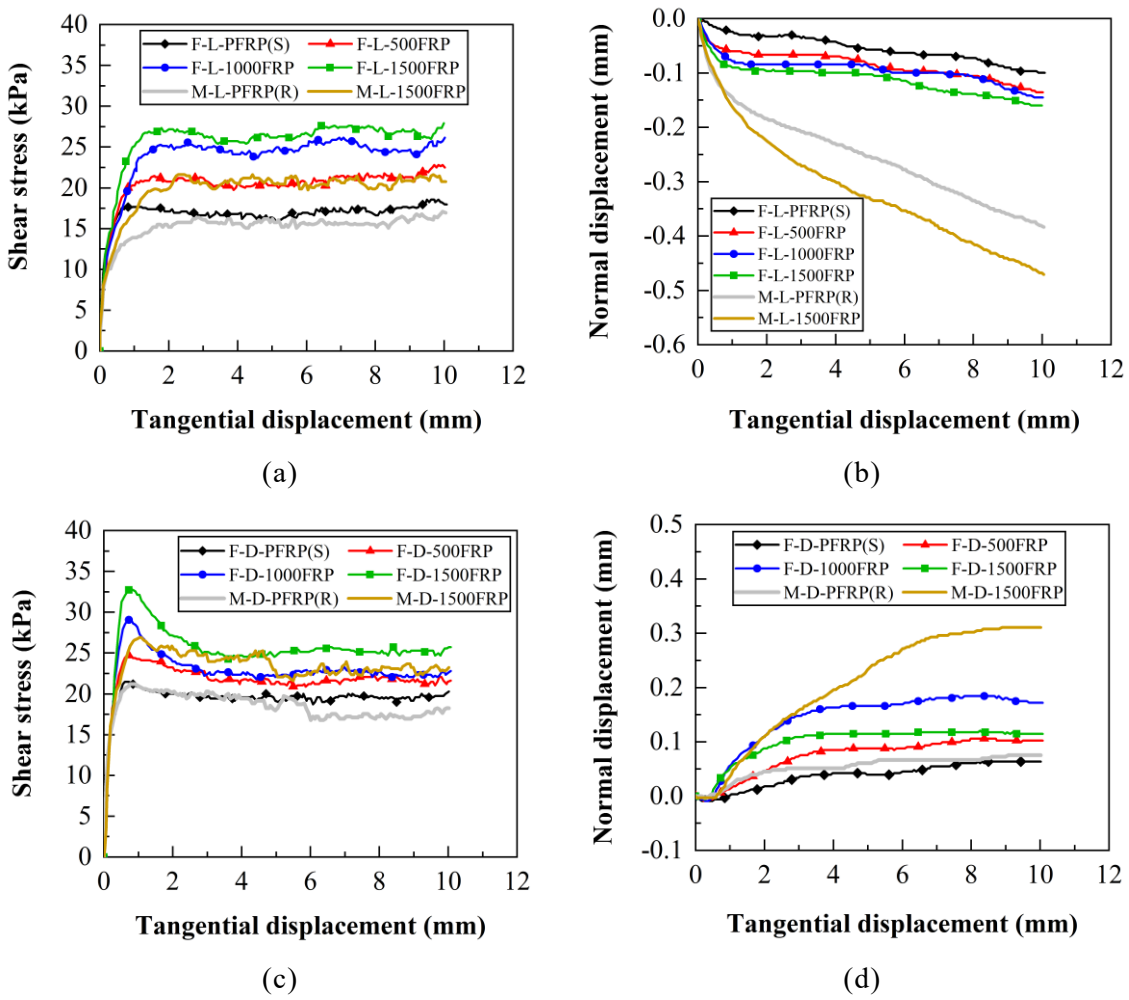

Figure 3-7 Mechanical responses of loose sand-GFRP and dense sand-GFRP interfaces under 50 kPa normal stress: (a) shear stress versus tangential displacement and (b) normal displacement versus tangential displacement for loose sand specimens; (c) shear stress versus tangential displacement and (d) normal displacement versus tangential displacement for dense sand specimens

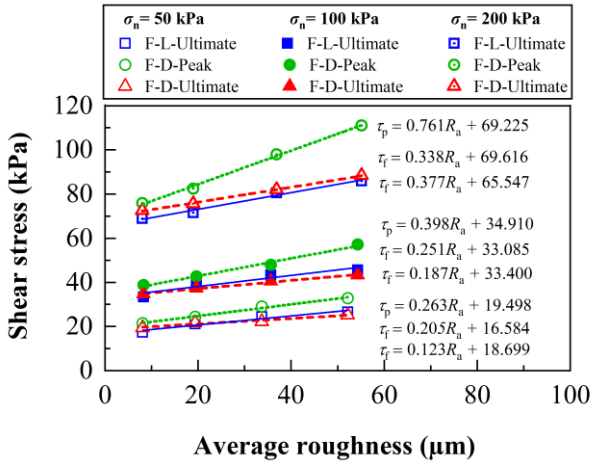

Figure 3-8 Variations in peak and ultimate shear stress of fine sand-GFRP interfaces with average roughness of GFRP at direct shear under 50 kPa, 100 kPa, and 200 kPa normal stress

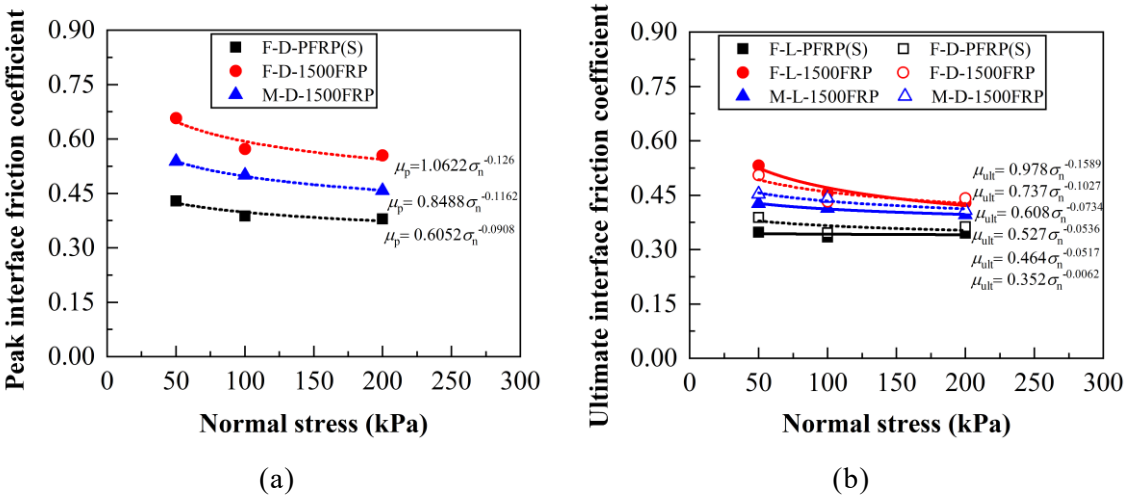

(a) (b)

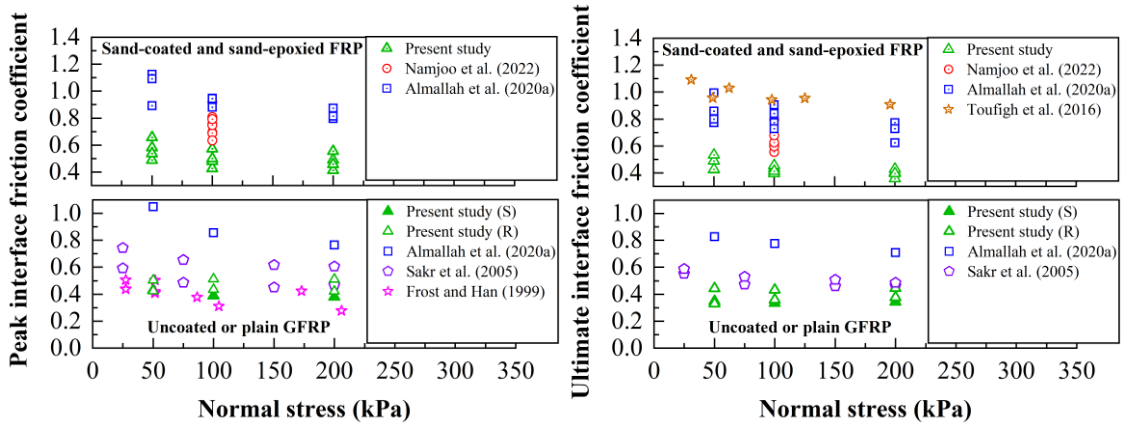

(c) (d)

Figure 3-9 Influence of normal stress on interface friction coefficient: (a) peak

interface friction coefficient and (b) ultimate interface friction coefficient at F-PFRP(S), F-1500FRP, and M-1500FRP interfaces; (c) comparison of peak interface friction coefficient between the present study and literature; (d) comparison of ultimate interface friction coefficient between the present study and literature

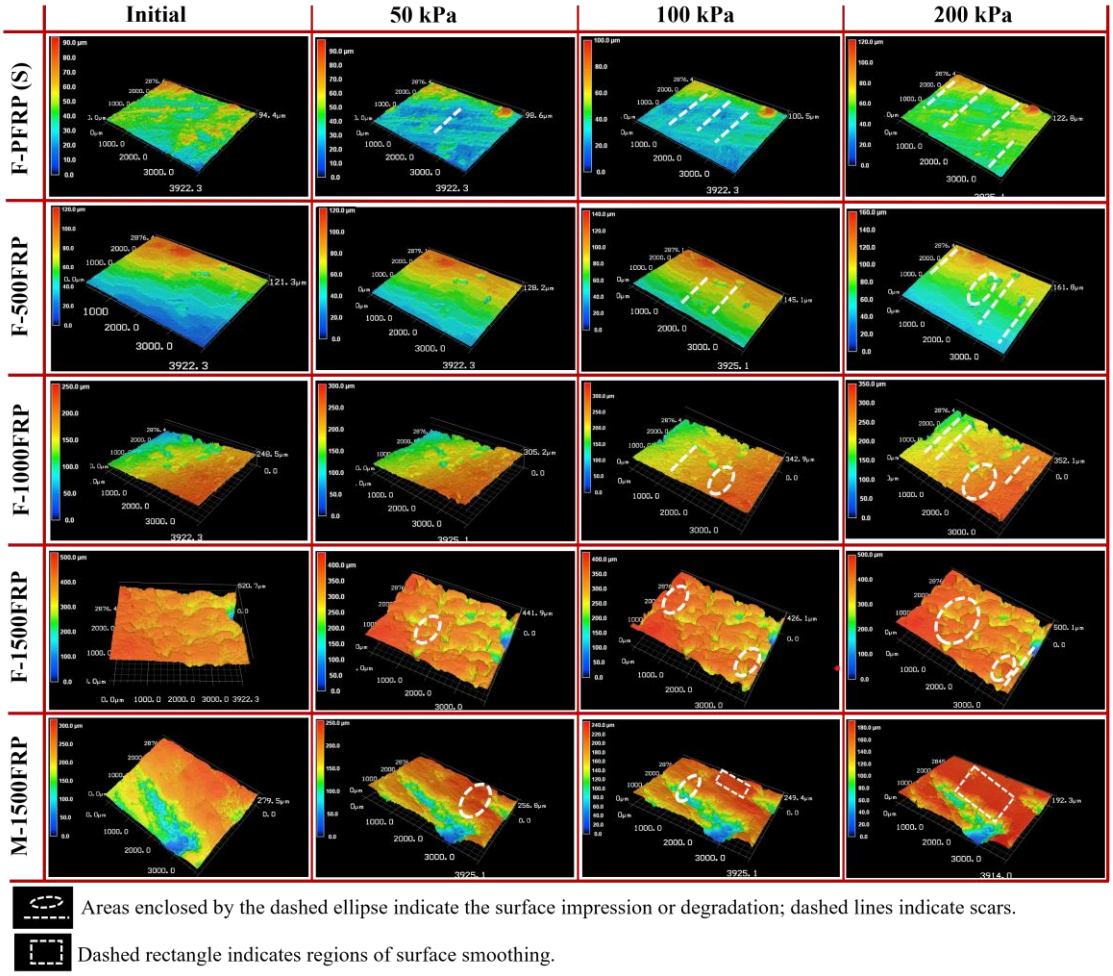

Figure 3-10 3D surface profiles of GFRP shearing surfaces adjacent to the middle mark: before testing (initial state) and after shearing under normal stresses of 50, 100, and 200 kPa, for fine sand sheared against plain and sand-epoxied GFRP, and medium sand sheared against sand-epoxied GFRP

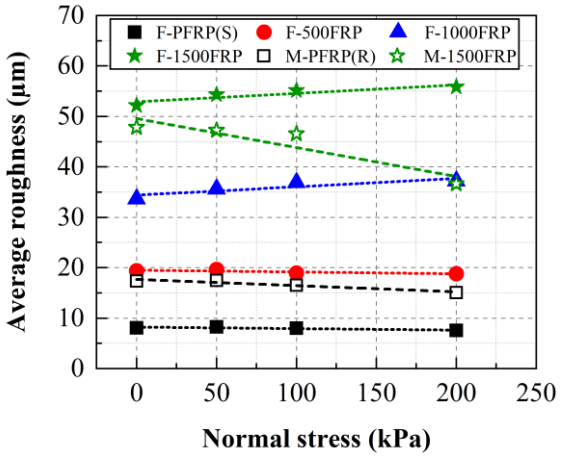

Figure 3-11 Variations in average roughness (R_a) of plain and sand-epoxied GFRP plates before and after shearing with fine and medium sand under different normal stresses

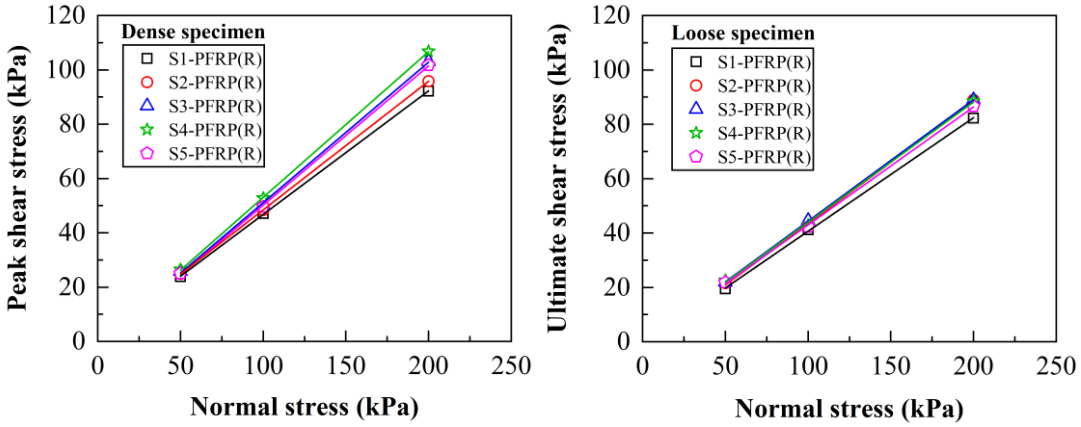

(a) (b)

Figure 3-12 Variation in peak shear stress and failure envelope: (a) variation in peak shear stress of dense specimens; (b) failure envelope of loose specimens of sand mixture-PFRP(R) interface

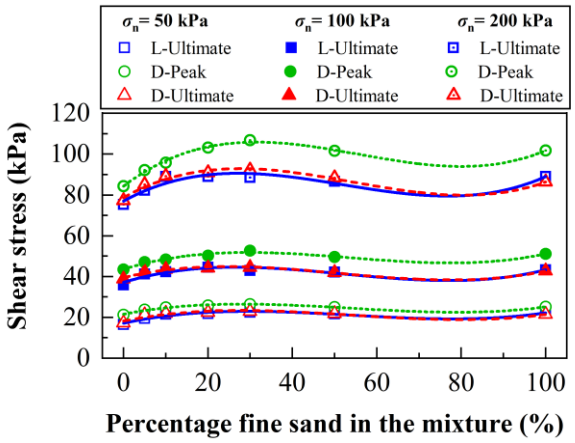

Figure 3-13 Influence of fine sand content on shear stress

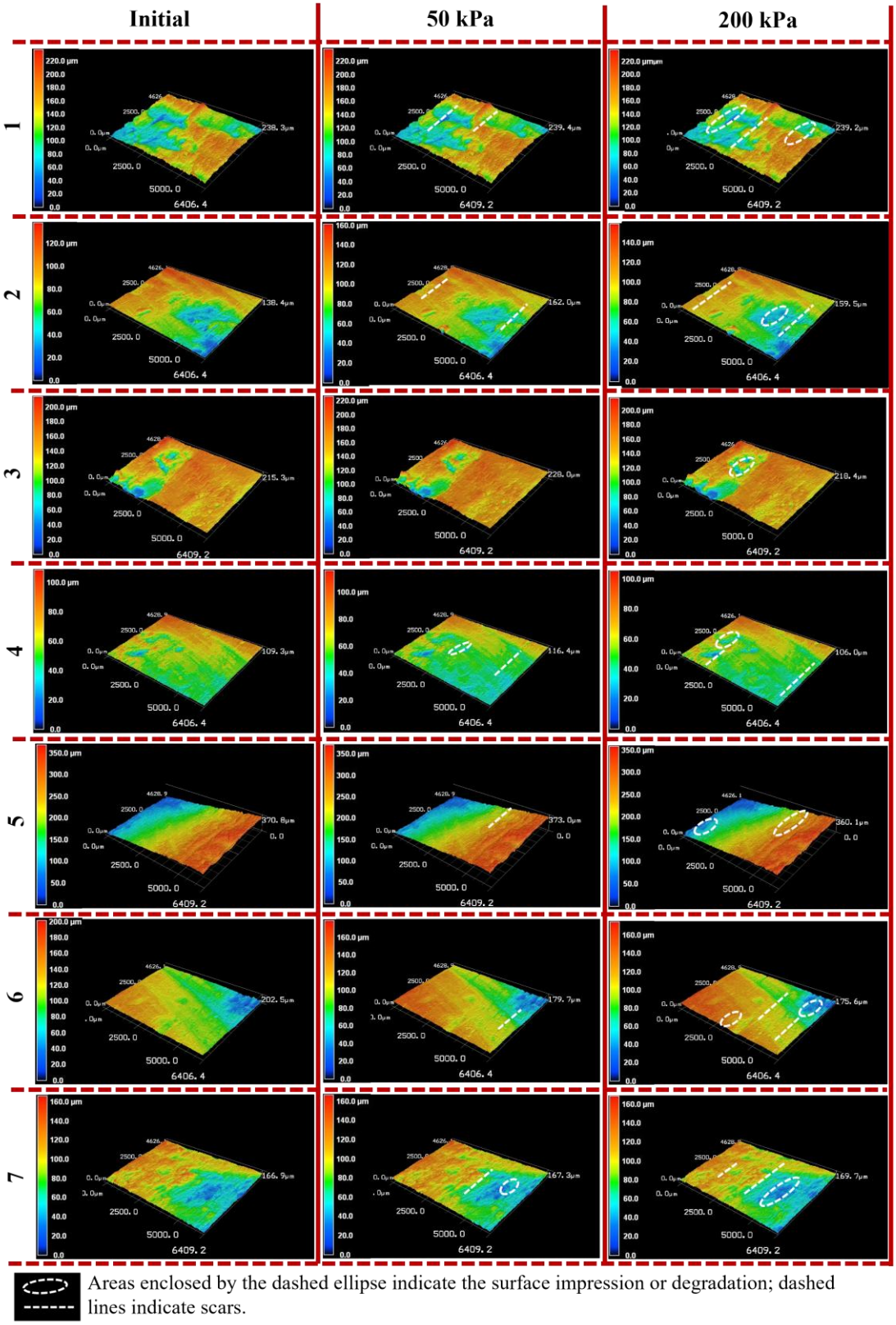
Initial
50 kPa
200 kPa
1
2
3
4
5
6
7
Areas enclosed by the dashed ellipse indicate the surface impression or degradation; dashed lines indicate scars.

(a)

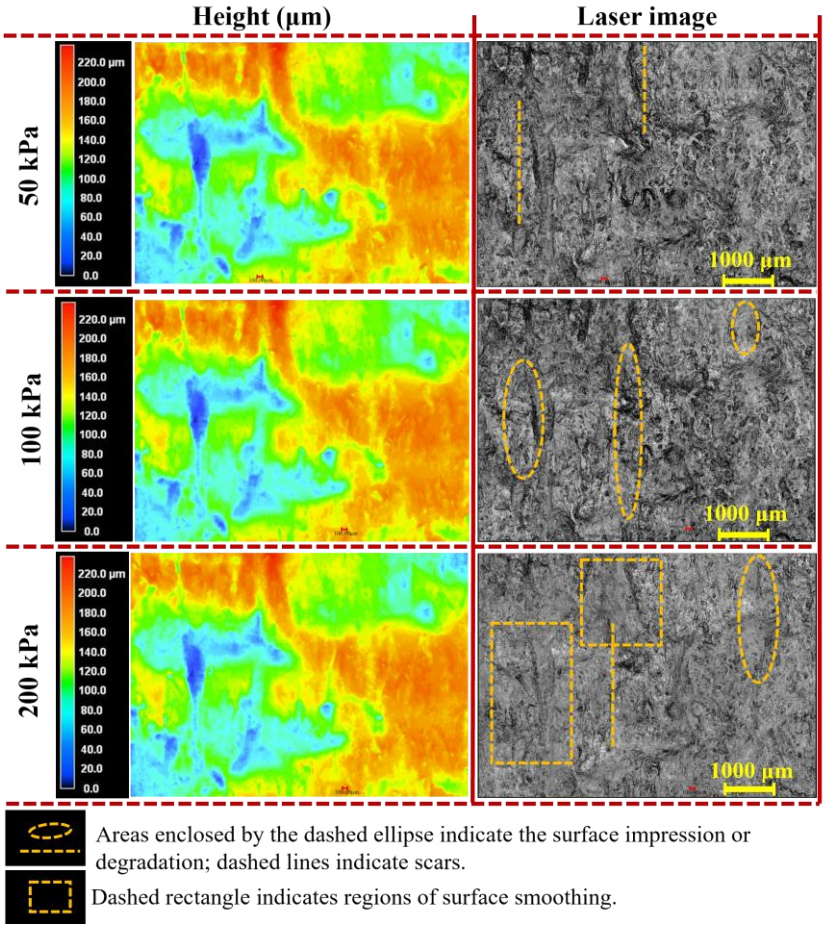

(b)

Figure 3-14 3D surface profiles and Laser scanning images of the plain GFRP (Rough) shearing surface: (a) 3D surface profiles at seven marked locations for the S4-PFRP(R) interface in the initial state and after shearing under 50 kPa and 200 kPa normal stress; (b) surface height profile and Laser image at Mark 1 after shearing under 50–200 kPa normal stress

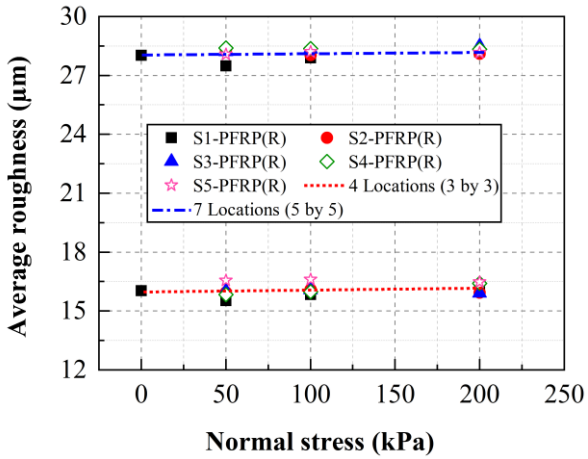

Figure 3-15 Variations in average roughness of plain GFRP (Rough) plate with normal

stress

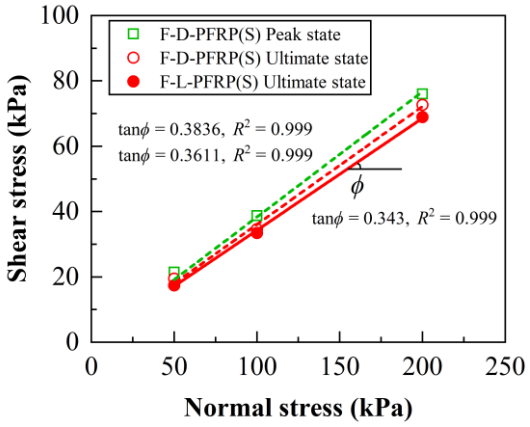
F-D-PFRP(S) Peak state
F-D-PFRP(S) Ultimate state
F-L-PFRP(S) Ultimate state
tanϕ = 0.3836, R² = 0.999
tanϕ = 0.3611, R² = 0.999
ϕ
tanϕ = 0.343, R² = 0.999
Shear stress (kPa)
Normal stress (kPa)
0
20
40
60
80
100
0
50
100
150
200
250

(a)

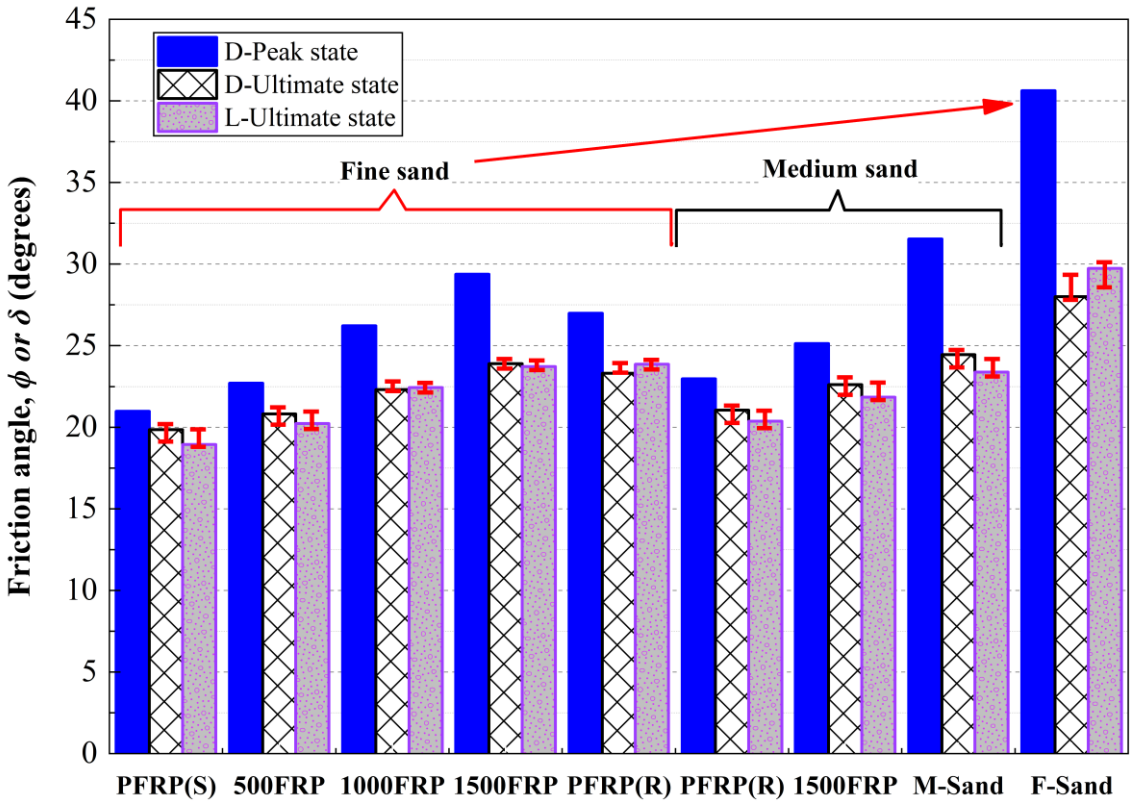
D-Peak state
D-Ultimate state
L-Ultimate state
Fine sand
Medium sand
Friction angle, ϕ or δ (degrees)
0
5
10
15
20
25
30
35
40
45
PFRP(S)
500FRP
1000FRP
1500FRP
PFRP(R)
PFRP(R)
1500FRP
M-Sand
F-Sand

(b)

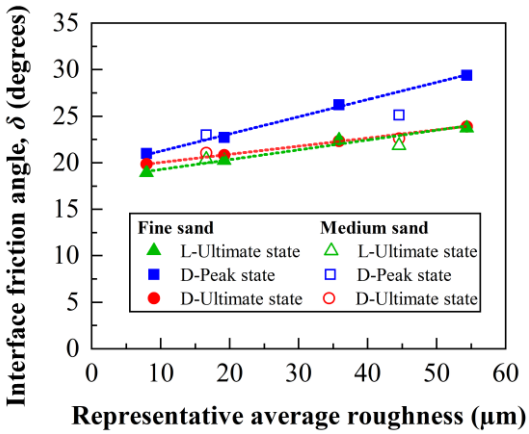

(c)

Figure 3-16 Determination and comparison of friction angles: (a) determination of friction angles for fine sand-plain GFRP (Smooth) interface; (b) comparison of internal friction angles with interface friction angles for dense and loose specimens of fine and medium sand; and (c) variation of interface friction angle versus representative average roughness

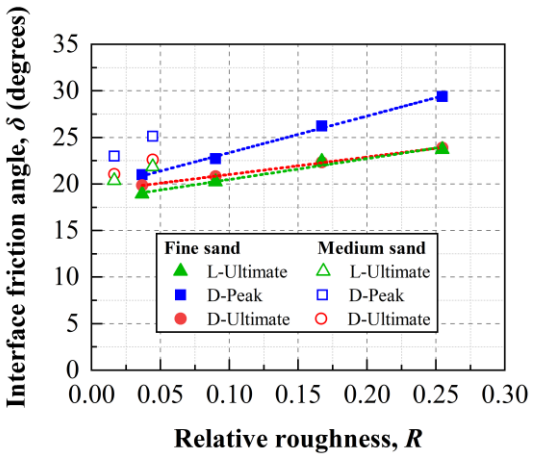

(a)

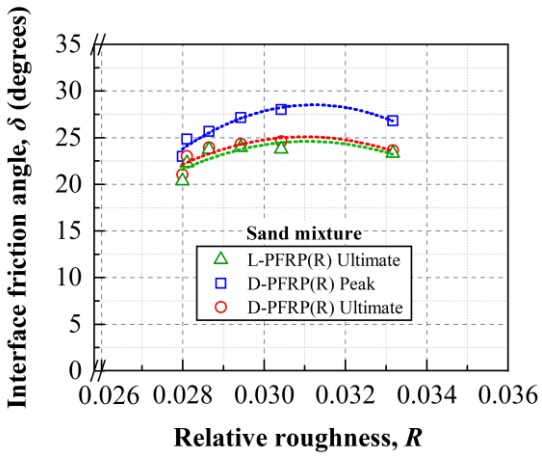

(b)

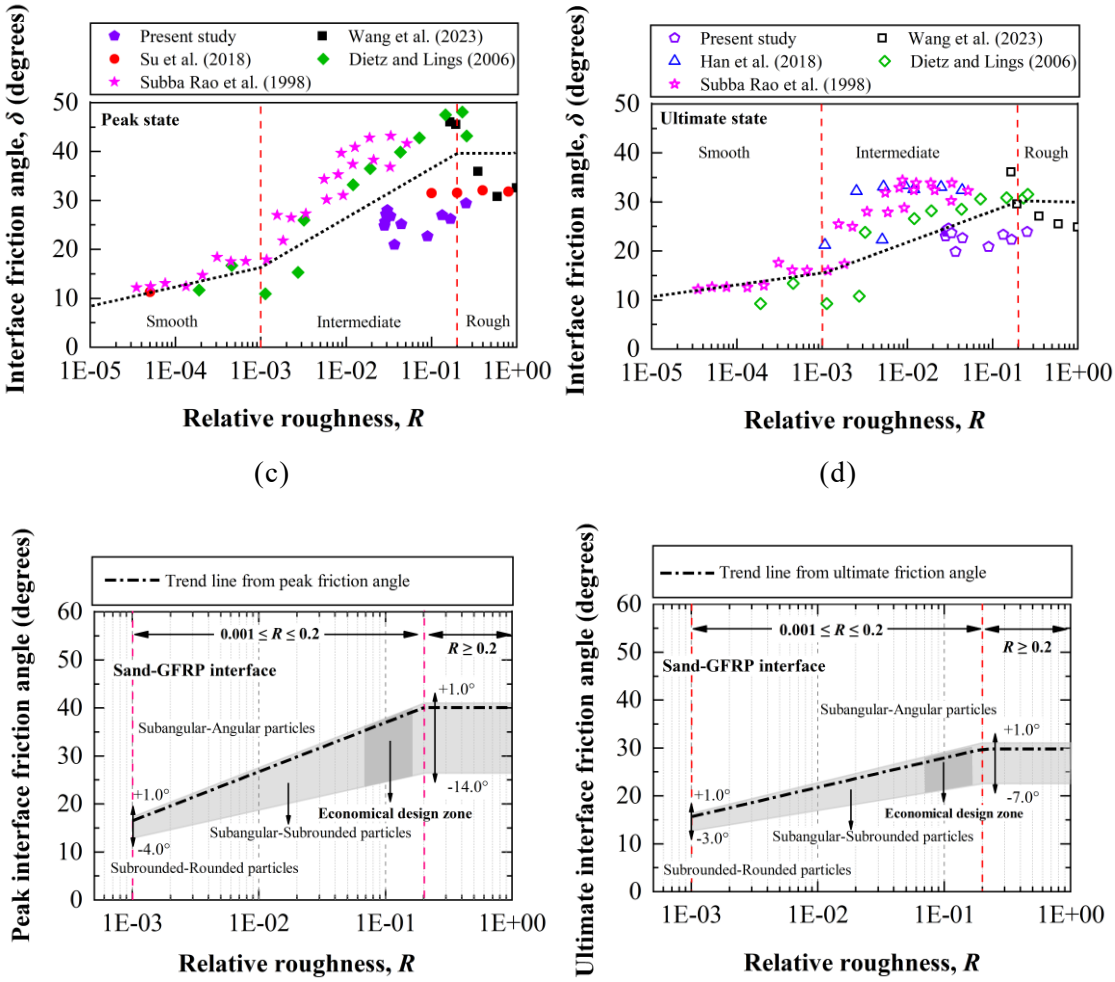

Figure 3-17 Variation of interface friction angles with respect to relative roughness for loose and dense specimens of (a) fine sand and medium sand, and (b) sand mixture; comparison of interface friction angle from the present study and literature with respect to relative roughness at (c) peak state and (d) ultimate state; simplified design charts for estimating (e) peak interface friction angle and (f) ultimate interface friction angle at sand-GFRP interfaces

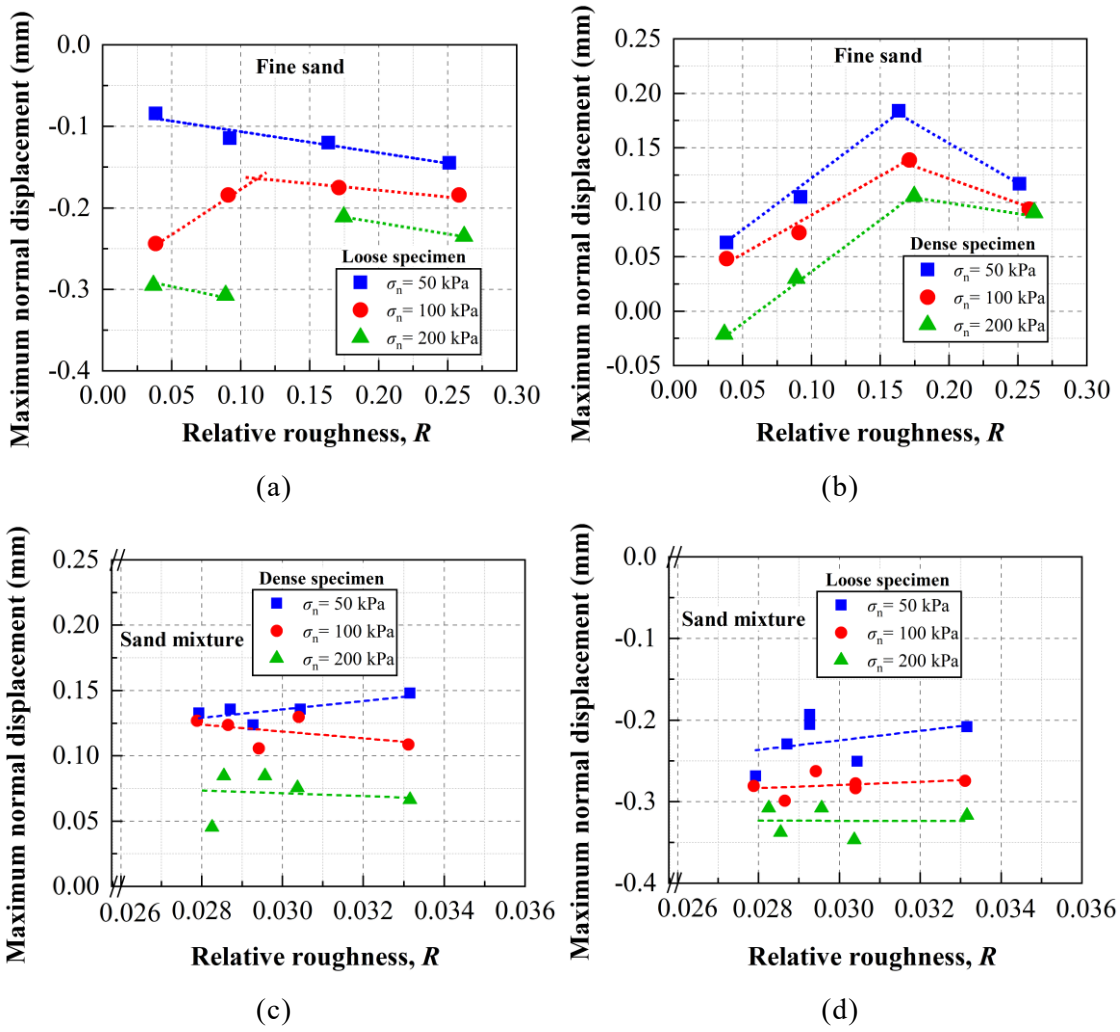

Figure 3-18 Variations in maximum normal displacement with respect to relative roughness for: (a) loose specimens of fine sand, (b) dense specimens of fine sand, (c) loose specimens of sand mixture, and (d) dense specimens of sand mixture

Table 3-1 Properties of sand and mixtures

Sample	Sand mixture (%)	d_{50} (mm)	C_u	G_s	e_0	
					Loose (D_r = 35% ±2%)	Dense (D_r = 90% ±2%)
M	100% Medium sand	1.001	1.178		0.785	0.621
S1	95% M+ 5% F	0.993	1.188		0.754	0.565
S2	90% M+ 10% F	0.983	3.400		0.698	0.501
S3	80% M+ 20% F	0.961	4.721	2.66	0.625	0.426
S4	70% M+ 30% F	0.934	5.177		0.596	0.404
S5	50% M+ 50% F	0.850	5.268		0.618	0.458
F	100% Fine sand	0.212	1.414		0.874	0.703

Note: d_{50} refers to the median particle size, C_u refers to the coefficient of uniformity, G_s refers to the specific gravity, ρ_{dmax} refers to the maximum dry density (ASTM D 4253-16a, 2016)), $\rho_{d\mathrm{min}}$ refers to the minimum dry density (ASTM D4254-16b, 2016), D_r refers to the relative density, $D_r = \{[\rho_{d\mathrm{max}}(\rho_d - \rho_{d\mathrm{min}})]/[\rho_d(\rho_{d\mathrm{max}} - \rho_{d\mathrm{min}})]\} \times 100$ (ASTM D4254-16b, 2016), and e_0 refers to the initial void ratio.

Table 3-2 Properties of GFRP

GFRP types	Mean Vickers' Hardness (HV)	Initial average roughness, R_a (μm)
Smooth surface finish plain GFRP (PFRP(S))	27.9	8.06
500 g/m^2 sand-epoxied GFRP (500FRP)	29.1	19.37
1000 g/m^2 sand-epoxied GFRP (1000FRP)	48.5	33.67
1500 g/m^2 sand-epoxied GFRP (1500FRP)	51.4	52.18
Rough surface finish plain GFRP (PFRP(R))	27.2	17.33

Table 3-3 Testing program of interface direct shear test

Specimen ID	Sand type/mixture [1st term in ID]	Specimen type [2nd term in ID]	Amount of epoxied sand [3rd term in ID] (g/m^2)	Surface type	Normal stress (kPa)
F-L-PFRP(S)	Fine	Loose	0	Smooth	50, 100, 200
F-D-PFRP(S)		Dense			
F-L-500FRP	Fine	Loose	500	n/a	
F-D-500FRP		Dense			
F-L-1000FRP	Fine	Loose	1000	n/a	
F-D-1000FRP		Dense			
F-L-1500FRP	Fine	Loose	1500	n/a	
F-D-1500FRP		Dense			
M-L-PFRP(R)	Medium	Loose	0	Rough	
M-D-PFRP(R)		Dense			
M-L-1500FRP	Medium	Loose	1500	n/a	
M-D-1500FRP		Dense			
S1-L-PFRP(R)	5% Fine + 95% Medium	Loose	0	Rough	
S1-D-PFRP(R)		Dense			
S2-L-PFRP(R)	10% Fine + 90% Medium	Loose	0	Rough	
S2-D-PFRP(R)		Dense			
S3-L-PFRP(R)	20% Fine + 80% Medium	Loose	0	Rough	
S3-D-PFRP(R)		Dense			
S4-L-PFRP(R)	30% Fine + 70% Medium	Loose	0	Rough	
S4-D-PFRP(R)		Dense			
S5-L-PFRP(R)	50% Fine + 50% Medium	Loose	0	Rough	
S5-D-PFRP(R)		Dense			
F-L-PFRP(R)	Fine	Loose	0	Rough	
F-D-PFRP(R)		Dense			

Note: '0' indicates no coating of sand on GFRP, representing plain (P) GFRP, and is denoted as 'PFRP'; n/a refers to not applicable.

Table 3-4 Summary of the key strength parameters for fine sand and medium sand

Sand specimen	Normal stress (kPa)	Dilation angle (degrees)	Peak friction angle (degrees)	Ultimate friction angle (degrees)
Fine sand (loose)	50, 100, 200	n/a	n/a	29.7
Fine sand (dense)		12.7, 10.3, 8.8	40.6	28.0
Medium sand (loose)	50, 100, 200	n/a	n/a	23.4
Medium sand (dense)		10.9, 9.6, 7.8	31.6	24.5

Note: n/a refers to not applicable.

Table 3-5 Interface materials and testing setup

Reference	Soil	d_{50} (mm)	D_r (%)	Particle shape	Structure type	R_{ra} or R_a (μm)	R	Testing type
Present study	Fujian sand	0.212–1.001	90±2	C_{irc} = 0.72–0.855 R_{rd} = 0.59–0.678	GFRP and sand-epoxied GFRP	7.96–54.38	0.028–0.256	IDST
Wang et al. (2023)	Fujian sand	0.252–1.514	90	C_{irc} = 0.7–0.872 R_{rd} = 0.55–0.627	Sawtooth steel	250*	0.165–0.993	IDST
Su et al. (2018)	Fujian sand	1.001	90	Subrounded	Stainless steel Sawtooth steel	0.056** 100–795*	0.00003–0.794	IST
Han et al. (2018)	Silica sand	0.212, 1.001	80 ±1	S = 0.78, 0.82 R_{rd} = 0.4, 0.35	Smooth steel Rusted steel	1.08 2.53–9.31	0.00108–0.044	IST
Dietz and Lings (2006)	Silver fine sand	0.13	92–99	Subrounded	Machine and ground mild steel	0.147–9.4	0.00018–0.259	IDST
	Virgin Leighton Buzzard	0.78	83–94	Rounded	Sand-coated mild steel	33.7–180		
Subba Rao et al. (1998)	Quartz sand	0.27, 0.42, 0.74, 1.10, 1.60	85	Well rounded	Stainless steel Mild steel Ferrocement	0.056 0.491, 2.49 8.85, 13.98	0.00005–0.0517	IST

Note: d_{50} refers to the median particle size, D_r refers to the relative density, R_{ra} refers to the representative average roughness of the present test, R_a refers to average roughness of literature, R refers to relative roughness, C_{irc} refers to circularity, R_{rd} refers to roundness, S refers to sphericity, IDST refers to interface direct shear test, IST refers to interface shear test. *The average roughness derived from the maximum roughness of a sawtooth plate having regular isosceles groove geometry. **The average roughness value supposed for smooth stainless steel is identical to that reported by Subba Rao et al. (1998).

CHAPTER 4: EXPERIMENTAL INVESTIGATION OF SAND-GFRP INTERFACE UNDER CYCLIC SHEAR LOADING

4.1 Introduction

The findings presented in Chapter 3 revealed variations in GFRP surface roughness; however, these variations exerted a negligible influence on interface strength under single-surface shearing at normal stresses ≤ 200 kPa. Previous investigations into sand-polymer interfaces have demonstrated that interface strength can be markedly affected by the evolution of surface roughness under critical normal stress, a phenomenon known as the ploughing effect (Shooter and Tabor, 1952; Dove and Frost, 1999; Fleming et al., 2006; Chen et al., 2021). In practical engineering contexts, it is essential to determine whether a critical stress in the range of 200-800 kPa induces measurable changes in interface shear behaviour, particularly under cyclic shear loading.

This chapter examines the surface characteristics of GFRP and sand-epoxied GFRP before and after testing, as well as their shear stress-tangential displacement behaviour, volumetric response, and the influence of particle size under moderate to high normal loads in cyclic interface shearing against silica sand. To evaluate the evolution of surface roughness and clarify its progression pattern, large GFRP specimens (115 × 100 mm) are employed together with correspondingly larger sand specimens to better capture the volumetric response. A comprehensive programme of cyclic and monotonic tests is performed to elucidate frictional mechanisms and classify interface roughness under field-relevant conditions. Three gradations of air-dried standard silica sand are sheared against both uncoated and sand-epoxied GFRP, with the optimal sand coating gradation identified through monotonic testing and long-term performance evaluated via cyclic testing. Surface roughness evolution is quantified using a

three-dimensional (3D) laser confocal microscope, while particle breakage is documented and analysed post-testing to elucidate its role in the contact and shearing mechanisms. The findings advance the understanding of roughness stability and interface mechanics, thereby supporting durability evaluation and guiding the robust application of sand-epoxied GFRP in practical engineering contexts.

4.2 Materials and methods

4.2.1 Silica sand

The silica sand specimens used for testing were prepared following the sieve designations specified in ASTM E11-24 (2024), specifically 10-14, 16-20, and 50-100 mesh sizes. Based on the available range of particle sizes, these specimens were classified as coarse (C), medium (M), and fine (F) sands, following a local designation system. Three distinct grades of silica sand, classified by particle size range (0.1–0.8 mm, 0.15-0.85 mm, and 0.3-0.85 mm), were used to produce sand-epoxied GFRP surfaces with controlled roughness levels, categorised as smooth, medium rough, and rough. The normal and magnified images of the sands used for the specimen and the coating on the GFRP are illustrated in Figure 4-1. The morphological characteristics of the three sand types used for the specimens were determined based on the estimated mean values of circularity (C_{irc}), roundness (R_{rd}), and roughness factor (R.F.) (Wadell, 1932; Janoo, 1998; Wang et al., 2023). The mean values obtained were C_{irc} = 0.725, R_{rd} = 0.587, and R.F. = 1.085 for fine sand; C_{irc} = 0.742, R_{rd} = 0.632, and R.F. = 1.076 for medium sand; and C_{irc} = 0.761, R_{rd} = 0.693, and R.F. = 1.069 for coarse sand. Based on these indices, the particles of fine, medium, and coarse sands can be categorised as sub-angular to sub-rounded, with a summary of their physical properties presented in Table 4-1.

4.2.2 GFRP composites

This study utilises two distinct types of GFRP composites, industrially manufactured GFRP and laboratory-fabricated GFRP for sand-GFRP interface testing. The industrial GFRP was produced via the pultrusion process, whereas the laboratory-made GFRP was fabricated using either the prepreg or dry hand lay-up method. For the industrial GFRP, ATLAC 430 epoxy was employed in combination with a 600 g/m^2 chopped strand mat, yielding a glass fibre content of approximately 48-50% by weight. In contrast, the laboratory-fabricated GFRP utilised GXA120 prepreg adhesive along with unidirectional prepreg glass fibre arranged in a 90/0 orientation, achieving a fibre content of approximately 42-45% by weight (150 g/m^2). Industrial GFRP plates were prepared in both plain (uncoated) and sand-epoxied configurations. The plain variants included a smooth surface finish (PFRP(S)) and a rough surface finish (PFRP(R)).

To fabricate sand-epoxied GFRP with three distinct roughness levels, silica sand of varying particle size distributions (0.1–0.8 mm, 0.15–0.85 mm, and 0.3–0.85 mm) was incorporated, corresponding to smooth, medium rough, and rough surface textures, respectively (Figure 4-2; Table 4-2). A sand concentration of 750 g/m^2 resulted in partial surface coverage, whereas complete surface coverage was achieved using particle size ranges of 0.15-0.85 mm and 0.3-0.85 mm at an increased concentration of 1500 g/m^2. The silica sand was thoroughly blended with epoxy to achieve a uniform consistency and applied to the semi-cured plain GFRP surface. The mass of the applied sand-epoxy mixture was measured by weighing the specimen before and after application to determine the adhered sand per unit area, ensuring consistent and reproducible surface coverage. Following application, a curing pressure of 6 kPa was applied to promote effective bonding between the sand-epoxy layer and the GFRP substrate (e.g., Toufigh et al., 2016). Finally, any exposed sand surfaces were sealed with a thin epoxy coat to ensure proper bonding. For laboratory-fabricated GFRP, surface textures were modulated through the application of non-perforated peel plies. A tight peel ply was used to create a smooth surface finish (HFRP(S)), whereas a loose peel ply produced a rough surface finish (HFRP(R)). Figure 4-2 presents the longitudinal

2D surface profiles of all GFRP types, while Table 4-2 provides detailed properties, including mean Vickers hardness values (He et al., 2021; ASTM E384-22, 2022) and the initial average roughness (S_a) of the respective surfaces.

4.2.3 Specimen preparation and testing methods

A cyclic shearing system with in-house software was utilised to perform monotonic and cyclic testing. Figure 4-3(a) shows the details of the system, and this system can be found in the study by Feng et al. (2024). Three constant normal loadings, 200, 400, and 800 kPa, were involved in the testing. All tests were conducted at a constant shearing rate of 0.6 mm/min for the lower half of the shear box (e.g., Wang et al., 2023), under a controlled laboratory temperature of 20 ± 2ºC.

The shear box consisted of two halves, each with a depth of 30 mm. Sand specimen preparation was conducted in the upper half of the shear box, which had internal dimensions of 100 mm (length) × 100 mm (width) × 25 mm (depth), placed over a modified lower shear box filled with GFRP. The modified lower shear box, designed to accommodate two different sizes of GFRP, had an inner space of 115 mm (length) × 100 mm (width) × 20 mm (depth) for industrial GFRPs and 115 mm (length) × 100 mm (width) × 8 mm (depth) for laboratory-made GFRPs. These sizes were maintained for interface monotonic and cyclic shearing tests. The grid screw steel plates, paired with plain head screws, were utilised to securely constrain and adjustably support the GFRPs from the bottom while ensuring coplanarity with greater precision, as illustrated in the schematic diagram in Figure 4-3(b). The dense sand specimens were controlled with a relative density of 90% to maintain initial void ratios of 0.684, 0.623, and 0.601 for fine, medium, and coarse sand, respectively, in the entire experiment. Sample preparation involved pouring air-dried sand of predetermined mass into the upper half shear box with respective configurations, then levelling and compacting in 3 consecutive layers.

An advanced VK-X1000 confocal microscope equipped with a Laser scanning feature, a 5× objective lens, and a z-pitch of 8 μm was used to measure

the surface roughness of the GFRP specimens (Figure 4-3(c)). Surface roughness was evaluated at four sampling locations on each GFRP plate to determine the average roughness parameter (S_a). As shown in Figure 4-3(c), the arithmetic average roughness of each location can be obtained by,

$$S_{a,i} = \left\{ \frac{1}{A} \iint_{0}^{A} |z(x,y)| dxdy \right\}_i \tag{4-1}$$

where A is the sampling area and $|z(x,y)|$ is the absolute height from the mean roughness height of the area (DeJong and Westgate, 2009; Araújo et al., 2022; ISO 25178-2, 2012) along the shearing direction. These locations were selected within a surface area of approximately 7650 µm × 5750 µm, corresponding to a 3 × 3 pitch grid positioned directly in front of each reference mark (black dot). The S_a parameter was selected for its suitability in capturing the surface characteristics and roughness evolution of sand-epoxied GFRP, which exhibits irregular and non-directional asperities. In addition to the average roughness parameters, the average maximum roughness has been included for comparative analysis in the monotonic part. The maximum roughness values from four distinct locations are averaged, resulting in a metric referred to as the average maximum roughness of the surface.

$$S_{\mathrm{z,avg}} = \frac{1}{n} \sum_{i=1}^{n} S_{\mathrm{z},i} \tag{4-2}$$

where n refers to the number of the sampling area, $S_{\mathrm{z},i}$ refers to the sum of the maximum height of the peak (S_{p}) and the maximum depth of the valley ($S_{\mathbf{v}}$) over a sampling area. To address the variation in surface roughness before and after testing, a parameter called representative average roughness can be calculated as,

$$S_{\mathrm{ra}} = \sum_{i=0}^{n-1} (S_a)_i \Big/ n \tag{4-3}$$

where n refers to the total number of average roughness measurements at a specific location before $(S_a)_{i=0}$ and after $(S_a)_{i=1,2,\ldots,n-1}$ interface shear testing for a particular GFRP (parameter modified from Chapter 3 for surface roughness).

Eventually, relative roughness is given by,

$$R = S_{\mathrm{ra}}/d_{50} \tag{4-4}$$

herein d_{50} is the median particle size estimated to represent the interface roughness, which is based on average roughness as an appropriate roughness measuring metric for low to medium hard structural units (e.g., Araújo et al., 2022).

4.2.4 Testing programme

The interface testing plan was carried out in two phases. After knowing the mechanical response of pure sand in the direct shear test (Figure B-1; Table B-1), the initial phase involved performing 18 sets of interface direct shear tests under 200 to 800 kPa normal stress. The performance of sand-GFRP interfaces is analysed based on their frictional characteristics and variations in roughness. Subsequently, the second phase of the testing plan was initiated to assess long-term cyclic performance. After understanding the cyclic response on pure sand shearing, cyclic interface tests were conducted (Figures B-2 to B-4). A total of 101 interface shear tests were conducted in this phase, including three sets of tests designed to investigate the effect of cyclic displacement amplitude, with semi-amplitudes of 1.0, 2.5, and 5.0 mm. The experimental plan led to a total of 155 interface tests after ensuring good repeatability between tests with similar strength, stiffness, and stress-displacement responses from multiple repeatability tests on spare GFRP (Figure B-5). The roughness of each GFRP specimen was measured before and after the interface shear tests. After each interface shear test was completed, each sand specimen was carefully taken for particle size distribution analysis.

A comprehensive description of the cyclic interface shear tests can be found in Table 4-3. For specimen IDs with a numeric middle term, the bracketed term represents the texture by the particle size range of epoxied sand. (Figure 4-1; Table 4-2). For example, specimen ID “M-750FRP(R)” stands for interface shearing of medium sand against rough surface sand-epoxied GFRP (0.3-0.85 mm range of epoxied sand) and 750 g/m^2 concentration of silica sand epoxied on the

industrial GFRP (Table 4-3).

4.3 Interface shear behaviour and evolution of surface properties under moderate to large normal stress

4.3.1 Effect of particle size and normal stress

Studies consistently demonstrate that sand particle size and normal stress significantly affect both interface shear strength and frictional properties of sand-FRP interface (e.g., Frost and Han, 1999; Pando et al., 2002; Abuel-Naga and Shaia, 2014; Almallah et al., 2020a; Namjoo et al., 2020). Shear strength typically increases with an increase in normal stress, while the relationship between friction and normal stress is dependent on surface roughness and hardness (e.g., Shooter and Tabor, 1952; Archard, 1957; Dove and Frost, 1999; Chen et al., 2021). Generally, as normal stress increases, the particles near the interface experience greater confinement, restricting their rearrangement and limiting surface contact, ultimately reducing the friction coefficient. Polymeric materials such as geomembrane and geotextile surface textures are relatively softer compared to GFRP surfaces exhibiting ploughing and trenching effects attributed to enlarged roughness after testing at critical normal stress, thereby enhancing friction (Archard, 1957; Dove and Frost, 1999; Fleming et al., 2006; Zettler et al., 2000; Teng et al., 2024). As long as the specimen particles undergo particle rotation effect and ploughing effect, the formation of scars and trenches or grooves appears to alter the roughness (Sakr et al., 2005; Teng et al., 2024). Knowing the pattern and the quantification of the roughness evolution, whether GFRP roughness enhancement or degradation under the applied normal stress, the friction property enhances or degrades accordingly. Moreover, the combined effect of normal stress (Archard, 1957; Dove and Frost, 1999) and particle size promotes deeper trench formation, further increasing the friction coefficient (Vangla and Latha, 2015). The aforementioned friction property alteration was observed on materials with softer textures, while GFRP was not under normal

stress of ≤ 200 kPa during monotonic shearing (Sakr et al., 2005; Chapter 3). Therefore, the analysis in this section exhibits the evolution of surface roughness and corresponding effects on friction property under 200 to 800 kPa normal stress.

Figure 4-4 illustrates the influence of normal stress and sand size on the sand-PFRP(R) interface. The results show the expected trends of increasing shear strength and stiffness as the normal stress increases. As illustrated in Figure 4-4(a), the sand-PFRP(R) interface exhibits a slight strain-hardening behaviour when subjected to medium and coarse sands under normal stresses ranging from 200 kPa to 800 kPa. Fine sand demonstrates a strain-softening behaviour under similar conditions. The dilation behaviour of fine sand stabilises after 3 mm of tangential displacement, whereas medium and coarse sands exhibit continuous dilation until the termination of interface shearing (Figure 4-4(b)). This transition can be explained by the suppression of dilative tendencies with increasing confinement: at low normal stresses (<200 kPa), particle interlocking and surface roughness effects dominate, leading to peak strength followed by post-peak softening and pronounced dilation, whereas at higher normal stresses (>200 kPa), confinement constrains volumetric expansion, promoting sustained shear resistance and post-peak hardening (Figure B-6). This is due to the reduced effective contact of particles at the interface as the median particle size increases, which causes mass sliding, as reported by O'Rourke et al. (1990) and Sakr et al. (2005). In addition, under higher normal stresses, particles at the interface are suppressed; therefore, dilation is reduced due to confinement, suppressing particle rearrangement and the consequent reduction in shear zone thickness (e.g., DeJong and Westgate, 2009).

Figure 4-5 illustrates the interface behaviour of medium sand against three varieties of sand-epoxied GFRP with 750 g/m^2 concentration of epoxied sand. The sand-epoxied surface of 750FRP(S) consists of a low value of initial average roughness (≤ 21 μm; Table 4-2) compared to medium rough (750FRP(MR)) and rough (750FRP(R)) surfaces, which have higher initial average roughness (i.e., S_a > 60 μm). As a result, the relative roughness of the medium sand-750FRP(S) interface is lower than that of the interfaces having medium rough and rough

surfaces (i.e., 0.02 < 0.06), leading to strain-hardening behaviour on 750FRP(S) and strain-softening on 750FRP(MR) and 750FRP(R). The lower relative roughness limits the particle interlocking at the interface, promoting strain-hardening with increased interface strength attributed to the mass sliding effect. In comparison, higher roughness enhances interlocking, but the increased particle rearrangement reduces shear strength after the peak stress is reached, thereby causing strain-softening.

As interlocking at the interface increases with larger relative roughness, localised displacement and the development of shear bands are promoted, which in turn enhance energy dissipation and induce significant volumetric changes. Consequently, dilation behaviour becomes more pronounced, particularly on medium rough and rough surfaces, as reported in previous studies (e.g., DeJong and Westgate, 2009; Martinez and Frost, 2017; Han et al., 2018). The sand-epoxy coating combination with larger particle size ranges, such as 0.15-0.85 mm and 0.3-0.85 mm, facilitates sufficient space for effective contact of medium sand specimens along the interface, enhancing interface strength. These observed trends are similar to those of Namjoo et al. (2022) regarding sand against sand-coated CFRP. However, the study by Namjoo et al. (2022) involved complete surface coverage with coated sand, and an increase in coated sand particle size yielded enhanced resistance up to a median particle size of 0.89 mm. As shown in Figure 4-5(a), the peak values for medium sand against both sand-epoxied surfaces are almost the same, but the slight hardening behaviour after strain-softening in 750FRP(R) distinguishes it from 750FRP(MR). This difference is attributed to the effect of clogging-prone surface roughness, as reported by Martinez and Frost (2017).

Figure 4-6 shows the variation in the interface friction coefficient at peak and ultimate state of sand against the 1500FRP(MR) and 1500FRP(R) interfaces with respect to normal stress. This relationship holds good with power equation fittings. The peak interface friction coefficient variation shows that both the constant and power indices increase with increasing normal stress, larger particle size, and greater surface roughness of sand-epoxied GFRP. This finding is well

established, as is the finding of Frost and Han's (1999) study on blasting sand-FRP interface. However, the fittings of the ultimate friction angle remain relatively flat, suggesting a significant influence in reducing interlocking mechanisms at the interface by potential alterations in surface texture, especially for M-1500FRP(MR). Furthermore, the effects of normal stress on the F-1500FRP(R) interface are found to be prolific for fine sand in the reduction of ultimate interface friction coefficient, which could be due to no potential alterations in the surface texture of sand-epoxied GFRP (Figure 4-6(b)).

4.3.2 Evolution of surface roughness

Mass sliding at the sand-GFRP interface occurs when sand particles slide across the GFRP surface under applied normal stress, leading to alterations in the GFRP contact surface (Pando et al., 2002; Sakr et al., 2005; DeJong and Westgate, 2009). This sliding generates surface wear, forming linear scars and shallow grooves (Vangla and Latha, 2015; He et al., 2021). The rotational effect occurs when sand particles twist or spin due to the surface roughness, creating mechanical interlock and increasing contact points, which amplifies friction and resists particle movement (Lashkari and Jamali, 2021). When shear stress exceeds the interlock resistance, surface degradation accelerates, leading to groove formation and epoxy breakdown (Vangla and Latha, 2015; Vangla and Gali, 2016; Chen et al., 2021; He et al., 2021). The rotational effect is further intensified by particle size and angularity. The mass sliding and the rotational coupling effect promote significant surface wear, as reflected in the evolving surface roughness profiles presented in Figure 4-7, which are analysed qualitatively and quantitatively to assess the wear patterns after shearing.

Optical images, 3D surface profiles, and laser images have been performed on GFRP shearing surfaces to investigate the evolution of surface properties before and after shearing, as shown in Figure 4-7. The rough texture of prepreg GFRP features protrusions with thinner epoxy, provides resistance during shearing, and acts as weaker zones for roughness evolution compared to the smooth texture of industrial with discontinuous patches, as depicted in Figure 4-

7(a). The formation of discontinuous linear fine scars along the shearing length can be observed in PFRP(R) at F-PFRP(R) interface, whereas a few shallow trenches can be observed at M-PFRP(R) and C-PFRP(R) interfaces under 200 kPa. Under higher normal stresses, linear scars become continuous and deepen, while shallow trenches widen, as illustrated in Figure 4-7(b). In the images of height analysis under 800 kPa, the linear dashed lines represent the continuous and deepened scars, while the dashed ellipses, in conjunction with the linear dashed lines, indicate the formation of trenches accompanied by a few deepened scars. Sliding of particles prevalent in uncoated surfaces causes scar formation and is predominated by fine sand particles. However, the effect of this mechanism is amplified under higher normal stress to increase the length and width of scars, as observed at the F-PFRP(R) interface. Mass inertia and rotational impact increase with median particle size.

Thus, significant surface damage is attributed to trench formation accompanied by a few scars. It is consistent with the interface contact mechanism analysed in particle image velocimetry (PIV) for sands against smooth steel and geomembrane (DeJong and Westgate, 2009; Lashkari and Jamali, 2021), where sliding followed by rotation was reported for increasing median particle size. However, no abrupt changes were observed in the shear stress-tangential displacement and normal displacement trends, despite the progressive changes in GFRP surface roughness (Figure 4-4).

Figure 4-7(c) shows the Laser images and 3D profiles of fresh sand-epoxied GFRP, where sand particles are coated with epoxy, allowing for the evaluation of the epoxy-sand-epoxy bond. Larger sand particles offer a greater surface area, facilitating stronger bonding between the epoxy and the GFRP surface at the semi-cured stage. This enhanced bonding mechanism results in more effective adhesion compared to finer particles, ultimately contributing to greater surface hardness in 1500FRP(R) relative to 1500FRP(MR) (Table 4-2). Figure 4-7(d) highlights the degradation of surface peaks under varying normal stress conditions. Under 200 kPa, minimal peak degradation is observed, particularly for the sand-epoxy GFRP interfaces marked with white dashed circles or ellipses.

However, under 400 kPa, noticeable degradation is seen across all GFRP types. Nearly all sharp peaks are degraded at 800 kPa for sand-epoxy coatings with a 0.15-0.85 mm particle size range (medium rough surface) compared to the 0.3-0.85 mm range (rough surface). This is attributed to the superior integrity of the rougher surface, where larger sand particles create stronger bonding with the epoxy, enhancing surface hardness. As shear stress increases, the epoxy layer, which previously protected the sand particles, begins to break down due to rotational and interlocking effects at rough interfaces. The shear stress required to overcome accumulating resisting forces at the interface leads to the degradation of the sand peaks, as observed in interfaces like C-750FRP(MR) and M-1500FRP(MR), where the epoxy fails to maintain its integrity under higher stress.

The 750 g/m^2 concentration of epoxied sand surface is partially covered, resulting in fewer protruding asperities compared to the 1500 g/m^2 coating. This partial coverage facilitates significant particle accumulation in the valley regions, increasing the dragging force during shearing and contributing to surface degradation. The roughness variation in 1500FRP(R) is linked to the progressive removal of the protective epoxy layer, which serves as the primary contact surface at the interface.

This process is influenced by differences in toughness caused by the concentration and particle size of epoxied sand at the interface. The quantification of roughness variation presented in Figure 4-7(e) shows that the average roughness variation in M-1500FRP(R) is -4.2%, while M-1500FRP(MR) exhibits a variation of -10.5%. This trend of decreasing roughness variation with increasing normal stress suggests that sand-epoxied GFRP with a rougher surface (e.g., M-750FRP(R) and M-1500FRP(R)) exhibits superior surface integrity compared to those with a medium rough surface. Table 4-4 summarises the surface properties for both uncoated and sand-epoxied GFRP, including average roughness, maximum roughness parameters, friction angles, and efficiency factors. Note that the ultimate shear stress of sand-GFRP interfaces is considered at 12 mm of tangential displacement (e.g., Lashkari and Jamali et al., 2021). The

detailed definition and engineering design parameters can be found in Appendix B (Equations (B-1a) to (B-3); Table B-1).

As illustrated in Table 4-4, the maximum efficiency factor of sand-epoxied GFRP is 1.26 at the F-1500FRP(R) interface. Coarse sand exerts a dominant influence on the ultimate friction angle of uncoated GFRP, primarily through mass sliding, with limited rotational effects on the smooth surface. The friction angle increases with rougher sand-epoxied surfaces, with both peak and ultimate friction angles elevated in interfaces with partial to full coverage of epoxied sand. Medium sand induces less abrasive contact on rougher surfaces, reducing damage to the sand-GFRP interface compared to coarse sand. Average surface roughness variation ranges from 3.6% to -14.1% on rough surfaces, where negative values indicate a reduction in roughness. Average maximum roughness shows a wider variation, between 17.2% and -20.7%, suggesting that it is more sensitive to surface changes than average roughness, which may not fully represent the surface condition in materials with lower hardness.

The average maximum roughness is more applicable to harder materials like stainless steel (Uesugi and Kishida, 1986b; DeJong and Westgate, 2009; Araújo et al., 2022). Except for the C-1500FRP(R) interface, all sand-epoxied GFRP surfaces in the 0.3-0.85 mm range (both 750 g/m^2 and 1500 g/m^2 concentrations) show approximately -5% mean roughness variation after testing The surface roughness of uncoated GFRP is influenced by its lower initial hardness and increased flatness, primarily driven by mass sliding effects under high normal stress (O'Rourke et al., 1990; Teng et al., 2024). However, this mechanism is significantly reduced under lower normal stress (Namjoo et al., 2022; Chapter 3). Although roughness variations are observed, the impact on shear behaviour remains difficult to quantify during single-surface shearing. No drastic changes in shear stress are noted, unlike the variations reported in polymers and geomembrane materials (Shooter and Taboor, 1952; Dove and Frost, 1999; Fleming et al., 2006). However, a slight increase in ultimate friction angles is observed at the M-PFRP(R) and C-PFRP(R) interfaces (e.g., Figure 4-4(a); Table 4-4; Table B-1).

4.3.3 Comparison of interface friction angles

Figure 4-8 compares the interface friction angles of the present study with those from previous research (Subba Rao et al.,1998; Dietz and Lings, 2006; Han et al., 2018; Su et al., 2018; Wang et al., 2023; Figures 3-17(c) and 3-17(d) of Chapter 3), with respect to relative roughness. The curvilinear fitting of peak and ultimate states in Figure 4-8(a) identifies a relative roughness of 0.2 as the transition point between intermediate and rough interfaces, where the friction angle reaches its maximum value. Beyond this threshold, further increases in relative roughness have a negligible effect on friction, as interface behaviour is dominated by internal soil failure rather than frictional enhancement (e.g., Paikowsky et al., 1995). Figures 4-8(b) and 4-8(c) present a comparison between the current study and previous studies on quartz-dominated, subrounded to rounded sands in contact with various structural materials (e.g., stainless steel, rusted steel, sand-coated steel, sawtooth steel, and GFRP).

The data from Chapter 3 has been updated, incorporating results for coarse sand (d_{50} = 1.536)-steel interfaces from Han et al. (2018) and Su et al. (2018). The trend lines for the intermediate and rough zones are shifted downward by 1° in the peak state chart and upward by 1° in the ultimate state chart, respectively. Notably, the majority of the present study's results align closely with these trend lines, reflecting the high precision of the monotonic interface testing.

Although Chapter 3 utilised a similar 1500 g/m^2 sand-epoxied concentration, that study was focused primarily on fine sand-GFRP interfaces with a smooth surface (0.1–0.8 mm range of epoxied sand), resulting in lower asperity heights and consequently a reduced friction angle compared to the present study.

4.4 Interface shear behaviour and evolution of surface properties subjected to cyclic shearing

4.4.1 Effect of shear amplitude

Investigation of the influence of amplitude on shear stress, shear stiffness, and

the average roughness of GFRP was conducted considering three different cyclic displacement amplitudes, ±1.0 mm, ±2.5 mm, and ±5.0 mm on prepreg GFRP (HFRP(S) and HFRP(R). These cyclic displacement amplitudes represent three different stress-displacement regions based on the mechanical response at monotonic shearing: the elastic region, the peak stress regions, and the post-peak stress states in the plastic region, respectively. Although the imposed displacement amplitude (±1.0 to ±5.0 mm) may exceed typical field values, it was selected to ensure full shear mobilisation and to accelerate interface degradation processes. The relative displacement is nonetheless representative of localised strain zones in field conditions such as seismic or traffic-induced loading. Figure 4-9 shows the effect of cyclic displacement amplitudes for F-HFRP(S), M-CHFRP(R), and C-HFRP(R) under 200 kPa. Figures 4-9(a) to 4-9(c) illustrate that as displacement amplitudes increase, the enclosed hysteresis loops transition from narrow to wide, approaching a rectangular shape for F-HFRP(S) interfaces, followed by elliptical loops for M-HFRP(R) and C-HFRP(R), similar to the trends observed by Samanta et al. (2022) at sand-geomembrane interface. Interface strength increased for the first 15 cycles, followed by a slower progression approaching the 50th cycle. The secant shear stiffness (see Appendix B Figure B-1) of the interfaces reduces exponentially with increasing cyclic displacement and agrees with the previous investigators' research in the sand-steel interface (Desai et al., 1985). The M-HFRP(R) interface exhibited the highest shear stiffness, potentially due to the rough texture of the GFRP surface. (Figure 4-9(d)).

Furthermore, the linearly decreasing trend of average roughness with increasing displacement amplitudes can be observed for the F-HFRP(S) interface, while C-HFRP(R) shows an unstable pattern of average roughness variation. This trend might be due to void formation during manufacturing, leading to lower toughness in some FRP regions. However, the maximum variation in the roughness of HFRP(R) can be regarded at ±2.5 mm and ±5.0 mm. Furthermore, the movement of particles outside the interface in ±2.5 mm was significantly less compared to ±5.0 mm. Thus, the experiments proceeded by considering ±2.5 mm

of tangential displacement to study various influential factors.

4.4.2 Influence of particle size

Figure 4-10 shows the cyclic response of particle sizes against PFRP(S) and 1500FRP(R) interfaces at ±2.5 mm cyclic displacement amplitude under 200 kPa normal stress. Mobilised shear stress (Equation (2-9a)) is plotted against cyclic tangential displacement at the end of each cycle, while normal displacement is presented at the mid-cycle zero crossing point (e.g., Westgate and DeJong, 2023). The rectangular hysteresis loops for sands against PFRP(S) are preceded by strain-softening for fine sand and strain-hardening for medium and coarse sand in the initial cycle (Figure 4-10(a)). In contrast, elliptical hysteresis loops with initial strain-softening can be observed for sands against 1500FRP(R) (Figure 4-10(b)). With increasing cycle numbers, sand specimens undergo contraction, particularly when shearing against 1500FRP(R), with medium sand dominating this behaviour (Figures 4-10(a) and 4-10(b)), consistent with Shahrour and Rezaie's (1997) study for dense silica sand against a sand-epoxied steel surface.

Figure 4-10(c) shows that M-PFRP(S) and C-PFRP(S) exhibit an increase in shear stress of approximately 50% within 15 to 20 cycles, whereas F-PFRP(S) displays a decrease of approximately 15%. The system stabilises around 45 to 50 cycles, reflecting the evolution of surface roughness and particle breakage, which is attributed to energy dissipation in the originally dense specimen, leading to a stable state. A virgin GFRP exhibited significant roughness alteration during the initial contacts, and the rate of alteration decreased with the increasing number of repetitions, as reported by Teng et al. (2024) in their study on repeated monotonic shearing effects. In cyclic shearing, interface and interparticle debonding and bonding with stress reversal cause particle fragmentation during shearing. Broken fine particles later fill the asperities of the structural surface, thereby contributing to significant energy dissipation along with minimisation of surface roughness alteration (Al-Douri and Poulos, 1992; Zhou et al., 2020; Rui et al., 2021; Yang and Yin, 2021). The hardening behaviour of medium and coarse sand against PFRP(S) is similar to that of Rui et al. (2021) for silica sand with a

particle range of 0.5-1 mm against steel with an average roughness of 3.25 μm.

However, fine sand against 1500FRP(R) exhibited a decrease in shear stress during the first five cycles, followed by a rapid increase until stabilising after 15 cycles, potentially due to the significant particle rearrangement and clogging along the rough surface (Figure 4-10(c)). Coarse sand demonstrates more stable shear stress than medium sand against 1500FRP(R) interfaces. Fine sand particles tend to move outward from the interface and compress more easily during cyclic shearing against PFRP(S), leading to higher compression. On the other hand, the roughness of 1500FRP surfaces induces rearrangement in medium and coarse sand, initially exhibiting dilative behaviour and transitioning to contractive behaviour with increasing cycles, indicating significant densification due to rough surface effects.

Figure 4-11 illustrates the effect of median particle size on surface roughness during cyclic interface shearing. As shown in Figure 4-11, the average roughness of PFRP(S) increases while that of 1500FRP(R) decreases, following the general trend observed after 50 cycles. During cyclic shearing, scars and trenches enlarge in width and depth. On PFRP(S), with lower surface hardness (e.g., O'Rourke et al., 1990), weaker regions deepen significantly, while stronger areas show minor changes (e.g., Shooter and Tabor, 1952). This effect is more pronounced with increasing median particle size, which enhances surface degradation and increases the average roughness of PFRP(S). In contrast, the reduction in roughness with increasing median particle size on 1500FRP(R) is attributed to particle rotation and bonding-debonding during interlocking mechanisms in cyclic shearing (Rui et. al., 2021). These phenomena are amplified as normal stress increases from 200 kPa to 800 kPa, with surface roughness changes on PFRP(S) and 1500FRP(R) amplifying by approximately five times and 1.2 times, respectively (Figures 4-11(a) to 4-11(c)). Coarser sand particles have a greater impact on roughness variation, contributing to a higher rate of shear stress increment, as observed in Figure 4-11(c). Consequently, significant effects on the particles themselves can be anticipated.

4.4.3 Effect of surface roughness

Figure 4-12 illustrates the effect of surface roughness on the cyclic response and normal displacement of medium sand against uncoated and various sand-epoxied surfaces under 800 kPa normal stress. The first hysteresis loop (Figure 4-12(a)) shows an increase in cyclic shear stress, reaching approximately 600 kPa on 750FRP(R) and 1500FRP(R). Elliptical hysteresis loops display pronounced protrusions at both the forward and reversal tips, with loop width diminishing as initial surface roughness increases, especially by the fiftieth cycle. During forward shearing, normal displacement against smooth surfaces (e.g., PFRP(S) and 750FRP(S)) primarily exhibits contractive behaviour. However, backwards shearing, influenced by the long shearing length, variation in dip direction of the GFRP roughness, and sand particles' aeolotropy, results in dilation. A rough sand-epoxied surface counteracts particle suppression, leading to slight dilation during forward shearing (Figure 4-12(a)).

Mobilised shear stress enhances as cycles progress, particularly along rough surfaces, reaching a steady state after 15 cycles. This indicates intense resistance and roughness evolution at the rough interface (Figure 4-12(b)). The shear stress for 750FRP(R) increases by 5% compared to 750FRP(S) between the first and the fiftieth cycle (from 36% to 41%), reflecting greater interlocking due to particle breakage and surface roughness evolution (Zhou et al., 2020; Rui et al., 2021). Consequently, medium sand specimens contract more on rough surfaces, with a 50% greater contraction at the fiftieth cycle compared to PFRP(S) and 750FRP(S), resulting in a linear decline in normal displacement under 800 kPa normal stress (Figure 4-12(b)).

The effect of surface roughness in mobilised shear stress at the 50th cycle is illustrated in Figure 4-13. During cyclic shearing, a rougher sand-epoxied GFRP surface provides sufficient areas for effective interlocking of medium sand compared to uncoated or smooth surfaces, sand-epoxied GFRP to enhance interface shear strength. This phenomenon is further amplified with increasing normal stress, as illustrated in Figure 4-12(b), which emphasises the importance of normal stress in investigating the underlying mechanisms.

4.4.4 Influence of normal stress

The effect of normal stress on the mobilised shear stress during the first and fiftieth cycles can be analysed through the cyclic stress envelope presented in Figure 4-14. For three median particle sizes tested against uncoated GFRP, the interface strength evolved over the loading cycles depending on the material type. At the limit state, represented by the mobilised shear stress at the fiftieth cycle, the cyclic stress envelope passed close to the origin, suggesting minimal apparent adhesion (Equation (2-14b)).

As shown in Figure 4-14(a), this finding contrasts with the results reported by Desai et al. (1985) for the sand-steel interface. The discrepancy can be attributed to the effects of mass sliding followed by particle rotation, while the increased roughness of the uncoated GFRP contact surface at the fiftieth cycle is crucial to improve the interface roughness, thereby enhancing mobilised shear strength. Figure 4-14(b) presents the cyclic stress envelope for medium sand against sand-epoxied GFRP interfaces. The envelope for both the first cycle and the limit state exhibits an increasing inclination with cycle number. Ultimately, the stress envelope passes through the origin, highlighting the influence of applied normal stress on surface interaction and particle behaviour. Although surface degradation occurs in sand-epoxied GFRP, the interparticle bonding-debonding mechanism at the interface, coupled with the degraded surface, strengthens the shear resistance. This behaviour governs the development of the mobilised shear stress response.

Figure 4-15 illustrates that the mobilised friction coefficient for all sand types against both uncoated and sand-epoxied GFRP decreases from 200 kPa to 400 kPa normal stress and then increases under 800 kPa. This intermediate dip at 400 kPa may correspond to a transitional regime where sliding-dominated behaviour gives way to localised particle crushing, reducing frictional resistance. The observed increase at 800 kPa is attributed to enhanced frictional mechanisms: for uncoated GFRP, this involves the amplification of surface scars and trenches; for sand-epoxied GFRP, it is driven by intensified interlocking and particle rotation. Since the data corresponds to the fiftieth cycle, this trend also indicates

the potential reformation of the interface shear zone on degraded surfaces, where accumulated broken and source particles promote better bonding for elevating the friction coefficient, which can be identified via microscopic investigations.

Figure 4-16(a) presents microscopic and scanning electron microscopy (SEM) images (last six images) of fine, medium, and coarse sands after 50 cycles (equivalent to a cumulative displacement of 0.5 m) of interface cyclic shearing against plain GFRP (smooth). As shown in Figure 4-1 and Table 4-1, particle roundness increases with median particle size. Following cyclic shearing, particles become smoother, concavities enlarge, and finer particles disperse around the source particles, as illustrated in Figure 4-16(a). This trend becomes more pronounced with increasing median particle size, accompanied by a growth in both the size and concentration of broken particles (Al-Douri and Poulos, 1992; Rui et al., 2021). Larger particles tend to concentrate stress at their contact points and edges due to their irregular geometry and limited contact area, making them more susceptible to fragmentation under applied loads. For sand-PFRP(S) interfaces, increasing normal stress from 200 to 800 kPa leads to higher concentrations of finer particles and wrapping of larger source particles, as reported by Zhou et al. (2020) and Rui et al. (2021) for silica sand-steel interfaces under 200 kPa normal stress and large cumulative tangential displacement (i.e., 2 m or more). Additionally, SEM images reveal fractured sand particles mixing with dry epoxy powder or lumps, which disperse around the source particles. The size of these detached epoxy lumps increases with the median particle size of the sand specimen, particularly under 800 kPa normal stress.

Particle size distribution curves in Figures 4-16(b)-4-16(d) indicate particle breakage rates of approximately 6%, 12%, and 18% for coarse sand; 2%, 5%, and 9% for medium sand; and 2%, 3%, and 7% for fine sand under normal stresses of 200, 400, and 800 kPa, respectively, at the PFRP(S) interface. When coarse sand is sheared against sand-epoxied GFRP, such as 750FRP(R) and 1500FRP(R), breakage increases to 10%, 15%, and 21%, respectively, following a consistent trend with rising normal stress. This amplified breakage on rough sand-epoxied GFRP surfaces is associated with increased resisting forces and progressive

GFRP degradation. Therefore, identifying the cycle number at which abrupt GFRP degradation occurs is essential.

4.4.5 Impact of cycle number on roughness evolution

To investigate how surface roughness evolves with an increasing number of cycles, four cyclic tests were conducted on each GFRP specimen under a single normal stress condition: 1 cycle, 4 cycles, 15 cycles, and 30 cycles, culminating in a total of 50 cycles. Figure 4-17 presents representative 3D surface profiles of both uncoated and sand-epoxied GFRP, illustrating the effect of cumulative cycles on roughness development. As the cumulative number of cycles increases from 1 to 5, scars and trench formations along the shearing direction (i.e., pitch width of the evaluation areas) deepen and subsequently widen towards 20 and 50 cumulative cycles for smooth surfaces such as 750FRP(S) and PFRP(S). This widening of trenches results from the combined effects of mass sliding and particle rotation. From 5 to 20 cumulative cycles, the peak regions of HFRP(R) progressively flatten at the M-HFRP(R) interface, while the crest regions continue to deepen. Eventually, by 50 cumulative cycles under 200 kPa normal stress, the surface becomes relatively flatter; however, exposed fibres in the middle of the degraded surface cause a localised elevation in the maximum height of the 3D profile, as shown in Figure 4-17(a).

For M-750FRP(R) interfaces, the peak regions of the sand-epoxied surface exhibit minor reductions between 1 and 5 cumulative cycles, whereas significant degradation becomes evident by 50 cumulative cycles. As cyclic shearing progresses, the bond strength of the epoxied sand weakens, leading to the gradual detachment of protective epoxy layers and the removal of some epoxied particles. This results in a more pronounced surface roughness degradation compared to monotonic shearing.

The degradation intensifies further with increasing normal stress, causing the surface asperities to evolve towards a smoother state. This trend is particularly evident at 50 cumulative cycles under 400 and 800 kPa normal stress for the 750FRP(R) interface, as shown in Figure 4-17(b).

Figure 4-18 illustrates the quantitative trend of roughness evolution on GFRP surfaces, accounting for the influence of the cumulative number of cycles and the extrapolated trend of roughness variation. As shown in Figure 4-18(a), the variation in average roughness increases by approximately 1%, 1%, 5%, and 10% across four consecutive C-PFRP(S) tests as the cyclic tests progress. Notably, the first five cumulative cycles exhibit the most pronounced deterioration, with roughness increasing by approximately 4% to 5%, followed by a more gradual increase over the next 15 cumulative cycles for medium and coarse sand against 750FRP(R) and 1500FRP(R) under 200 kPa normal stress. In contrast, a significant decreasing trend in average roughness variation ranging from approximately 7% to 8% can be observed over the first 20 cumulative cycles for rough sand-epoxied GFRP surfaces under 800 kPa normal stress. This is followed by a further decline of approximately 6% to 7% over the subsequent 30 cycles, as illustrated in Figure 4-18(b). Furthermore, Figure 4-18(c) presents a power-law extrapolation of the average surface roughness decay for M-750FRP(R) and M-1500FRP(R) interfaces, extending from 50 up to 10^5 cumulative cycles under normal stresses ranging from 200 to 800 kPa. Extrapolated trends show substantial degradation for 750FRP(R) (6.5% to 18%) compared to 1500FRP(R) (5% to 12.1%) with increasing normal stress (200 kPa to 800 kPa), suggesting that the 1500FRP(R) surface offers greater durability. The maximum overall degradation for M-1500FRP(R) remains approximately 26% after 10^5 cumulative cycles under 800 kPa normal stress.

4.4.6 Performance of sand-epoxied GFRP in cyclic tests

Table 4-5 summarises the cyclic test results. The interface friction coefficient increases with normal stress from 400 kPa to 800 kPa for all interfaces and sand types. Efficiency factors for rough sand-epoxied GFRP surfaces are highest for medium sand (1.45), followed by fine sand (1.3), irrespective of the epoxy sand concentration (Table 4-5; Figure 4-19). The maximum roughness variation is primarily influenced by normal stress and coarse sand particles. Roughness on sand-epoxied GFRP decreases with increasing normal stress, while roughness on

PFRP(S) severely increases. GFRP degradation is most notable when normal stress exceeds 400 kPa for softer GFRP (~30 HV) combined with increasing median particle size, leading to a shift from mass sliding to a combination of mass sliding and rotation, accelerating surface degradation.

For medium and coarse sand against sand-epoxied rough surfaces, interlocking and particle rotation evolve into intense dragging under 800 kPa normal stress, reducing average roughness more than 2.5 times compared to monotonic shearing. Overall, sand-epoxied GFRP, such as 750FRP(R) and 1500FRP(R), performs well in enhancing frictional properties; their use under large normal stress requires high-strength epoxy or consideration of a safety factor to account for GFRP degradation.

The variation in the limit state interface friction angle with respect to the representative average roughness plot of Figure 4-20 shows that medium sand outperforms coarse sand with the inclusion of large representative average roughness ($\geq$ 100 μm). This trend is due to the greater relative roughness of medium sand to rough surface interfaces, which enhances friction compared to the less effective engagement of coarse sand.

4.5 Influence of relative roughness on friction and volumetric behaviour

Figure 4-21 presents the interface friction angles obtained from both monotonic and cyclic tests, along with a comparison between the present study and previous monotonic studies (Subba Rao et al.,1998; Sakr et al., 2005; Dietz and Lings, 2006; DeJong and Westgate, 2009; Han et al., 2018; Su et al., 2018; Lashkari and Jamali, 2021; Wang et al., 2023), with respect to relative roughness. It also includes generalised design charts developed from the present test data. Figure 4-21(a) illustrates a comparison between friction angles obtained from monotonic and cyclic interface shear tests reveals that the limit-state friction angles observed in the cyclic tests consistently exceed the peak values from monotonic tests, corroborating the trends reported by Rui et al. (2021), who

observed enhancements of approximately 2° to 4° under cyclic conditions (Figure B-4). This enhancement is due to the synergistic interplay of multiple factors, including particle breakage, the epoxy detachment from GFRP surfaces, evolution of surface roughness, and the formation of interfacial bonds between broken particles, source particles, detached coating fragments, and fines. These mechanisms contribute to localised shear zone reformation, stress redistribution, and enhanced particle interlocking through complex inter-particle rearrangements, functioning as an interdependent dynamic that ultimately improves relative roughness and interface performance. These effects are further amplified by higher normal stress and increased cycle numbers (e.g., Desai et al., 1985; Al-Douri and Poulos, 1992).

SEM images under 800 kPa show redistribution of fine particles and epoxy fragment concentrations along the interface, indicating dynamic shear zone reformation through particle rearrangement and material mixing. Ho et al. (2011), Zhou et al. (2020), and Rui et al. (2021) observed significant particle breakage of sand specimens under large or cyclic displacements on steel interfaces with limited dependence on surface roughness evolution for shear zone restructuring. In contrast, the present findings show a stronger dependence on surface roughness evolution, leading to more pronounced restructuring, particularly for medium and coarse sands interacting with GFRP and sand-epoxied GFRP interfaces. In these cases, roughness evolution and epoxy fragmentation further contributed to particle morphological changes, thereby influencing interface restructuring and friction mobilisation. Thus, the evolution of surface roughness and the development of stronger interlocking bonds enhance the mobilised interface friction property, in contrast to monotonic shearing, where minimal particle breakage and roughness variation cause a lesser impact.

Figures 4-21(b) and 4-21(c) present both a comparison with previous studies and a generalised design chart for the silica sand-GFRP interface. Figure 4-21(b) focuses on peak interface friction angles, while Figure 4-21(c) presents corresponding data for ultimate friction angles, incorporating results from the present study and previous studies involving glass beads and silica-based natural

sands, nearly angular to rounded particles in contact with various structural materials (e.g., stainless steel, rusted steel, sand-coated steel, sawtooth steel, geomembrane and GFRP) (Tables B-1and B-2). Based on the available data and the natural trend of friction angle variation with relative roughness, three distinct interface roughness zones can be identified: smooth ($R \leq 0.001$), intermediate ($0.001 \leq R \leq 0.2$), and rough ($R \geq 0.2$). A trend line (black dashed dotted) is plotted to reflect this relationship, with the rough interface zone anchored to the mean internal friction angle of the particles used in this study (Table B-2), following the approach of Paikowsky et al. (1995). Building on this, Figures 4-21(b) and 4-21(c) further illustrate the development of generalised design charts for the silica sand-GFRP interface, based on empirical data obtained from both monotonic and cyclic interface shear tests. These charts incorporate variations in particle morphology, surface roughness, and coating configurations. Shaded regions represent the empirically derived range of interface conditions, from smooth to rough, based on a consolidated dataset combining results from the present study with relevant literature. Key parameters integrated into the design envelope include normal stress levels (200-800 kPa), sand-epoxy coating configurations (e.g., particle sizes and areal concentrations), and particle morphology (sub-angular to sub-rounded; roundness $\approx$ 0.4–0.69). For instance, coarser sand grades with higher relative roughness were found to enhance interface friction, supporting optimal coating selection tailored to loading conditions in specific applications (e.g., seawalls, anchors). However, a friction angle reduction of approximately 2–3° should be accounted for as normal stress increases from 200 to 800 kPa. As illustrated in Figure 4-21, surrounding soils with angular particles exhibit higher interface friction due to interlocking, whereas rounded particles result in lower friction angles, relevant for field applications, as detailed in Appendix B (Table B-2).

A full-coverage epoxy coating of 1500 g/m^2 with sand particle sizes between 0.3–0.85 mm was identified as optimal, offering a favourable balance of monotonic friction efficiency and cyclic durability. Based on observed degradation trends ranging from 4.2% to 18.7% over 50 cycles under 800 kPa

normal stress, the cumulative degradation for M-1500FRP(R) interfaces reached 13.8%, with post-cyclic surface roughness averaging 92.7 μm (standard deviation=11.6 μm). Using a conservative serviceability threshold of 80 μm, this yields a reliability index of approximately 1.2, corresponding to an 88% probability of satisfactory long-term performance. Accordingly, a 20% design reduction in initial roughness is adopted. In combination with a mean interface efficiency factor of 0.89 and a design utilisation ratio of 0.95, this supports the application of a safety factor of 1.20 on initial roughness (Table B-1). This margin is consistent with geotechnical design principles and sufficiently accounts for cyclic degradation and roughness evolution. Although extrapolated trends indicate potential degradation up to 26% at 10^5 cycles under similar stress conditions, the adopted safety margin conservatively accommodates such potential loss without compromising interface performance. In practice, the peak state (Figure 4-21(b)) is utilised for temporary structures and material characterisation, whereas the ultimate state (Figure 4-21(c)) is recommended for the safer design of permanent structures. A friction angle tolerance of ±1.0° is assumed in these charts to reflect experimental and material variability.

Figure 4-22 illustrates the variation in maximum normal displacement versus relative roughness for both monotonic and cyclic shearing at the ultimate state and the limit state, respectively. In monotonic shearing (Figures 4-22(a) and 4-22(b)), the maximum normal displacement increases exponentially for medium and coarse sands in the relative roughness range of 0.02 to 0.05, while fine sand exhibits a linear increase from 0.05 to 0.5. As normal stress increases, the maximum normal displacement decreases for both trends. In cyclic shearing (Figures 4-22(c) and 4-22(d)), medium sand shows the maximum compression with approximately -2.0 mm of maximum normal displacement at relative roughness around 1.0 compared to coarse sand, while fine sand shows the greatest overall compression (-2.3 mm) at higher relative roughness around 0.5 under normal stress of 800 kPa. Findings indicate that fine sand undergoes particle movement, densification at the interface, and a small degree of outward leakage from the interface. The larger particles exhibit less ability to reorient and pack

more closely under higher normal stress, limiting the extent of void space reduction and resulting in less overall compression.

In contrast to medium and coarse sand particles, fine sand exhibits greater particle rearrangement under higher normal stress, driven by its higher relative roughness and greater ease of densification (e.g., Uesugi et al., 1989). The larger the median particle size, the more favourable it is to dilation (expansion) rather than contraction, as larger particles have fewer contact points and less interlocking, promoting expansion instead of compression (Rui et al., 2021; Lashkari and Jamali, 2021; Namjoo et al., 2022). Coarse sand leads to more significant degradation on the GFRP surface due to higher stress concentrations; however, rotation and intense dragging favour medium sand under large normal stress.

4.6 Design implications for geotechnical-reinforced structures and future perspectives

The critical role of surface engineering in optimising the performance of GFRP reinforcements within geotechnical systems (e.g., foundations, pipelines, and sea walls) is highlighted through the application of sand-epoxy coatings. These coatings significantly improve interface shear strength, wear resistance, and cyclic durability under moderate to high normal stresses. This study presents a novel integration of sand-epoxy treatments on GFRP laminates using varied sand grades and concentrations, resulting in improved surface hardness, interfacial roughness, and frictional efficiency, key for structural applications in particulate-rich environments. The current vinyl ester-based sand-epoxy coating on GFRP laminates, limited to controlled laboratory conditions, shows promising initial properties and interfacial frictional efficiency against air-dried silica sand specimens, but its long-term performance under marine exposure requires further validation. Under monotonic shear loading, increased particle size and normal stress initiate a transition from sliding to rotation-dominated bonding-debonding. In cyclic shear, a synergistic interplay of surface roughness evolution, particle

morphological changes, and stress redistribution governs shear zone reformation, contributing to improved frictional efficiency and structural stability.

Elevated normal stress conditions provide valuable insights into material behaviour under extreme loading scenarios, such as those encountered in deeper soil layers or applications involving high loads (e.g., pile foundations and retaining walls). Designers should carefully consider sand gradation and concentration levels not only to enhance peak interface strength but also to mitigate degradation mechanisms and delay the breakdown of soil particles in contact with the reinforcement. Improved interface strength under cyclic shear loading directly enhances the resilience of foundation elements, pipelines, and seawalls against dynamic loads generated by wave action, tidal currents, and seismic events. Enhanced frictional resistance reduces displacement and deformation, thus increasing service life and structural reliability in demanding marine environments.

Design charts presented in Figure 4-21 offer practical guidance for material selection in applications such as pile foundations, anchors, submerged pipelines, and seawalls. The adopted safety factor of 1.20, derived from cyclic roughness degradation and reliability analysis, ensures robust performance of the optimal coating under service conditions, aligned with geotechnical design practice. This constitutes the first application-specific design framework tailored for sand-epoxied GFRP systems in silica-rich sub-angular to sub-rounded particulate environments. However, we acknowledge that the current dataset is limited in scale and scope. Further large-scale, multi-condition cyclic testing is required to refine and generalise the design recommendations. The observed dependency of interface strength on roughness evolution and bonding-debonding dynamics under cyclic shearing underscores the critical necessity to incorporate time-dependent interface degradation models into design practices.

4.7 Summary

In this Chapter, a series of cyclic shear tests with insights into monotonic tests

for sand-GFRP interfaces under moderate to large constant normal stress was conducted with dense sand specimens. Three median particle sizes of silica sand were sheared against three types of GFRP: prepreg, plain GFRP, and sand-epoxied GFRP, along with three grades of epoxied silica sand. The findings clarify the roughness evolution of the sand-coating approach and its impact on interface shear behaviour, offering practical guidance for geotechnical design while highlighting novel research fields. The main findings can be summarised as follows:

1) Optimal interface strength and durability are achieved using 0.3–0.85 mm sand at 1500 g/m^2, balancing interface interlocking with minimal degradation. Surface roughness evolution is strongly dependent on contact mechanisms: sliding-rotation dominates on smooth or uncoated GFRP, while rotation and bonding-debonding with interlocking effect govern on rough or sand-epoxied GFRP.
2) Under elevated normal stress and cyclic mobilisation, particle breakage of sand specimens and surface degradation of both uncoated and sand-epoxied GFRP intensify. The synergistic interplay of multiple factors reforming the localised shear zone at degraded surfaces enhances the mobilised friction coefficient, particularly at normal stresses exceeding 400 kPa. In contrast, surface roughness variations induced by monotonic shearing do not yield comparable gains in frictional resistance. This distinction clarifies the critical role of high normal stress in frictional strengthening at the sand-GFRP interface under cyclic shearing.
3) Dilative tendencies under monotonic shearing are influenced by surface roughness and median particle size. Specifically, within the relative roughness range of 0.02–0.05, significant dilation occurs for larger particles. This governs shear strength mobilisation and indicates a zone of volumetric instability. With the progression of cyclic shearing, the initial dilation of sand specimens transforms into contraction. This contraction tendency increases with the cycle number, relative roughness, and normal stress, suggesting progressive densification and specimen

compression that can alter structural behaviour.

4) Attrition- and abrasion-driven morphological changes, surface degradation, and volumetric densification scale with particle size, cycle numbers, and normal stress, highlighting the need for fatigue-aware design.
5) The efficiency factor and relative roughness framework provide a robust metric for comparing interface performance across surface treatments with epoxied sand grades and median particle size. The generalised design chart provides valuable insights and design implications for geotechnical-reinforced structures.

After completing the experimental investigation of monotonic and cyclic shearing, the study progresses to a numerical exploration of the underlying mechanisms governing the sand-GFRP interface. While the laboratory tests established the overall shear response, numerical modelling enables a deeper examination of both micromechanical interactions and macroscopic behaviour that cannot be directly observed in experiments. Accordingly, Chapters 5 and 6 present DEM and FEM simulations, respectively, to capture contact-scale mechanisms and to reproduce large-scale interface responses. Together, these approaches provide complementary perspectives and support the validation of experimental findings.

.

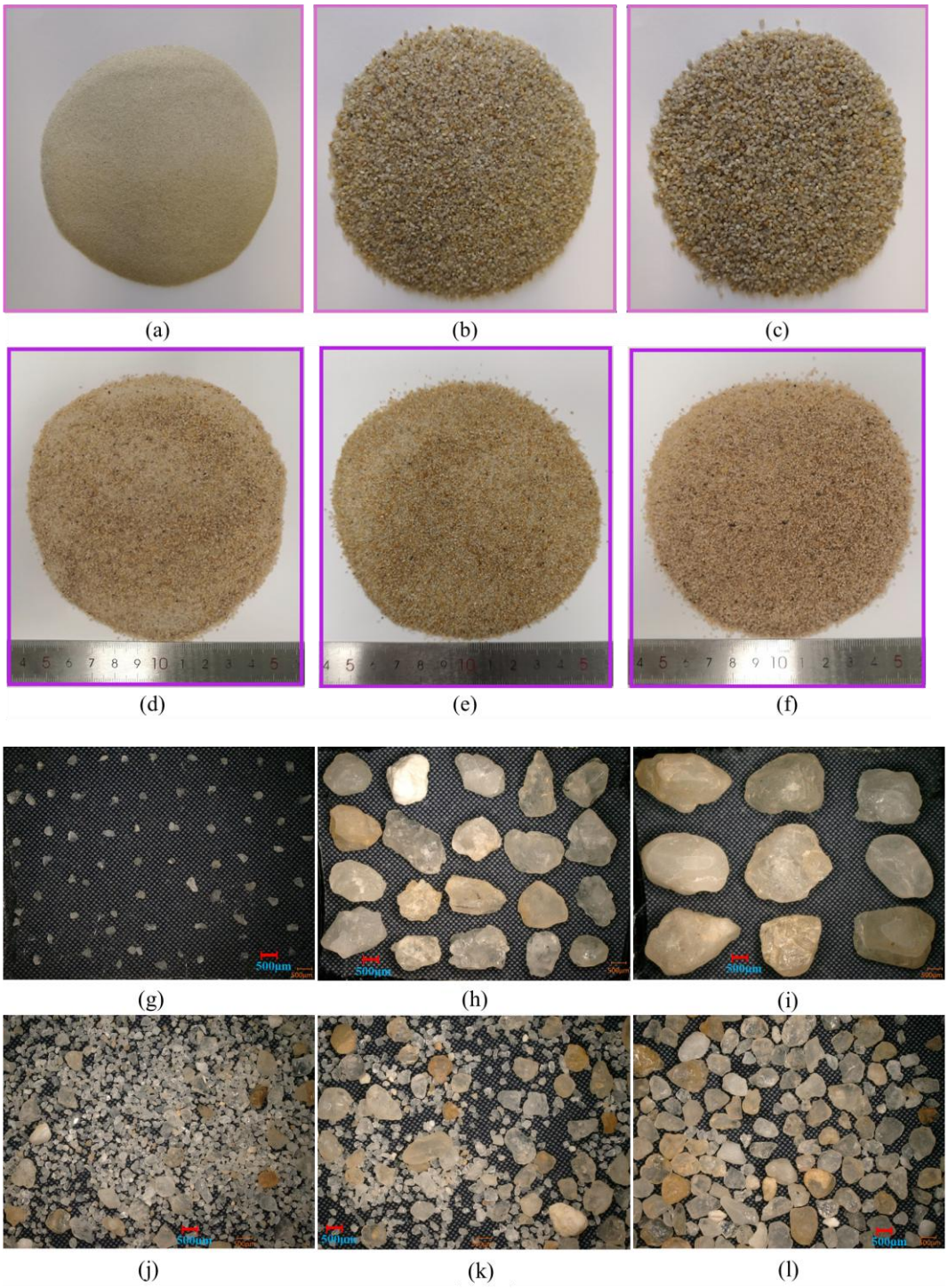

Figure 4-1 Photos of silica sand (each sand sample in images (a)-(f) is 100 g): (a) and (g) fine sand (0.15–0.3 mm), (b) and (h) medium sand (0.85–1.18 mm), (c) and (i) coarse sand (1.4–2.0 mm), (d) and (j) epoxied sand for a smooth surface (0.1–0.8 mm), (e) and (k) epoxied sand for a medium rough surface (0.15–0.85 mm), and (f) and (l) epoxied sand for a rough surface (0.3–0.85 mm) (Note: images (g)-(l) were

captured using a VHX multi-scan microscope with 30× magnification)

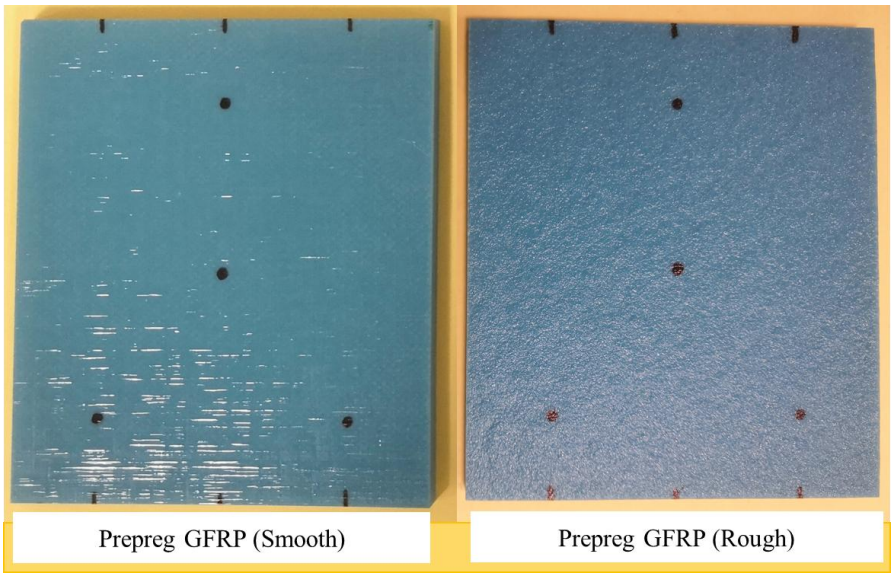

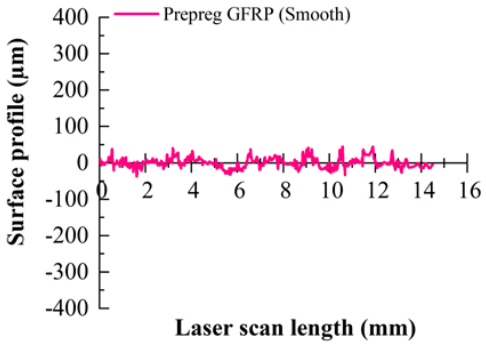

(a)

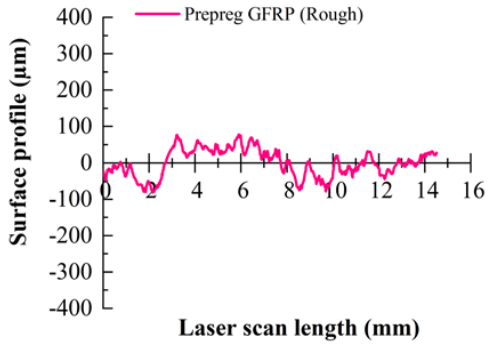

(b)

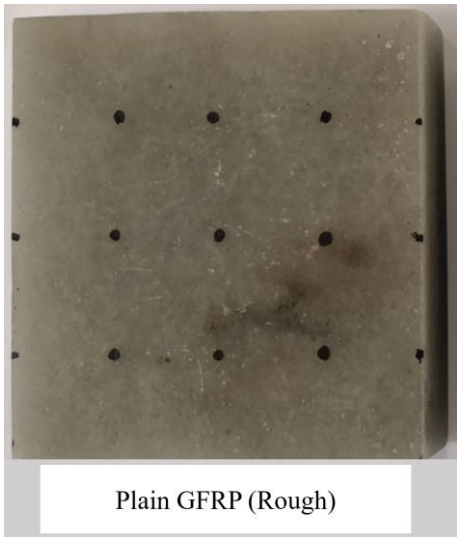

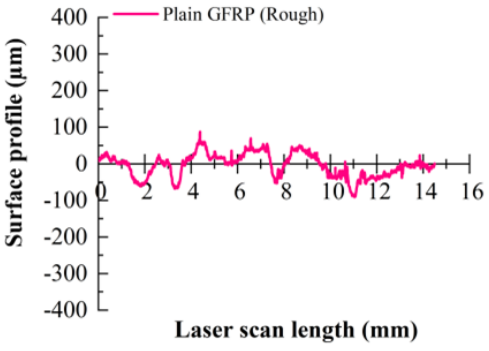

(c)

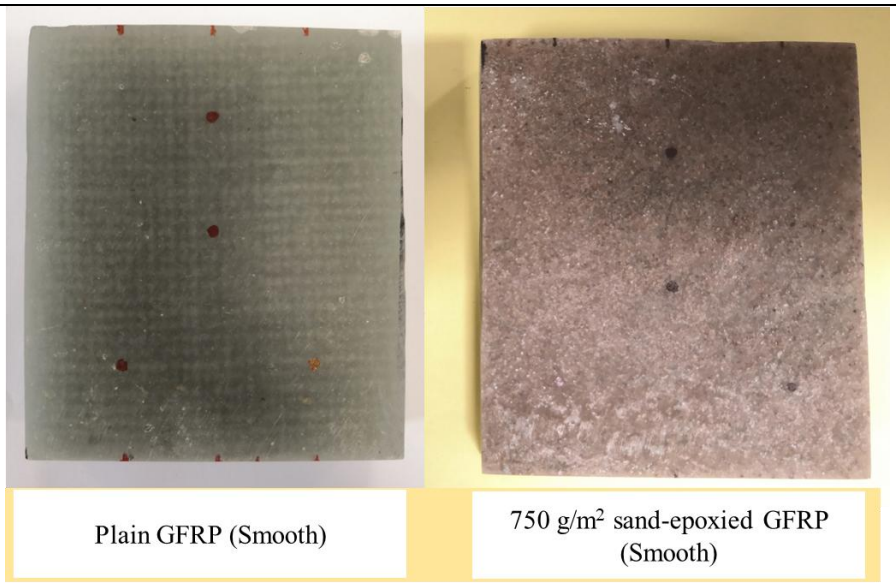

Plain GFRP (Smooth)

750 g/m^2 sand-epoxied GFRP (Smooth)

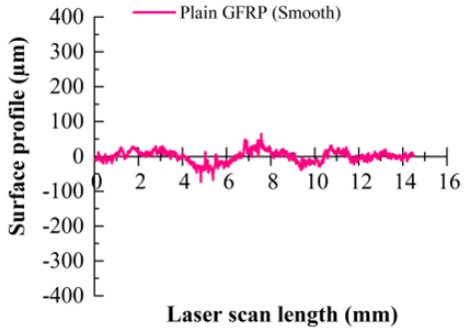

(d)

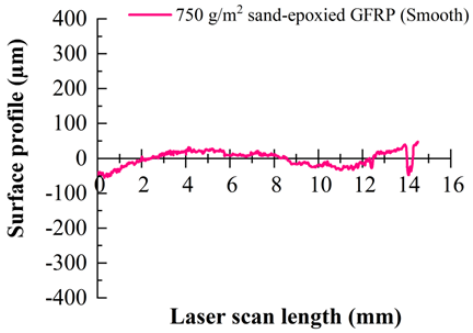

(e)

750 g/m^2 sand-epoxied GFRP (Medium rough)

1500 g/m^2 sand-epoxied GFRP (Medium rough)

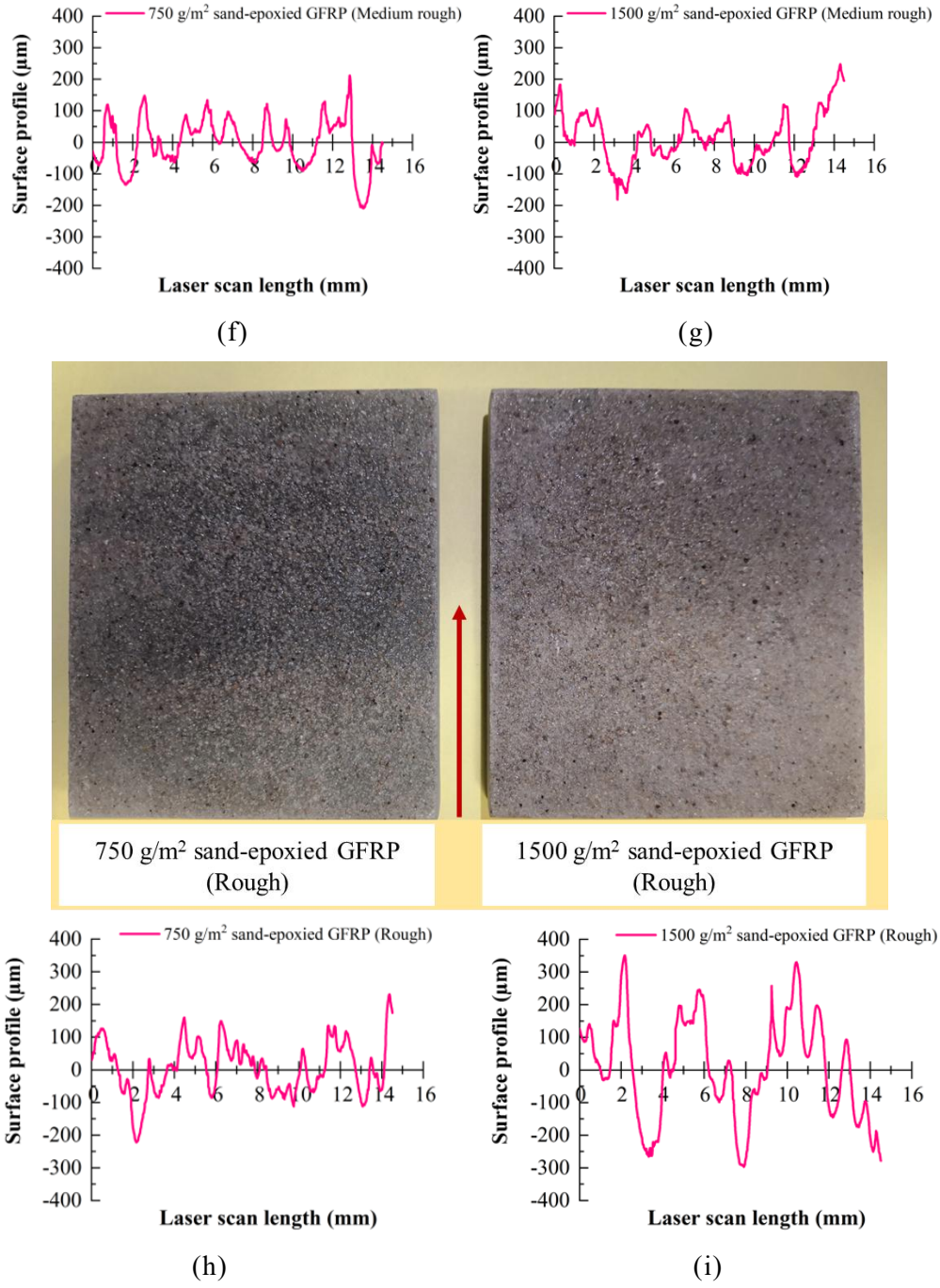

Figure 4-2 Photos of GFRP and sand-epoxied GFRP with corresponding 2D Laser-scanned surface profiles along the shearing direction: (a) smooth prepreg GFRP and (b) rough prepreg GFRP prepared in the Composite Lab at the Industrial Center, Hong Kong Polytechnic University; (c) rough surface plain GFRP, (d) smooth surface plain GFRP, (e) smooth surface sand-epoxied GFRP (0.1–0.8 mm sand range) with 750 g/m^2 sand concentration, (f) and (g) medium rough surface sand-epoxied GFRP (0.15–0.85 mm sand range) with 750 g/m^2 and 1500 g/m^2 sand concentrations, respectively, (h) and (i) rough surface sand-epoxied GFRP (0.3–0.85 mm sand range) with 750 g/m^2 and 1500 g/m^2 sand concentrations, respectively, in industrial GFRP by Lianyungang

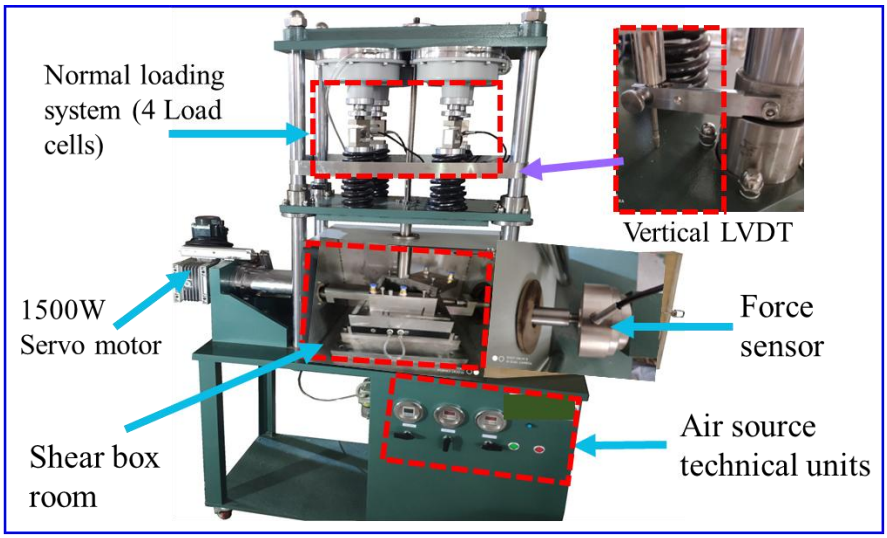
Normal loading system (4 Load cells)
Vertical LVDT
1500W Servo motor
Force sensor
Shear box room
Air source technical units

(a)

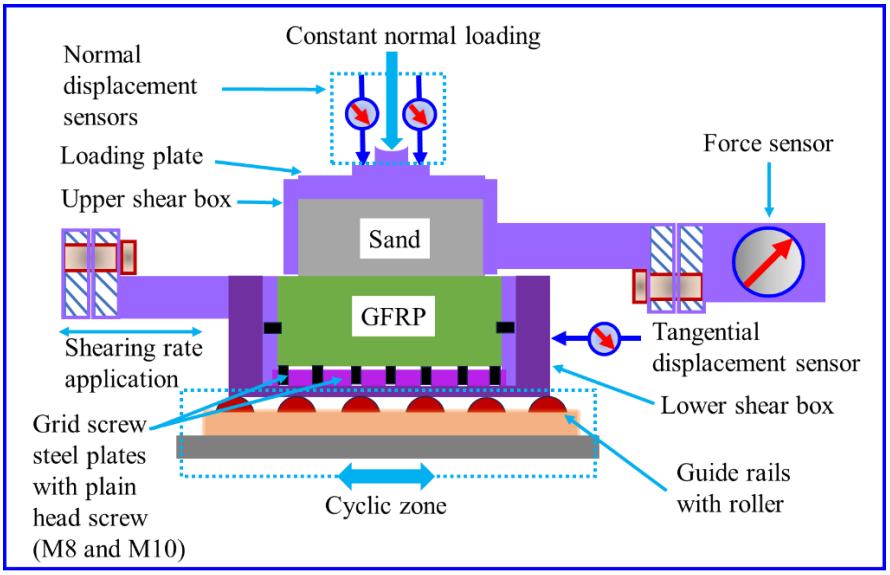
Constant normal loading
Normal displacement sensors
Loading plate
Upper shear box
Force sensor
Sand
GFRP
Shearing rate application
Tangential displacement sensor
Lower shear box
Grid screw steel plates with plain head screw (M8 and M10)
Cyclic zone
Guide rails with roller

(b)

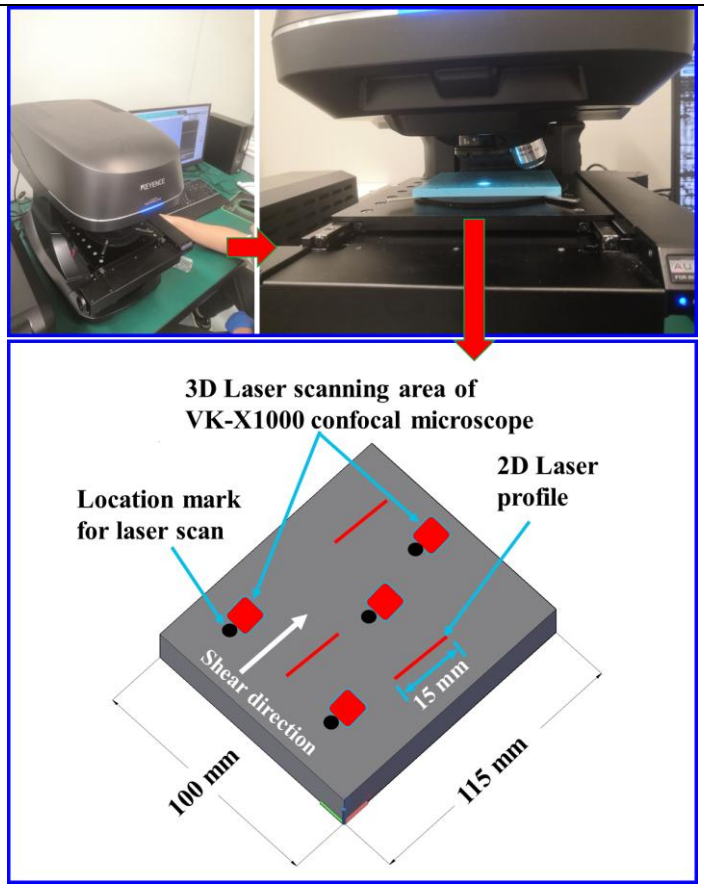

(c)

Figure 4-3 Photos of (a) multifunctional direct shear system, (b) schematic diagram of interface shearing apparatus, and (c) VK-X1000 confocal microscope with GFRP location mark for roughness measurement

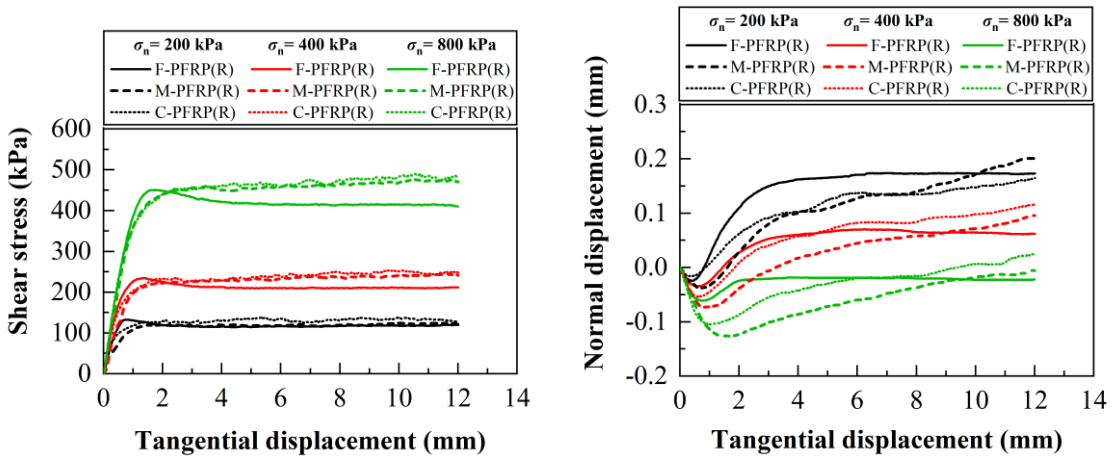

(a) (b)

Figure 4-4 Mechanical responses of fine sand, medium sand, and coarse sand against PFRP(R) interfaces (a) shear stress versus tangential displacement and (b) normal displacement versus tangential displacement

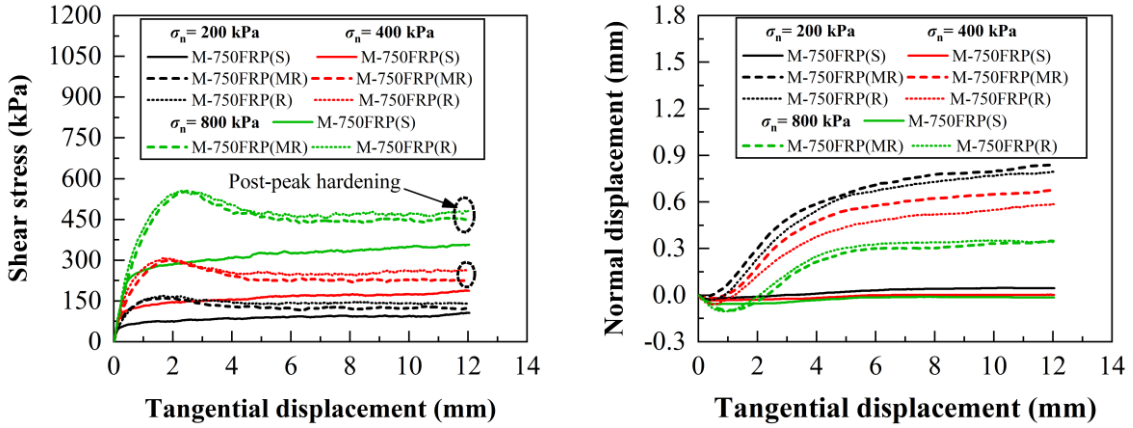

(a) (b)

Figure 4-5 Mechanical responses of medium sand shearing against three varieties of sand-epoxied GFRP surfaces having a concentration of 750 g/m^2 sand (a) shear stress versus tangential displacement and (b) normal displacement versus tangential displacement

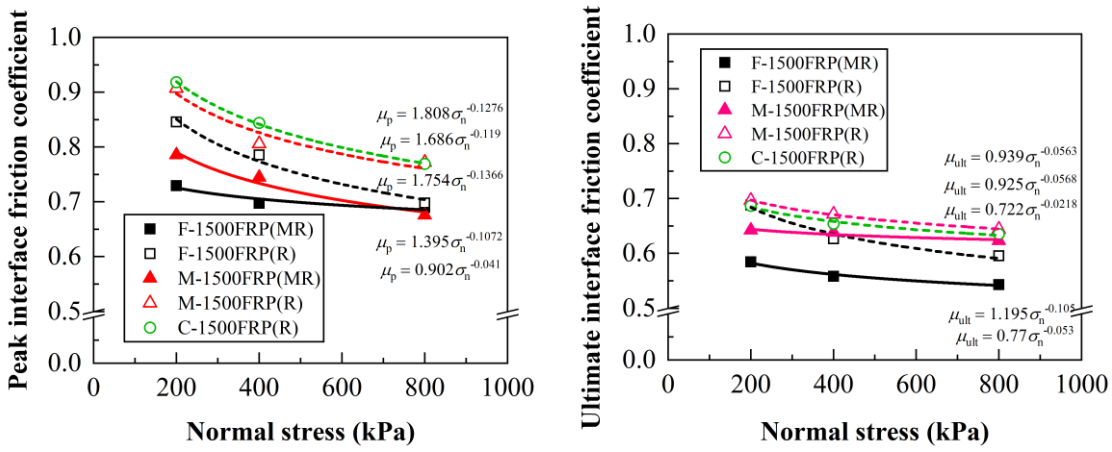

(a) (b)

Figure 4-6 Influence of normal stress on (a) peak interface friction coefficient, and (b) ultimate interface friction coefficient for fine sand, medium sand, and coarse sand against the 1500 g/m^2 concentration of sand-epoxied GFRP interfaces

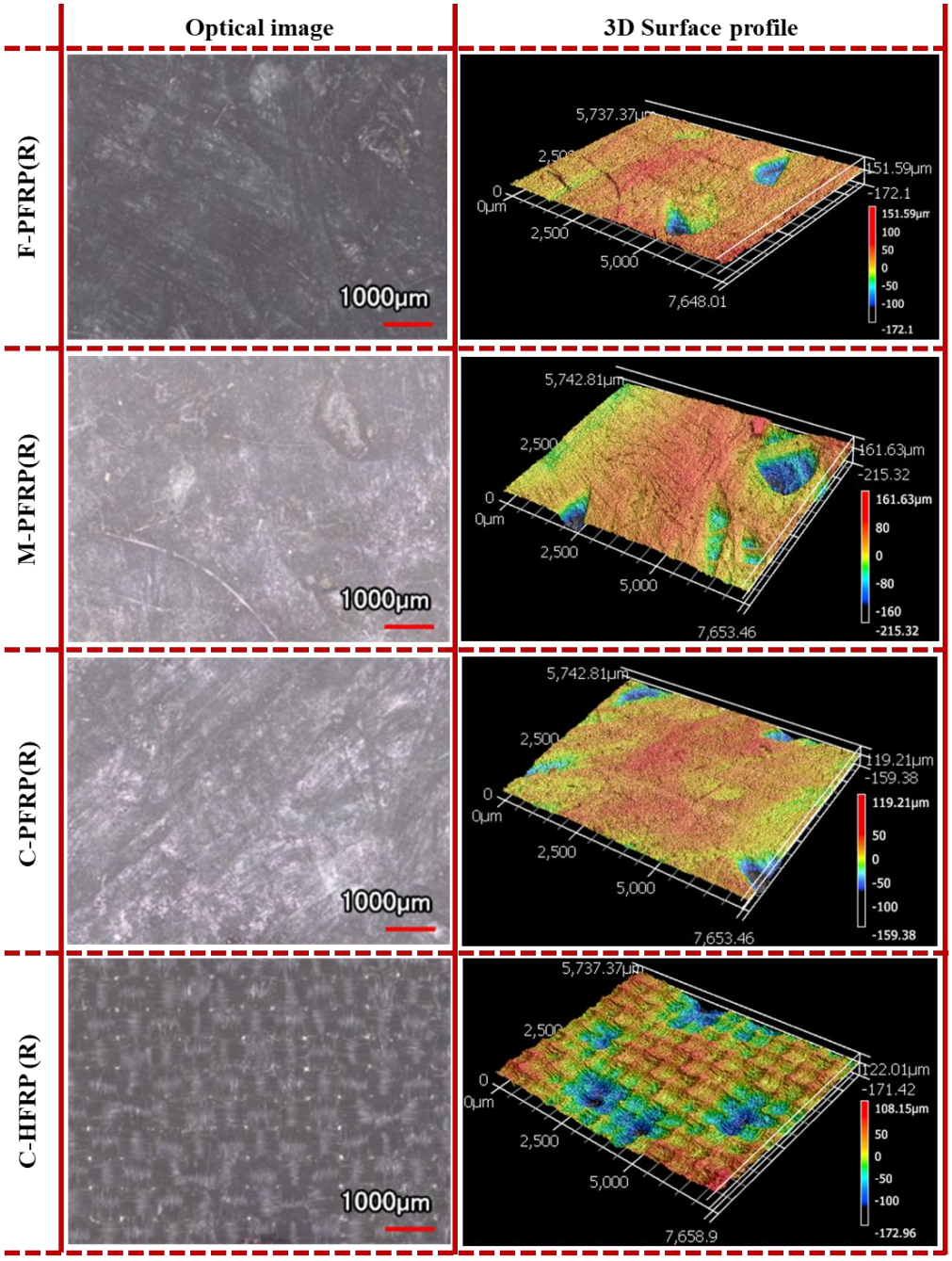
Optical image
3D Surface profile
F-PFRP(R)
M-PFRP(R)
C-PFRP(R)
C-HFRP (R)
1000µm
5,737.37µm
151.59µm
-172.1
5,742.81µm
161.63µm
-215.32
119.21µm
-159.38
122.01µm
-171.42
0µm
2,500
5,000
7,648.01
7,653.46
7,658.9

(a)

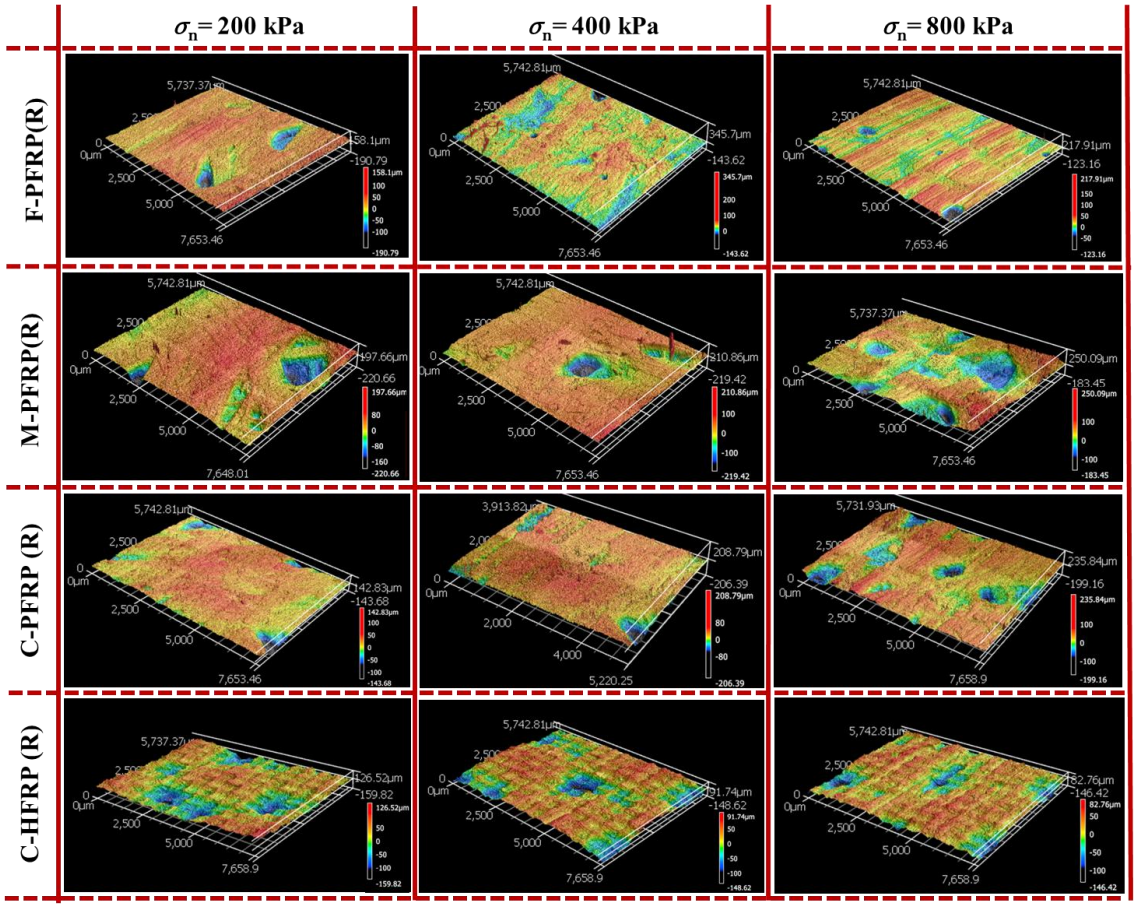

Height analysis

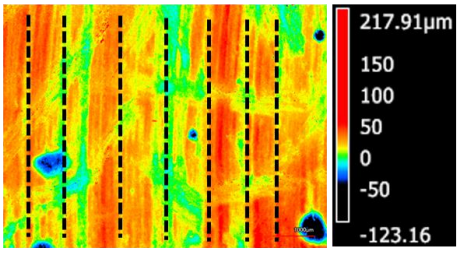

F-PFRP(R) 800 kPa

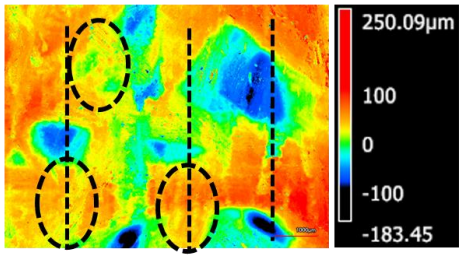

M-PFRP(R) 800 kPa

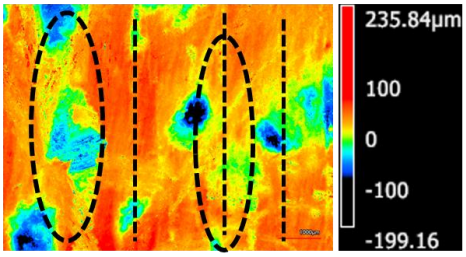

C-PFRP(R) 800 kPa

(b)

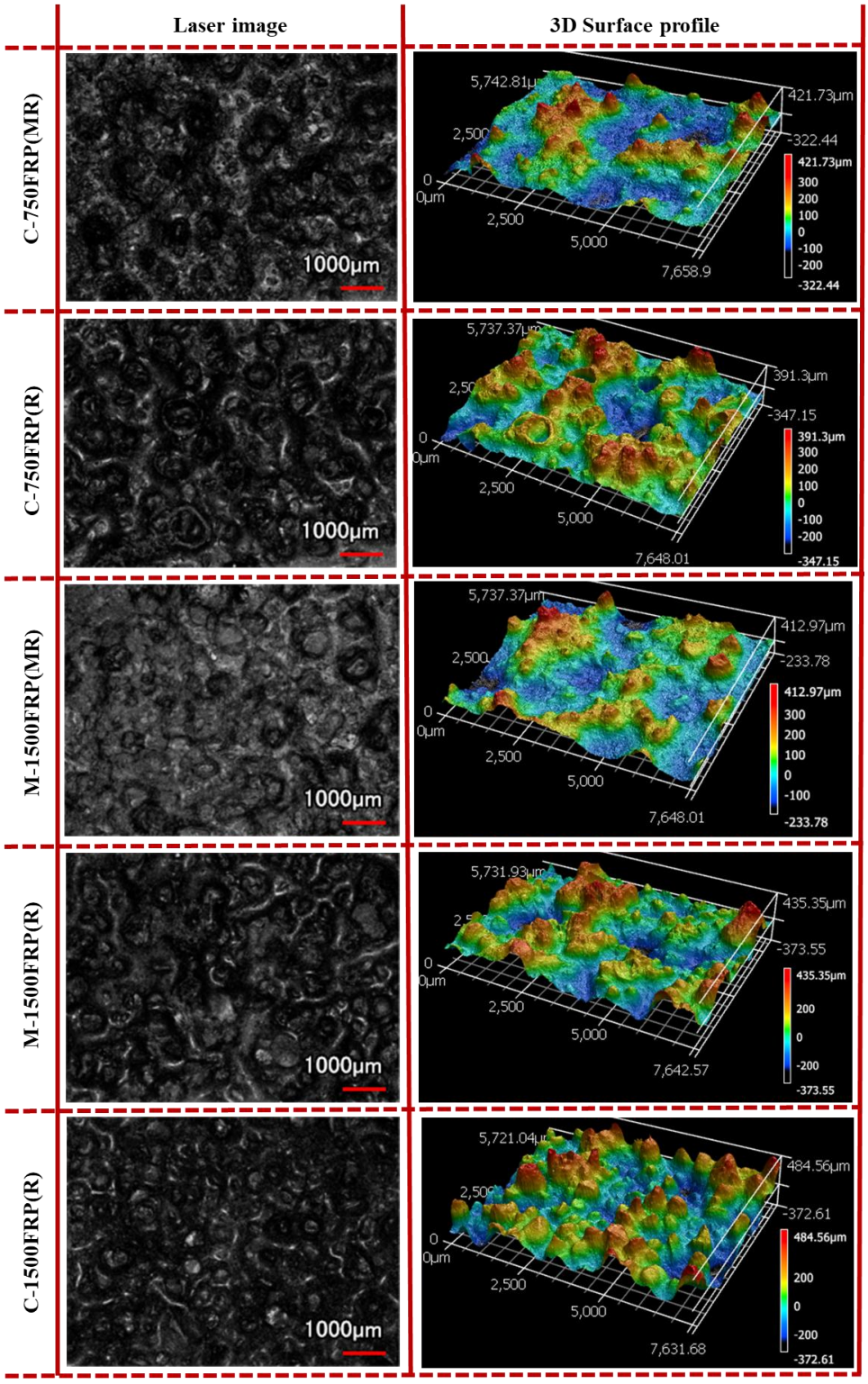
Laser image
3D Surface profile
C-750FRP(MR)
C-750FRP(R)
M-1500FRP(MR)
M-1500FRP(R)
C-1500FRP(R)
1000µm
5,742.81µm
421.73µm
-322.44
7,658.9
5,737.37µm
391.3µm
-347.15
7,648.01
412.97µm
-233.78
5,731.93µm
435.35µm
-373.55
7,642.57
5,721.04µm
484.56µm
-372.61
7,631.68

(c)

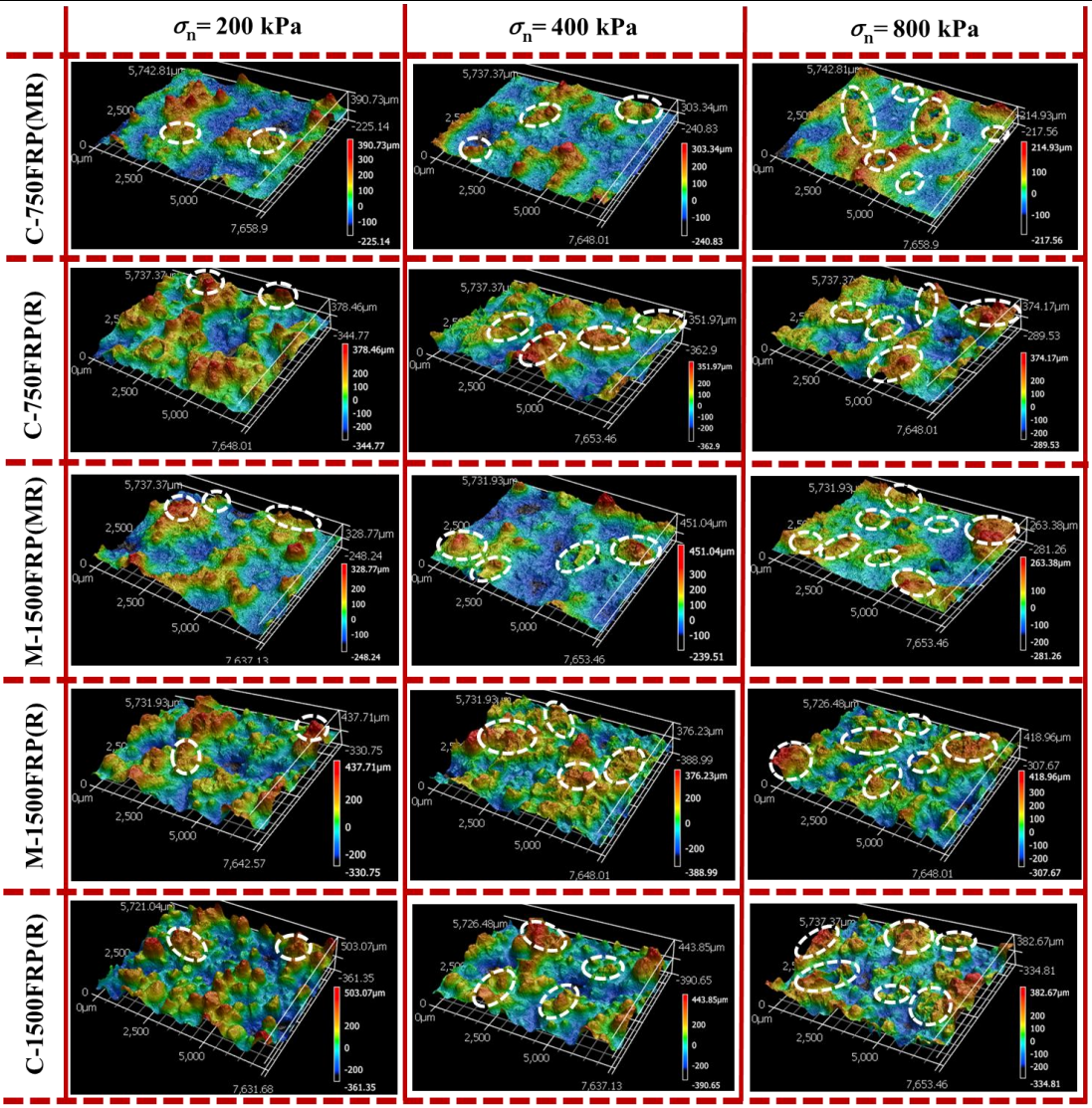
σ_n= 200 kPa
σ_n= 400 kPa
σ_n= 800 kPa
C-750FRP(MR)
C-750FRP(R)
M-1500FRP(MR)
M-1500FRP(R)
C-1500FRP(R)
Areas enclosed by the dashed ellipse or circle represent the degradation of peaks

(d)

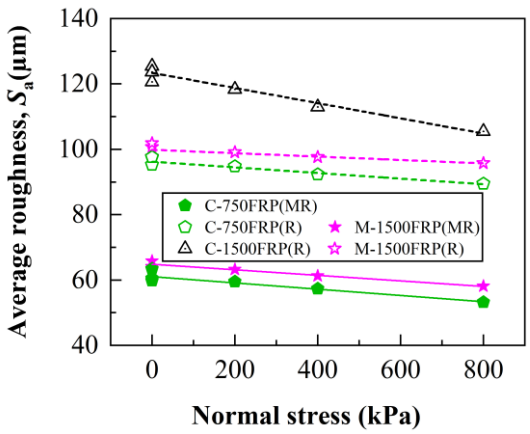
Average roughness, S_a(μm)
Normal stress (kPa)
C-750FRP(MR)
C-750FRP(R)
C-1500FRP(R)
M-1500FRP(MR)
M-1500FRP(R)

(e)

Figure 4-7 Optical image and 3D surface profile of uncoated GFRP (a) fresh specimens before testing and (b) specimens after interface direct shear tests; Laser image and 3D surface profile of sand-epoxied GFRP (c) fresh specimens before testing and (d) specimens after interface direct shear tests, and corresponding (e) average roughness variation under 200, 400, and 800 kPa normal stress

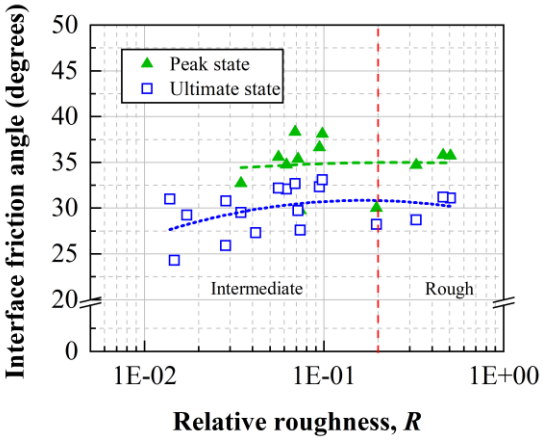

(a)

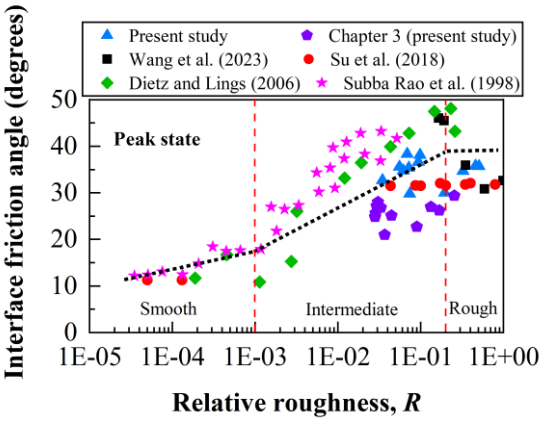

(b)

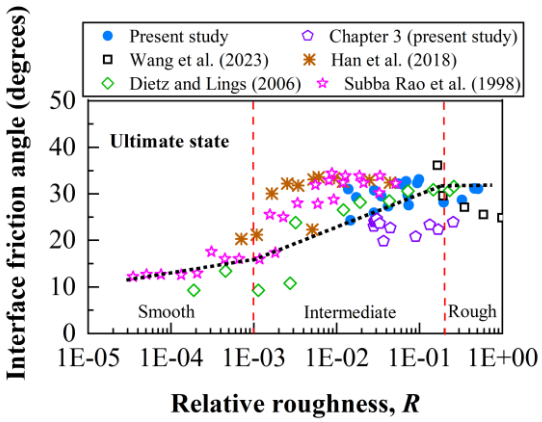

(c)

Figure 4-8 (a) Variation in interface friction angle with respect to relative roughness for fine, medium, and coarse sand against GFRP interfaces; comparison chart of interface friction angle (b) at peak state and (c) at ultimate state with respect to relative roughness between the present test and literature (dash line represents the trend of all the presented data; updated with minor modification in Figures 3-17(c) and 3-17(d) of Chapter 3)

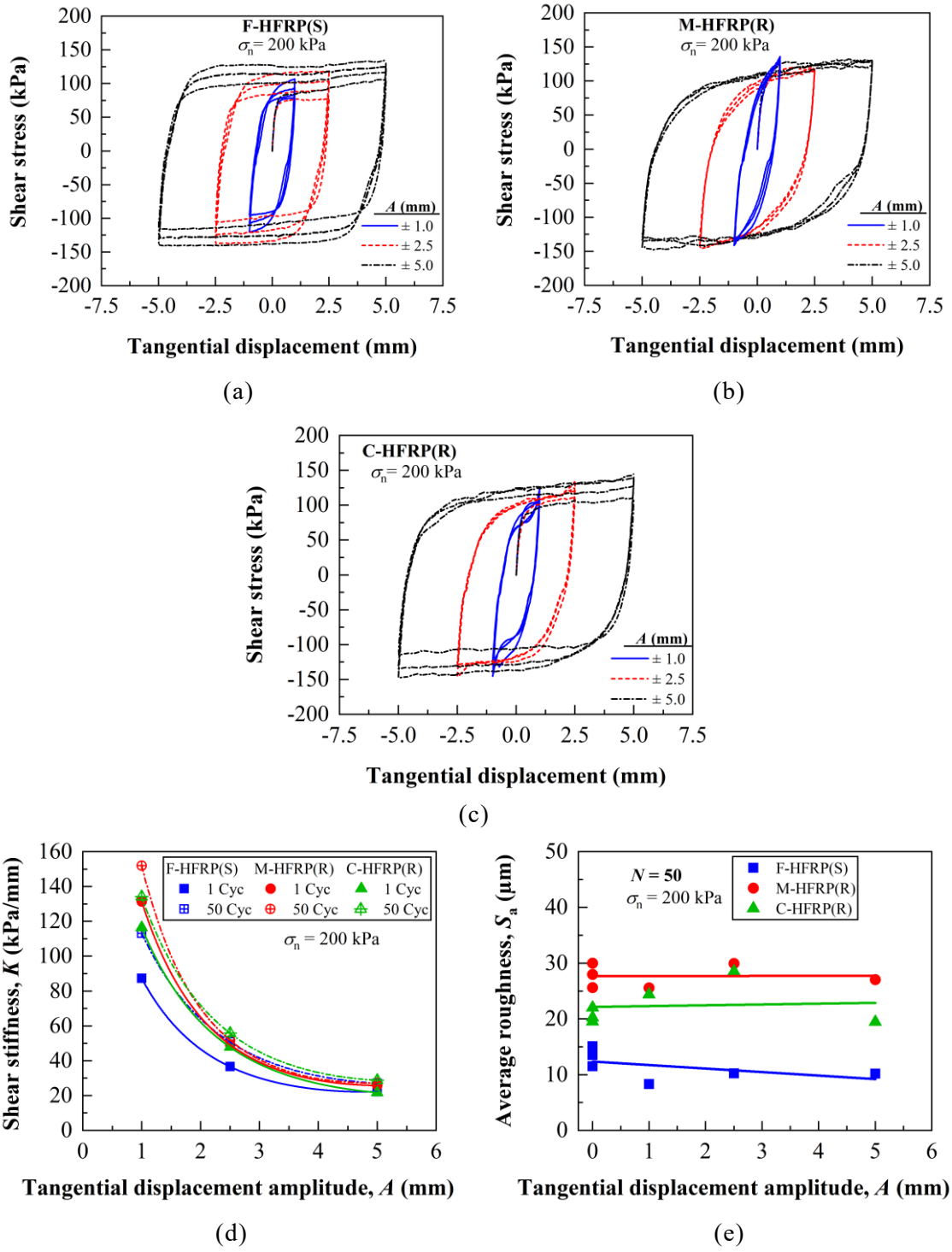

Figure 4-9 (a)-(c) Cyclic shear stress versus tangential displacement of fine sand-HFRP(S), medium sand-HFRP(R), and coarse sand-HFRP(R) interfaces, respectively, under 200 kPa normal stress at ±1.0, ±2.5, ±5.0 mm amplitude (cycle number 1, 5, and 50), and corresponding (d) shear stiffness versus tangential displacement amplitude for first and fiftieth cycle and (e) average roughness variation against tangential displacement amplitudes

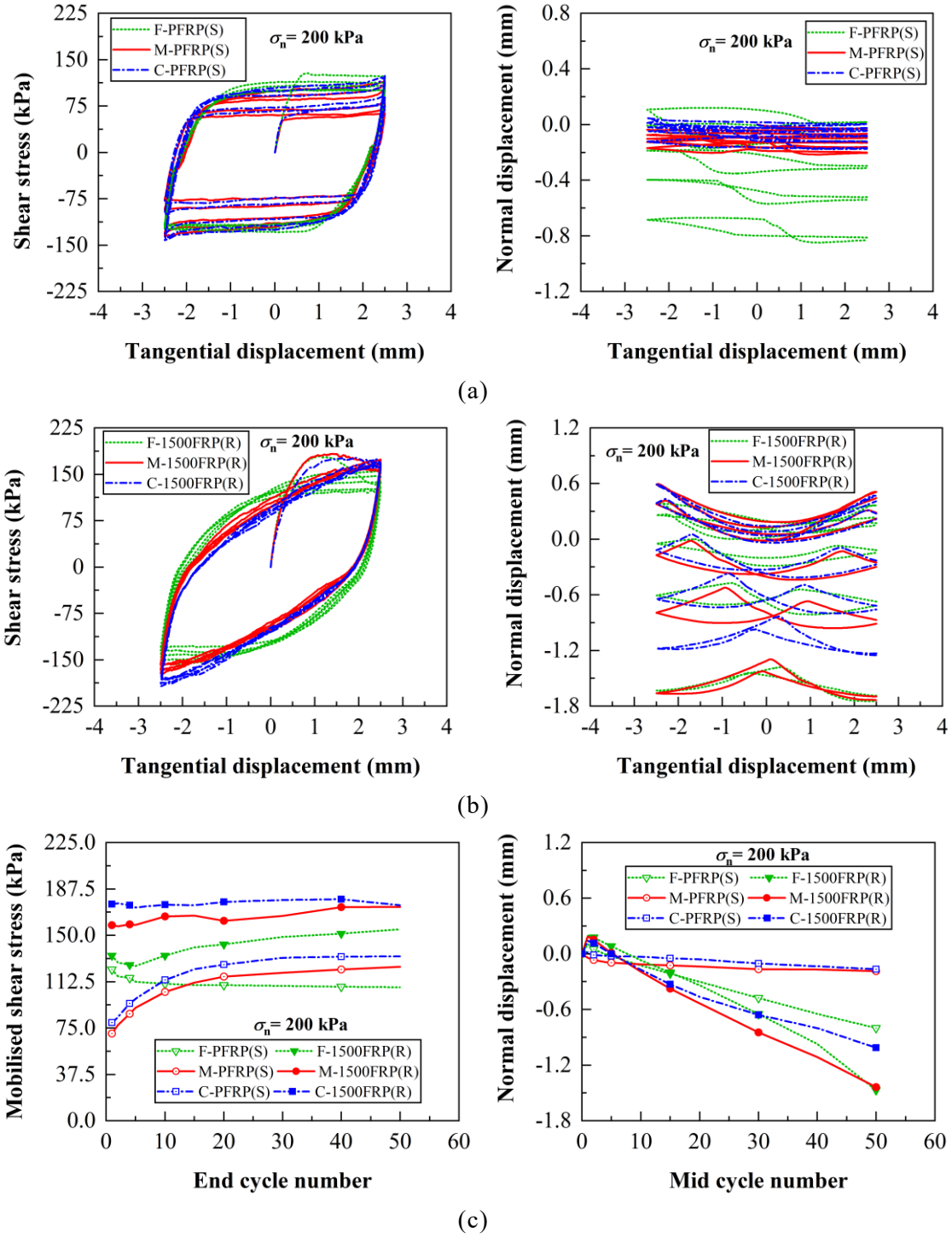

Figure 4-10 Cyclic response of particle sizes on (a) PFRP(S) and (b) 1500FRP(R) for first, fifth, fifteenth, thirtieth, and fiftieth cycles, data (a) and (b) are summarised in (c), which presents trends based on the 50 cycles

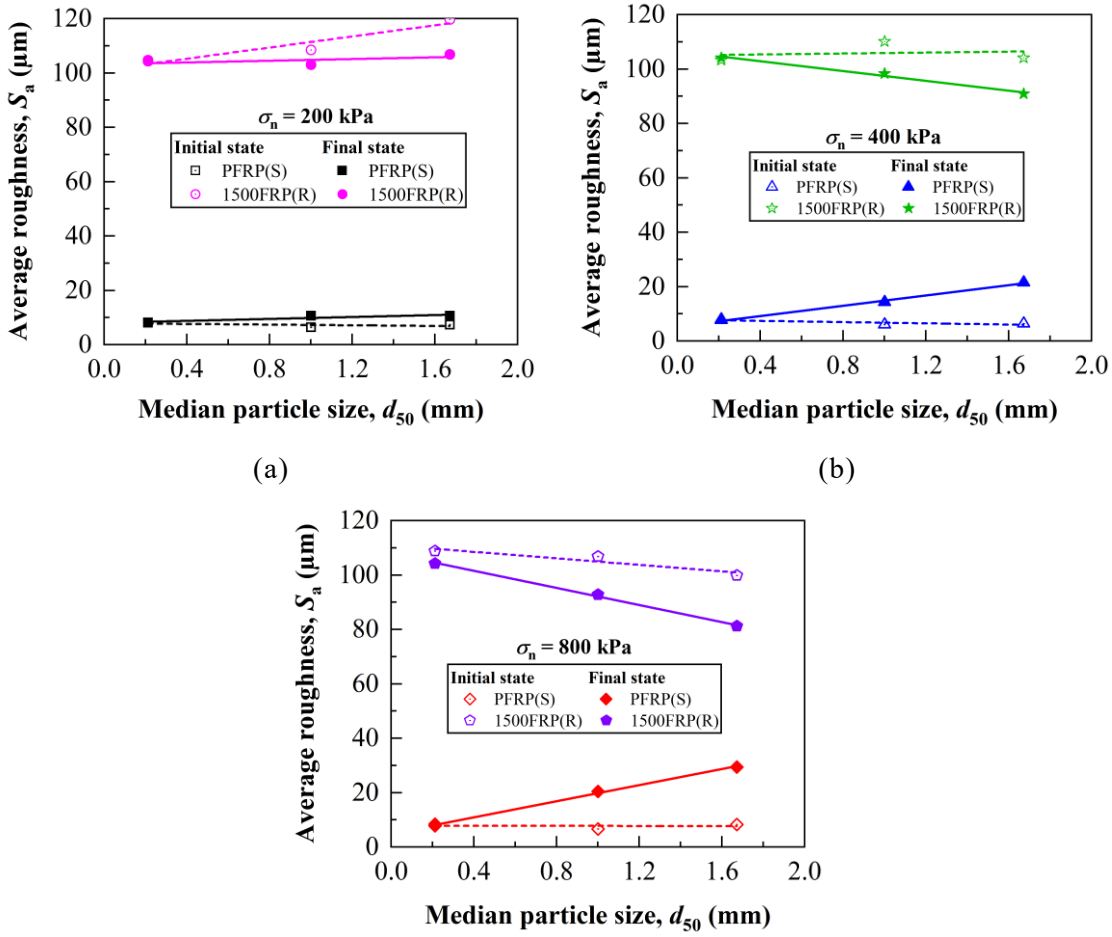

Figure 4-11 Variation in average roughness of PFRP(S) and 1500FRP(R) in cyclic interface tests after 50 cycle number with respect to median particle size under (a) 200 kPa, (b) 400 kPa, and (c) 800 kPa normal stress

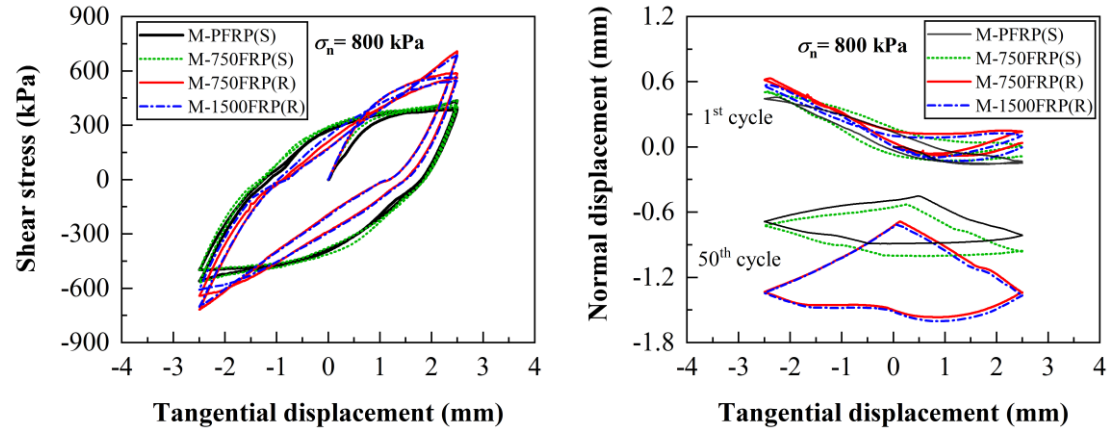

(a)

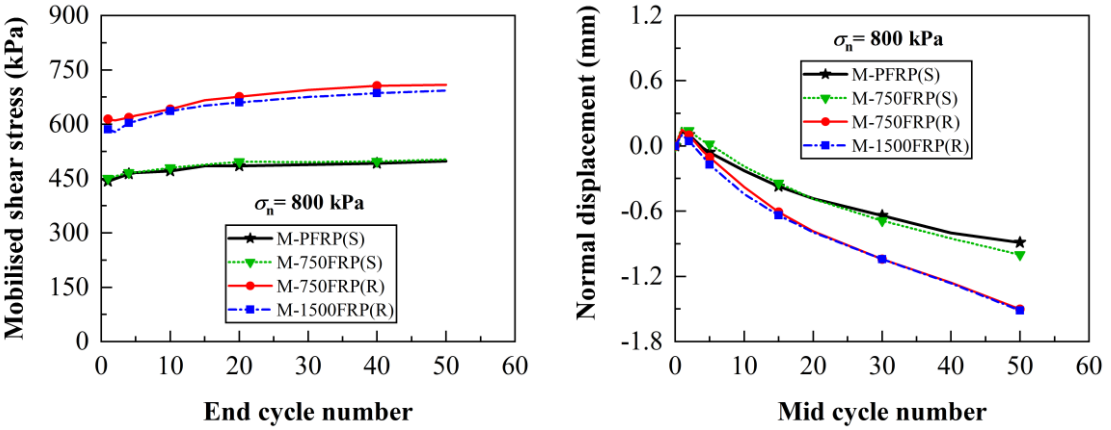

(b)

Figure 4-12 Effect of sand-epoxy coated surface roughness in cyclic response of (a) medium sand against PFRP(S) and sand-epoxied GFRP interface (first and fiftieth cycle), data (a) are summarised in (b), which presents trends based on 50 cycles

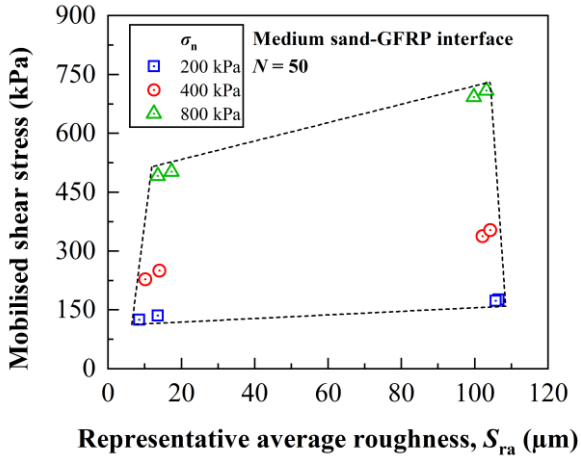

Figure 4-13 Mobilised shear stress versus representative average roughness at the

fiftieth cycle

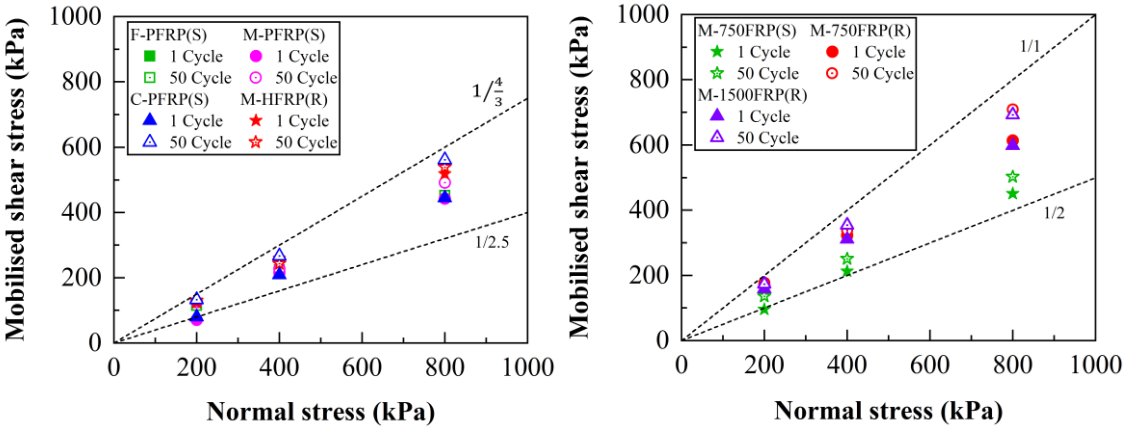

(a) (b)

Figure 4-14 Effect of normal stress on mobilised shear stress: (a) fine sand, medium sand, and coarse sand against uncoated GFRP, and (b) medium sand against sand-epoxied GFRP interfaces at the first and the fiftieth cycle

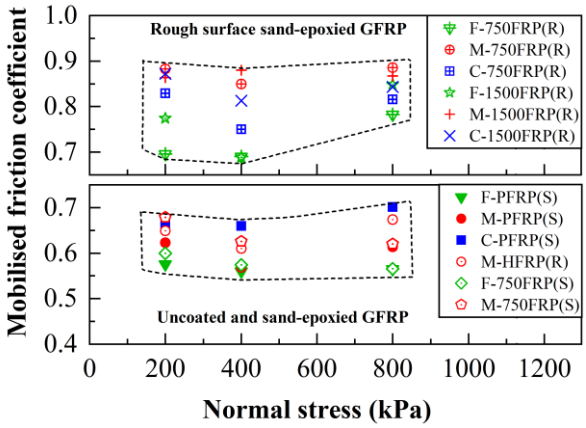

Figure 4-15 Variation in mobilised interface friction coefficient versus normal stress

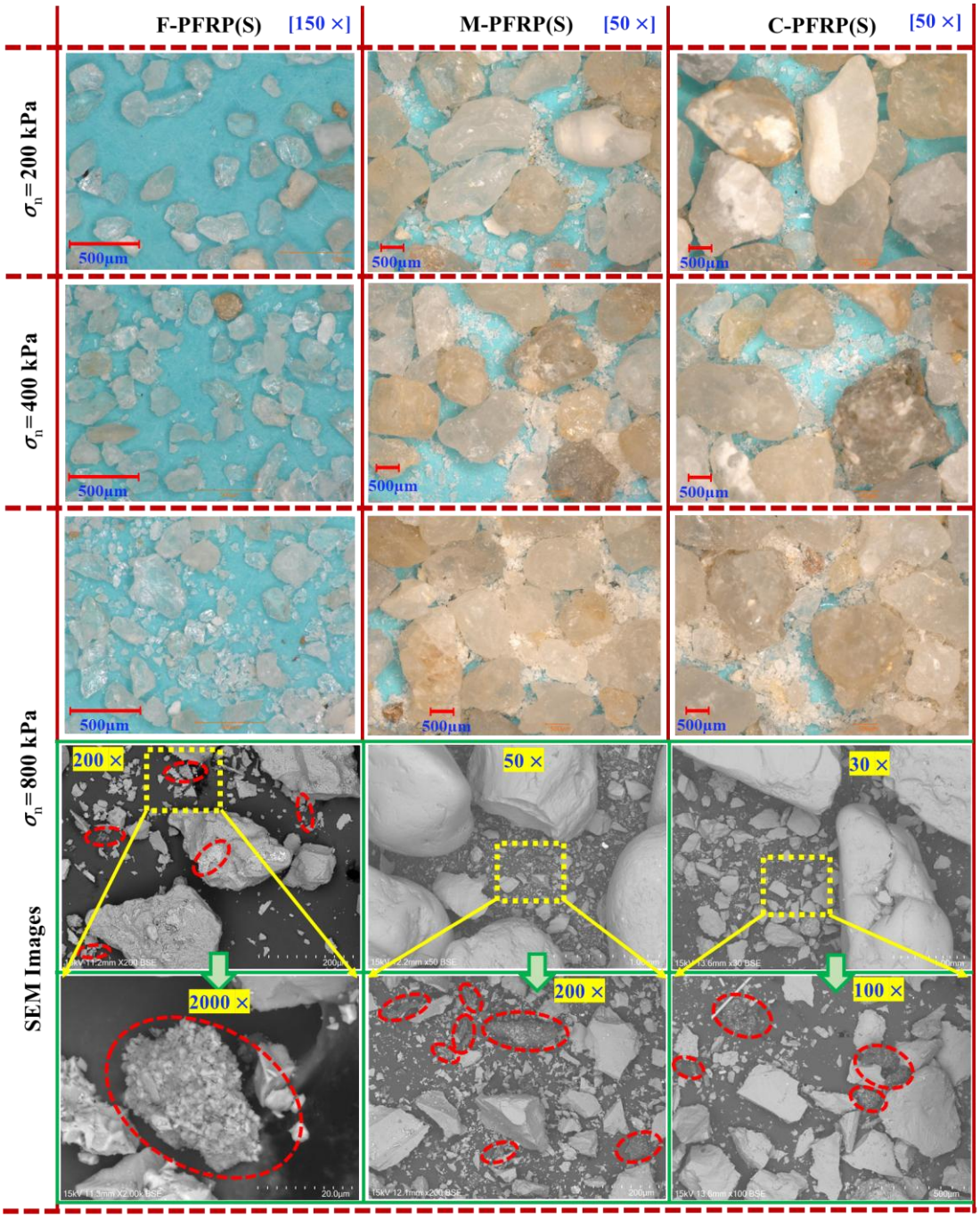
F-PFRP(S) [150 ×]
M-PFRP(S) [50 ×]
C-PFRP(S) [50 ×]
σn = 200 kPa
σn = 400 kPa
σn = 800 kPa
SEM Images
500μm
200 ×
50 ×
30 ×
2000 ×
200 ×
100 ×
Powder of epoxy dispersed along the interface or concentrated around the edges of interfaced sand particles

(a)

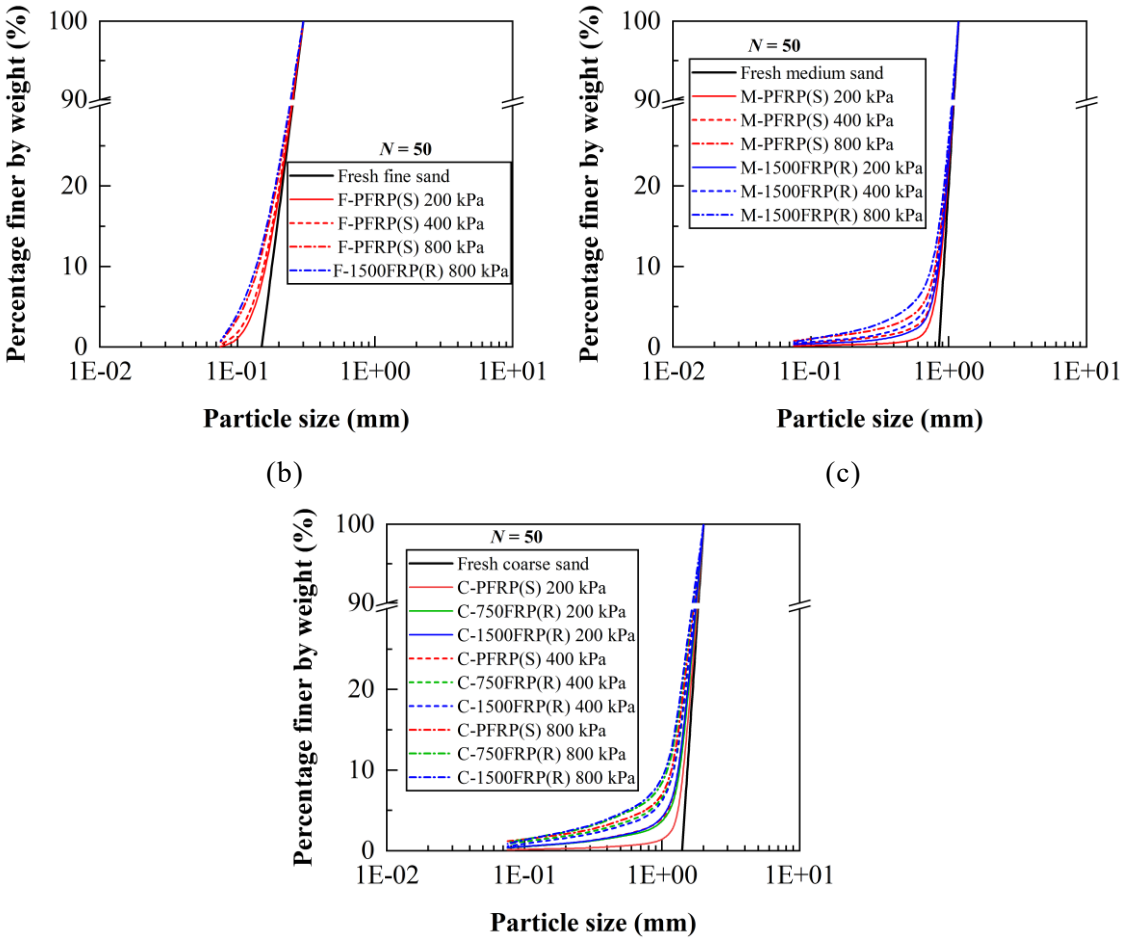

Figure 4-16 Magnified microscopic and SEM images showing breakage at the interface between PFRP(S) and all three sand types; particle size distribution curves before and after cyclic interface tests for (b) fine sand, (c) medium sand, and (d) coarse sand

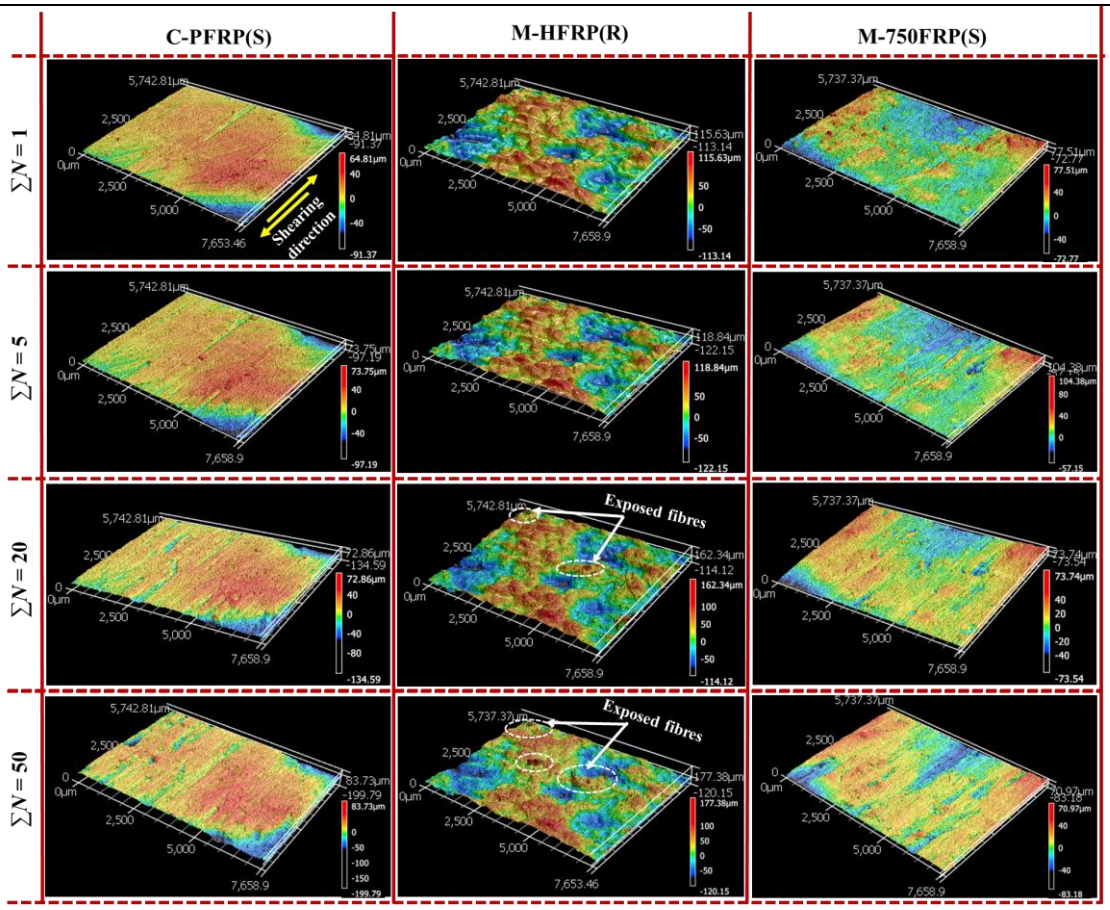

(a)

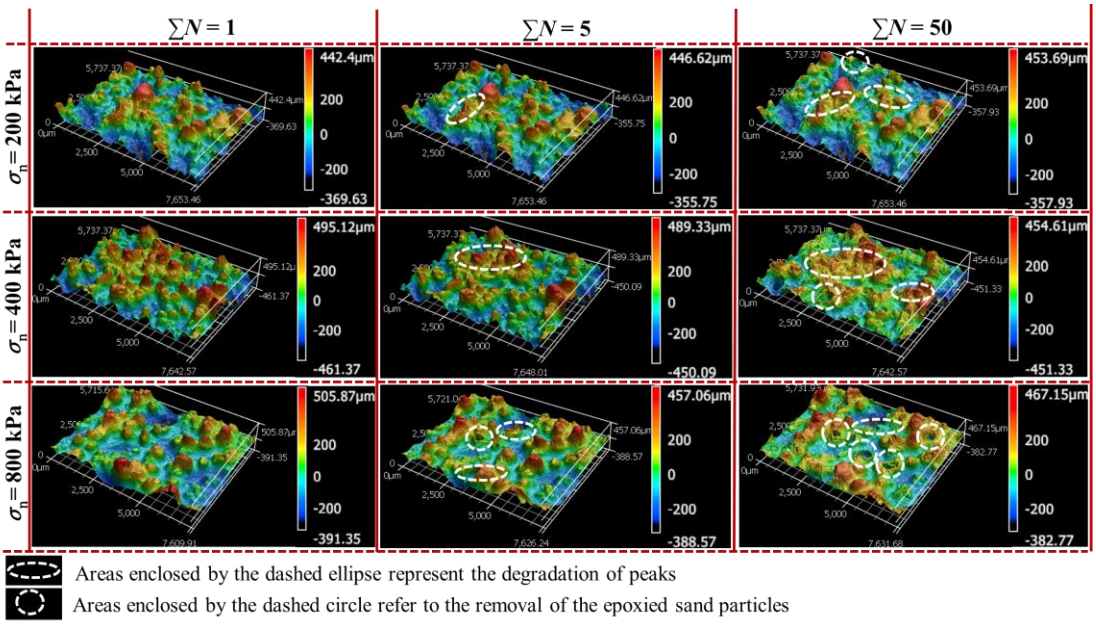

(b)

Figure 4-17 3D surface profiles of uncoated and sand-epoxied GFRP at various cumulative cycle numbers: (a) C-PFRP(S), M-HFRP(R), and M-750FR(S) interface

under 200 kPa normal stress, and (b) M-750FRP(R) interfaces under 200 kPa, 400 kPa, and 800 kPa normal stress

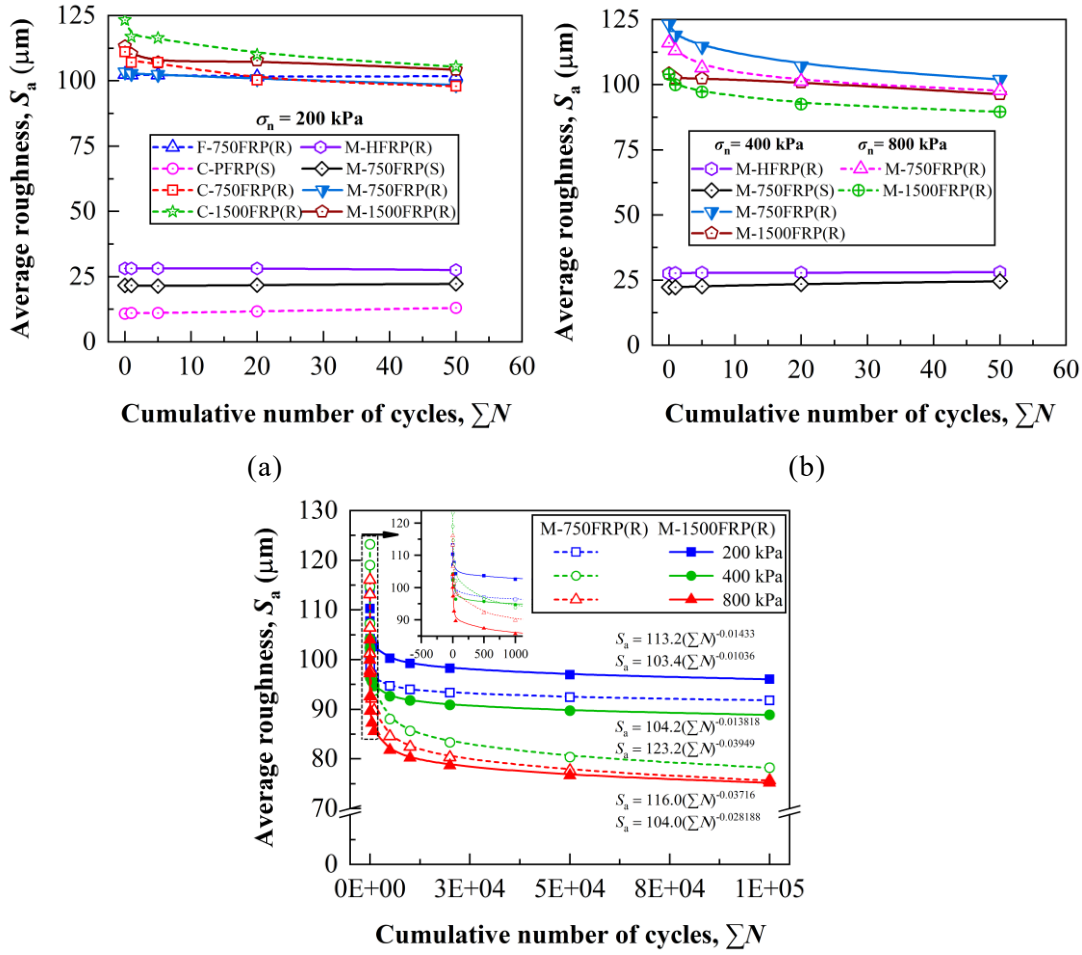

Figure 4-18 Effect of the cumulative number of cycles on variations in average roughness of GFRPs while shearing fine sand, medium sand, and coarse sand under (a) 200 kPa, (b) 400 kPa and 800 kPa normal stress; (c) average surface roughness decay for M-750FRP(R) and M-1500FRP(R) interfaces under cyclic shear loading, showing experimental data up to 50 cycles and extrapolated values up to 10^5 cycles using a power-law function (a B-spline curve is overlaid for visual continuity; power-law equations are shown in the figure)

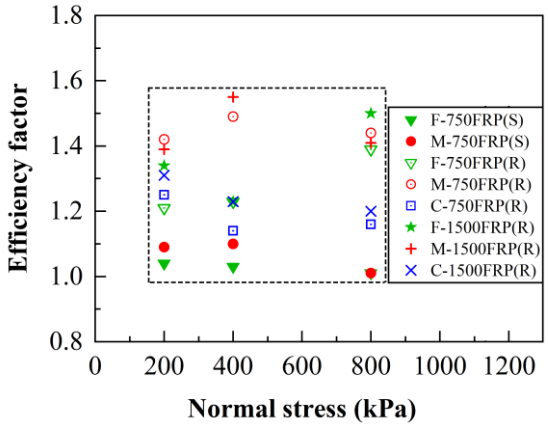

Figure 4-19 Variation in the efficiency factor for sand-epoxied GFRP with respect to normal stress

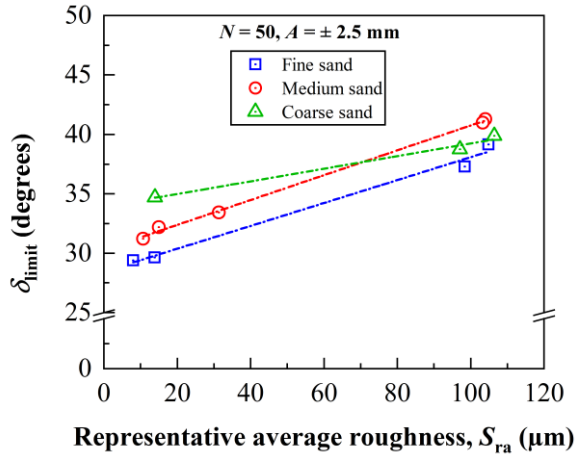

Figure 4-20 Limit state friction angle versus representative average roughness

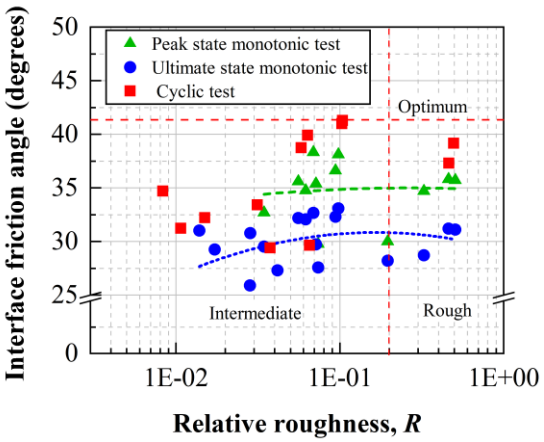

(a)

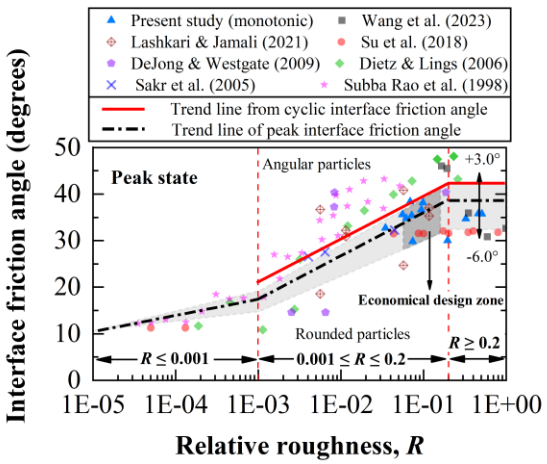

(b)

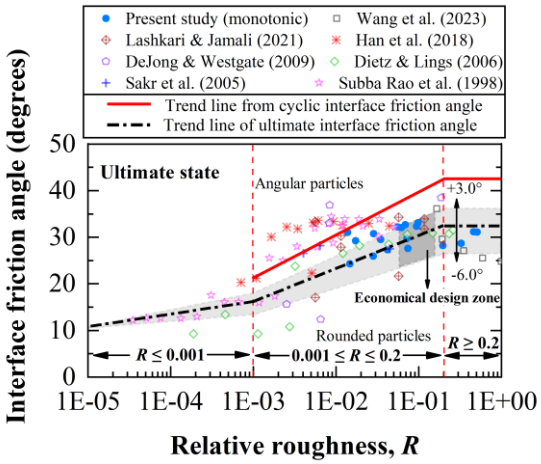

(c)

Figure 4-21 (a) Variation of interface friction angle for fine sand, medium sand, and coarse sand sheared against GFRP interfaces under monotonic and cyclic (at 50 cycles) shear loading; comparison of interface friction angles from the present study with previous studies, along with the generalised design chart for dense sand-GFRP interface: (b) peak state and (c) ultimate state (dashed dot line represent the trend of all the presented data and shaded zone represent generalised range for silica sand-GFRP interface based on closely aligned data)

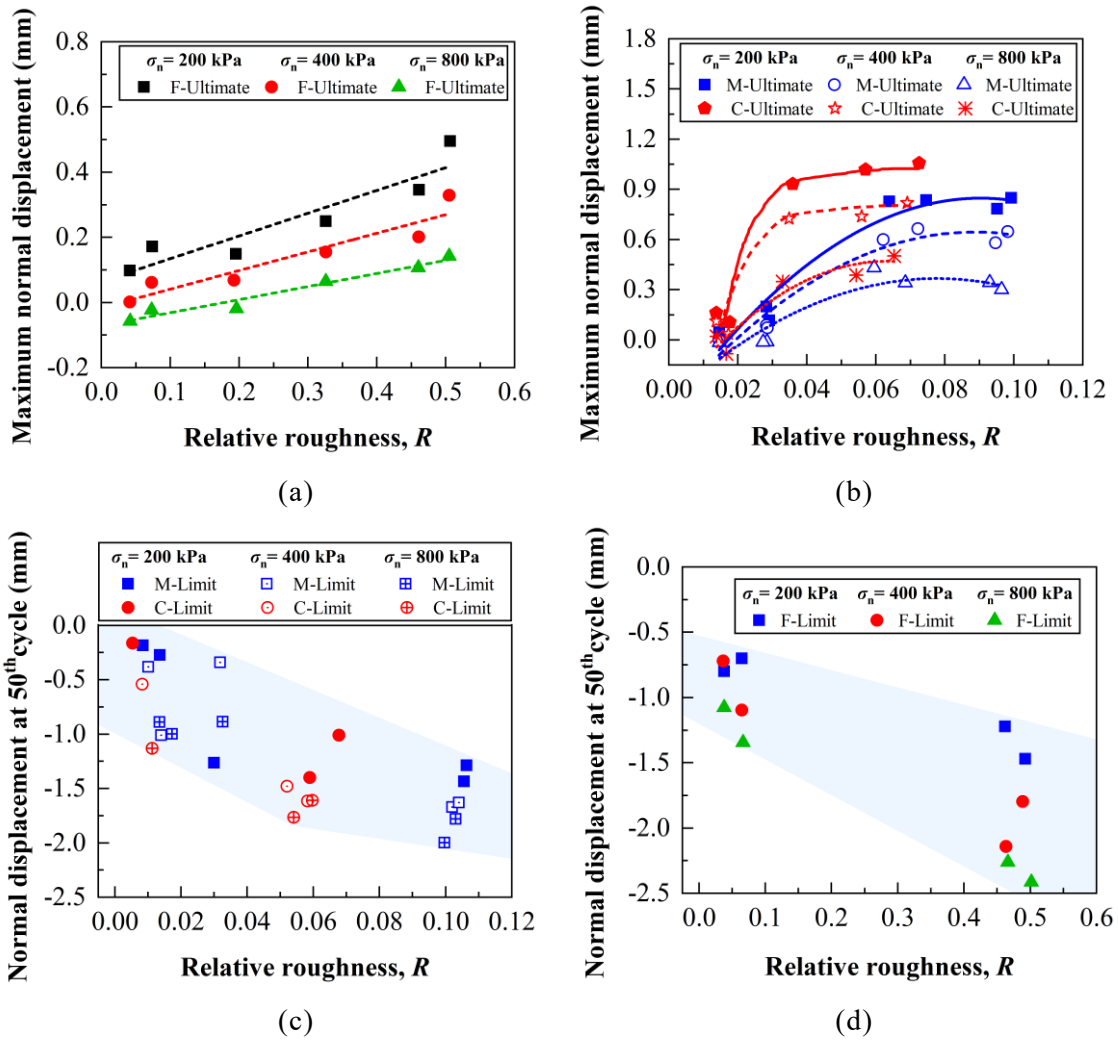

Figure 4-22 Variation in maximum normal displacement with respect to relative roughness for (a) medium and coarse sands, and (b) fine sand sheared against GFRP and sand-epoxied GFRP interfaces in monotonic shear tests; and (c) medium and coarse sands, and (d) fine sand sheared against GFRP and sand-epoxied GFRP interfaces in cyclic shear tests showing normal displacement at the middle of the fiftieth cycle

Table 4-1 Properties of the test sands

Sand	G_s	d_{50} (mm)	C_u	e_{max}	e_{min}	Morphology		
						C_{irc}*	R_{rd}*	R.F.*
Fine (F)	2.66	0.212	1.414	0.974	0.651	0.725	0.587	`1.085
Medium (M)		1.001	1.178	0.876	0.591	0.742	0.6316	1.076
Coarse (C)		1.673	1.195	0.831	0.572	0.761	0.693	1.069

Note: *Mean values.

Table 4-2 Properties and features of GFRP composites

GFRP group designation	GFRP ID	Particle size of epoxied sand, d (mm)	Amount of epoxied sand [Numeric term in ID] (g/m^2)	Surface type [Bracketed term in ID]	Vickers hardness (HV)		Initial average surface roughness range (μm)	
					Mean	SD	S_a	$S_{z,avg}$
Prepreg or dry hand lay-up GFRP	HFRP(S)	NA	0	Smooth	29.8	3.17	11.5–15.1	330.1–351.7
	HFRP(R)			Rough			19.5–41.7	232.6–273.7
Plain GFRP	PFRP(S)	NA	0	Smooth	36.0	2.47	6.0–10.9	143.7–214.7
	PFRP(R)			Rough	33.6	3.43	15.9–28.4	371.7–385.4
Sand-epoxied GFRP	750FRP(S)	0.1–0.8	750	Smooth	52.5	5.81	8.9–21.6	192.0–311.4
	750FRP(MR)	0.15–0.85	750	Medium rough	49.0	6.43	60.7–75.8	592.4–644.7
	1500FRP(MR)		1500		58.4	6.02	64.8–69.3	609.7–668.7
	750FRP(R)	0.3–0.85	750	Rough	58.5	5.39	95.6–123.2	745.5–884.4
	1500FRP(R)		1500		64.1	5.07	97.7–124.3	781.4–977.9

Note: ‘0’ refers to uncoated GFRP, which represents plain ‘P’, designated as PFRP and prepreg/dry hand lay-up ‘H’, designated as. ‘HFRP’; NA = not applicable; SD refers to standard deviation.

Table 4-3 Cyclic interface shear testing program

S.N.	Specimen ID	Sand type [First term in ID]	Number of cycles, N	Cyclic semi-amplitude, A_c (mm)	Normal stress (kPa)
1	F-HFRP(S)	Fine	50	1.0, 2.5, 5.0	200
2	M-HFRP(R)	Medium			
3	C-HFRP(R)	Coarse			
4	F-PFRP(S)	Fine	50	2.5	200, 400, 800
5	F-750FRP(S)				
6	F-750FRP(R)				
7	F-1500FRP(R)				
8	M-PFRP(S)	Medium			
9	M-HFRP(R)				
10	M-750FRP(S)				
11	M-750FRP(R)				
12	M-1500FRP(R)				
13	C-PFRP(S)	Coarse			
14	C-750FRP(R)				
15	C-1500FRP(R)				
16	F-750FRP(R)	Fine	1, 4, 15, 30	2.5	200
17	M-HFRP(R)	Medium			200, 400
18	M-750FRP(S)				200, 400
19	M-750FRP(R)				200, 400, 800
20	M-1500FRP(R)				200, 400, 800
21	C-PFRP(S)	Coarse			200
22	C-750FRP(R)				200
23	C-1500FRP(R)				200

Table 4-4 Summary of interface friction angle and evolution of surface properties in monotonic shearing

Interface materials	interface friction angle (degrees)		Roughness variation from linear fitting slope (%)		Efficiency factor of sand-epoxied GFRP
	Peak	Ultimate	ΔS_{a}	$\Delta S_{\mathrm{z,avg}}$	$E.F._{\mathrm{s-e\ GFRP}}$
F-PFRP(R)	29.78	27.58	-1.7	-8.4	1.0
F-HFRP(R)	30.01	28.22	2.9	1.3	1.01
F-750FRP(S)	n/a	27.30	-2.0	-1.0	n/a
F-1500FRP(MR)	34.72	28.73	-0.3	0.5	1.21
F-750FRP(R)	35.73	31.10	-0.2	1.0	1.25
F-1500FRP(R)	35.89	31.25	0.4	-3.5	1.26
M-PFRP(R)	n/a	30.80	1.3	17.2	n/a
M-HFRP(R)	n/a	25.92	-9.9	0.8	n/a
M-750FRP(S)	n/a	24.29	3.6	8.0	n/a
M-750FRP(MR)	35.39	29.74	-12.5	-12.9	n/a
M-1500FRP(MR)	34.76	32.08	-10.5	-14.1	n/a
M-750FRP(R)	36.63	32.32	-4.0	-2.4	n/a
M-1500FRP(R)	38.13	33.10	-4.2	-5.5	n/a
C-PFRP(R)	n/a	31.01	-1.7	15.7	n/a
C-HFRP(R)	n/a	29.25	-8.7	-13.2	n/a
C-750FRP(MR)	32.71	29.52	-12.6	-20.7	n/a
C-750FRP(R)	35.6	32.19	-7.2	-10.0	n/a
C-1500FRP(R)	38.33	32.68	-14.1	-14.2	n/a

Note: n/a refers to not available.

Table 4-5 Comparative table of mobilised friction coefficient and roughness variation

Interface materials	Normal stress (kPa)	Mobilised interface friction coefficient (N = 50, A_c = 2.5 mm)	Efficiency factor based on PFRP(S)	Roughness variation ΔS_a	
	σ_n	$\tan\delta_{\text{limit}}$	$E.F._{\text{s-e GFRP}}$	(%)	Trends
F-PFRP(S)	200, 400, 800	0.576, 0.56, 0.565	1.0, 1.0, 1.0	-0.89, -3.76, -6.46	Decreases
F-750FRP(S)		0.6, 0.574, 0.566	1.04, 1.03, 1.01	1.33, 4.42, 4.84	Increases
F-750FRP(R)		0.696, 0.69, 0.783	1.21, 1.23, 1.39	0.53, 0.28, -1.33	Negligible
F-1500FRP(R)		0.774, 0.689, 0.848	1.34, 1.23, 1.50	-0.35, 0.89, -4.23	Decreases
M-PFRP(S)	200, 400, 800	0.623,0.569, 0.614	1.0, 1.0, 1.0	66.6, 136.4, 207.7	Severely increases
M-HFRP(R)		0.649, 0.61, 0.674	1.04, 1.07, 1.09	-0.2, -4.92, 14.38	Mixed
M-750FRP(S)		0.679, 0.626, 0.62	1.09, 1.10, 1.01	16.4, 50.9, 49.8	Moderately increases
M-750FRP(R)		0.883, 0.85, 0.886	1.42, 1.49, 1.44	-4.26, -6.28, -16.1	Decreases
M-1500FRP(R)		0.864, 0.88, 0.867	1.39, 1.55, 1.41	-4.99, -10.7, -13.1	Decreases
C-PFRP(S)	200, 400, 800	0.665, 0.66, 0.701	1.0, 1.0, 1.0	45.1, 240.0, 255.9	Severely increases
C-750FRP(R)		0.829, 0.75, 0.816	1.25, 1.14, 1.16	-6.65, -15.8, -17.3	Decreases
C-1500FRP(R)		0.872, 0.813, 0.843	1.31, 1.23, 1.20	-10.9, -12.7, -18.7	Decreases

CHAPTER 5: DEM INVESTIGATION OF MONOTONIC SHEAR BEHAVIOUR AT THE SAND-GFRP INTERFACE

5.1 Introduction

Limitations in existing apparatus have constrained the comprehensive analysis of sand-GFRP interface contact mechanisms, restricting laboratory investigations of its micromechanical behaviour. The DEM has proven effective in examining microscopic interactions across various interfaces, including sand-steel (Jing et al., 2018; Wang and Yin, 2022), sand-geotextile (Feng et al., 2020; Feng et al., 2022; Jia et al., 2024), and sand-geomembrane (Feng et al., 2018), through interface direct shear test (IDST) simulations. By tracking particle behaviours such as rotation, slipping, shear zone development, and fabric evolution, DEM provides critical insights into the sand-GFRP interface at the particle scale. However, DEM alone struggles to fully capture FRP deformation, necessitating advanced modelling approaches. The Edinburgh-Elasto-Plastic-Adhesion (EEPA) contact model (Morrissey, 2013), implemented in PFC (Coetzee, 2020), offers a promising enhancement by better simulating sand-GFRP interactions. Utilising overlapped ball models to characterise surface roughness, this approach effectively incorporates sand-epoxy coatings and diverse roughness profiles. DEM simulations provide a more comprehensive understanding of sand-GFRP interface behaviour by accurately capturing particle-shape interactions and roughness evolution.

This study applies DEM to investigate the shear behaviour of sand-GFRP interfaces, focusing on the effects of epoxied sand coatings. The surface characteristics of uncoated and sand-epoxied GFRP (500-1500 g/m^2) are simulated using two layers of overlapped balls, calibrated against experimental results to establish accurate contact properties. Interface tests are conducted on

plain and sand-epoxied GFRP using fine and medium sand particles under loose and dense conditions. Particle shapes are approximated through both conventional spherical and alternative ellipsoidal models. Simulations under constant normal stresses of 50, 100, and 200 kPa yield crucial micromechanical insights into interface shear behaviour and surface roughness evolution, advancing the understanding of complex sand-GFRP interactions.

5.2 Materials

5.2.1 Modelling of sand particles

Two sand types with uniform particle size distributions of 0.15–0.3 mm and 0.85–1.18 mm, designated as fine (F) and medium (M) sands, were used in this study (Figure 5-1). The mean particle sizes are 0.225 mm and 1.015 mm for fine and medium sands, respectively. The study assumes spherical particle shapes for baseline simulations. Additionally, as a special case, ellipsoids were modelled as clumps of three overlapping spheres (pebbles) to approximate natural grain morphology, as shown in Figure 5-1. The major radii of these ellipsoids were scaled up by factors of 1.270 for fine sand and 1.113 for medium sand relative to the radius of sand particles ($D_{50}/2$). A random particle generation algorithm was implemented to distribute particles within the domain. The experimental particle size range was discretised into ten slices, each representing a 10% interval from 0–100% passing, to ensure randomness while maintaining a uniform particle size distribution, as shown in Figure 5-1(c).

A quantitative comparison of particle morphology is provided in Table 5-1. The DEM particles show circularity (i.e., diameter ratio of the largest inscribed circle to the minimum circumscribed circle in the 2D projected image; Wadell, 1932; Liu et al., 2019), diameter values comparable to experimental measurements, indicating effective shape approximation in two dimensions. However, the sphericity (Vangla and Latha, 2015) of the ellipsoids is 0.972 for fine sand and 0.989 for medium sand is higher than the experimental values of 0.852 and 0.924. This increase results from the smooth and regular surfaces of

the ellipsoidal clumps, except for minimal concavities around the overlapped zone; ellipsoids lack the angularity and surface irregularities present in natural grains. Despite this, the clumped ellipsoids provide a simplified and computationally efficient representation of particle morphology suitable for capturing micromechanical behaviour in DEM simulations.

5.2.2 Modelling of GFRP composites

Plain or uncoated GFRP and sand-epoxied GFRP with epoxied sand concentrations varying from 500 to 1500 g/m^2 were modelled using a bonded assembly of 2 mm diameter spheres arranged in two layers, as depicted in Figure 5-2. A similar approach, as demonstrated by Feng et al. (2018) in Figure 2-20, can be adapted to simulate the FRP and approximate the various rough surface characteristics of FRP with sand-coating. Through iterative calibration, the centre-to-centre overlapping length (l) can be approximated using Equations (2-5a) and (5-1) to (5-3), ensuring that the simulated surface roughness aligns with the experimental conditions, whether in terms of average roughness or average maximum roughness (Uesugi et al., 1988; DeJong and Westgate, 2009; Feng et al., 2018).

$$R_{\mathrm{n}} = \frac{R_{\max}\,(L_{\mathrm{G}} = D_{50})}{D_{50}} \tag{5-1}$$

$$R_n = \frac{R_{max}}{D_{50}} = \frac{(R_{\mathrm{GFRP}} + r) - \sqrt{(r + R_{\mathrm{GFRP}})^2 - \frac{l^2}{2}}}{2r} \tag{5-2}$$

$$l = D_{50}\sqrt{2\left(1 + \frac{2R_{\mathrm{GFRP}}}{D_{50}}\right)R_n - 2{R_n}^2} \tag{5-3}$$

Herein, R_{n} refers to the normalised roughness, $R_{\max}$ refers to the maximum roughness, L_{G} refers the gauge length, l refers centre-to-centre overlapping length, D_{50} refers to mean particle size, R_{GFRP} refers to the radius of the GFRP ball, and r refers to the radius of sand particles ($D_{50}/2$). For semi-rigid surfaces such as GFRP, variations in surface roughness following interface shearing have

been observed in experimental studies (He et al., 2021; Teng et al., 2024).

The complexity increases with sand-epoxy coatings, where sand provides brittle bonding, and epoxy offers ductile bonding, allowing for roughness to increase or decrease. The EEPA model is particularly valuable because it allows for the simulation of these nuanced surface changes through its ability to represent plastic deformations and nonlinear force-displacement behaviour (Morrissey, 2013). The assembly of GFRP utilises the overlapped balls model in two layers and the EEPA contact model in PFC, which addresses regular surfaces with a wide range of roughness (Morrissey, 2013; Feng et al., 2018). By incorporating plastic overlap between the contact balls and considering material toughness as a primary parameter, the EEPA model offers a realistic representation of wear and abrasion processes. This is achieved by varying the overlapped distance in response to the shear forces generated during interface shearing and transmitted through sand particles to the GFRP balls, while recognising that only plastic deformation is measurable under field conditions (Archard, 1953; Morrissey, 2013; Choudhry et al., 2024).

An illustration of the DEM simulation flowchart for the sand-GFRP interface shear test is provided in Appendix C (Figure C-1). The procedure includes model setup, material and contact law assignment, loading application, shear simulation, and model calibration to ensure an accurate representation of the sand-GFRP interface shear test.

5.3 Modelling of the sand-GFRP interface direct shear tests

5.3.1 Indentation simulation in GFRP

The identification of FRP balls' shear modulus becomes convenient using the EEPA model. The test results of Vickers' hardness testing are used to simulate indentation tests in the DEM model. The mean indentation diagonals of 5 different GFRPs, as shown in Table 5-2, are used to compute the equivalent depth of a steel ball having a 60 μm diameter. The indentation simulation is performed by pushing the steel ball into the GFRP ball, which has a diameter of 2 mm. Note

that the pushing force of 1N, similar to the test load, is used till a minimum time of loading and unloading for all cases. From the several trial tests with the minimum loading-unloading cycle time and estimated values of shear modulus, the best-matched shear modulus is obtained when the indenter depth of the steel ball's indentation depth is equivalent to the mean indentation diagonal. The corresponding values of the shear modulus of each GFRP type are presented in Table 5-2. Figure 5-3 depicts the indentation simulation images at three different steps of steel ball indenting for the PFRP(R) case and the plot of plastic overlap of the steel ball on five GFRP types.

5.3.2 Generation of the sand-GFRP interface model

Three-dimensional DEM simulations are conducted using the particle flow code (PFC^{3D}) software on a 13th Gen Intel® Core™ i9-13900K computer. Based on the findings of Jacobson et al. (2007), who reported that an L/D_{50} ratio of ≥ 33 results in a well-defined shear band, and Feng et al. (2018), who observed that a sand specimen with a length 35 times D_{50} and height 10 times D_{50} yielded shear band thicknesses between 2.7D_{50} and 4.4 D_{50} at the sand-geomembrane interface, the present study adopts specimen sizes of 60 mm (length) × 35 mm (width) × 18 mm (height) for medium sand, and 11.5 mm (length) × 11.5 mm (width) × 4 mm (height) for fine sand (Figure 5-4). The fine sand specimen is significantly reduced from the experimental size of 60 mm (length) × 60 mm (width) × 18 mm (height) to fit within the computational limits. Both medium and fine sand models were designed for a 10 mm interface shear, consistent with the experimental setup. The interface model includes four fixed boundaries for the sand, with all particles generated over the GFRP plate, which is modelled with two layers of balls and supported by five fixed walls. Finally, a clump loading plate, represented by overlapped small-diameter spheres, is placed on top of the sand specimen, as illustrated in Figure 5-4.

In the 3D model, the linear rolling resistance contact model (e.g., Hou et al., 2021; Wang and Yin, 2022; Feng et al., 2022) is used for sand particles and between soil particles and GFRP; however EEPA contact model is used for GFRP.

Also, a linear contact model is adopted between sand particles and walls and between sand particles and loading plates. These contact models are applied to achieve a stable state with a large number of model cycles before applying constant normal loading on the top plate.

Loose and dense specimens are simulated for both fine and medium sand with a predefined initial void ratio obtained after calibration. Since it is very sensitive to attaining a similar loose packing state as in experimental conditions because of particle size and shape constraint (Wang et al., 2022a; Zhou and Xu, 2025), loose packing is obtained by considering initial interparticle friction at 1.0. However, dense packing is obtained by setting interparticle friction to 0.2. After the contact forces reach a stable state, initial compression is achieved with applied normal stress. As the model attains the next stable state after initial compression, the friction coefficient values are changed to final values, and the final cycling is carried out until the particle equilibrium state, i.e., an unbalanced force ratio smaller than 0.001, is achieved prior to shearing. For interface shearing, the bottom GFRP plate moves with a shearing velocity of 0.05 m/s in the positive X-axis until the displacement of 10.0 mm. To observe the deformation of GFRP at the sand-GFRP interface during shearing, the top layer of GFRP balls, which is free to move in the vertical direction, experiences an induced resisting shear force. This force results in continuous overlap between the top layer and the fixed bottom layers of GFRP balls, with the interaction persisting throughout the duration of the interface shearing process. During shearing, both micromechanical and macromechanical responses are recorded.

5.3.3 Model calibration and simulation scheme

Previous studies found that the friction coefficient and rolling resistance friction coefficient have significant effects on peak and ultimate interface strength as well as volumetric behaviour (e.g., Huang et al., 2014; Feng et al., 2018; Wang and Yin, 2022). Through several trial tests with varying initial void ratios, GFRP roughness, and combinations of friction and rolling friction coefficients, the simulation results that best matched the experimental findings of Chapter 3 for

the interface shear test under a 50 kPa normal stress are identified. The approach ensuring uniform packing prior to shearing across stress levels maintains comparable initial conditions and fabric across simulations while enabling meaningful extrapolation of the calibrated model to higher stress regimes. While the approach assumes stress-independent contact parameters, it may introduce minor uncertainties related to stress-dependent contact behaviour or subtle changes in fabric evolution. These calibrated parameters are presented in Table 5-3 and are based on the first eight interfaces listed in Table 5-3. Based on the calibrated initial void ratio values, the total number of spherical particles for dense and loose specimens of fine sand is about 60,000 and 57,500, respectively. The total number of spherical particles for dense and loose specimens of medium sand is about 41,500 and 39,000, respectively. For the special case of ellipsoid particles, almost a three times increase in pebbles number compared to spherical particles.

Table 5-3 provides a summary of the calibrated parameters used in the DEM simulation model. The particle densities for silica sand and GFRP particles are set to 2650 kg/m^3 (Huang et al., 2019; Wang et al., 2022a) and 1800 kg/m^3, respectively, reflecting the characteristics of real materials. In previous studies, the values for normal and shear stiffness in simulations have varied widely, ranging from 10^5 to 10^{10} N/m. The ratio of normal to shear stiffness has also been reported between 1 and 2 (Chen et al., 2023). However, this study uses parameter values closer to the minimum values of previous studies, which matches the experimental results of having lower elastic stiffness in the stress-displacement curve. Additionally, nonlinear plastic parameters such as plasticity ratio and pull-off force for GFRP are presented in Table 5-3. To facilitate energy dissipation and achieve a steady state in the model, damping coefficients of 0.2 and 0.4 are applied to spheres and ellipsoids, respectively.

Figure 5-5 depicts the comparison between experimental and DEM simulation results for F-PFRP(S), F-1500FRP, and M-1500FRP interfaces. Both loose (Figure 5-5(a)) and dense specimens (Figure 5-5(b)) show trends consistent with experimental results, except for the F-1500FRP case, which exhibits a

sharper peak strain-softening response and a narrower contraction-dilation range in the simulations. Differences arise from the surface texture representation between experimental sand-GFRP interfaces and the DEM model. Although overlapping particle assemblies represent similar average surface roughness (R_a), they lack the weave pattern and directional irregularities present in the GFRP surface (Chapter 3; Thomas, 1998; Araújo et al., 2022; Teng et al., 2024). Consequently, the regular roughness of the GFRP model and idealised smooth particles significantly influence interfacial volumetric behaviour and interaction accuracy. While the DEM model primarily relies on stiffness and friction parameters, it may have limited capacity to capture complex interfacial effects during dilation and contraction (Feng et al., 2018; Grabowski et al., 2021a). Nonetheless, shear stress, being the principal parameter in both experiments and simulations, is predicted with high accuracy, as shown in Figure 5-5. Among these two particle shapes, spheres tend to better predict normal displacement trends, whereas ellipsoids offer improved shear stress representation. Importantly, the accuracy and reliability of the subsequent analysis are not anticipated to be significantly affected, as the overall mechanical responses between DEM and experimental results are closely aligned.

The simulation scheme was carried out in two phases. The initial phase involved performing the first 6 sets, including loose and dense specimens of simulation with spherical particles, as conducted in experiments in Chapter 3, and the next 2 sets, including loose and dense specimens as a special case by using ellipsoid particles, under 50 kPa, 100 kPa, and 200 kPa. Subsequently, the second phase involved medium sand against 1500FRP interface with 5 types of varying roughness categorised from 1500FRP I to 1500FRP V with increasing order of roughness, to explore roughness effect at dense spherical particles of medium sand-1500FRP interface by utilising the similar hardness properties.

The practical implications of varying surface roughness can be achieved by altering the grain size of the applied sand to the sand-epoxy coating (Namjoo et al., 2022). The simulation scheme led to a total of 63 simulations, including calibrated results. A comprehensive description of the simulation scheme can be

found in Table 5-4. For those specimen IDs in which a numeric middle term is present, "M-L-1500FRP" stands for interface shearing of loose medium sand against 1500 g/m^2 concentration and 0.1–0.8 mm size of sand-epoxied GFRP, just as in experiments (Table 5-4).

5.4 Macromechanical behaviour

5.4.1 Shear stress and volumetric behaviour

Figure 5-6 shows the shear stress and normal displacement simulation results in the interface tests. The increase in roughness of 1500FRP is attributed to the evolution of larger stress and dilation for dense specimens and contraction for loose specimens compared to fine sand sheared against PFRP(S) (Figures 5-6(a) and 5-6(b)). The increase in normal stress further increases shear stress and contractions, similar to the theoretical trends. Fine sand shows greater interface strength, whereas medium sand shows greater evolution of normal displacement consistent with experimental results (Figures 5-6(b) and 5-6(d); Chapter 3). Due to the limitations of particle angularity and textures in DEM, interparticles interact only with friction properties. The loose specimen under 100 kPa and 200 kPa normal stress performs almost similar contraction, while this scenario even worsens with ellipsoids, as their specimens compress easily than spheres.

Furthermore, a gradual strain-softening, accompanied by a progressive decline along the interface shearing length, as observed in the ellipsoid case (Figure 5-6(e)), suggests that the reduction in sphericity and the increase in angularity contribute to a more realistic evolution of shear stress at the interface compared to spheres. The reduced contraction and early onset of dilation under higher normal stress (Figure 5-6(e)) are attributed to enhanced confinement and interlocking at the interface combined with the natural rotational resistance of loose ellipsoidal particles (e.g., medium sand: circularity = 0.85, sphericity = 0.989) in the absence of interparticle rolling resistance, as reported on shape- and stress-dependent volumetric responses (Danesh et al., 2020; Necochea et al., 2024).

As shown in Figure 5-7, the loose and dense specimen of fine sand shares a narrow vicinity of void ratio compared to medium sand, and it converges with the progression of interface shearing. Since fine sand is calibrated with a smaller stiffness compared to medium sand in order to match the experimental results, the influence of overlapped spherical particles during particle generation can cause an increase in void ratio compared to the initial void ratio at the generation stage for the dense specimen (Wang and Yin, 2022). As the normal stress increases, a slight reduction in the void ratio along the shearing length is identified. However, the reduction in the void ratio of medium sand when compared with the initial void ratio could be due to the smaller friction coefficient of medium sand particles (i.e., 0.6) than that of fine sand (i.e., 0.76). In loose specimens, ellipsoids compress more easily than spheres due to their shape, which promotes tighter packing and fewer voids. In dense specimens, ellipsoids dilate earlier, as their elongated shape resists inter-particle movement, leading to greater reorientation and void expansion. These shape-dependent behaviours, as discussed by Danesh et al. (2020) and Nguyen et al. (2021), affect the shearing response of granular materials.

5.4.2 Comparison of friction angles and interface roughness

Thirteen sets of interface simulations in dense specimens were conducted to investigate the variation in the peak and ultimate interface friction coefficients with normal stress, as illustrated in Figures 5-8(a) and 5-8(b). Additionally, for the first eight sets of interface simulations in loose specimens, the variation in the ultimate friction coefficient with normal stress is shown in Figure 5-8(c). The results reveal that the nonlinear decreasing trend of the interface friction coefficient with increasing normal stress aligns with previous studies (Archard, 1957; Frost and Han, 1999). However, the decline rate diminishes as the sand-epoxied GFRP's roughness decreases, i.e., with the application of finer sand of epoxied sand, medium sand, and the transition from ellipsoids to spheres. No abrupt changes in the friction coefficient were observed, as reported in studies by Dove and Frost (1999), Zettler et al. (2000), Vangla and Latha (2015), and

Vangla and Gali (2016). This suggests that the sand-GFRP contact mechanism, within the examined range of normal stress, did not experience the ploughing effect typically associated with such transitions.

The prediction plot of simulation results in terms of friction angles is illustrated in Figure 5-9. A total of 8 sets with peak and ultimate friction angles of dense specimens and similar sets with ultimate interface friction angles of loose specimens show ± 8 % error in the prediction of friction angles. However, the interface friction angle at peak and ultimate states predicted by ellipsoids is more accurate compared to spheres while significantly dominated over spheres at ultimate states, which might be convexity of shape and clusters of particles containing small concavities lead to a closer approximation to that of experiments, consistent with Danesh et al. (2020), Huang et al. (2014), and Necochea et al. (2024) reports. By employing sand-epoxy coating on GFRP surfaces, the friction angle increased significantly by 37% for fine sand and 98% for medium sand at the peak state (see Appendix C, Table C-1). A comprehensive summary of interface materials and model setups used in the present study, along with those findings documented in related DEM studies (Jing et al., 2018; Feng et al., 2018; Feng et al., 2020; Grabowski et al., 2021a), is presented in Table 5-5. The experimental data presented in Chapter 3 are also included for comparison.

The comparative chart of the peak friction angle versus normalised roughness is shown in Figure 5-10. Based on the available data and literature, three interface zones can be categorised from the chart: (a) smooth interface ($R_n \leq 0.1$), (b) intermediate interface ($0.1 \leq R_n \leq 0.3$), and (c) rough interface ($R_n \geq 0.3$). The trend line shows a slight increase in friction angles with normalised roughness in the smooth interface zone, followed by an abrupt increase in the intermediate zone and a steady state in the rough interface zone. The logic of this chart is qualitatively similar to the experimental study of Paikowsky et al. (1995) in glass beads and sand against varieties of the roughness of aluminium plates.

In Figure 5-10, the majority of friction angles of sand particles against the sawtooth plate are aligned around or above the trend line (dashed line), while

friction angles against overlapped ball structures, such as geomembrane, geotextile, and FRP, are aligned around or below the trend lines. It indicates that the surface roughness created by sharp sawtooth forms a clogging-prone surface (Martinez and Frost, 2017) attributed to significant resistance compared to the surfaces made by smooth overlapped balls, resulting in higher peak friction angles. However, the close alignment between the experimental peak friction angle and the DEM peak friction angle demonstrates the model's predictive accuracy in replicating the experimental shear response.

5.5 Micromechanical behaviour

5.5.1 Particle displacement and rotation

The displacement of sand particles at fine sand-PFRP(S) and medium sand-1500FRP interfaces under 100 kPa normal stress is shown in Figures 5-11 and 5-12, respectively. At early stages of shearing, i.e., 0.005 mm and 0.025 mm at F-PFRP(S) (Figures 5-11(a) and 5-11(b)) and M-1500FRP (Figures 5-12(a) and 5-12(b)) interfaces, a portion of sand particles move in the positive X-direction in both loose and dense specimen. Although an apparent displacement localisation is identified in dense sand specimens compared to loose specimens in these stages, thickness continuously reduces to the next stage of 1.0 mm tangential displacement (i.e., Figures 5-11(c) and 5-12(c). In Figures 5-11(d) to 5-11(f) and 5-12(d) to 5-12(f), substantial displacement localisation can be observed at the bottom of the specimens with a small portion of particles, above which a large portion of particles remain almost steady. Figures display two thinner edges at both ends, forming an arc-shaped shear zone, as reported in the literature (e.g., Wang et al., 2007; Jing et al., 2018). This configuration exhibits a relatively consistent shear zone thickness in the middle, measuring a few times the mean particle diameter (D_{50}) for both loose and dense sand specimens.

The plot of specimen height against the ratio of the average horizontal displacement of particles to the tangential displacement of the specimen provides a clearer visualisation of the two-dimensional representation of displacement

localisation, as illustrated in Figure 5-13. At an early stage of tangential displacement (0.25 mm), both loose and dense specimens of fine and medium sands exhibit minimal displacement localisation. The displacement profiles increase quasi-linearly towards the GFRP surface at the F-PFRP(S), F-1500FRP, and M-1500FRP interfaces, except for the dense specimen's curve at F-PFRP(S), which displays a pronounced bending at the bottom. This bending in close proximity to the PFRP(S) results likely from full sliding of particles with minimal interlocking along the intermediate interface (Feng et al., 2018). In contrast, the rough surface of 1500FRP provides larger effective contact areas, enhancing particle interlocking at the rough interface.

Similar distinctive characteristics are observed in M-1500FRP at tangential displacements of 1.0 mm and 2.5 mm, indicating strong interlocking and dilation in dense specimens. In contrast, loose specimens continue to compress, preventing clear bending and the localisation of displacement thickness. Beyond 2.5 mm of tangential displacement, the pronounced bending of the curves at the bottom remains steady for both sands in loose and dense conditions until reaching the ultimate state of 10 mm tangential displacement. Ultimately, a stable shear zone thickness develops at a tangential displacement of 6.0 mm; herein, particles adjacent to the GFRP plates move synchronously with the plates, while the other particles remain nearly static until reaching the ultimate displacement state.

Figure 5-14 illustrates particle displacement and rotation at the end of the interface shear tests (10 mm), highlighting the micromechanical aspects of particle movement. Particles at the bottom exhibit significantly larger displacement and rotation, effectively contributing to the formation of the shear zone (Figures 5-14(a) to 5-14(c)). However, the magnitude of particle displacement decreases with a reduction in the roughness of GFRP, specifically with normalised roughness for both loose and dense specimens of fine sand, as observed in the study of Grabowski et al. (2021a). The maximum particle displacement for fine sand is observed to be 3.2 mm at the F-L-1500FRP interface. The majority of particle rotations in the clockwise (+) direction are identified at a vertical position of 0.5 mm from the bottom in both loose and dense fine sand

specimens, consistent with Grabowski et al. (2021a), though with approximately 10 times smaller magnitudes.

The differences in results likely arise from the broader scope of the present study, which considers the entire specimen size with overlapped particles as a GFRP surface, compared to the focused mid-region ($5D_{50}$ by $5D_{50}$) and grooved plates with sharp contact edges in their study. A maximum rotation of 4° is identified on the 1000FRP interface, with a rough interface ($0.3 < R_n < 1.3$) promoting rotation. Notably, the loose specimen at the GFRP contact surface exhibited anticlockwise rotation due to a low void ratio and reduced particle interaction, resulting in backward rotation (Figure 5-14(a)). Overall, dense specimens show a slight reduction in displacement and rotation compared to loose specimens (Figure 5-14(b)).

For medium sand, the M-D-1500FRP V interface, with the largest roughness (R_n = 0.34), dominates particle displacement (4.8 mm) and rotation (-4°). As R_n > 0.1, rotations followed an anticlockwise (-) trend, increasing with roughness, likely due to increased resistance at the contact points (Figure 5-14(c)). Larger particle sizes, with greater mass, contribute to higher forces and rotational resistance, influencing rotation direction and magnitude.

As expected, ellipsoid particles exhibit lesser displacement and rotation compared to spherical particles at similar interfaces, attributed to their asymmetric shape. Rougher interfaces enhance interlocking, promoting particle displacement and rotation. The concentration of particle rotation at the shear zone aligns with previous studies (Zhao et al., 2015; Gu et al., 2017; Necochea et al., 2024), demonstrating a balance between rotational and displacement movements, particularly for fine sand with $R_n \geq 0.49$ and medium sand with $R_n \geq 0.16$ against sand-epoxied GFRP.

5.5.2 Localised shear zone thickness and interface slip

The localised region at the end of the tangential displacement stages is crucial for estimating the influencing zone of soil-structure interfaces, particularly in terms of shear zone thickness, which is of key importance for designers and is

plotted with a similar concept to Wang and Yin (2022). As illustrated in Figure 5-15, the principle behind this plot is to identify shear zone thickness by knowing the lower boundary with an obvious change in the gradient of particle displacement (solid blue curve) and the upper boundary with the point of maximum curvature (red mark on the dotted red line). The dense specimen of fine sand exhibits a shear zone thickness of approximately 0.8 mm (Figure 5-15(a)), while the medium sand shows a shear zone thickness of 3 mm, nearly 3 times the D50 value (Figure 5-15(b)). Notably, the tangential displacement of particles at various vertical positions is more pronounced in fine sand than in medium sand. This trend may be due to the smaller particle size, which facilitates easier reorientation, rotation, and rearrangement of static particles during shearing.

Generally, the percentage of interface slip (S_l) or slide is quantified using Equation (5-2) (e.g., DeJong and Westgate, 2009; Lashkari and Jamali, 2021) to explore the sliding effect due to interface slip.

$$S_\mathrm{l} = 100\% \left(1 - \frac{d_\mathrm{p}}{d_\mathrm{t}}\right) \tag{5-2}$$

Herein, d_p refers to the average horizontal displacement of particles to form a shear zone along the total tangential displacement d_t. In general, sliding implies a smooth and continuous relative motion across the entire contact interface, whereas slip refers to localised or intermittent relative motion affected by the friction of the interface. For instance, 100% interface slip refers to slides.

Figure 5-16 shows the interface slip and shear zone thickness at various interfaces with respect to normal stress. Despite fine sand being sheared across PFRP(S) to 1500FRP with a wide range of normalised roughness ($0.21 \leq R_\mathrm{n} \leq 1.32$), large interface slip (approximately 70% to 90%) is observed, with slightly lower slip in loose specimens (Figures 5-16(a) and 5-16(b)). In contrast, Grabowski et al. (2021a) observed interface slip under 30% against a sawtooth plate in a rough interface zone, highlighting the increased vulnerability of GFRP and sand-epoxied GFRP to slip. Between 50 kPa and 100 kPa normal stress, minimal changes in interface slip can be observed. However, as normal stress increases from 100 kPa to 200 kPa, interface slip increases by 3% to 6% in all

loose specimen cases. In terms of shear zone thickness, loose specimens of fine sand exhibit larger shear zone thickness ($3D_{50}$ to $4.5D_{50}$) compared to dense specimens ($2.5D_{50}$ to $3.5D_{50}$) across the tested normalised roughness range. As normal stress increases, shear zone thickness decreases, with the F-L-1500FRP interface showing a fluctuation of nearly 1 D_{50}. Similarly, a decreasing trend in shear zone thickness with increasing normal stress has been observed in previous studies (Jing et al., 2018; Feng et al., 2018). Figure 5-16(c) illustrates that medium sand at smooth interfaces (e.g., 1500FRP I and II plates) showed almost full slip, increasing by 6% to 10% with normal stress from 50 to 200 kPa.

As normalised roughness increased from 0.08 to 0.34, the rate of interface slip increment decreased significantly, with total slip ranging from 50% to 70%. This contrasts with the findings of DeJong and Westgate (2009), who observed slip between 60% and 100% during shearing of subangular to rounded particles (Ottawa 20-30 and glass beads) against a sandblasted steel plate, with a lower normalised roughness range (R_n = 0.058 to 0.074). The shear zone thickness for medium sand ranges between $1D_{50}$ and $3D_{50}$ and shows no significant dependence on normalised roughness after $R_n > 0.16$, stabilising at $3D_{50}$. Additionally, shear zone thickness in medium sand was unaffected by normal stress within the tested roughness range. Ellipsoid particles exhibited slightly lower shear zone thickness and higher interface slip than spherical particles, which is aligned with the Danesh et al. (2020) report.

The observed shear zone thickness in this study is lower than that found in sand-steel interfaces ($4D_{50}$ to $9D_{50}$, e.g., Uesugi et al., 1988; DeJong and Westgate, 2009; Wang and Yin, 2022), but aligns with Feng et al. (2018) in sand-geomembrane interfaces ($2.7D_{50}$ to $4.4D_{50}$) and Feng et al. (2020) in sand-geotextile interfaces ($2.2D_{50}$ to $3D_{50}$). This discrepancy likely arises from the smoother asperities of overlapped sand particles compared to the grooved steel plates commonly used in wall-based modelling. Surfaces consisting of smooth overlapped balls tend to favour mass sliding with minimal particle rotation and displacement, while grooved surfaces promote particle displacement with partial sliding, rotation, and rolling motion, enhancing the thickness of the localised

zone (Jiang et al., 2015; Lashkari and Jamali, 2021). However, larger particle sizes, with their greater inertial mass, contribute to rotational effects, which might influence the evolution of GFRP roughness.

5.5.3 Distribution of force chains and contact forces

Figures 5-17 and 5-18 illustrate the force chain distribution for loose and dense sand specimens in contact with the GFRP plates at the ultimate state of 10 mm tangential displacement (front view). Figure 5-17 corresponds to fine sand in contact with PFRP(S) and 1500FRP interfaces under 100 kPa normal stress, while Figure 5-18 represents medium sand against 1500FRP under normal stresses of 50 kPa, 100 kPa, and 200 kPa, respectively. At the initial state of F-PFRP(S) (Figure 5-17(a)) and M-1500FRP (Figure 5-18(a)) interface, i.e., d_t = 0.0 mm, both loose and dense sand specimens exhibit vertical orientation of force chains with almost homogenous patterns. At the end of the test, i.e., d_t = 10.0 mm, increased magnitudes of force chains, a stronger concentration of force chains in the right part of the specimen, and specifically the bottom right corner, along with slight rotation of force chains towards a diagonal direction, can be identified, consistent with Feng et al. (2018) and Grabowski et al. (2021a) findings.

A more uniform distribution is observed in loose specimens due to a higher void ratio and lesser sphere contact (Grabowski et al., 2021a; Grabowski et al., 2021b). The higher concentration towards the right side of the bottom corner in dense specimens of fine sand under 100 kPa is consistent for medium sand sheared under 50 kPa normal stress. The inclination of force chains decreases, and the magnitude of force concentration increases with an increase in interface roughness, as illustrated in Figure 5-17(b) and 5-17(c) at the F-1500FRP interface compared to F-PFRP(S), which is due to the enhanced interlocking at the interface. Considering the provided stiffness, ellipsoid particles were applied with a magnitude 1.75 times lower than that for spherical particles. However, the force chain distribution appears to be significantly closer, which suggests that ellipsoid particles facilitate stronger interlocking at the interface. Note that the particle size and stiffness for medium sand are approximately 4 to 5 times greater

than those for fine sand, and the magnitude of the force chain is nearly 10 times larger, as evident in Figures 5-17(b) and 5-18(b). A greater non-uniformity is observed in the specimen with an ellipsoid shape compared to the sphere, as reported by Zhao et al. (2015), concerning the effect of angularity in pure sand shearing. Additionally, the magnitude of the force chain significantly increased with an increase in normal stress (Figure 5-17) to resist the shear deformation, as reported by Wang and Yin (2022).

Figure 5-19 presents the variations in the distribution of contact normal, normal forces, and shear forces with normal stress for medium sand against 1500FRP, while Figure 5-20 illustrates the variations of these quantities with interface roughness for both fine and medium sand. Initially, at d_t = 0 mm, both loose and dense specimens of medium sand against 1500FRP show a uniformly distributed, vertically directed contact normal, normal force, and shear force under the applied constant normal stress of 50 kPa. The average force ratio (average shear force/average normal force) for loose and dense specimens is 0.1 and 0.05, respectively. The slightly higher magnitude of initial shear force in the loose specimen is attributed to early compression. At the ultimate state of interface shearing, a vertically aligned normal force and an almost vertical shear force can be observed under 50 kPa normal stress. However, a slight inclination of shear force can be observed under 100 kPa normal stress. As normal stress increases from 100 kPa to 200 kPa, a noticeable anisotropy is induced in the contact normal and normal force, while the alignment of the shear force remains similar. This behaviour is consistent with the observation of Wang and Yin (2022). The magnitudes of the contact force and shear forces increase with increasing normal stress in a pattern that maintains an average force ratio of 0.12 for both loose and dense specimens, with the distribution of the contact normal increasing as the contact gap reduces.

Furthermore, with increasing normalised roughness from 0.21 to 1.32 for fine sand, the average force ratio changes from 0.13 to 0.14, with a few more degrees of inclination towards diagonal favoured by the rough interface (i.e., F-1500FRP), while a uniform distribution of contact normal and normal force is

favoured by the smooth interface (i.e., F-PFRP(S)) (Figure 5-20), consistent with previous studies (e.g., Feng et al., 2018; Grabowski et al., 2021a). In contrast, the ellipsoid particle enhances the average force ratio (~0.15) but with backward diagonal alignment, which might be due to the ellipsoid particle shape and less ability to rotate at the contact surface, causing the concentration of force chain at the bottom right corner of the interface, as observed in the force chain. Thereby changing the orientation of the fabric in a backward direction. Similarly, a significant increase in the average force ratio (from 0.1 to 0.14), along with a change in preferential direction from roughly vertical to diagonal with slight anisotropy, is identified as the normalised roughness increases from 0.04 to 0.34 (i.e., M-1500FRP I to M-1500FRP V) for medium sand. The higher fabric anisotropy observed for M-1500FRP compared to M-1500FRP V is consistent with previous reports, where similar anisotropy was attributed to the formation of localised bands resulting from higher interfacial resistance forces (Chen et al., 2023; Jia et al., 2024).

5.6 Evolution of GFRP surface roughness

Experimental findings revealed that the evolution of interface friction is accompanied by inevitable surface wear, including the formation of scars and shallow trenches on the contact surface of sand-epoxied GFRP during shearing. This section focuses on the change in GFRP surface roughness due to surface wear rather than volumetric wear. Wear is quantified as a change in roughness measured perpendicular to shearing to capture particle-induced wear patterns. This measurement approach is consistent with the experimental quantification of roughness variation; however, in the DEM, roughness is quantified along the shearing direction to evaluate surface deformation induced by shear forces. These forces act at the particle-interface, where they are transmitted through changes in the position of overlapped GFRP balls, as represented using the EEPA contact method.

Figures 5-21 and 5-22 show the 3D surface deformation and 2D plots of

average roughness profiles along the shearing length of GFRP. Figure 5-21 illustrates the surface roughness after shearing loose and dense specimens of fine sand against PFRP(S) and 1500FRP interface under 100 kPa, while Figure 5-22 presents the sphere and ellipsoid particle shape effect of dense medium sand on surface roughness evolution of 1500FRP under 50 kPa, 100 kPa, and 200 kPa normal stress. Figure 5-21 illustrates that the loose specimen at both interfaces results in a 35-40% lower impact on roughness evolution, attributed to weaker contact between sand particles and the GFRP surface, as observed at the bottom of the force chain.

The 1500FRP surface exhibits significantly larger roughness changes compared to PFRP(S), with changes approximately 9 times greater for both loose and dense specimens. Despite the 1500FRP surface being 1.8 times harder than PFRP(S), the greater roughness evolution is due to its higher normalised roughness and the effect of localised particles' displacement zone, which leads to increased resistance forces to promote deformation. The largest deformation occurs at the right corner, decreasing towards the left, consistent with the force chain evolution at the end of shearing. The effect of ellipsoid-shaped fine sand is evident, with roughness evolution 8.5% greater for loose and 13% greater for dense specimens compared to spherical particles on 1500FRP, resulting in an overall 3-4% reduction in the surface average roughness profile.

Figure 5-22 shows that ellipsoid particles of medium sand cause a 3.5%, 6%, and 9% reduction in the average surface roughness of 1500FRP under 50 kPa, 100 kPa, and 200 kPa normal stress, respectively, which is 0.5-1% greater than the effect of spherical particles. As mentioned in the literature, the roughness evolution mechanism is primarily due to the sliding mechanism, and rolling is secondary. Increasing roughness demotes the sliding mechanism and is progressively supplemented by rolling with the rotation mechanism as observed in interface slip and particle rotation trend. Moreover, the influence of the rotation mechanism due to the larger mass inertia preferably enhances the magnitude of surface roughness and increases with increasing normal stress. Thus, abrupt deformation, as observed in 2D plots, can be justified by the impact of

particle rotation on rough surfaces. The narrow zone of ellipsoid particles reduces inter-particle and interface rotation, resulting in an increased striking force at the point of contact. This amplifies GFRP degradation while enhancing frictional properties, as evidenced by the increased ultimate friction angle and the development of the force chain (Figures 5-10 and 5-17; Zhao et al., 2015).

Figure 5-23 compares the variation in average roughness with normal stress between experiments and DEM simulations. In the experiments, roughness measurements were taken after shearing loose and dense specimens under each normal stress for each GFRP. The DEM roughness data for loose and dense sand are summed to match the experimental approach. Overall, the surface roughness evolution predicted by DEM shows a declining trend with increasing normal stress, consistent with the experiments, except for F-1500FRP, which exhibited an increasing trend in the experiments. The assembly of GFRP shows regular surfaces with a wide range of roughness (8 μm $\leq R_a \leq$ 100 μm). However, the current model, which simulates only the vertical movement of large-diameter balls (2 mm), does not account for the particulate removal observed in sand-epoxy coating surfaces during experimentation. Despite this limitation, this reduction in roughness expresses the contact mechanisms during sand-GFRP interface shearing (Figures 5-21 and 5-22).

Figure 5-24 presents a detailed analysis of the trend of average roughness variation relative to normalised initial roughness. As shown in Figure 5-24(a), dense specimens exhibit consistently greater roughness degradation than loose specimens as normalised roughness increases. This degradation is further amplified with increasing normal stress, ranging from 50 kPa to 200 kPa, for both fine and medium sand (Figures 5-24(a) and 5-24(b)). While considering similar degrees of normalised roughness, the magnitude of roughness variation caused by medium sand appeared to be almost 6 times greater than fine sand, which is the impact of a larger mass in contact with GFRP and corresponding shear force. Overall, the key findings on roughness evolution suggest that on smooth interfaces, the sliding effect is dominant; on intermediate surfaces, sliding is followed by the rotation effect; and on rough interfaces, rotation dominates over

the sliding effect.

Balancing computational efficiency and modelling precision is essential for effective model selection. Using PFC3D on a 13th Gen Intel® CoreTM i9-13900K processor with 64 GB RAM, simulations with 40,000 to 60,000 spheres took approximately 67 to 74 hours against rough surfaces (e.g., 1500FRP). Smoother surfaces required denser overlapped ball packing, which increased contact calculations and extended computation time. Ellipsoids, requiring nearly three times more particles, resulted in 3.6-4 times longer runtimes but significantly enhanced micromechanical accuracy, better capturing interface interlocking, shear strength, and surface roughness evolution. While spherical particles better predict volumetric response and remain efficient for large-scale or preliminary analyses, ellipsoidal models are better suited for high-fidelity, small-scale studies. Furthermore, to better replicate the highly irregular surface roughness of GFRP, variation in ball size (along with the corresponding centre-to-centre spacing between bonded GFRP balls) would be required. This approach could become feasible with the use of advanced and powerful computational resources and would allow further improvement of the simulation model.

This study demonstrates that a calibrated DEM model, incorporating overlapped ball layers and sand specimens with spherical and ellipsoidal particles, effectively simulates the sand-GFRP interface, capturing complex micromechanical behaviours such as slip, force chain formation, and surface roughness evolution. The overlapped ball method combined with the EEPA contact model innovatively represents multi-scale surface textures of smooth and sand-epoxy coated GFRP, advancing beyond prior models designed for smoother geomembrane and geotextile surfaces (e.g., Chen et al., 2021; Feng et al., 2022). The model utilises a wide range of surface roughness aligned with laser-scanned data, enabling precise simulation of sliding, rotation, and surface degradation. By exploring particle shape, gradation, and density effects under varying normal stresses, the study offers novel micromechanical insights mostly consistent with experimental trends of surface roughness evolution. This integration of experimental calibration and numerical modelling presents a novel framework

for understanding sand-epoxy coating effects and optimising sand-epoxy coating in sand-FRP interface shear behaviour. Future work should investigate critical normal stress thresholds, the influence of fines content or sand mixtures, and the effects of particle angularity, in order to elucidate the micromechanical behaviour and support the development of continuum-mechanics-based constitutive models, while guiding the design of durable sand-epoxy coated GFRP surfaces.

5.7 Summary

This Chapter investigated sand-GFRP interface shear behaviour under three constant normal stress levels (i.e., 50, 100, and 200 kPa) using DEM. The surface characteristics of plain GFRP and sand-epoxied GFRP were reasonably simulated through overlapped ball layers along with approximated surface roughness as measured in experiments. The simulation results were calibrated against experimental data, showing a good match followed by a series of interface tests. Effects of sand gradation, density, surface roughness, and particle shape (spheres versus ellipsoids) were systematically examined at both macro and micromechanical scales. Findings underscore the importance of surface roughness characterisation and particle morphology in designing efficient sand-GFRP interfaces, offering a robust numerical framework for understanding and optimising geotechnical interface systems.. The main findings can be summarised as follows:

1) The use of sand-epoxy coatings on GFRP surfaces significantly enhances surface roughness, impacting shear stress and volumetric behaviour. Fine sand shows higher interface strength, while medium sand exhibits greater normal displacement evolution under constant normal stress. Ellipsoidal particles compress and dilate more readily than spheres, influencing shear stress and volumetric response, with a more pronounced effect on medium sand than fine sand.
2) Ellipsoid particles yield more accurate friction angle predictions due to their shape and concavity clustering compared to spheres. With sand-

epoxy coated GFRP surfaces, peak friction angles increase by up to 37% for fine sand and 98% for medium sand. Normalised roughness influences friction angles, categorising interfaces as smooth ($R_n \leq 0.1$), intermediate ($0.1 \leq R_n \leq 0.3$), or rough ($R_n \geq 0.3$), with a marked increase in friction angle in the intermediate zone.

3) Ellipsoid particles exhibit reduced displacement and rotation compared to spheres. Rougher GFRP surfaces enhance interlocking, promoting increased particle movement, especially in loose specimens, thereby balancing sliding and rotational effects.
4) Interface slip in fine sand decreases from 90% to 70% as normalised roughness increases from 0.21 to 1.32. In medium sand, slip remains near 100% on smooth interfaces, stabilising between 50% and 70% on intermediate to rough interfaces. Fine sand shows a larger shear zone ($3D_{50}$ to $4.5D_{50}$) in loose specimens, while medium sand maintains a consistent thickness of $3D_{50}$. Ellipsoid particles result in a lower shear zone thickness in loose specimens, with comparable interface slip to spheres.
5) Dense sand specimens show a greater concentration of force chains, particularly at the bottom corner, while loose sands exhibit a more uniform distribution due to higher void ratios. Ellipsoid particles facilitate stronger interlocking at the interface, leading to more concentrated force chains. Increasing normal stress and interface roughness enhances force chain magnitudes and anisotropy, with rougher interfaces promoting diagonal alignment and an increase in the average force ratio for both fine and medium sands.
6) Ellipsoid particles, dense sand specimens, medium sand, and higher normal stress cause more significant roughness changes. The deformation pattern shows the largest roughness increase at the right corner of the GFRP surface, progressively decreasing towards the left, consistent with force chain evolution and localised particle displacement zones. Higher normalised roughness leads to increased degradation, shifting the

dominant mechanism from complete sliding to partial sliding with rolling and rotation. On smooth interfaces, sliding predominates; on intermediate interfaces, sliding is followed by rotation; and on rough interfaces, rotation dominates over sliding in roughness evolution.

Building on the insights gained from the DEM-based interface direct shear test simulations under monotonic shear loading, where the micromechanical behaviour and failure mechanisms were clarified, the next chapter extends the investigation to FEM simulations under both monotonic and cyclic shearing, which offer complementary advantages for larger-scale modelling, direct comparison with experimental results, and validation purposes.

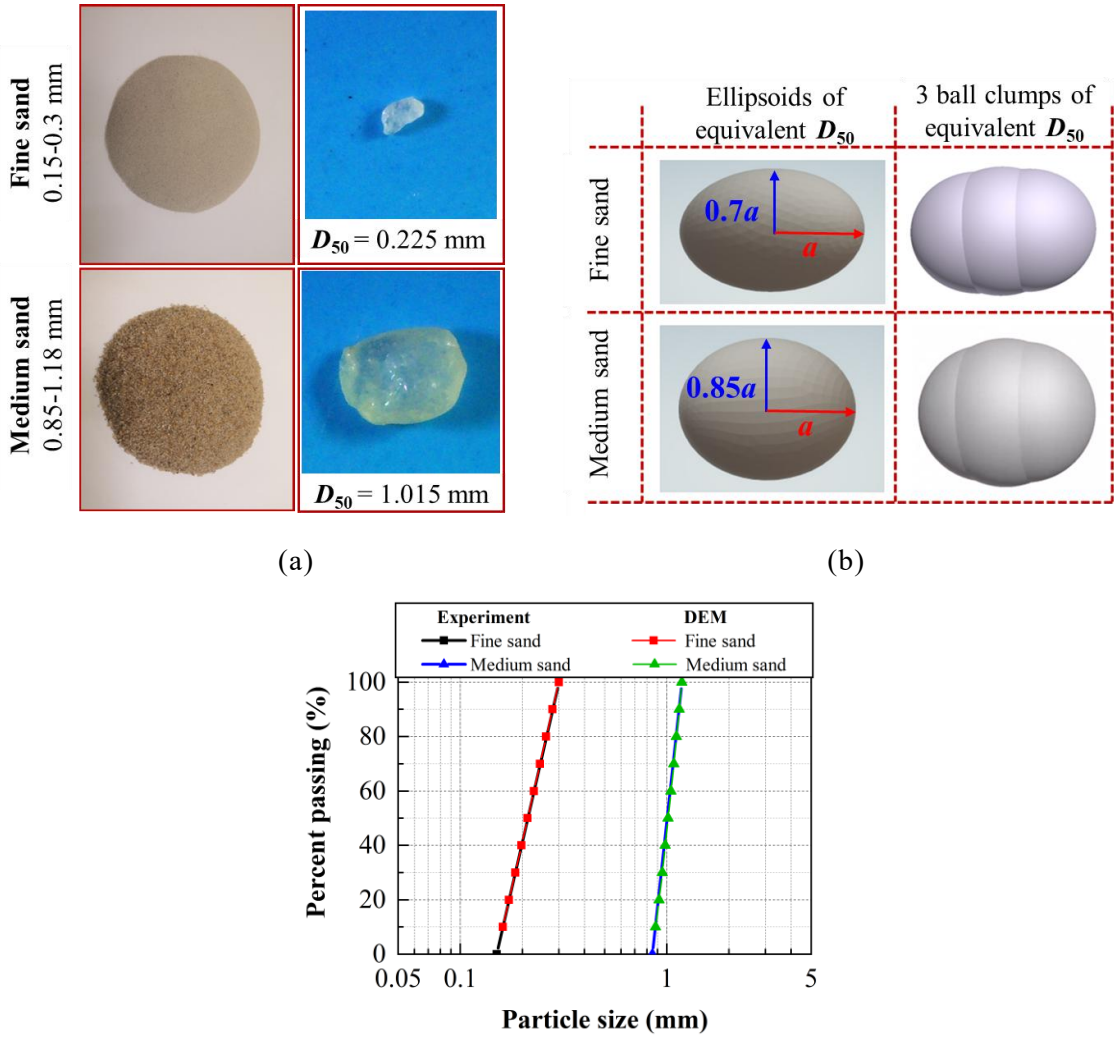

Figure 5-1 Sands used in the study (a) experimental testing sands and (b) special case of ellipsoid particles magnified to similar visual views for DEM simulation; (c) particle size distribution for experimental testing and DEM simulation

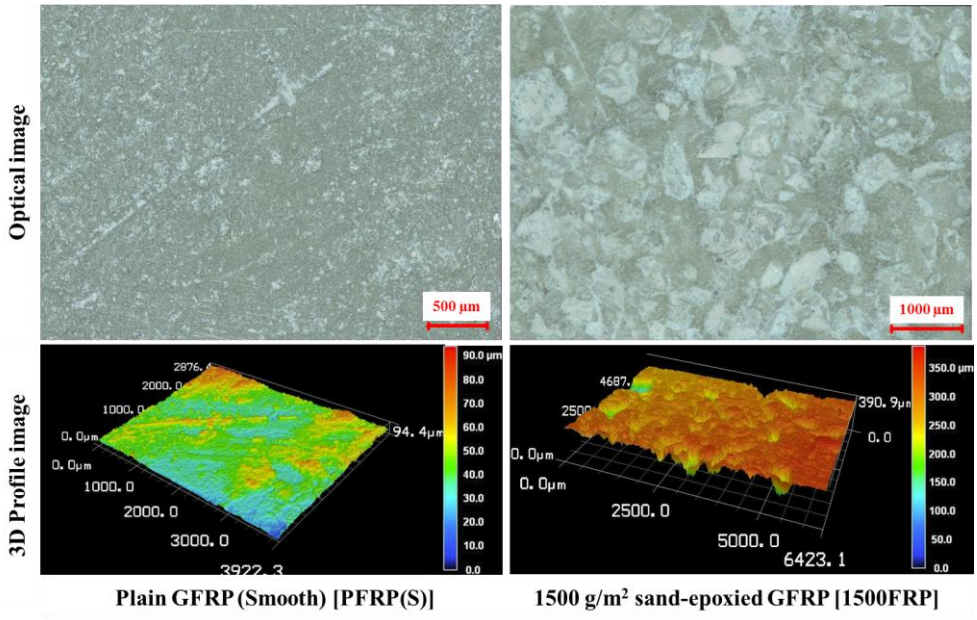

(a)

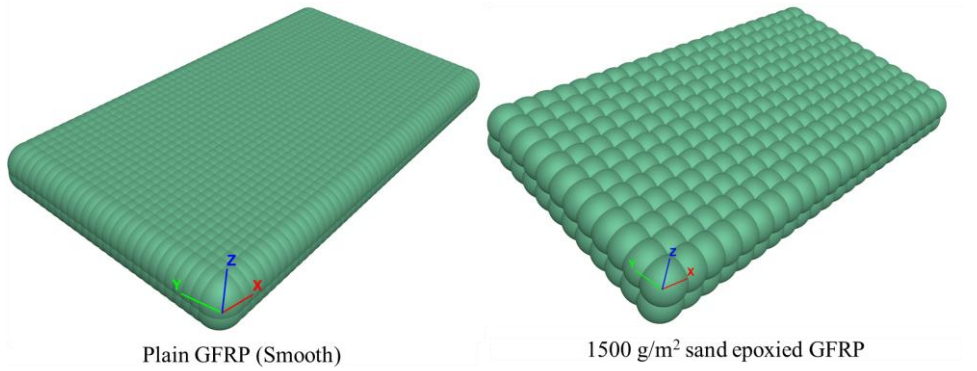

(b)

Figure 5-2 (a) Laser scan image and 3D profile of GFRP and sand-epoxied GFRP used in experiments (b) bonded assembly of GFRP for the approximation of plain GFRP and sand-epoxied GFRP

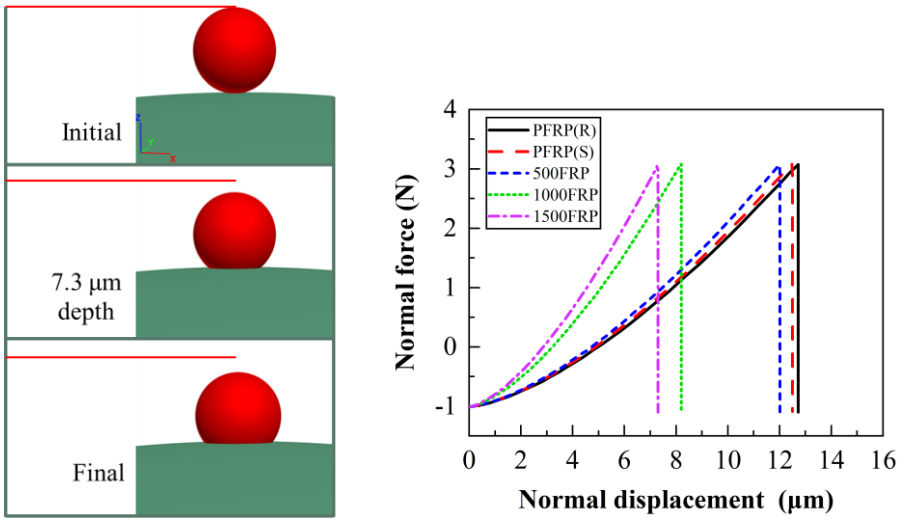

(a) (b)

Figure 5-3 Indentation simulation: (a) steel ball movement in the ball of PFRP(R) (red line indicates the initial benchmark); (b) normal force versus normal displacement for five GFRP types

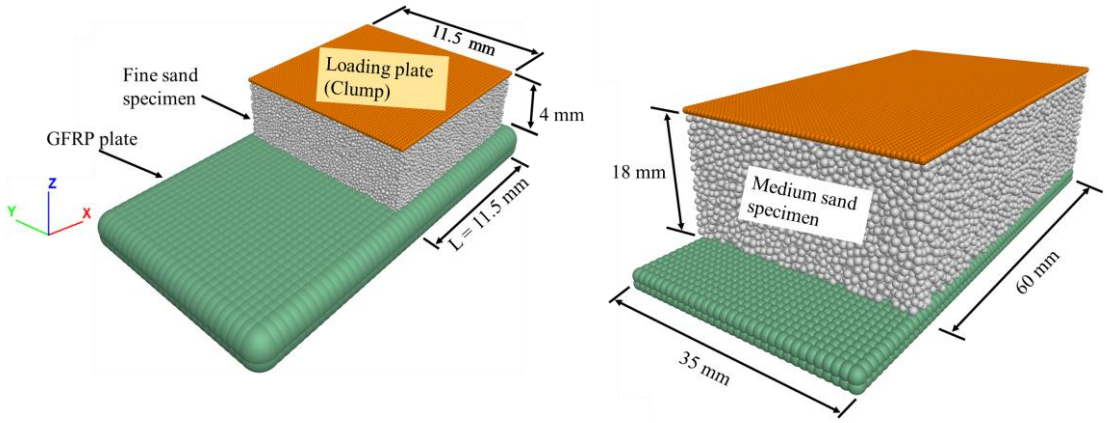

Fine sand-PFRP(S) interface model Medium sand-1500FRP interface model

Figure 5-4 DEM model for interface direct shear test

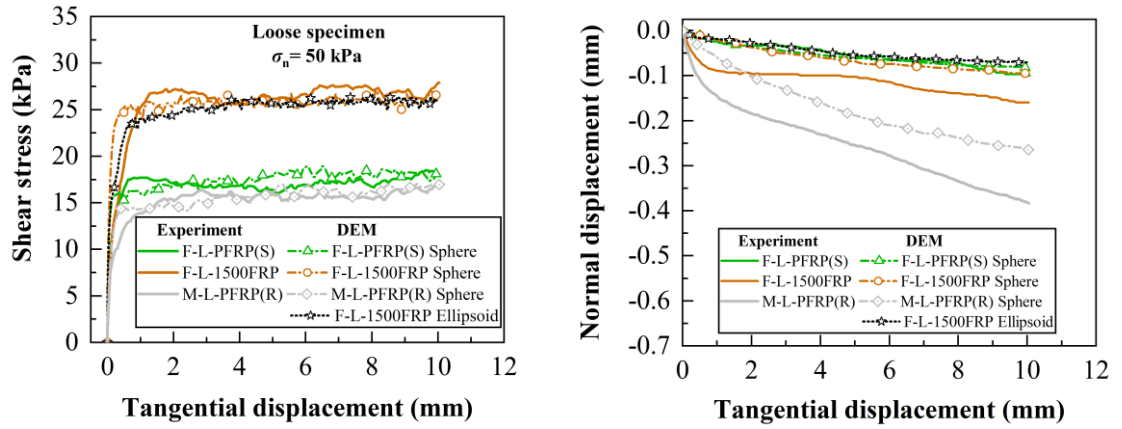

(a)

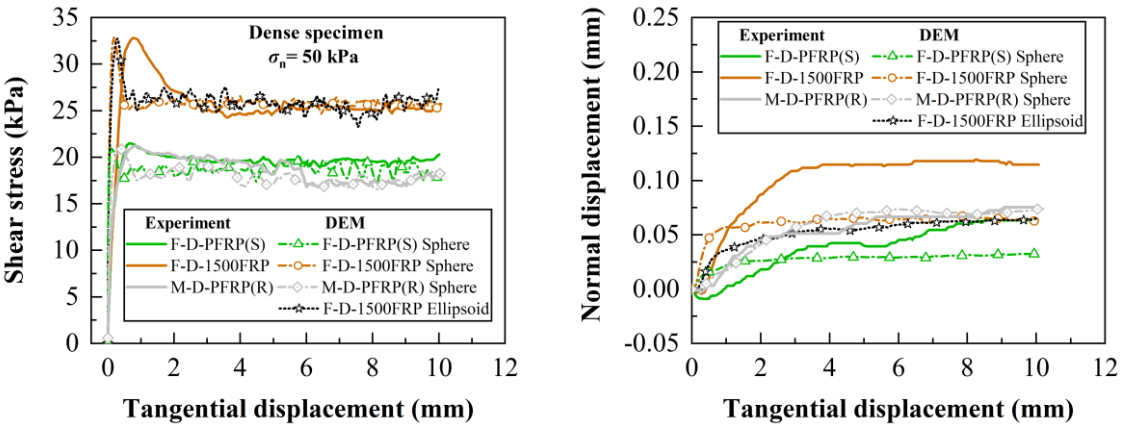

(b)

Figure 5-5 Comparison between tests and simulation results under 50 kPa normal stress: (a) loose specimen and (b) dense specimen of fine and medium sands against GFRP and sand-epoxied GFRP interface

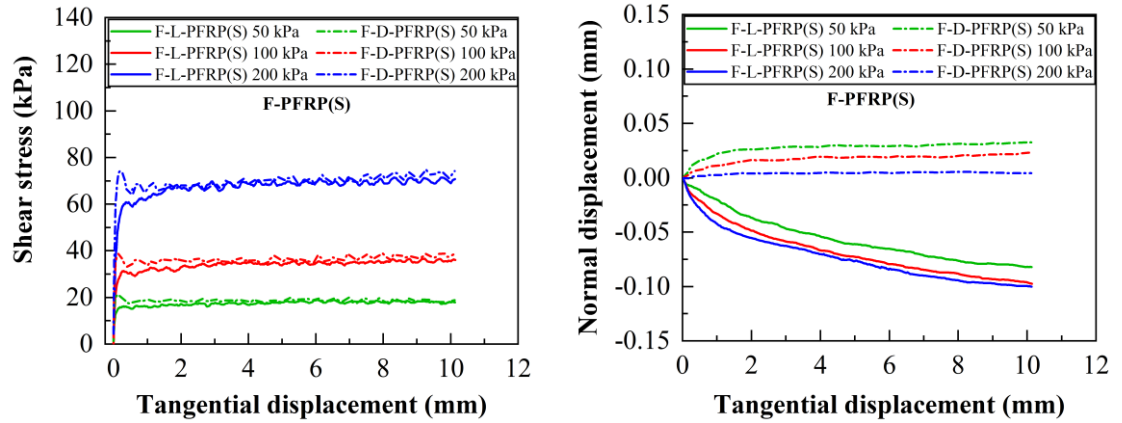

(a)

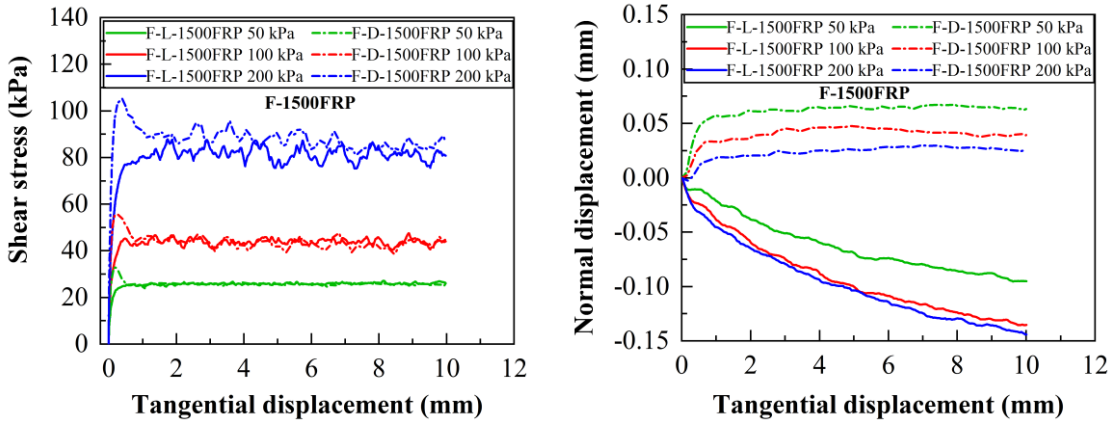
F-L-1500FRP 50 kPa
F-D-1500FRP 50 kPa
F-L-1500FRP 100 kPa
F-D-1500FRP 100 kPa
F-L-1500FRP 200 kPa
F-D-1500FRP 200 kPa
F-1500FRP
Shear stress (kPa)
Normal displacement (mm)
Tangential displacement (mm)

(b)

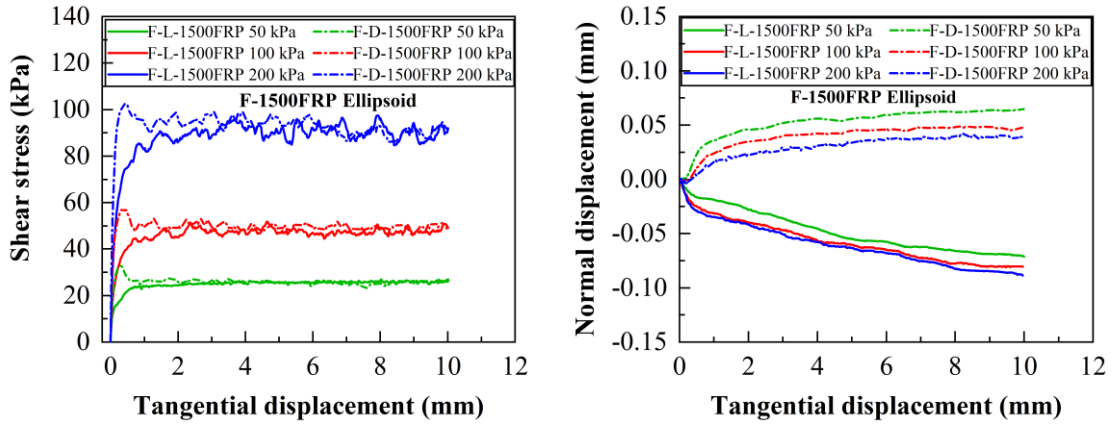
F-L-1500FRP 50 kPa
F-D-1500FRP 50 kPa
F-L-1500FRP 100 kPa
F-D-1500FRP 100 kPa
F-L-1500FRP 200 kPa
F-D-1500FRP 200 kPa
F-1500FRP Ellipsoid
Shear stress (kPa)
Normal displacement (mm)
Tangential displacement (mm)

(c)

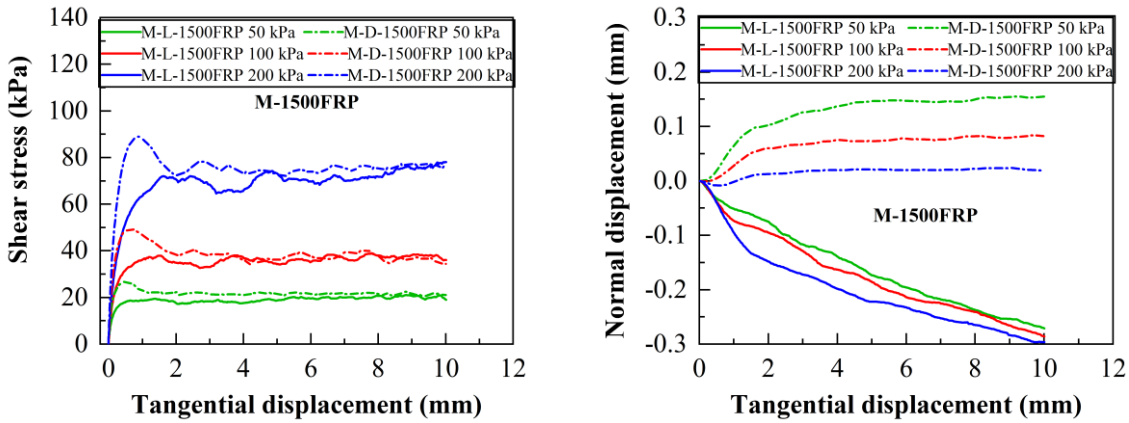
M-L-1500FRP 50 kPa
M-D-1500FRP 50 kPa
M-L-1500FRP 100 kPa
M-D-1500FRP 100 kPa
M-L-1500FRP 200 kPa
M-D-1500FRP 200 kPa
M-1500FRP
Shear stress (kPa)
Normal displacement (mm)
Tangential displacement (mm)

(d)

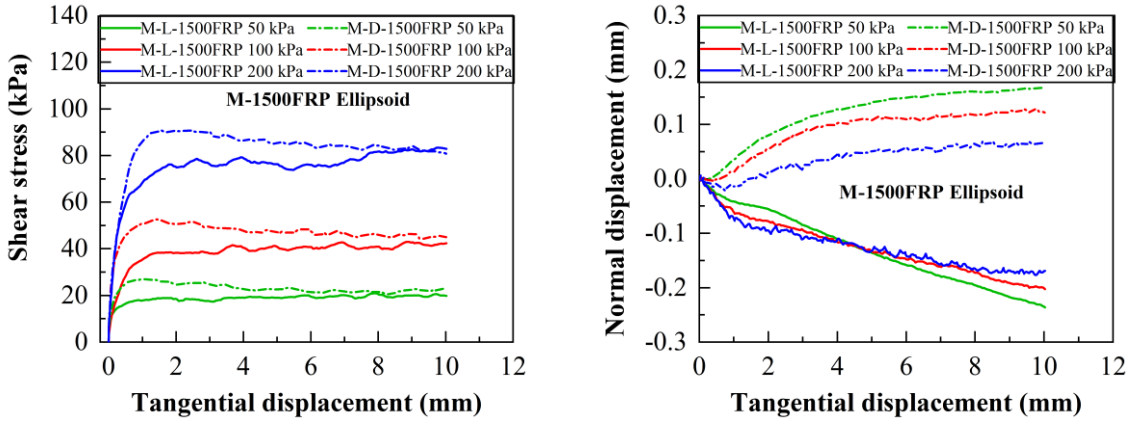

(e)

Figure 5-6 Simulation results for: (a) spheres of fine sand-PFRP(S), (b) spheres of fine sand-1500FRP, (c) ellipsoids of fine sand-1500FRP, (d) spheres of medium sand-1500FRP, and (e) ellipsoids of medium sand-1500FRP interfaces under 50, 100, and 200 kPa normal stress

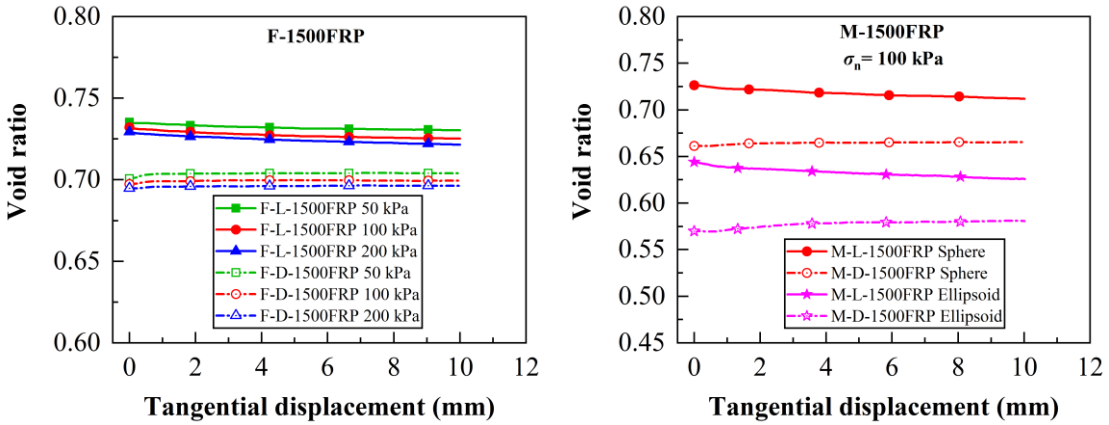

(a) (b)

Figure 5-7 Evolution of void ratio along the interface shearing length for: (a) sphere of fine sand-1500FRP interfaces under 50 kPa, 100 kPa, and 200 kPa normal stress, and (b) sphere and ellipsoid of medium sand-1500FRP interfaces under 100 kPa normal stress

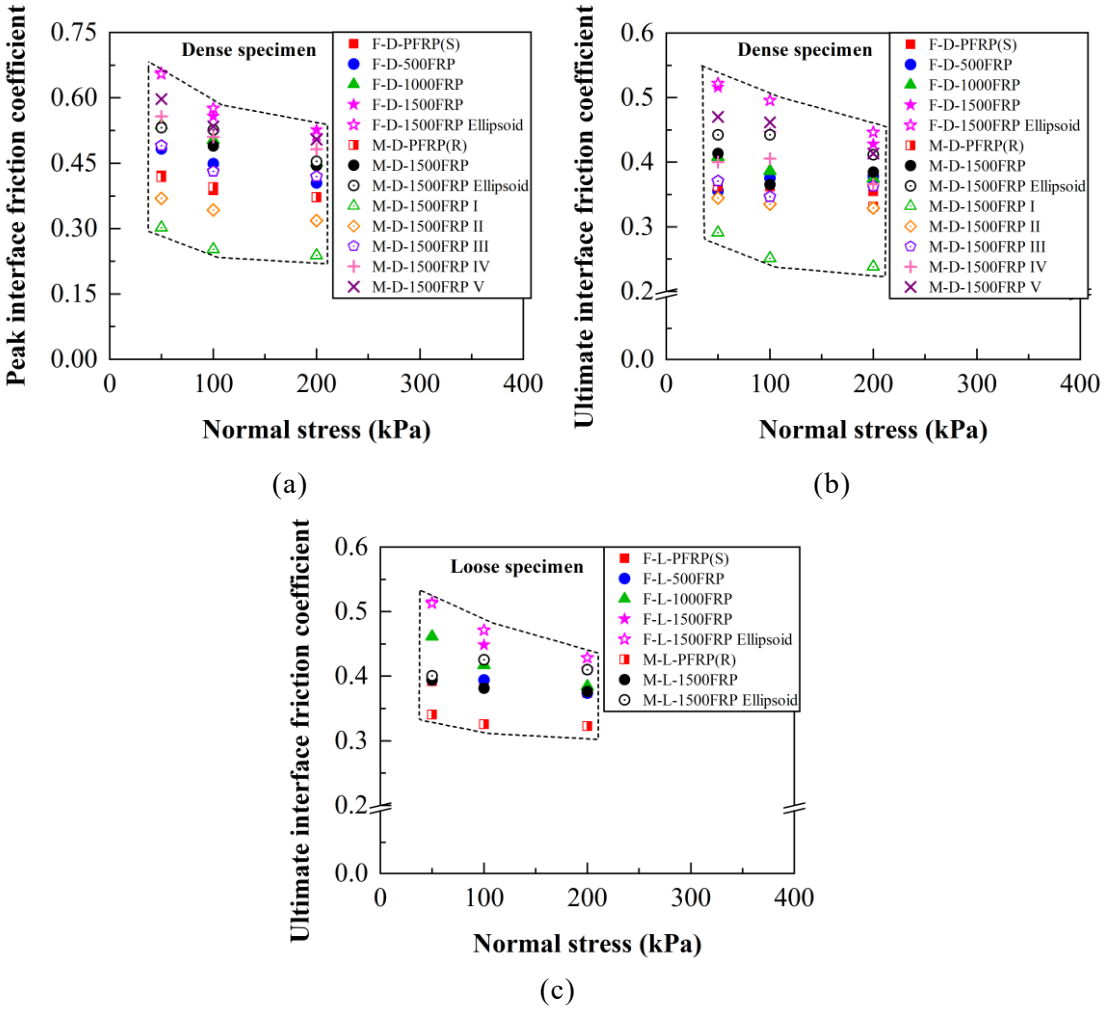

Figure 5-8 Variation in interface friction coefficient with respect to normal stress for: (a) peak state, (b) ultimate state of dense sand specimen, and (c) ultimate state of loose sand specimen

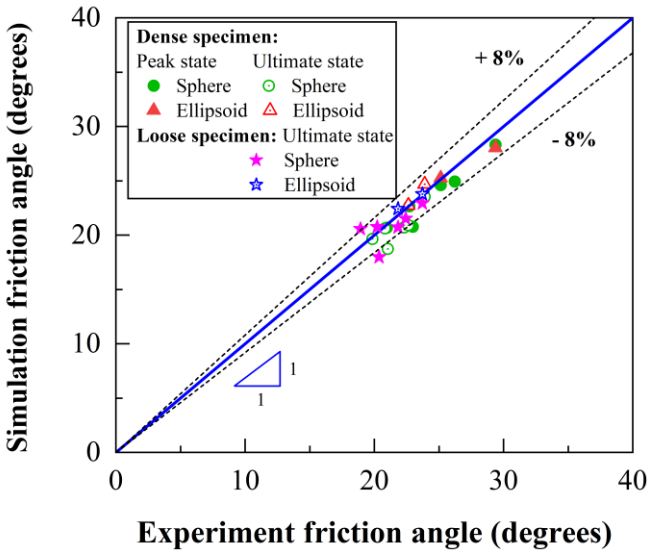

Figure 5-9 Simulation friction angle plotted against experiment friction angle for the first eight interfaces (Table 5-4)

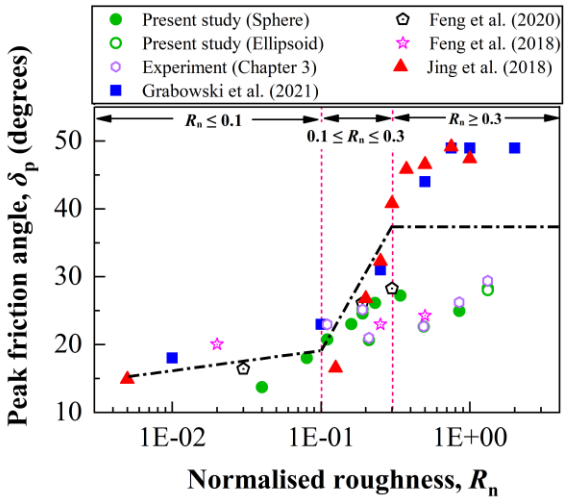

Figure 5-10 Comparison of peak friction angle with respect to normalised roughness

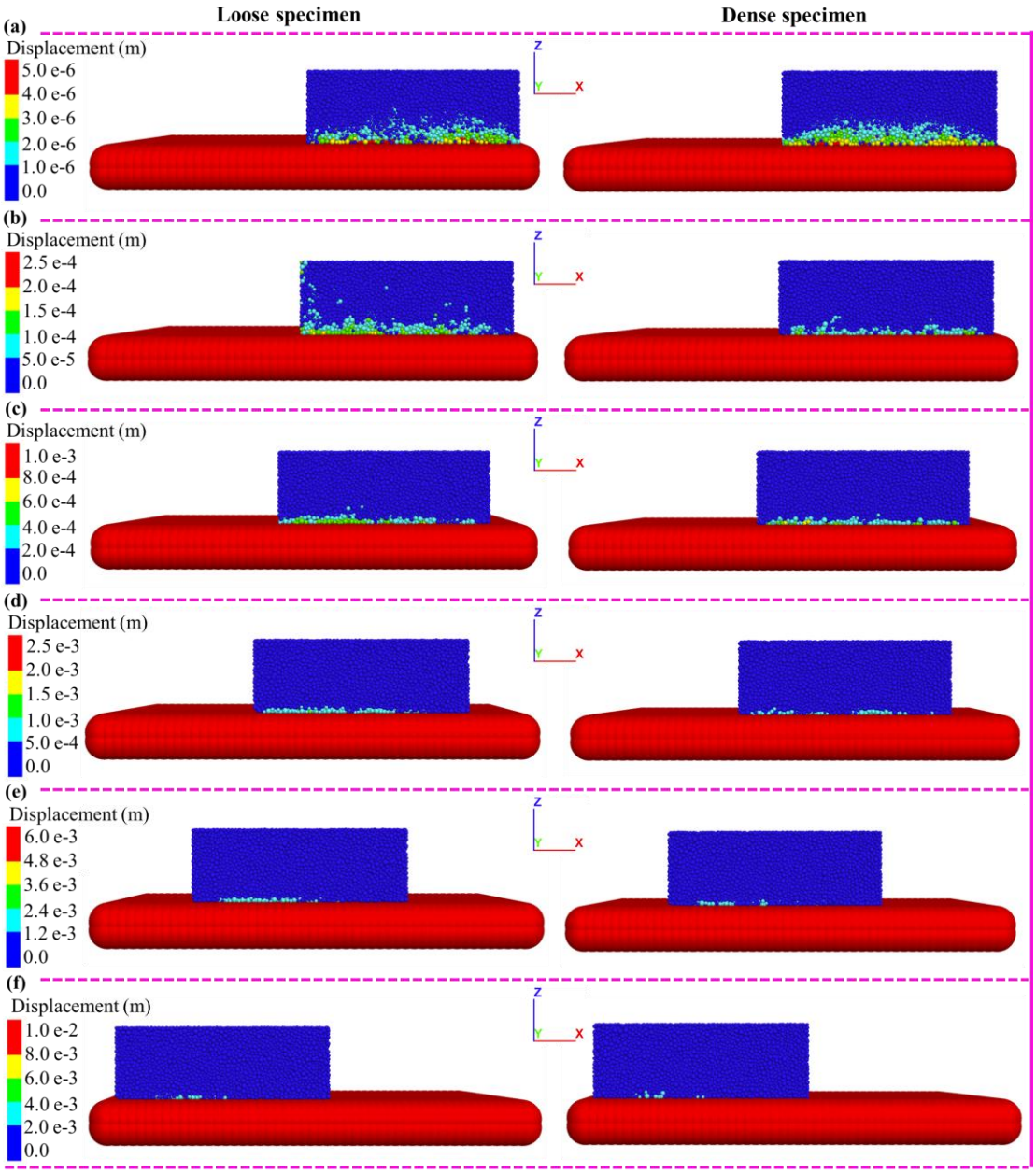

Figure 5-11 Particle displacement at F-PFRP(S) interface in the tangential displacement of (a) 0.005 mm, (b) 0.25 mm, (c) 1.00 mm, (d) 2.50 mm, (e) 6.00 mm, and (f) 10.00 mm under 100 kPa normal stress

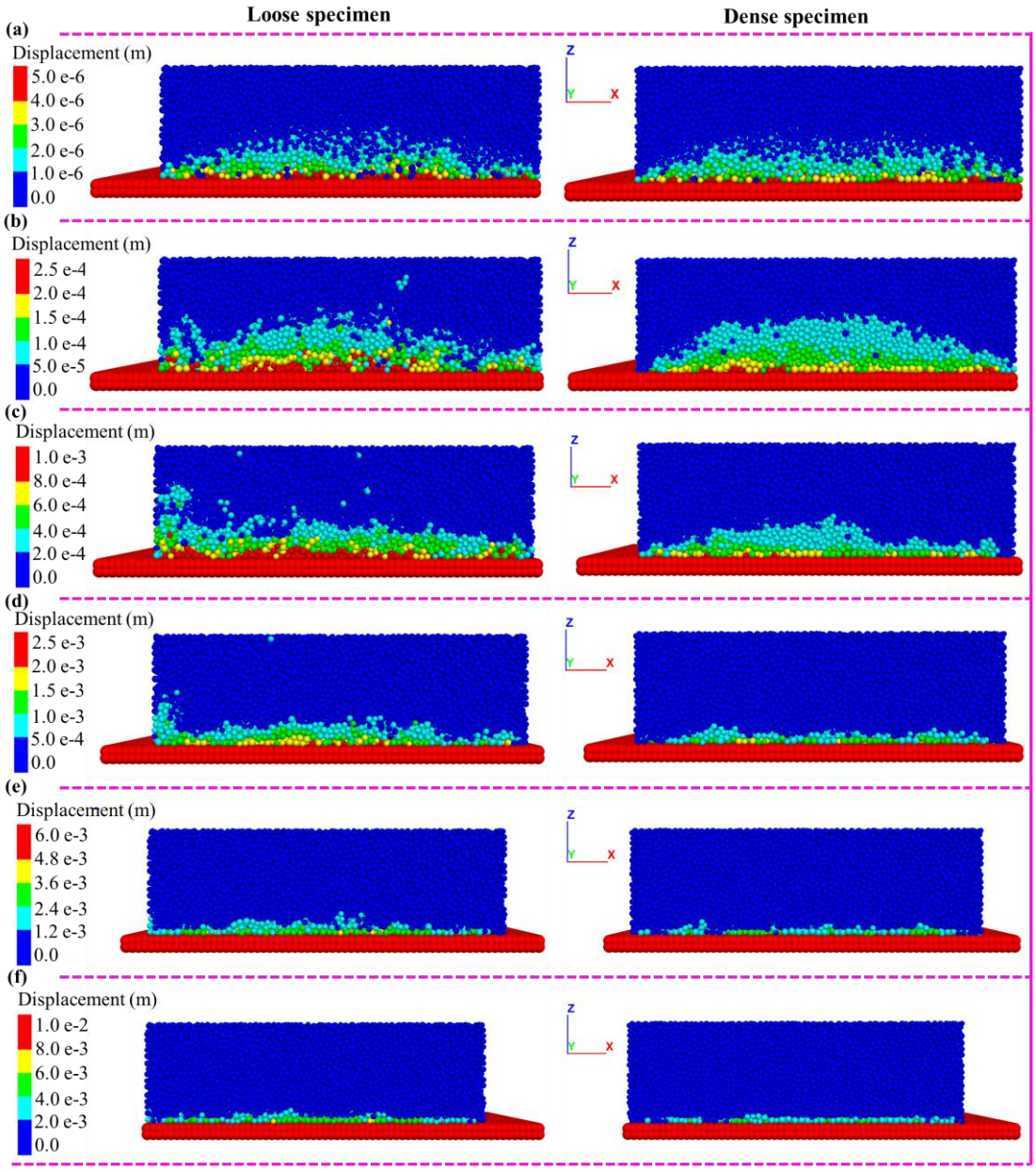

Figure 5-12 Particle displacement at M-1500FRP interface in the tangential displacement of (a) 0.00 mm, (b) 0.25 mm, (c) 1.00 mm, (d) 2.50 mm, (e) 6.00 mm, and (f) 10.00 mm under 100 kPa normal stress

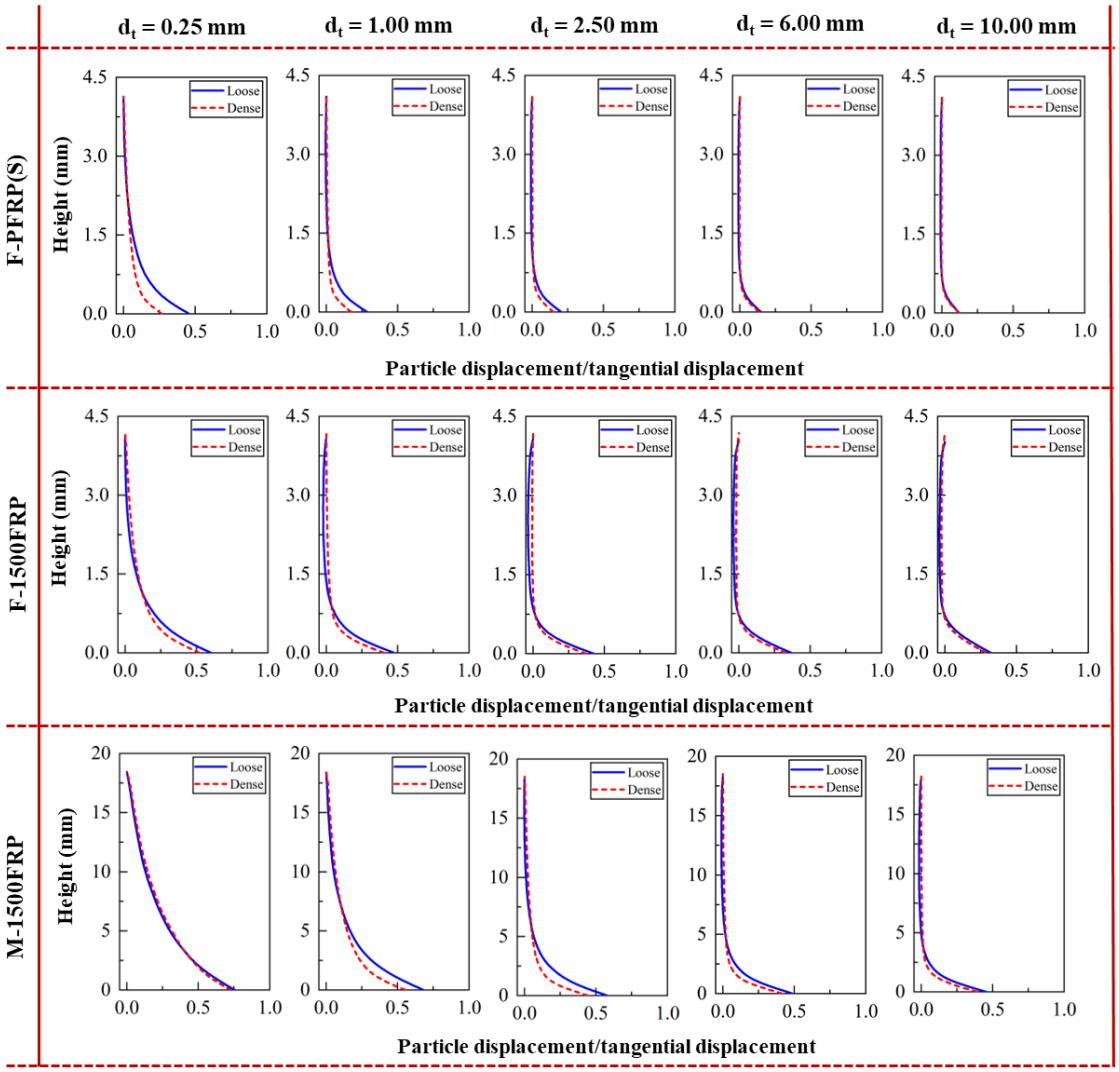

Figure 5-13 Average normalised displacement of particles at F-PFRP(S), F-1500FRP, and M-1500FRP interfaces with five different stages of tangential displacements under 100 kPa normal stress

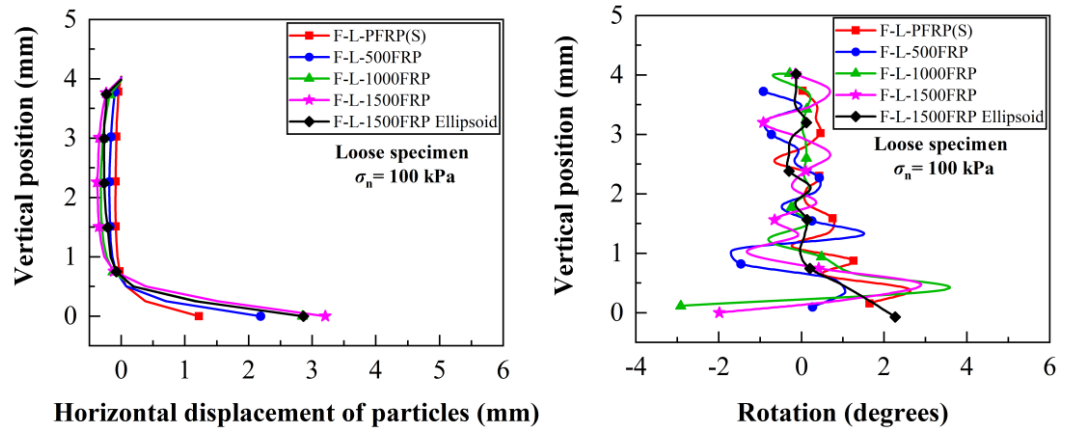

(a)

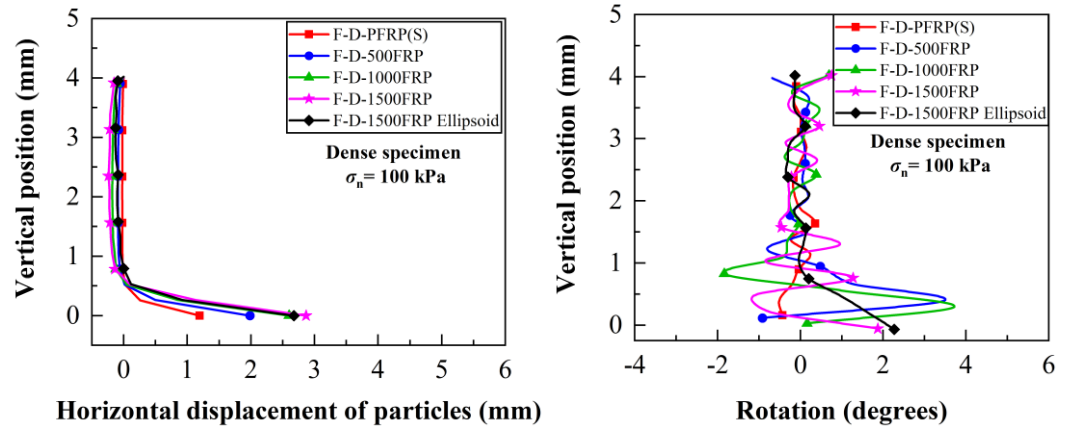

(b)

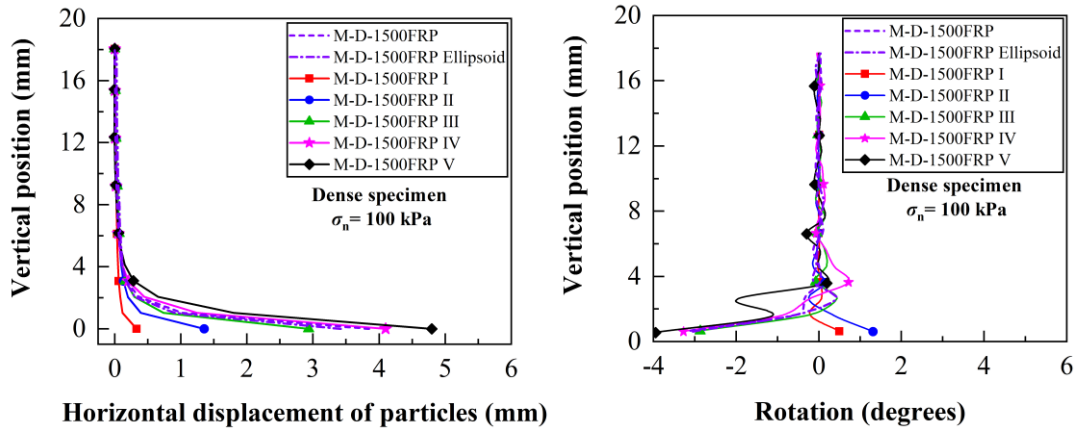

(c)

Figure 5-14 Particle displacement and rotation at the interface: (a) loose specimen of fine sand against GFRP (b) dense specimen of fine sand against GFRP (d) dense specimen of medium sand against varieties of roughness of 1500FRP under 100 kPa normal stress

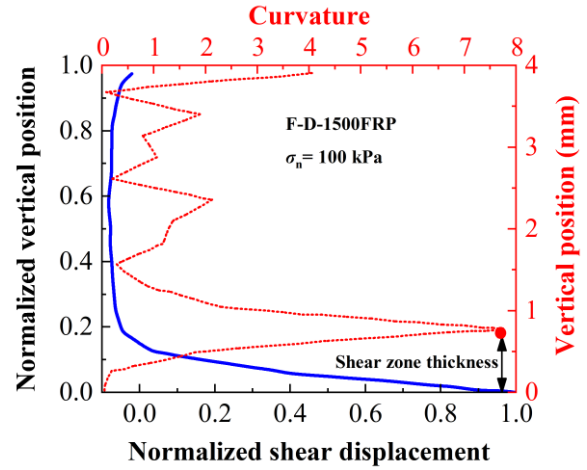

(a)

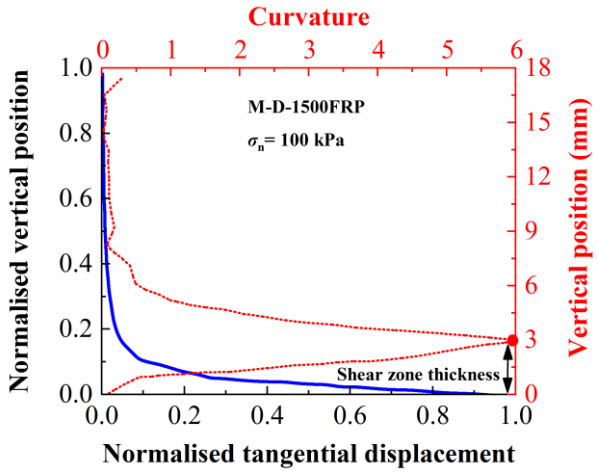

(b)

Figure 5-15 Determination of shear zone thickness (a) dense specimen of fine sand against 1500FRP and (b) dense specimen of medium sand against 1500FRP

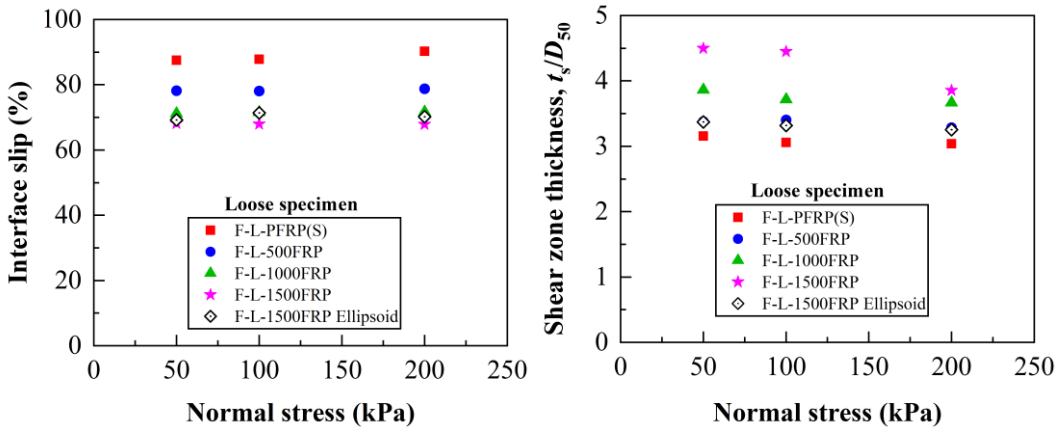

(a)

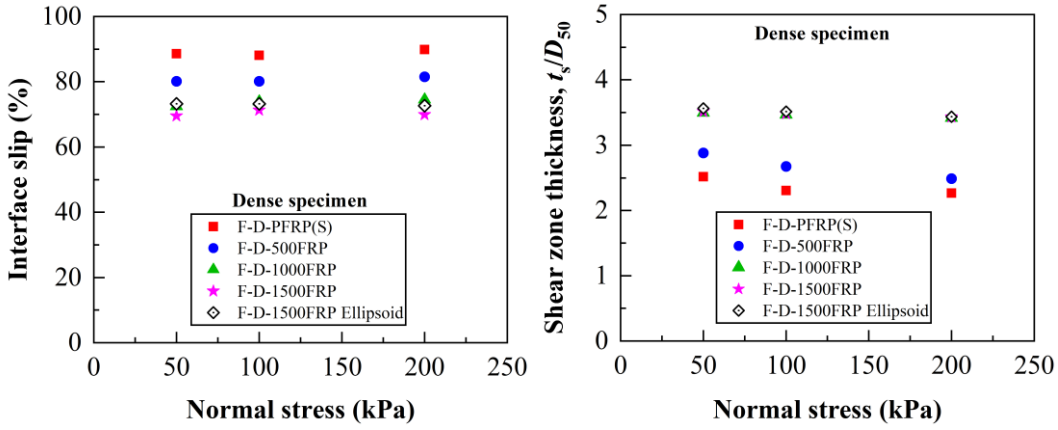

(b)

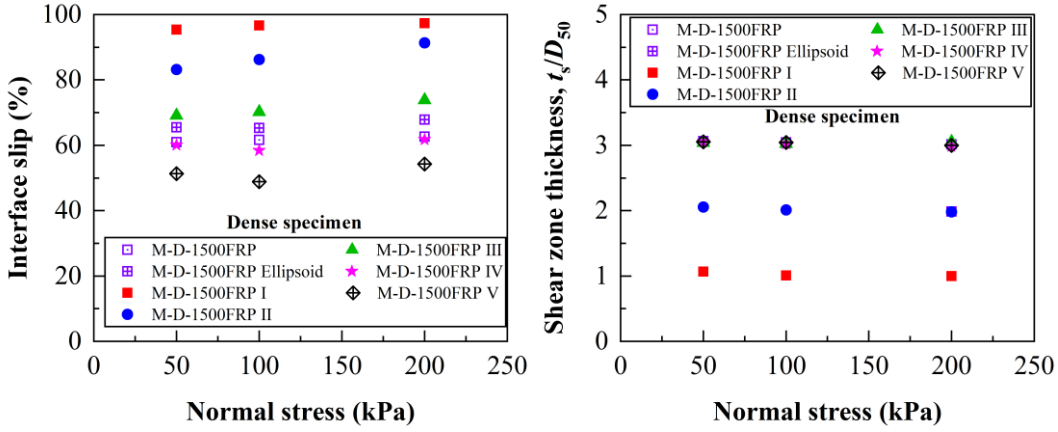

(c)

Figure 5-16 Interface slip and shear zone thickness at interfaces: (a) loose specimen and (b) dense specimen of fine sand; (c) dense specimen of medium sand

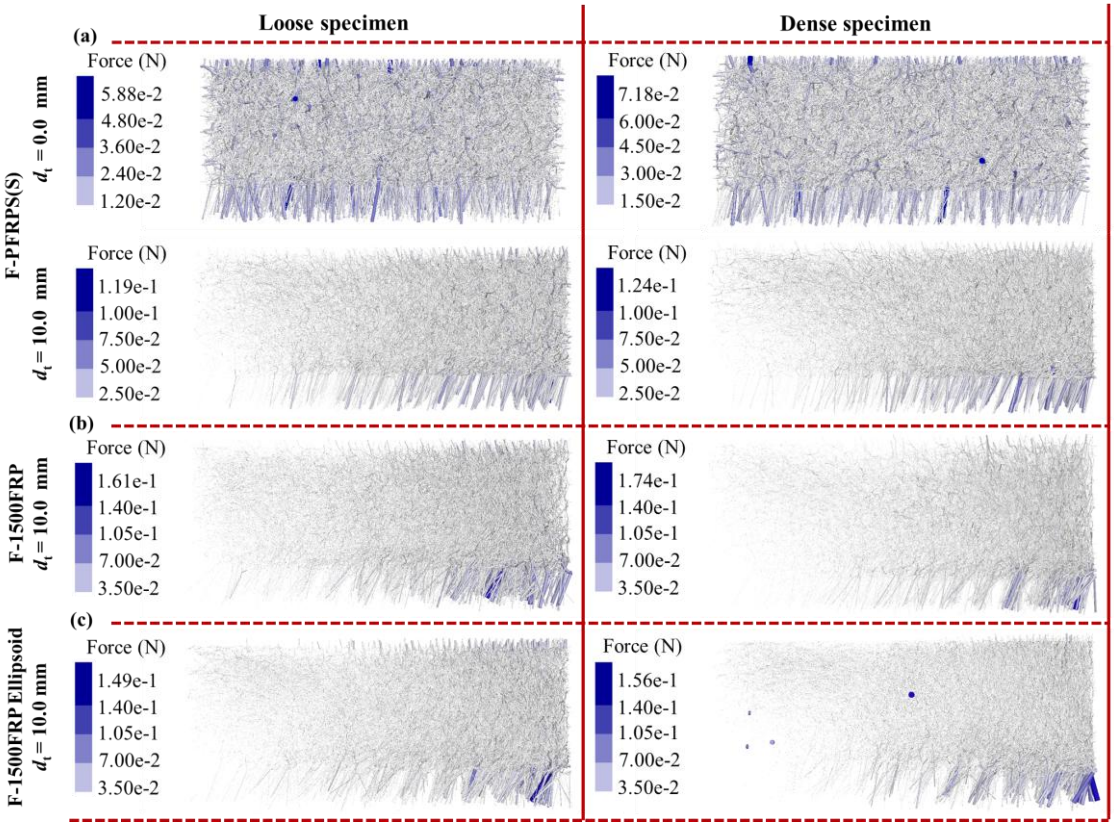

Figure 5-17 Force chains at (a) initial state and ultimate state of 10 mm tangential displacement at F-PFRP(S) interface; ultimate state of 10 mm tangential displacement for (b) F-1500FRP interface and (c) F-1500FRP interface for ellipsoid particles under 100 kPa normal stress

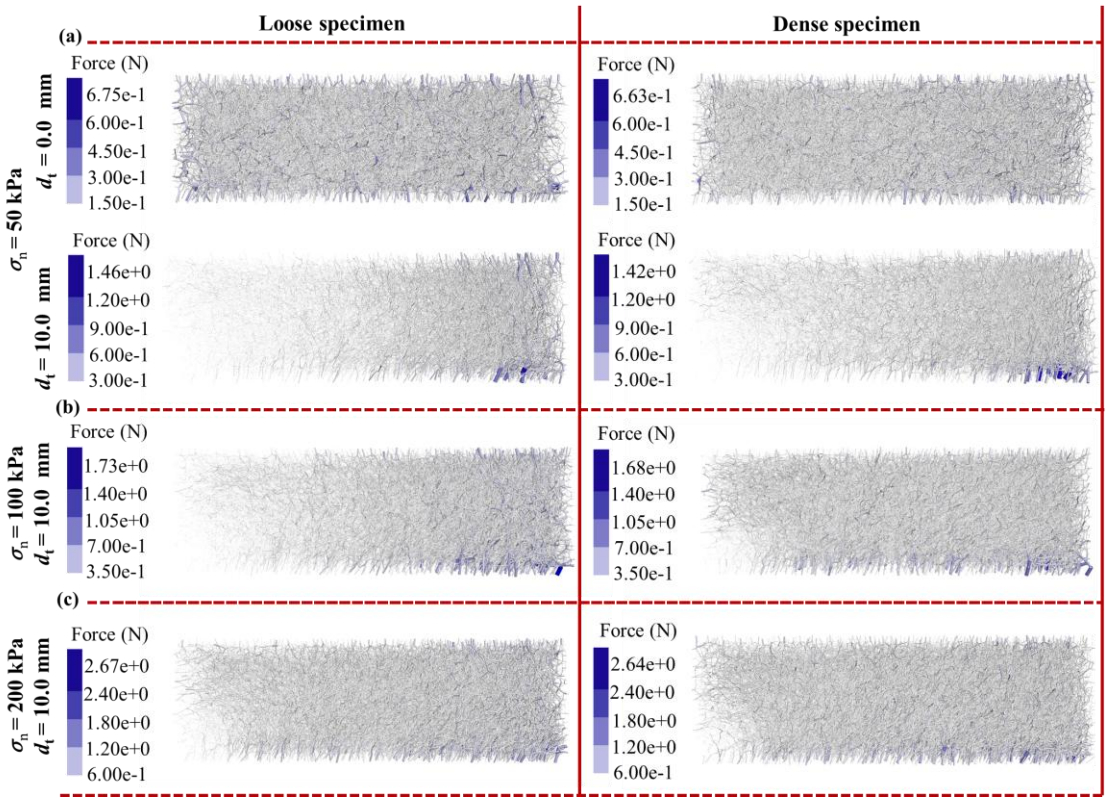

Figure 5-18 Force chains at M-1500FRP interfaces (a) initial state and ultimate state at 10 mm tangential displacement under 50 kPa normal stress; for the ultimate state of 10 mm tangential displacement (b) under 100 kPa normal stress and (c) under 200 kPa normal stress

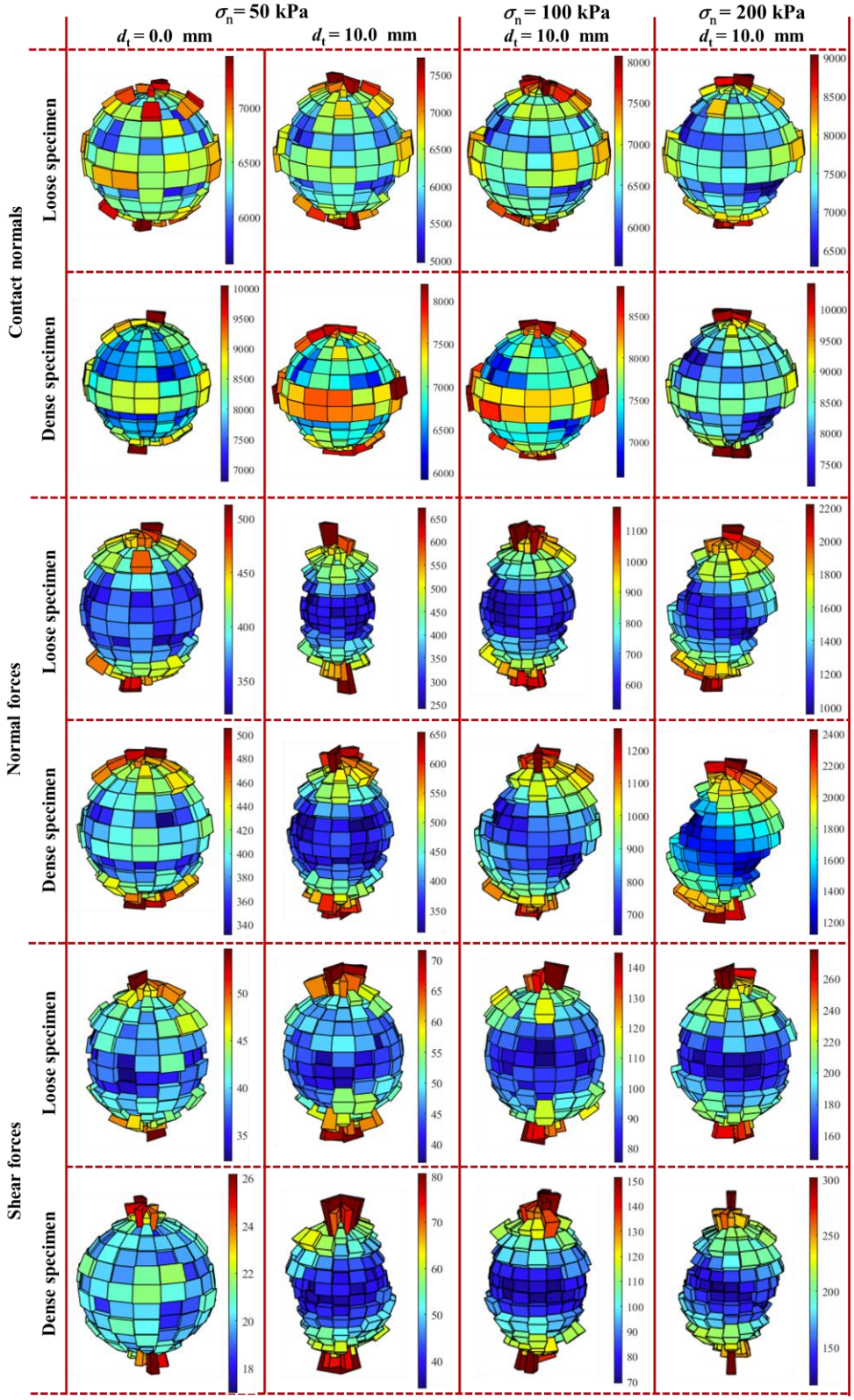

Figure 5-19 (a) Distribution of contact normals, normal forces, and shear forces in M-1500FRP interface for loose and dense sand specimens under 50 kPa, 100 kPa, and

200 kPa normal stress

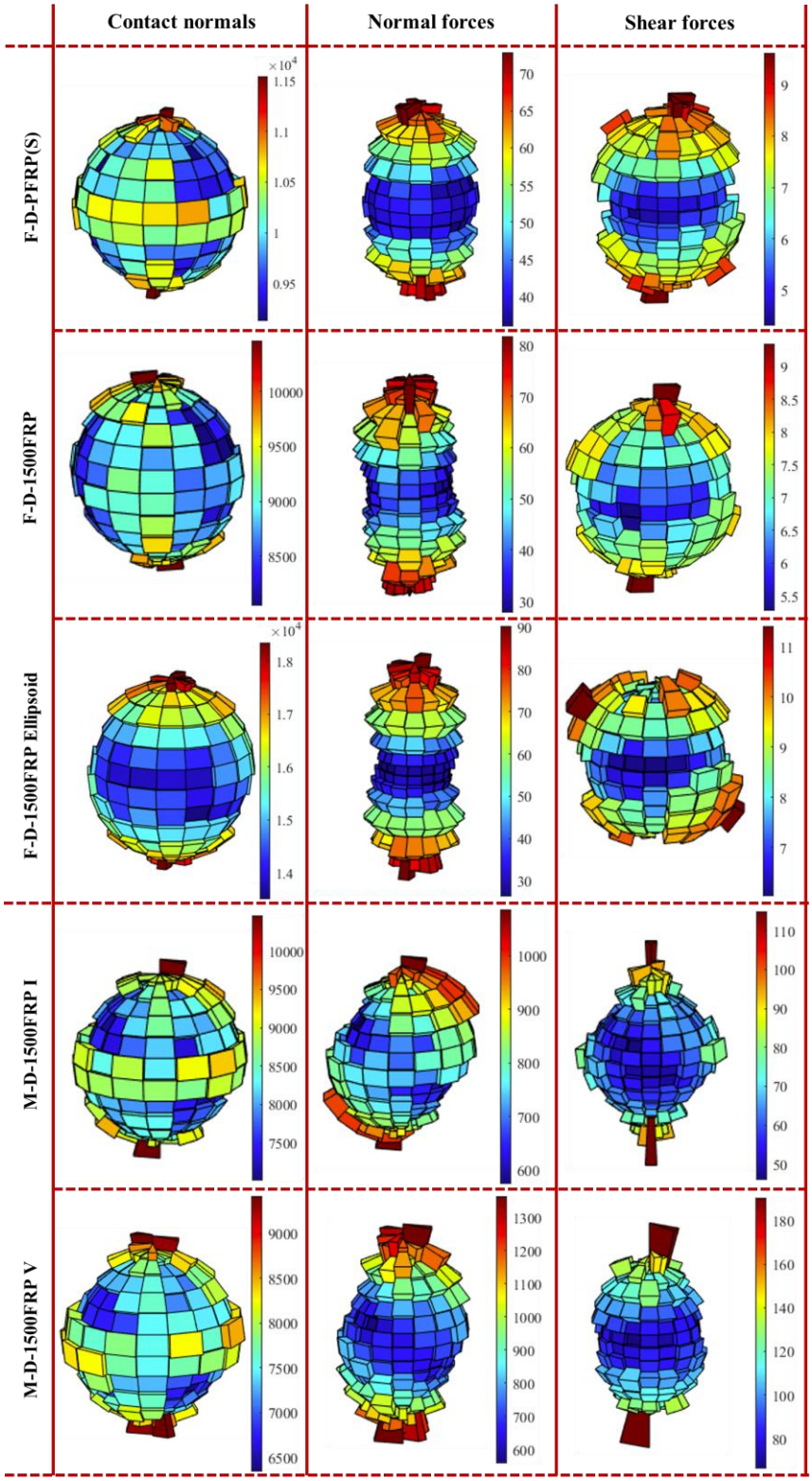

Figure 5-20 Variation in contact normals, normal forces, and shear forces at interfaces for dense specimens of fine and medium sands under 100 kPa normal stress

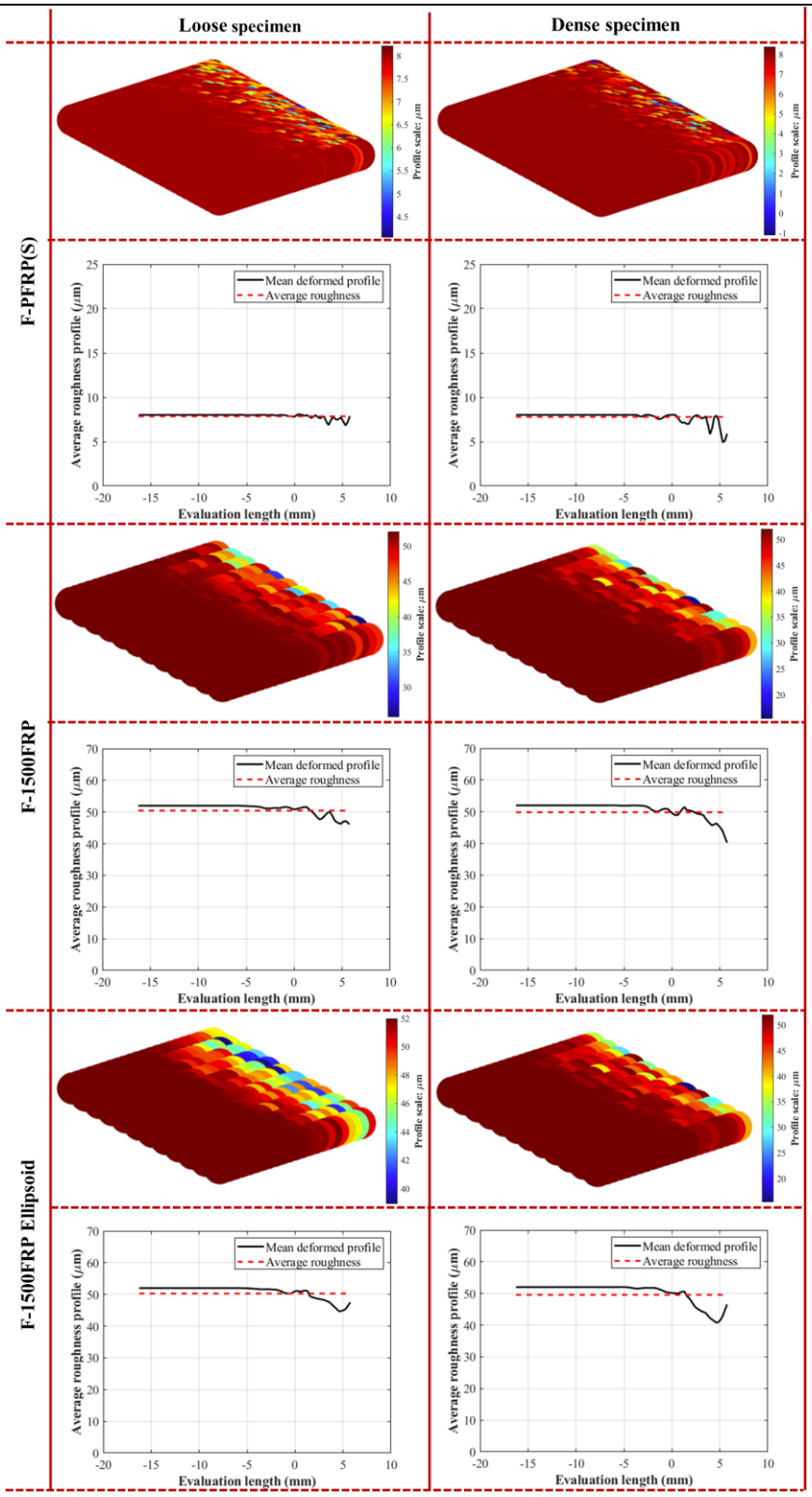

Figure 5-21 3D surface deformation and 2D plot of average roughness profile along the shearing length of GFRP while shearing loose and dense specimens of fine sand against PFRP(S) and 1500FRP under 100 kPa normal stress

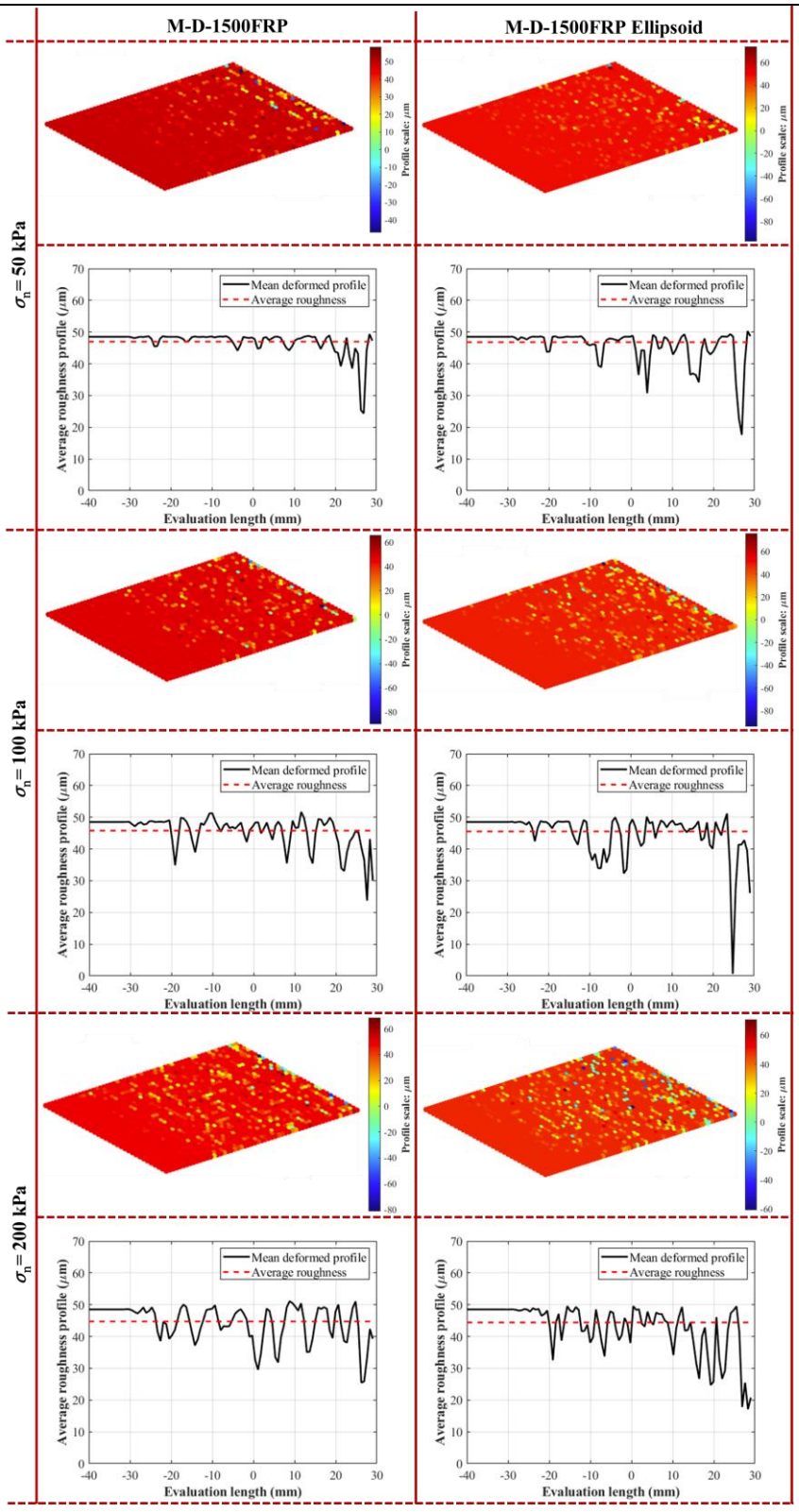

Figure 5-22 Particle shape effect of dense medium sand on surface deformation and average roughness profile of 1500FRP under 50 kPa, 100 kPa, and 200 kPa normal stress

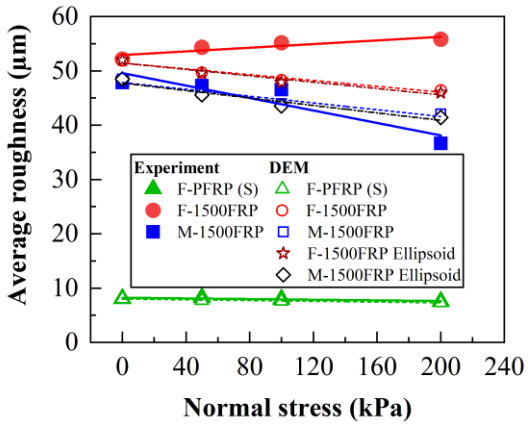

Figure 5-23 Comparison of GFRP average roughness variation with respect to normal stress at experiment and DEM

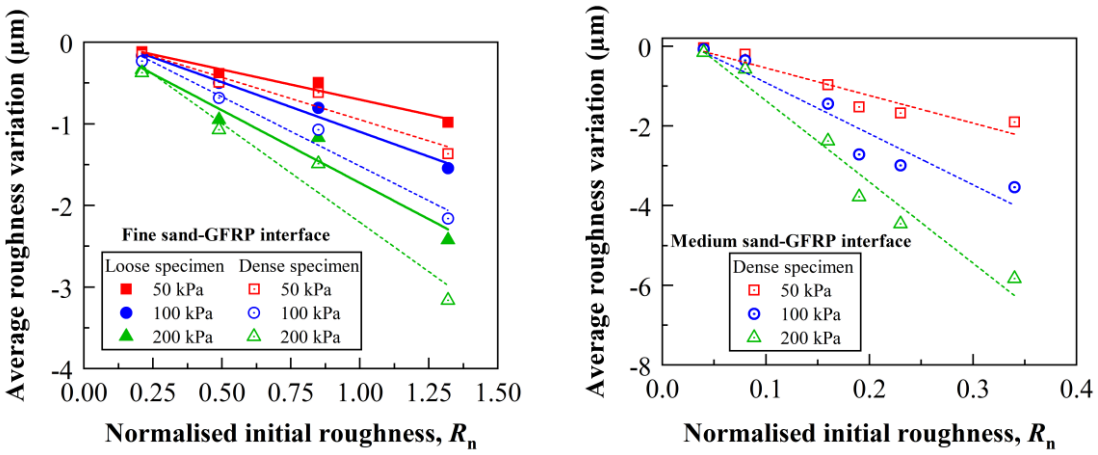

(a) (b)

Figure 5-24 Average roughness variation in GFRP with respect to normalised initial roughness for (a) loose and dense fine sand-GFRP interfaces and (b) dense medium sand-GFRP interfaces

Table 5-1 Comparison of particle morphology between experiments and DEM simulations

Sand type	D_{50} (mm)	DEM (Ellipsoids)		Circularity[1]		Sphericity[1]	
		a (mm)	a/b	Experiment	DEM	Experiment	DEM
Fine sand (F)	0.225	0.1428	1.428	0.726	0.7	0.852	0.972
Medium sand (M)	1.015	0.5648	1.176	0.855	0.85	0.924	0.989

Note: D_{50} refers to the mean particle size, a refers to the major radius of an ellipsoid corresponding to the mean particle size, a/b refers to the aspect ratio where b is the minor radius of an ellipsoid; [1]mean values.

Table 5-2 Indentation simulation data and calibrated results

GFRP type[1]	Mean indenter diagonal[1] (μm)	Equivalent depth of steel ball[2] (μm)	Shear modulus (GPa)
PFRP(S)	81	12.5	9.1
500FRP	79	12	9.5
1000FRP	62	8.2	17.2
1500FRP	60	7.3	21
PFRP(R)	82	12.7	8.8

Note: [1] Item and corresponding data are imported from Table 3-2; [2] steel ball consists of a 60 μm diameter.

Table 5-3 Calibrated model parameters for sand-GFRP interface direct shear test

Type	Parameters	Parametric values for spheres		Parametric values for ellipsoids	
		Fine sand	Medium sand	Fine sand	Medium sand
General properties	Density of sand particles, ρ_s (kg/m^3)	2650			
	Density of FRP balls, ρ_g (kg/m^3)	1800			
	Poisson's ratio for GFRP, ν_g	0.3			
	Initial void ratio, e_0 (dense)	0.681	0.667	0.518	0.563
	Initial void ratio, e_0 (loose)	0.754	0.765	0.626	0.672
Rolling resistance linear model	Normal stiffness of sand particles, k_n^p (N/m)	2.625e3	1.05e4	1.5e3	9.0e3
	Shear stiffness of sand particles, k_s^p (N/m)	1.75e3	7.0e3	1.0e3	6.0e3
	Normal stiffness of wall, k_n^w (N/m)	5.25e4	1.05e5	3.0e4	9.0e4
	Shear stiffness of wall, k_s^w (N/m)	3.5e4	7.0e5	2.0e4	6.0e4
	Sand particles' friction coefficient, μ	0.76	0.6	0.76	0.6
	Particle-wall friction coefficient, μ_w	0.2			
	Particle-particle rolling resistance coefficient for dense (loose) specimen, μ_r	0.05 (0.02)	0.05 (0.02)	0.02 (0.00)	
	Particle-GFRP rolling resistance coefficient for dense (loose) specimen, μ_r^g	0.1 (0.08)	0.1 (0.08)	0.08 (0.05)	

(Continued)

Table 5-3 (Continued) Calibrated model parameters for sand-GFRP interface direct shear test

Type	Parameters	Parametric values for spheres		Parametric values for ellipsoids	
		Fine sand	Medium sand	Fine sand	Medium sand
EEPA model	Effective surface adhesion energy, γ^* (energy/area)	1000			
	Pull-off force, F_0 (N)	-200			
	Plasticity ratio, λ_p	0.99			

Table 5-4 Simulation scheme of sand-GFRP interface shear tests and roughness

S.N.	Specimen ID	Particle shape	D_{50} (mm)	Specimen type	Amount of epoxied sand (g/m^2)	Surface type [Bracketed item]	Roughness			
							R_a[1] (μm)	R_a[2] (μm)	R_{max} (μm)	R_n
1	F-L-PFRP (S)	Sphere	0.225	Loose	n/a	Smooth	8.06	8	52.0	0.21
	F-D-PFRP(S)			Dense						
2	F-L-500FRP			Loose	500		19.37	19	123.2	0.49
	F-D-500FRP			Dense						
3	F- L -1000FRP			Loose	1000	n/a	33.67	33	217.2	0.85
	F- D -1000FRP			Dense						
4	F- L -1500FRP			Loose	1500		52.18	52	346.1	1.32
	F- D -1500FRP			Dense						
5	M- L -PFRP(R)	Sphere	1.015	Loose	n/a	Rough	28.03	27.5	180.3	0.11
	M- D -PFRP(R)			Dense						
6	M- L -1500FRP			Loose	1500	n/a	47.83	48.5	322.4	0.19
	M- D -1500FRP			Dense						
7	F-L-1500FRP	Ellipsoid	0.225	Loose	1500	n/a	52.18	52	346.1	1.32
	F-D-1500FRP			Dense						
8	M-L-1500FRP		1.015	Loose			47.83	48.5	322.4	0.19
	M-D-1500FRP			Dense						

(Continued)

Table 5-4 (Continued) Simulation scheme of sand-GFRP interface shear tests and roughness

S.N.	Specimen ID	Particle shape	D_{50} (mm)	Specimen type	Amount of epoxied sand (g/m^2)	Surface type [Bracketed item]	Roughness			
							R_a [1] (μm)	R_a [2] (μm)	R_{max} (μm)	R_n
9	M-D-1500FRP I	Sphere	1.015	Dense	1500	n/a	n/a	10	64.5	0.04
10	M-D-1500FRP II						n/a	20	131.0	0.08
11	M-D-1500FRP III						n/a	40	265.5	0.16
12	M-D-1500FRP IV						n/a	60	408.2	0.23
13	M-D-1500FRP V						n/a	100	725.8	0.34

Note: [1] refers to the data of average roughness (R_a) from S.N. 1 to 6 of plain GFRP and sand-epoxied GFRP imported from Chapter 3; [2] refers to the approximation for average roughness (R_a) and corresponding maximum roughness (R_{max}) of bonded assembly of GFRP for simulation; R_n refers to normalised interface roughness; bold letters refer to the special case of ellipsoid particles.

Table 5-5 Summary of interface materials and model setup

Reference	D_{50} [Particle size range] (mm)	e_0	Structure type	Normal stress (kPa)	R_n	Testing type
Present study (Sphere)	0.225 [0.15–0.3], 1.015 [0.85–1.18]	0.66–0.76	GFRP and sand-epoxied GFRP (overlapped balls)	50, 100, 200	0.11–1.32	IDST
Present study (Ellipsoid)		0.51–0.67			0.19, 1.32	
Experiment (Chapter 3)		0.61–0.70	GFRP and sand-epoxied GFRP		0.11–1.32	
Grabowski et al. (2021a)	0.5 [0.25–0.75]	0.55	Sawtooth rigid plate (wall)	100[1]	0.01–2.0	
Feng et al. (2020)	0.65 [0.38–0.87]	0.65	Woven geotextile (overlapped balls)	107[1]	0.03, 0.19, 0.3	
Feng et al. (2018)	0.74 [0.6–0.85]	0.66	Geomembrane (overlapped balls)	100[1]	0.02, 0.25, 0.5	
Jing et al. (2018)	3.48 [2.46–4.03]	0.34–0.54	Sawtooth rigid plate (wall)	40, 60, 80, 100	Smooth (0.005)–1.0	

Note: e_0 refers to the initial void ratio; [1]under the given normal stress conditions, friction angles are determined using methods other than the Mohr-Coulomb criterion, specifically the peak secant friction angle at the peak state.

CHAPTER 6: FEM MODELLING OF SAND-GFRP INTERFACE UNDER MONOTONIC AND CYCLIC SHEAR LOADING

6.1 Introduction

While the Discrete Element Method (DEM) in Chapter 5 provided valuable micromechanical insights into the sand-GFRP interface, its particle-scale approach is computationally intensive and limited in capturing large-scale interface behaviour. To bridge this gap, this chapter employs a continuum-based finite element approach to model the global response of the sand-GFRP interface, validating experimental findings and extending the understanding of interface shear behaviour under practical loading conditions.

The hyperbolic model by Duncan and Chang (1970) and Clough and Duncan (1971) is widely used for stress-dependent, non-linear soil-structure interfaces, but does not account for stress-dilatancy behaviour. To address this limitation, the enhanced hyperbolic model, introduced in Chapter 2, incorporates a non-linear shear modulus to capture incremental stress dilatancy, integrates critical state principles, considers particle breakage, and accounts for cyclic reversal effects. This refined constitutive model is calibrated against experimental data using an optimisation approach, ensuring predictive accuracy (Powell, 1964; Hansen, 2007; Yin et al., 2018a). The model is implemented in ABAQUS 2021 using the FRIC and VFRIC subroutines to simulate complex shear transmission behaviour at the interface. The numerical approach enables the evaluation of interface shear response under varying conditions, complementing DEM findings by providing a macroscopic perspective on interface mechanics. Simulation results are compared with experimental data to assess the model's predictive performance and validate the testing methodology.

The novelty of this work lies in extending the enhanced hyperbolic

framework, originally applied to soil-concrete and soil-steel systems, to capture the unique interfacial mechanisms of sand-GFRP, which has not been previously reported in the literature. This chapter is thus essential for developing a comprehensive understanding of sand-GFRP interactions, employing continuum-based macro-scale analyses to achieve a robust evaluation of interface behaviour.

6.2 Interface model and parameters

6.2.1 Model formulation

The complete constitutive derivation, energetic breakage formulation, and cyclic hysteresis model are presented in full in Chapter 2. For clarity of the present constant normal loading (CNL) simulations, the following presents only the core governing relations and the closed set of state updates used in the numerical implementation. Readers are referred to Chapter 2 for the full derivations and implementation details. The following equations constitute the compact set needed for CNL simulations; all other relevant expressions are referenced from Equations (2-26) to (2-46) (Biarez and Hicher, 1994; Daouadji et al., 2001; Daouadji and Hicher, 2010; Hu et al., 2011; Liu et al. 2014; Yin et al., 2018b; Yang and Yin, 2021; Wang et al. 2024a). The hyperbolic mobilised shear stress ratio (η) is expressed as:

$$\frac{\tau}{\sigma_n + \sigma_a} = \tan(\phi_p)\frac{\gamma}{a + \gamma} \tag{6-1}$$

where τ refers to the shear stress, σ_n refers to the normal stress, σ_a refers to the adhesion or apparent stress, ϕ_p refers to the peak friction angle, γ refers to the shear displacement, a refers to the characteristic displacement. The tangent shear modulus is obtained by differentiation:

$$G\ (\gamma, \sigma_n) = \frac{d\tau}{d\gamma} = (\sigma_n + \sigma_a)\tan(\phi_p)\left[\frac{1}{(a+\gamma)} - \frac{\gamma}{(a+\gamma)^2}\right] \tag{6-2}$$

where G refers to the tangent shear modulus obtained from the hyperbolic model. The characteristic displacement (initial tangent) prior to shearing ($\gamma = 0$) is defined as:

$$a = \frac{(\sigma_n + \sigma_a)\tan(\phi_p)}{G} \tag{6-3}$$

Under CNL conditions ($d\sigma_n = 0$), the incremental shear stress can be written as:

$$d\tau = G\left(\frac{a}{a+\gamma}\right)\left(1 - \frac{\eta}{\tan(\phi_p)}\right)d\gamma, \qquad \eta \equiv \frac{\tau}{\sigma_n + \sigma_a} \tag{6-4}$$

For CNL incremental normal displacement ($du_n = du_n^{in}$), the dilatancy or inherent normal displacement is:

$$du_n^{in} = A_d(\tan(\phi_{pt}) - \eta)d\gamma \tag{6-5}$$

where du_n^{in} refers to the incremental normal displacement, A_d refers to the dilatancy coefficient parameter, ϕ_{pt} refers to the phase transformation angle. Update shear modulus with nonlinearity caused by initial density and normal stress, is defined as:

$$G(\sigma_n, e) = G_0 \frac{(2.97 - e)^2}{1 + e}\left(\frac{\sigma_n + \sigma_a}{P_{at}}\right)^{n_g} \tag{6-6}$$

Where G_0 refers to the reference shear modulus, e refers to the current packing state, P_{at} refers to the atmospheric pressure at mean sea level, n_g refers to the stress exponent (n_g= 0.6). The breakage index (B_r^*) is expressed as:

$$B_r^* = \frac{\mathrm{W}^{n_w}}{b + \mathrm{W}^{n_w}}, \qquad W = \int (\langle \sigma_n du_n \rangle + \tau d\gamma) \tag{6-7}$$

where n_w refers to the material parameter, b fitting constant, and W refers to the work input. The translation of the critical state line (CSL) is obtained through reference critical void ratio (e_{ref}), and expressed as:

$$e_{ref} = e_{refu} + (e_{ref0} - e_{refu})\exp(-\rho B_r^*) \tag{6-8}$$

where e_{ref0} refers to the virgin reference critical void ratio and e_{refu} refers to the ultimate reference critical void ratio. Utilising the critical state concept, critical void ratio (e_c) dependent to reference critical void ratio and corresponding atmospheric pressure and applied normal stress can be obtained.

$$e_c = e_{ref} exp\left[-\lambda\left(\frac{\sigma_n}{P_{at}}\right)^{\xi}\right] \tag{6-9}$$

Where λ and ξ are the parameters which control the slope and the nonlinearity of the CSL in the $e-\sigma_n$ plane. The update in void ratio is essential due to a change in normal displacement, which is expressed as:

$$\Delta e = -du_n(1+e_0) \tag{6-10}$$

where e_0 refers to the initial void ratio. For cyclic shear conditions, the cyclic incremental normal displacement considering reversal is:

$$du_n^{in} = A_d\left(\tan\left(\phi_{pt}\right)^* - |\eta - \eta^R|\right)|d\gamma| \tag{6-11}$$

where η^R refers to the shear stress ratio at reversal and $|d\gamma|$ refers to the absolute shear displacement increment. All equations of the enhanced hyperbolic model are governed by three categories of property parameters: basic, critical state, and breakage. A total of 18 parameters, including the initial void ratio and mean particle size (D_{50}), are incorporated into the interface model to capture the experimentally observed behaviour of the sand-GFRP interface, as summarised in Table 6-1. This categorisation provides a clear framework for subsequent calibration, parameter identification, and numerical implementation.

6.2.2 Model calibration and parameter identification

The optimisation of the interface model parameters was conducted using the Covariance Matrix Adaptation Evolution Strategy (CMA-ES) algorithm, with the PyCMA implementation employed to regulate the step size covariance updates (Hansen, 2007). This stochastic optimisation method is particularly advantageous for handling the non-convex, ill-conditioned, multi-modal, and noisy nature of calibration data, enabling efficient parameter estimation even in a high-dimensional (18-variable) space within a short computational time in Python. By setting appropriate lower and upper bounds and initialising parameters within realistic ranges, the CMA-ES algorithm reduces the risk of convergence to local minima and increases the probability of identifying parameter sets that closely match experimental observations. Using this approach, the interface model parameters were determined through the calibration against experimental results, as summarised in Table 6-1 and Figure 6-1.

Among 18 parameters, 15 parameters were treated as variables during the calibration process. A minimum global step size of 1×10^{-4}, along with appropriately set lower and upper bounds, is crucial to achieving an efficient time-cost trade-off during optimisation. Furthermore, the initialisation involved assigning appropriate initial values within the bounds for each parameter and setting the covariance matrix as an identity matrix ($C = I$). The targeted objective was to achieve a good fit, with the root mean square error generally around 10%, closely matching the experimental results. The overall procedure for optimising these parameters is illustrated in Figure 6-1, which outlines a stepwise approach for adjusting and calibrating the key parameters, thereby enabling the enhanced hyperbolic interface model to provide a reliable representation of the experimental observations.

6.2.3 Numerical implementation

The sand-GFRP interface was modelled using ABAQUS software, employing the non-linear incremental hyperbolic model in conjunction with the finite element method. ABAQUS is a finite element analysis (FEA) computer-aided engineering program that incorporates implicit and explicit schemes, computational fluid dynamics, and computational electromagnetics. The constitutive equations of the enhanced hyperbolic model and the frictional behaviour between contact pair surfaces, as described in Chapter 2 with key governing equations explicitly stated in Section 6.2.1, were implemented using the Standard/Explicit user subroutine in FORTRAN (e.g., Saberi et al., 2019). This subroutine governs shear transmission at the soil-GFRP interface. Within the user subroutine script, stresses and strains were initially set to zero, with incremental strains and stresses updated over time. Similarly, all state variables, including dilatancy variables, void ratios, and particle breakage parameters, were updated at the end of each time increment to accurately capture the evolving interface behaviour.

The user subroutine FRIC, within the ABAQUS/Standard product, operates as an implicit global solution algorithm designed for general-purpose finite element analysis. In this framework, displacement-controlled boundary

conditions are defined. To allow relative displacement between the sand and GFRP contact surfaces, the relative motion flag (LM) is set to zero, and the frictional stresses are specified accordingly. Conversely, the user subroutine VFRIC, within the ABAQUS/Explicit product, employs an explicit global solution algorithm tailored for highly non-linear systems involving complex contact interactions under transient loading conditions. In this case, velocity-controlled boundary conditions are prescribed. To define contact constraint enforcement methods at the user interface, either kinematic or penalty contact algorithms can be utilised. In surface-to-surface contact modelling, the kinematic constraint is adopted. The specification of slip directions in VFRIC is crucial for capturing incremental slip behaviour. The characteristic length is considered within small time increments to prevent divergence issues in small-element analyses. A total of 33 state variables is allocated for the FRIC subroutine, while 36 state variables are assigned to VFRIC, as summarised in Table 6-2. Although ABAQUS adopts a negative sign convention for compressive stresses and volume contractions, shear stresses are consistently represented with a positive sign, while volume contractions remain negative. This ensures uniformity between experimental and simulation results.

For the 3D modelling of the sand-GFRP interface direct shear test, the sand specimen and GFRP plate dimensions were selected to match the experimental conditions. For monotonic shearing, the sand specimen measures 60 mm (length) × 60 mm (width) × 18 mm (height), while the GFRP plate measures 100 mm (length) × 100 mm (width) × 20 mm (height). For cyclic shearing, the sand specimen dimensions are 100 mm (length) × 100 mm (width) × 25 mm (height), and the GFRP plate dimensions are 300 mm (length) × 300 mm (width) × 20 mm (height). The sand specimen dimensions remain consistent between the experimental tests and numerical simulations, as presented in Figure 6-2. Similarly, a maximum displacement of 10 mm was set for monotonic shearing.

To evaluate the potential influence of mesh size on the soil-GFRP interface response, a sensitivity study was performed using different mesh discretisations, ranging from no mesh division to 2.0 × 1.0 mm and 2.0 × 3.0 mm (horizontal ×

vertical). The minimum mesh size in this study was chosen based on the estimated shear zone thickness, which typically extends to about 3 to 5 times the mean particle diameter (D_{50}) in DEM simulations. For experimental soil specimens, the shear zone can extend to slightly larger values, but this criterion provides a reasonable basis for mesh discretisation. Figure 6-3 presents the corresponding results under a normal stress of 200 kPa at the F-D-1500FRP interface. The comparison clearly shows that the variation in mesh size has an insignificant effect on the shear stress-tangential displacement and normal displacement-tangential displacement relationships. Although a nonlinear constitutive model was employed to represent interface behaviour, the influence of mesh dependency remains minimal due to the relatively simple soil model.

Both single-element and multi-element models were developed in ABAQUS/CAE to compare the simulation results of the FRIC and VFRIC subroutines in monotonic shearing (Figure 6-2). In the multi-element model, a mesh size of 6 mm is assigned to the sand specimen, whereas a mesh size of 10 mm is assigned to the GFRP plate, as illustrated in Figure 6-2. The displacement in the simulation is restricted to 10 mm, with the velocity set at 0.01 mm/s. Five selected monotonic shear tests from Chapter 3 are calibrated, simulated, and compared with experimental results. Based on the findings, several parameters are examined to understand parameter sensitivity in the model prediction and highlight crucial parameters.

For the cyclic interface model, a mesh size of 5 mm is applied to the sand specimen, while a 10 mm mesh size is used for the GFRP plate, as illustrated in Figure 6-2. Several test results from Chapter 4 are calibrated and then simulated by an enhanced hyperbolic model for plotting. Cyclic tests involving cyclic amplitudes of ±1.0 mm, ±2.5 mm, and ±5.0 mm are considered to examine the effect of amplitude at the interface and compared with experimental findings presented in Chapter 4. Furthermore, nine selected interface cyclic shear tests at the tangential displacement of ±2.5 mm from Chapter 4 are simulated and compared with experimental findings. A detailed summary of the simulation scheme is provided in Table 6-3.

6.3 Modelling of the sand-GFRP interface under monotonic shearing

The model parameters used for interface modelling under monotonic shearing are presented in Table 6-4. The calibration results demonstrate good agreement with experimental data, yielding a root mean square error (RMSE) within 8.5%. Figure 6-4 illustrates the single-element and multi-element simulation results for FRIC and VFRIC models applied to F-PFRP(S) under a 200 kPa normal stress, separately for dense and loose specimens. The results again confirm that the influence of meshing is negligible, indicating that both single-element and multi-element models are suitable for interface modelling. Furthermore, both FRIC and VFRIC predict comparable stress levels and normal displacement behaviours, demonstrating algorithmic consistency with no significant differences in their predictive capabilities. Although the simulation results of the single-element and multi-element models are consistent, all sand-GFRP interface simulations under monotonic shearing conditions were conducted using the multi-element model to ensure a more comprehensive representation of interface behaviour.

Figure 6-5 shows the model simulation and test results of shear stress-tangential displacement and normal displacement-tangential displacement for fine and medium sand against GFRP interfaces. In the case of softening behaviour in dense specimens, simulation results predicted for F-1500FRP are considerable, which might be influenced by the calibration of both loose and dense specimen interfaces. However, hardening effects are matched in F-PFRP(S). In the case of normal displacement, model prediction in dilation is in better agreement with experimental results than in contractive response. In the case of the M-1500FRP interface, more precisely, model results are matched with test results for stress state and dilative behaviour.

Model results for the S1-PFRP(R) interface in Figure 6-6 matched well for loose and dense specimens with test results, while simulation results for the S4-PFRP(R) interface are lacking in predicting strain-softening behaviour. These results might be attributed to poor fitting, which arises due to almost overlapping

one another's volumetric behaviour at testing under 100 and 200 kPa. The adopted model could capture the basic characteristics of the interface, such as dilative response for dense sand and contractive response and hardening for the loose sand, for all the interfaces. However, understanding the sensitivity of the parameters in strain-softening, hardening, dilation, and contraction response is further required.

6.3.1 Parametric study on model parameters

Among the 18 parameters of the enhanced hyperbolic model, seven key parameters are selected for a parametric study, representing all three categories: basic parameters, critical state parameters, and breakage parameters, as outlined in Table 6-5. Two interface types, F-1500FRP and S4-PFRP(R), are analysed under a 200 kPa normal stress as representative cases. The parameter variation ranges are determined based on calibrated parameter distributions, ensuring coverage from minimum to maximum values typically used for model training, fitting, and prediction (Powell, 1964; Yin et al., 2018a; Wang et al., 2024a). Each interface is monitored at three key locations for dense specimens: at 1 mm of tangential displacement, peak state, and ultimate state. For loose specimens, only two locations are considered: at 1 mm of tangential displacement and at the ultimate state. The elastic region is crucial in evaluating stiffness, initial contraction, and dilation behaviour. Therefore, 1 mm of tangential displacement is selected as a reference initial state for assessing these characteristics.

The effect of dilatancy parameter variation on the interface friction coefficient and normal displacement is illustrated in Figure 6-7. For loose specimens, the friction coefficient increases as the dilatancy parameter increases across the entire parameter range, indicating a gradual transformation from a loose to a dense state. In contrast, the interface friction coefficient remains stable for dense specimens, reflecting consistent stiffness within the elastic range at 1 mm of tangential displacement. The ultimate interface friction coefficient decreases as the dilatancy parameter increases up to 0.75, beyond which it stabilises. Conversely, the ultimate friction coefficient for loose specimens

follows an inverse trend, increasing with the dilatancy parameter. Figure 6-7(b) shows that normal displacement remains stable for dense specimens, whereas initial contraction increases sharply with higher dilatancy parameters for loose specimens. The ultimate normal displacement decreases until the dilatancy parameter reaches 0.5, after which it stabilises. This trend confirms that higher dilatancy parameters induce densification in loose specimens. Furthermore, the parameter range of 0.1 to 0.5 exhibits sensitivity to variations in both the friction coefficient and normal displacement, highlighting its critical influence on interface behaviour.

The shape factor (λ) governs the form of the critical state line. As illustrated in Figures 6-8(a) and (b), the initial interface friction coefficient is notably influenced by variations in the shape factor, exhibiting a declining trend as λ increases from 0.001 to 0.5, after which it stabilises. Conversely, the ultimate friction coefficient experiences a slight reduction until λ reaches 0.5, beyond which it remains constant. In the case of normal displacement, an increase in the shape factor results in a continuous decrease for both loose and dense specimens. This behaviour suggests that an increase in λ alters the shape of the critical state line, inducing a contractive response in dense specimens.

As illustrated in Figure 6-9(a), the influence of the non-linearity factor of the CSL on the interface is primarily observed in the initial interface friction coefficient. The friction coefficient decreases linearly as the non-linearity factor increases, indicating a reduced elastic stiffness. For normal displacement, initial and ultimate normal displacement decrease with an increasing non-linearity factor for loose and dense specimens of the F-1500FRP interface, accompanied by a transition from dilative to contractive behaviour. However, as shown in Figure 6-9(b), the S4-PFRP(R) interface exhibits a negligible response to variations in the non-linearity factor.

As shown in Figure 6-10(a), an increase in the exponent of the peak friction angle results in a significant increase in the interface friction coefficient for dense specimens. The friction coefficient increases with the exponent, with this effect being more pronounced for the S4-PFRP(R) interface. However, the ultimate

friction coefficient remains largely unaffected by variations in the exponent of the peak friction angle for both interfaces. As depicted in Figure 6-10(b), the dilative behaviour of dense specimens intensifies when the exponent exceeds 2, whereas the contractive behaviour of loose specimens remains stable. This suggests that an increase in the exponent of peak friction angle enhances softening behaviour in dense specimens.

Figure 6-11 shows the effect of variations in the exponent of mobilised phase transformation angle on the interface friction coefficient and normal displacement. For dense specimens, the initial and ultimate interface friction coefficients decrease slightly until the exponent value reaches 2, after which they stabilise. In contrast, no significant influence on the friction coefficient is observed for loose specimens in either interface. Regarding normal displacement, the enhanced dilative behaviour is apparent for dense specimens up to an exponent value of 2. Beyond this point, both interfaces for dense and loose specimens follow their respective natural dilative and contractive behaviour trends.

The effect of particle breakage in the interfaces can be understood by examining variations in the constant for the evolution rate of CSL due to particle breakage (b) and the parameter for the decreasing rate of CSL (ρ). The interface friction coefficient exhibits sensitivity to b up to a value of 1000, after which it stabilises, as shown in Figure 6-12(a). However, this effect is negligible for fine sand, while sand mixtures exhibit softening behaviour as b increases. As shown in Figure 6-12(b), dilative behaviour for dense specimens of the S4-PFRP(R) interface is significantly affected by changes in b. The increase in b may lead to the densification of the sand mixture, resulting in higher stiffness and potentially contributing to softening behaviour.

The variation in the breakage parameter for the decreasing rate of CSL (ρ) has a negligible effect on the ultimate interface friction coefficient. However, the interface friction coefficient for loose specimens decreases significantly in the elastic region, indicating that stiffness reduction occurs as ρ increases (Figure 6-13). When ρ is smaller than 50, the model transitions to densification, leading to

peak formation in the S4 specimen and a large dilation at the minimum values of the input parameter, as shown in Figure 6-13(b). With further increases in ρ, the contractive behaviour intensifies, and this sensitivity remains evident up to a ρ value of 10, after which it stabilises. Thus, this parametric analysis enables researchers to select suitable parameters by knowing the sensitive ranges. It assists in setting an initial calibration range and modification, if necessary, based on the results obtained.

6.4 Modelling of the sand-GFRP interface under cyclic shearing

The simulation schemes from 6 to 12 in Table 6-3 represent cases from Chapter 4, which examine the effects of amplitude, particle size, and surface roughness. The model parameters are calibrated based on the test results summarised in Table 6-6. These parameters are calibrated separately to capture the surface characteristics, with the evolution of surface roughness of GFRP differing for each case at the interfaces, which contrasts with the sand-steel interface (e.g., Yang and Ying, 2021; Wang et al., 2024b). The root mean square error for all the calibrated parameters is within 10%, except for C-D-PFRP(S).

As shown in Figure 6-14, the model successfully captures the hardening and contractive behaviour of the interface subjected to cyclic shearing at ± 1.0 mm amplitude. However, the dilative behaviour during the first few cycles at larger amplitudes (i.e., ± 2.5 mm and ± 5.0 mm) is not adequately captured, as observed in Figures 6-14(b) and 6-14(c). Furthermore, Figures 6-15 and 6-16 display the model's prediction for the particle size effects on PFRP(S) and 750FRP(R) surfaces. The hardening and contractive behaviour of sand-PFRP(S) interfaces and the softening and dilative behaviour of sand-750FRP(R) interfaces are associated with smooth and rough interfaces, respectively (e.g., Shahrour and Rezaie, 1997; Yin and Chang, 2013; Saberi et al., 2019; Yang and Yin, 2021). Although the initial void ratio of the dense specimen is already very small, the observed contractive normal displacement behaviour after the first few cycles of dilation remains considerable due to particle breakage. However, the predicted

dilative behaviour, which aligns with experimental results, is contingent on quality calibration and the selection of appropriate model parameters.

While the model's prediction of softening and dilative behaviour in the sand-steel interface, as presented in Yang and Yin (2021) and Wang et al. (2024b), was found to be inferior to the exponential model, a satisfactory prediction for the sand-GFRP interface under constant normal stress was achieved in the present study. Further research is needed to incorporate a roughness parameter into the model, which could effectively enhance this hyperbolic model, particularly in encapsulating the variable surface roughness at the sand-GFRP interface.

6.5 Linking DEM insights to continuum FEM and model limitations

While the FEM model operates at the continuum scale and does not explicitly resolve particle-level interactions, prior DEM analyses provide valuable perspectives that enhance both modelling and interpretation. DEM revealed key micromechanical mechanisms at the sand-GFRP interface, such as grain interlocking, surface roughness engagement, and local rearrangements under shear, which inform a more physically grounded understanding of continuum responses.

These insights guide mesh discretisation, parameter selection, and help define reasonable ranges for peak friction angle, dilatancy, and shear modulus, even without directly transferring DEM values. They also improve the interpretation of FEM results, linking observed stress-displacement trends and interface softening to underlying microscale behaviour.

Although the enhanced hyperbolic model successfully reproduces general shear stress-displacement behaviour across different surface roughness, particle sizes, and shearing amplitudes, discrepancies remain in predicting volumetric responses, particularly normal displacement under cyclic shearing (e.g., Figure 6-13). The parametric study (Section 6.3.1) demonstrates that key parameters such as dilatancy, shape factor, and critical state non-linearity strongly influence

interface contraction and dilation; however, the current continuum formulation treats these effects indirectly and cannot explicitly resolve localised particle rearrangements, progressive interlocking, or micro-scale densification that drive volumetric changes in loose specimens. Additionally, cyclic amplitudes beyond the initial elastic range exacerbate particle breakage and surface asperity interactions, which are only partially represented through parameter evolution. Consequently, while frictional hardening and softening trends are captured, the model underestimates initial dilative responses and subsequent contractive-dilative transitions, especially for rough or mixed sand interfaces. These limitations suggest that incorporating an explicit roughness evolution parameter or a microstructure-informed dilatancy function could improve the predictive capability of volumetric behaviour in future model developments, bridging the gap between continuum-scale FEM and microscale mechanisms revealed in DEM and experimental observations.

Finally, this sequential approach combines the strengths of both methods: DEM offers detailed physical insight at small scales, while FEM efficiently simulates continuum-scale behaviour. Together, they provide a robust framework for analysing sand-GFRP interfaces, enhancing confidence in predictions while maintaining computational efficiency.

6.6 Summary

In Chapter 6, an enhanced hyperbolic model was employed as the constitutive model for the sand-FRP interface. The simulation was carried out in ABAQUS using the FRIC and VFRIC user subroutines, with model parameters calibrated based on experimental results from monotonic and cyclic shearing tests on sand-GFRP interfaces. A total of 18 parameters were defined and calibrated using the Covariance Matrix Adaptation Evolution Strategy (CMA-ES) algorithm. The FRIC and VFRIC user subroutines, written in FORTRAN, were utilised to simulate representative cases of experimental interface shear tests. A parametric study was conducted to understand the effects of various parameters on the

interface's friction and normal displacement. The main findings can be summarised as follows:

1) An enhanced hyperbolic model was adopted to validate the sand-GFRP interface shear behaviour. Calibration of 15 active parameters using the stochastic optimisation method (PyCMA implementation of CMA-ES) achieved a good fit with an RMSE of about 10%, while a mesh sensitivity study confirmed that variations in discretisation had negligible influence on the numerical response. The predictive capability of the FRIC and VFRIC simulations was consistent under monotonic shearing, with the model effectively capturing the hardening behaviour, though some limitations remained in representing post-peak softening.
2) Shear modulus, the exponent of peak friction angle, and breakage parameters were found to be critical for the softening behaviour. Additionally, the variation in shear modulus, shape factor for CSL, and exponent for mobilised phase transformation angle were key factors influencing the variation in the interface friction coefficient. Furthermore, shape factors for CSL, dilatancy parameters, and breakage parameters were influential in the variation in dilative and contractive behaviour.
3) While the cyclic behaviour was simulated with greater accuracy, the dilative behaviour remained under-predicted. This indicates the need for further investigation, particularly with the inclusion of evolving surface roughness parameters in the constitutive models

The outcomes of the FEM simulations in Chapter 6, together with the preceding DEM analyses and experimental investigations, provide a comprehensive understanding of the monotonic and cyclic shear behaviour of the sand-GFRP interface across multiple scales. Having established and validated these findings, the thesis now turns to Chapter 7, which synthesises the key results, highlights the main contributions, and offers recommendations for future research and practical applications.

.

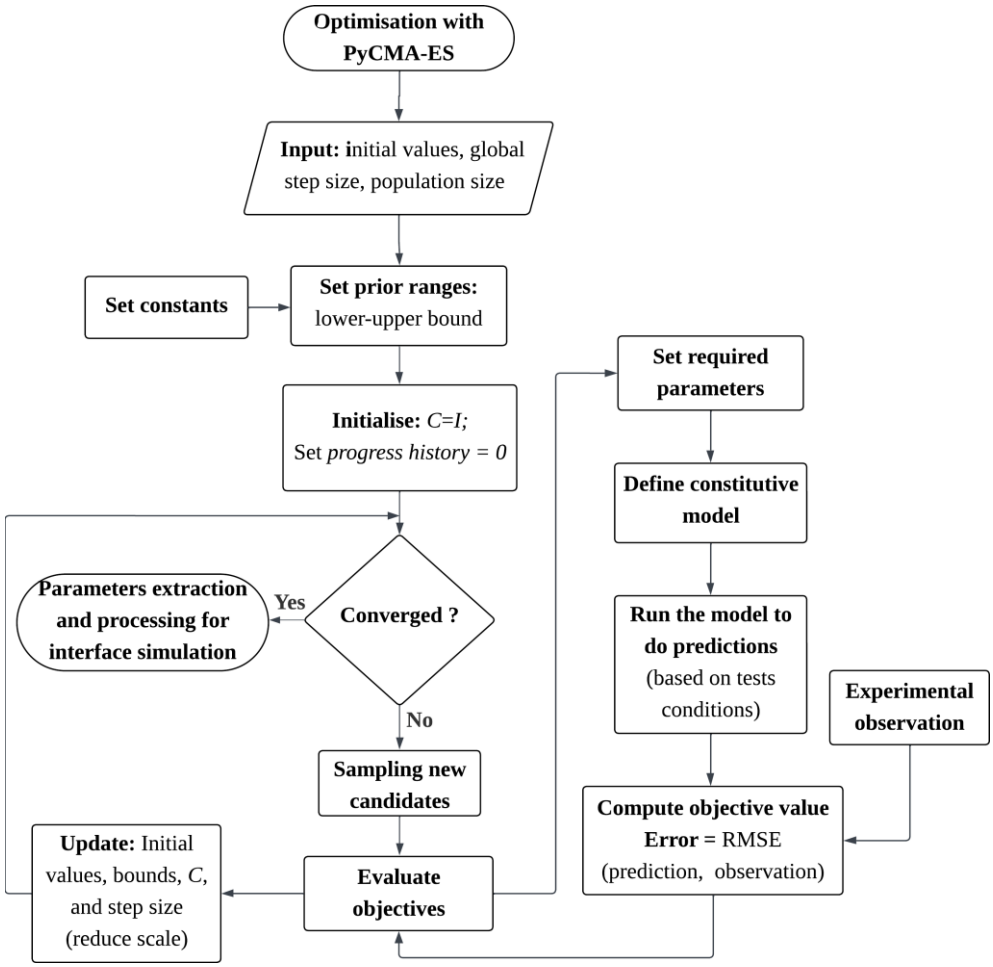

Figure 6-1 Flowchart illustrating the stepwise procedure for optimising model parameters

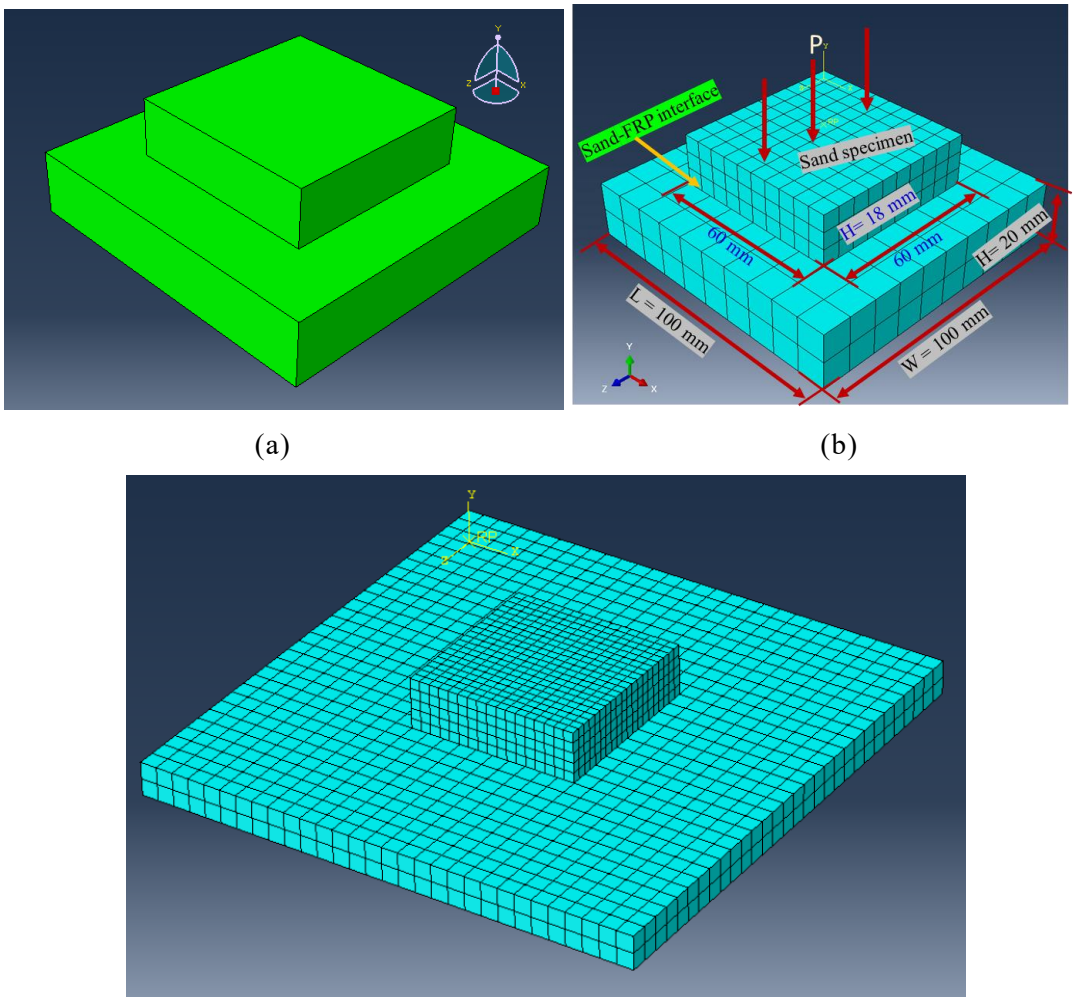

(a) (b)

(c)

Figure 6-2 ABAQUS model for the interface shearing: (a) single element (SE) model and (b) multi-element (ME) model for monotonic shearing; (c) multi-element model for cyclic shearing

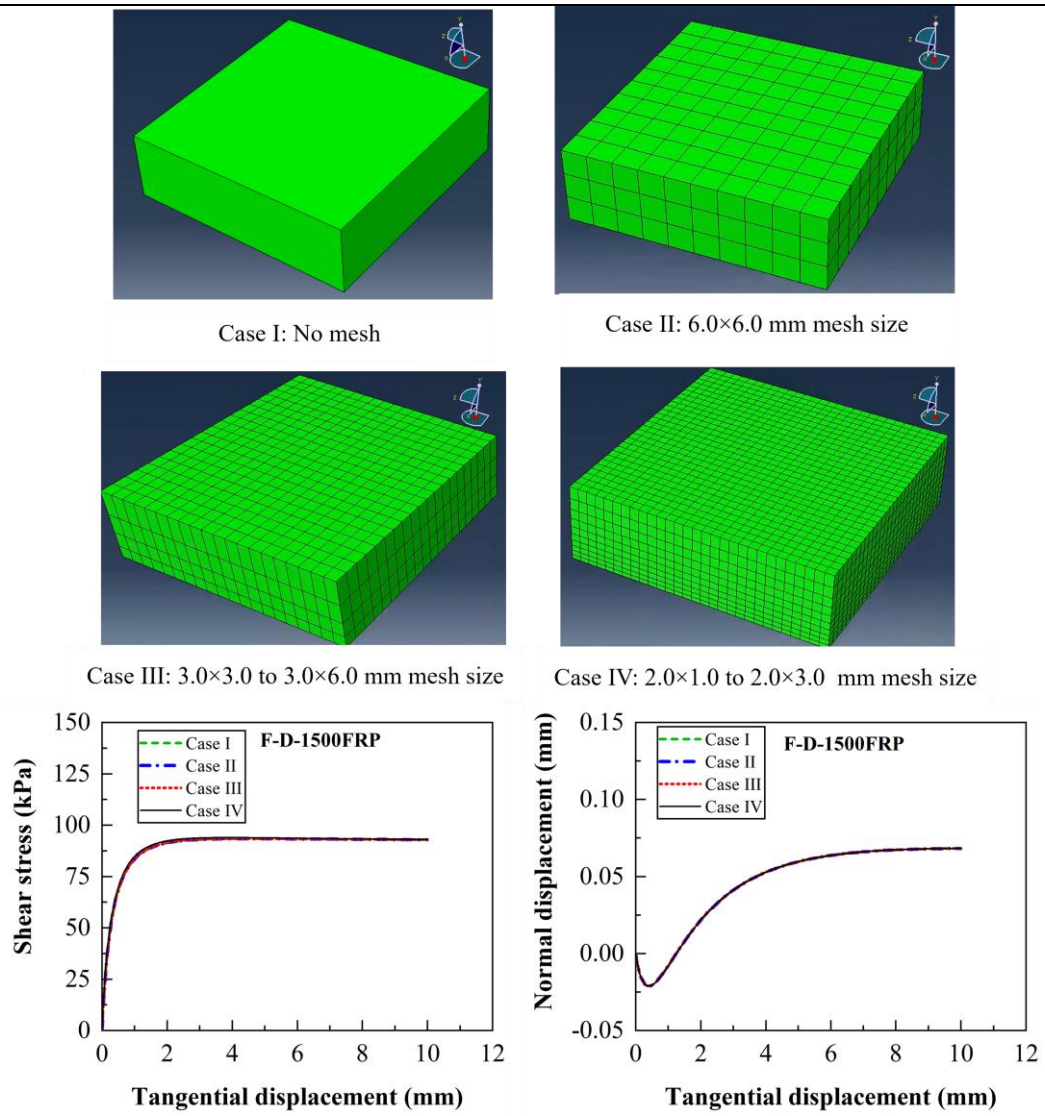

(a) (b)

Figure 6-3 Effect of mesh size (horizontal × vertical) on soil specimens at the F-D-1500FRP interface: (a) shear stress versus tangential displacement and (b) normal displacement versus tangential displacement under a normal stress of 200 kPa

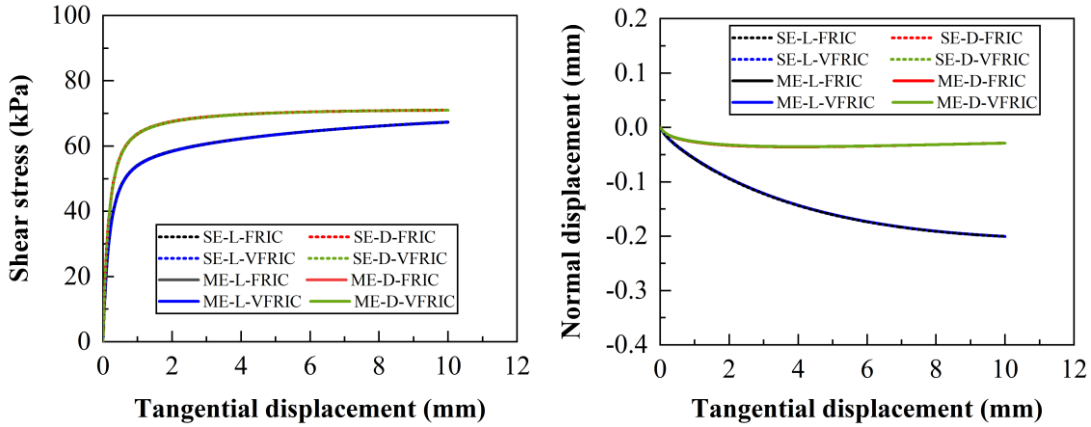

(a) (b)

Figure 6-4 Comparison between single-element (SE) model and multi-element (ME) model at F-PFRP(S) interface: (a) shear stress versus tangential displacement and (b) normal displacement versus tangential displacement under 200 kPa normal stress

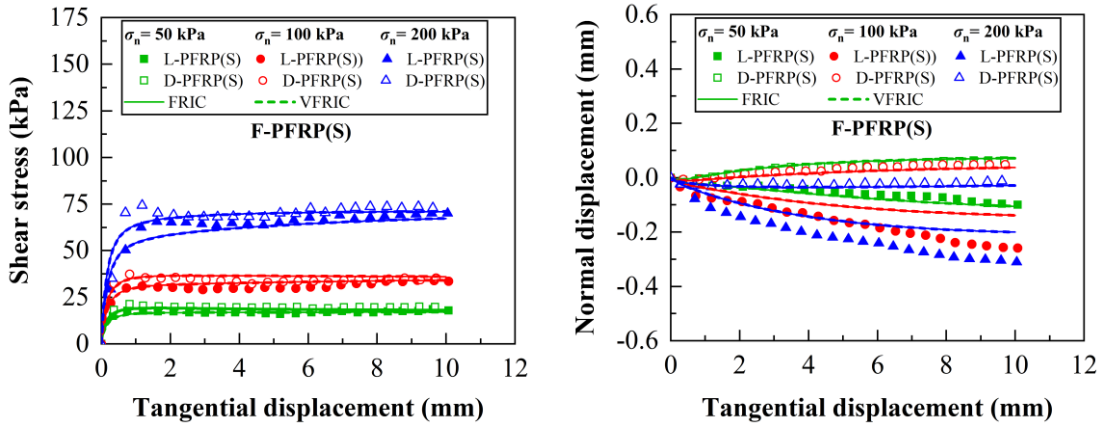

(a)

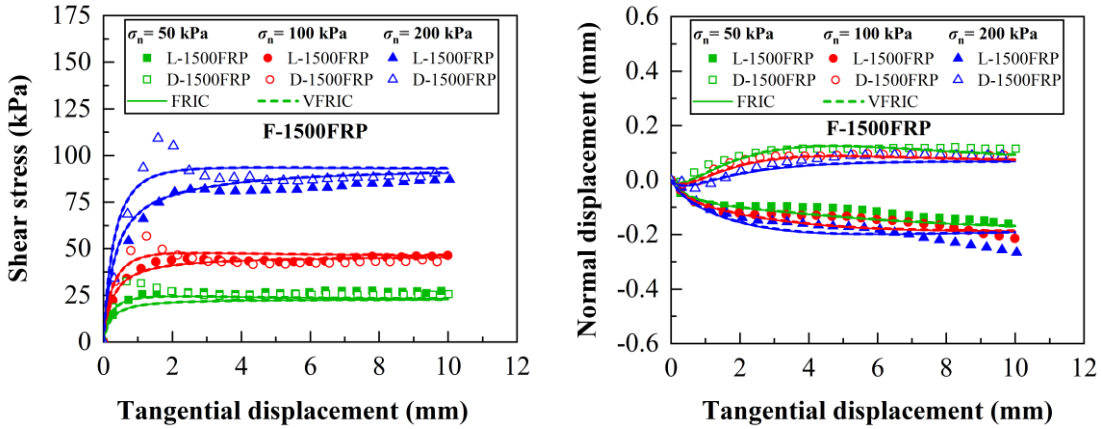

(b)

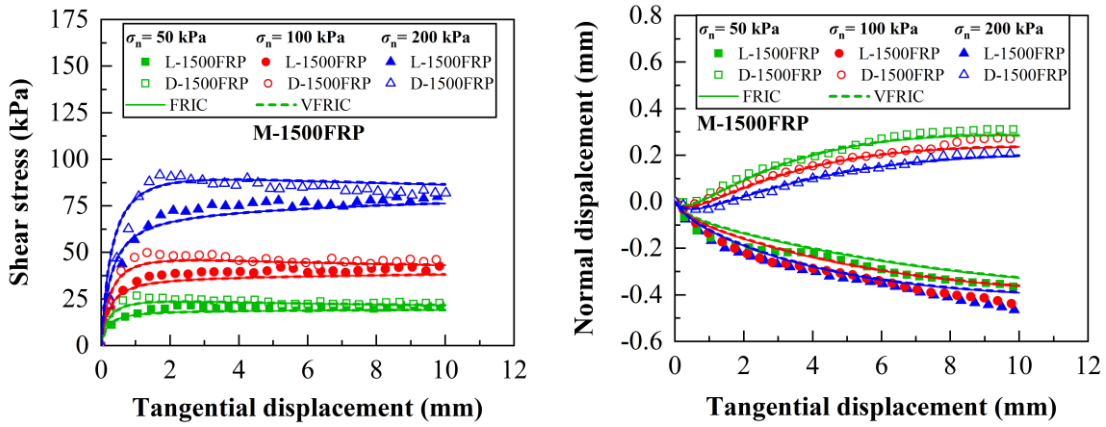

(c)

Figure 6-5 Plot of test results and model simulation (FRIC and VFRIC) for (a) F-PFRP(S), (b) F-1500FRP, and (c) M-1500FRP under 50 kPa, 100 kPa and 200kPa normal stress

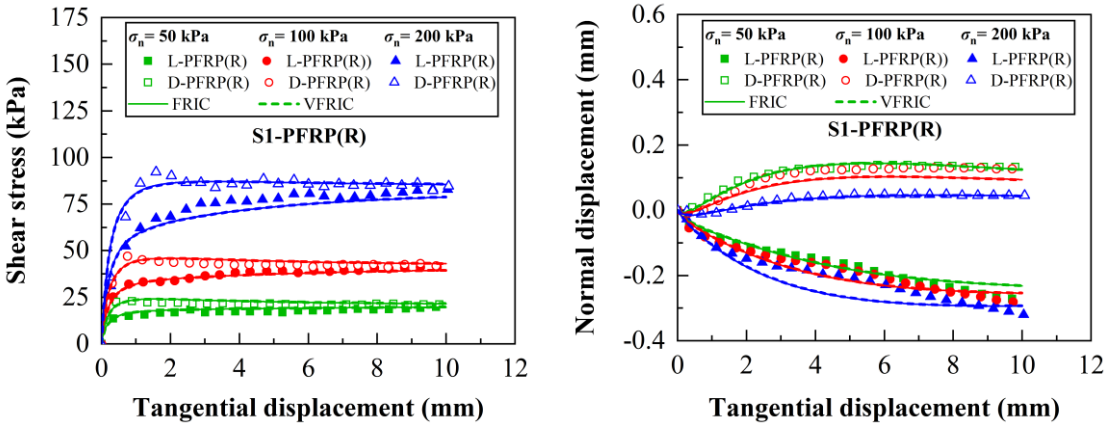

(a)

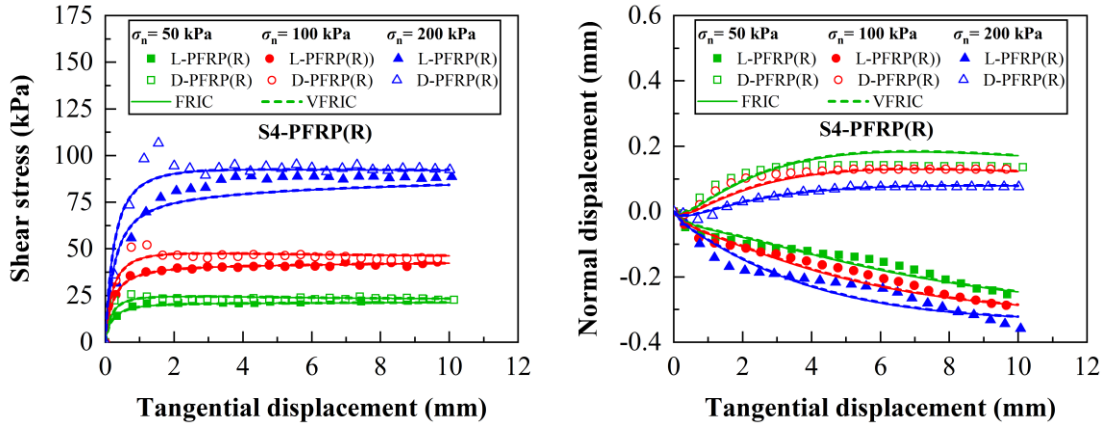

(b)

Figure 6-6 Plot of test results and model simulation (FRIC and VFRIC) for (a) S1-PFRP(R) and (b) S4-PFRP(R) interface under 50 kPa, 100 kPa, 200 kPa normal stress

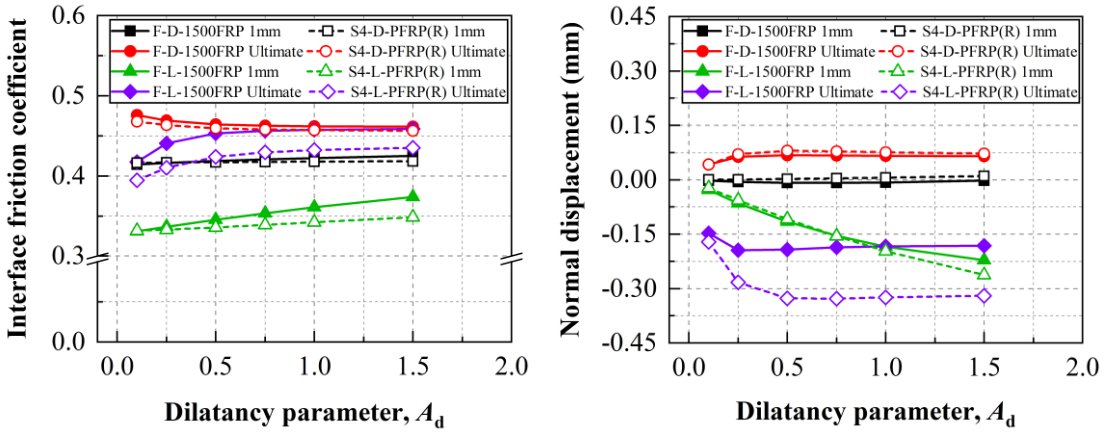

(a) (b)

Figure 6-7 Variations of (a) interface friction coefficient and (b) normal displacement with dilatancy parameter

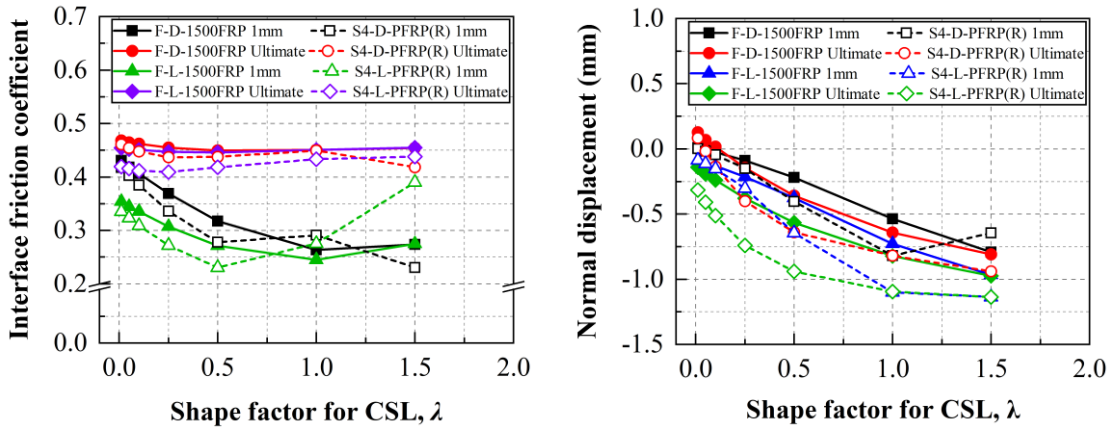

(a) (b)

Figure 6-8 Variations of (a) interface friction coefficient and (b) normal displacement with shape factor for critical state line (CSL)

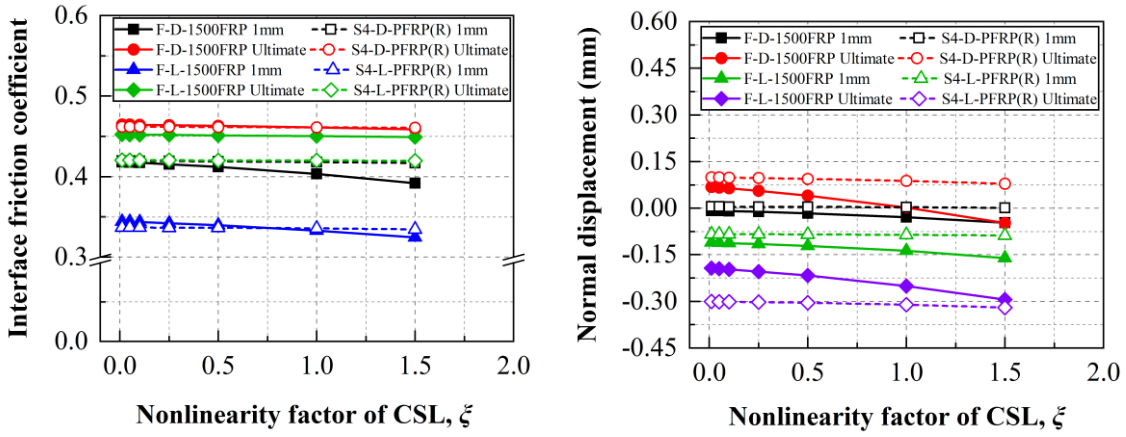

(a) (b)

Figure 6-9 Variations of (a) interface friction coefficient and (b) normal displacement with nonlinearity factor of CSL

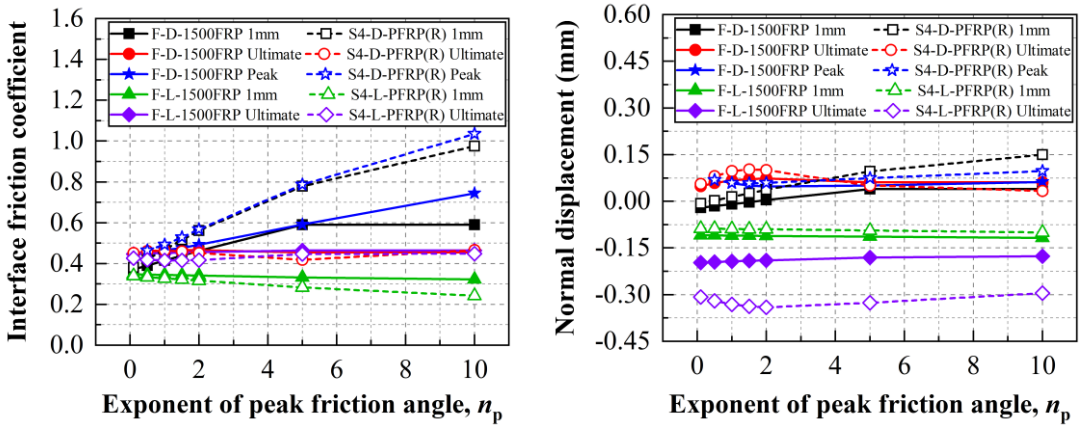

(a) (b)

Figure 6-10 Variations of (a) interface friction coefficient and (b) normal displacement with exponent of peak friction angle

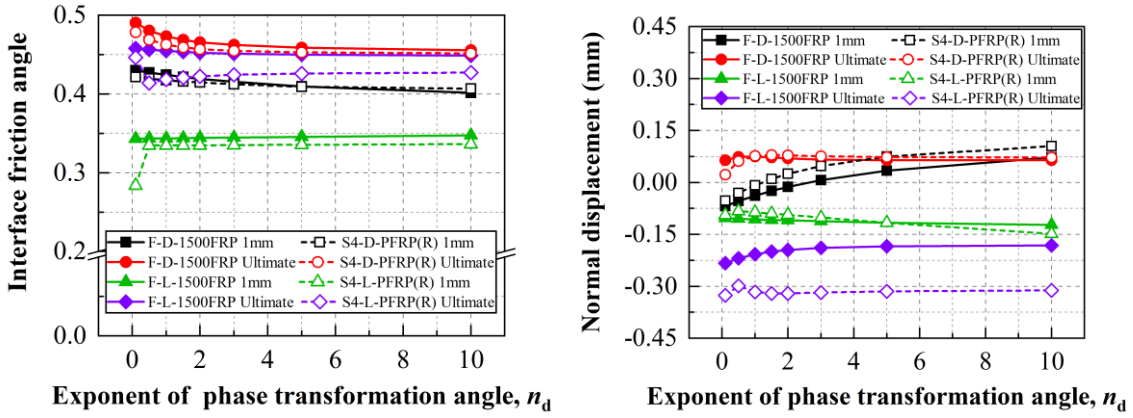

(a) (b)

Figure 6-11 Variations of (a) interface friction coefficient and (b) normal displacement with the exponent of mobilised phase transformation angle

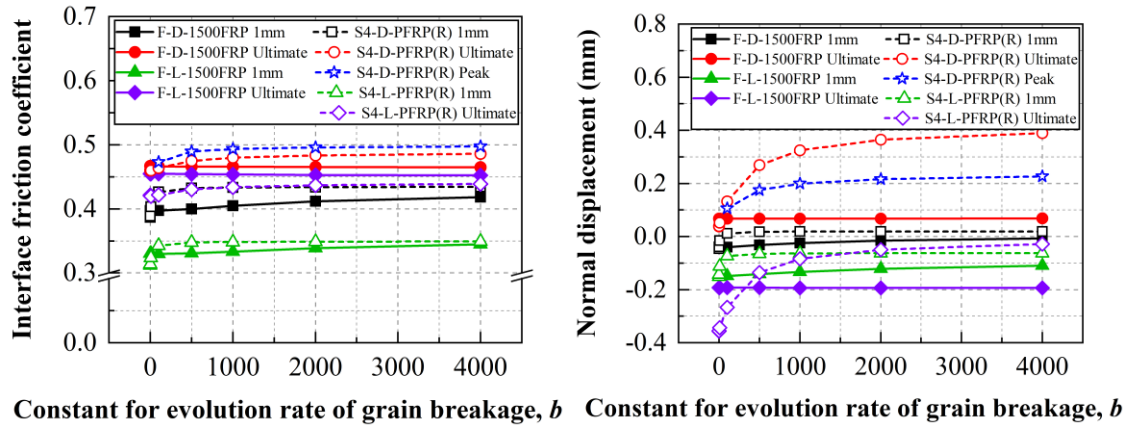

(a) (b)

Figure 6-12 Variations of (a) interface friction coefficient and (b) normal displacement with the constant for the evolution rate of grain breakage

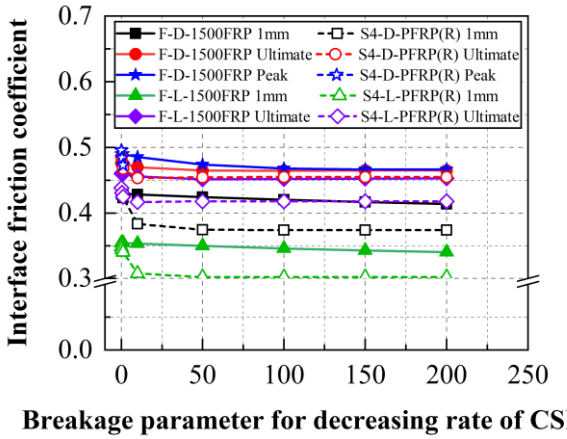

(a)

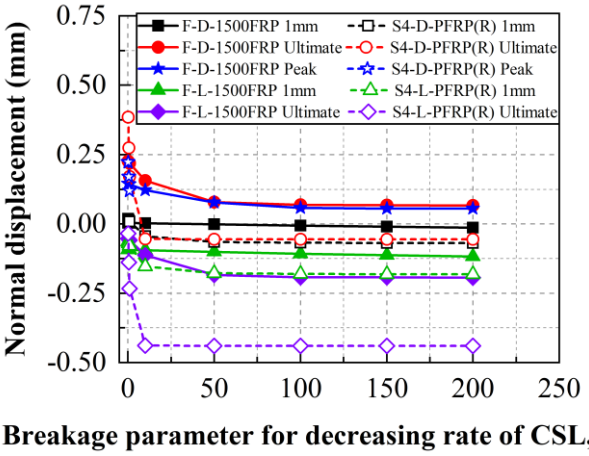

(b)

Figure 6-13 Variations of (a) interface friction coefficient and (b) normal displacement with breakage parameter for decreasing rate of CSL

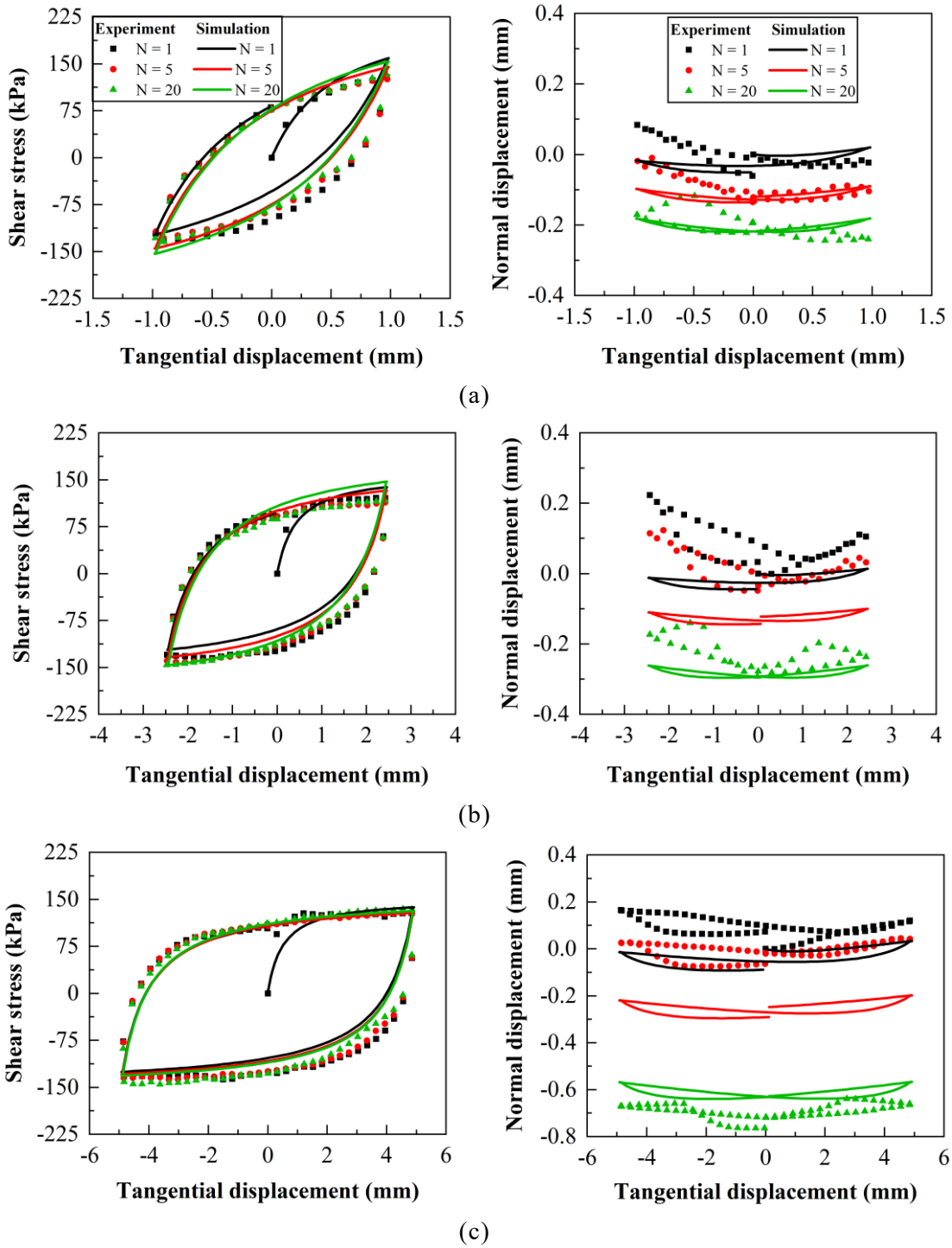

Figure 6-14 Effect of amplitude (a) ± 1.0 mm, (b) ± 2.5 mm, and (c) ± 5.0 mm on M-HFRP(R) interface under 200 kPa normal stress

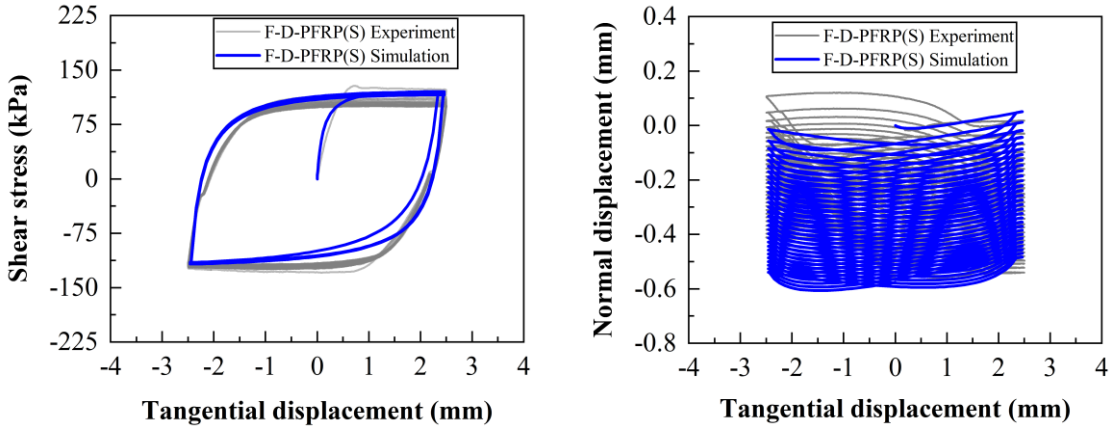

(a)

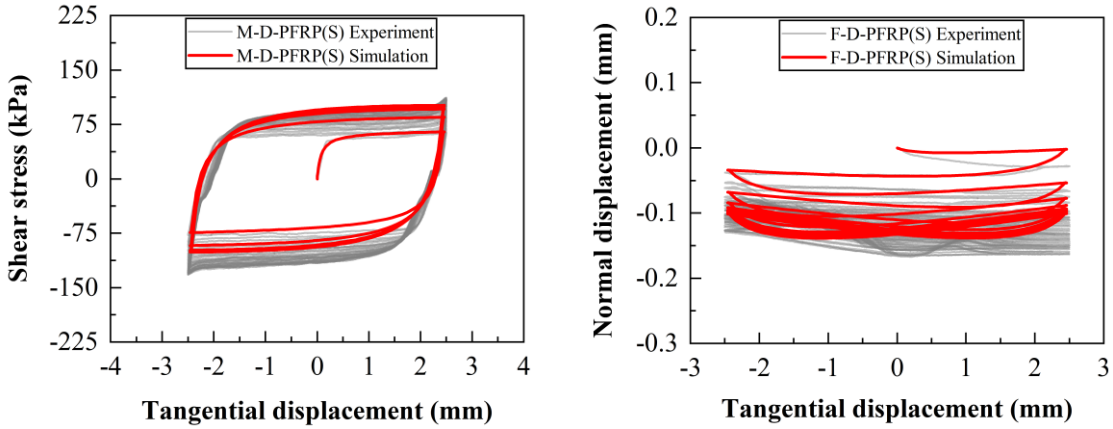

(b)

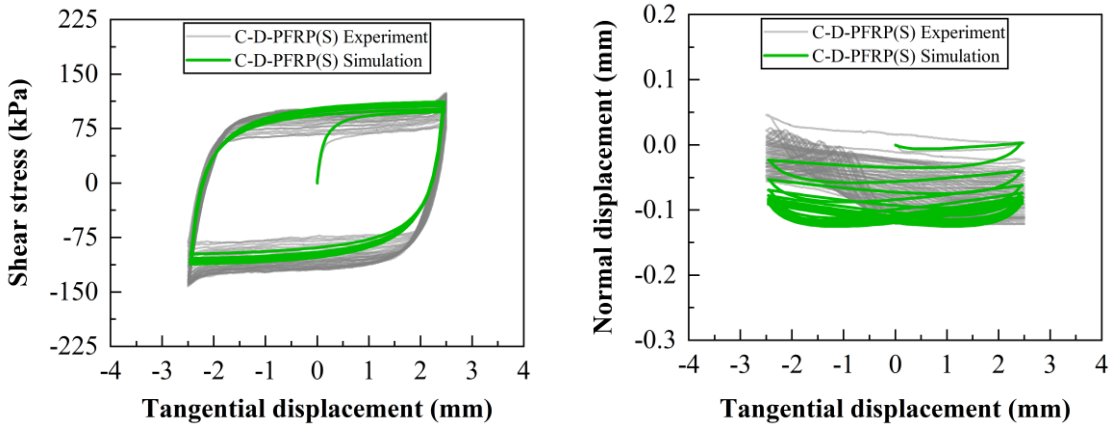

(c)

Figure 6-15 Comparison of plots on the effect of particle size (a) fine sand, (b) medium sand, and (c) coarse sand on PFRP(S) under 200 kPa normal stress

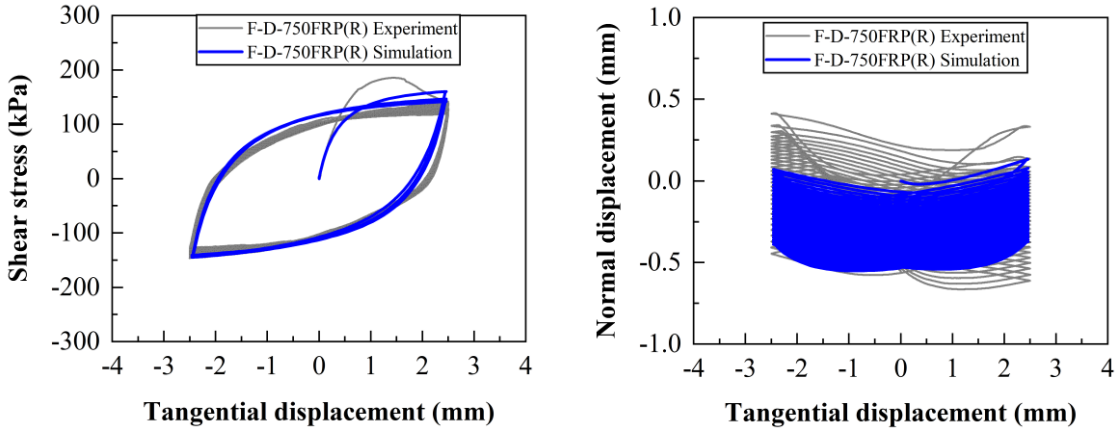

(a)

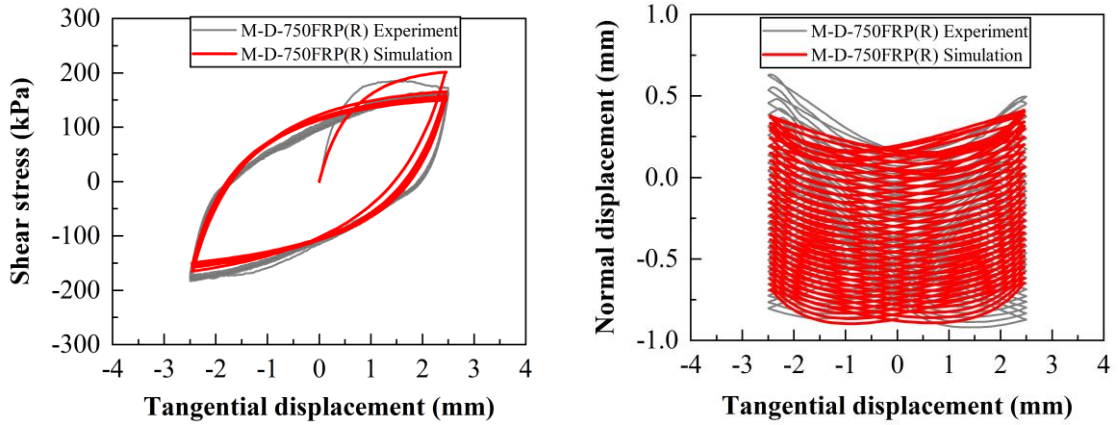

(b)

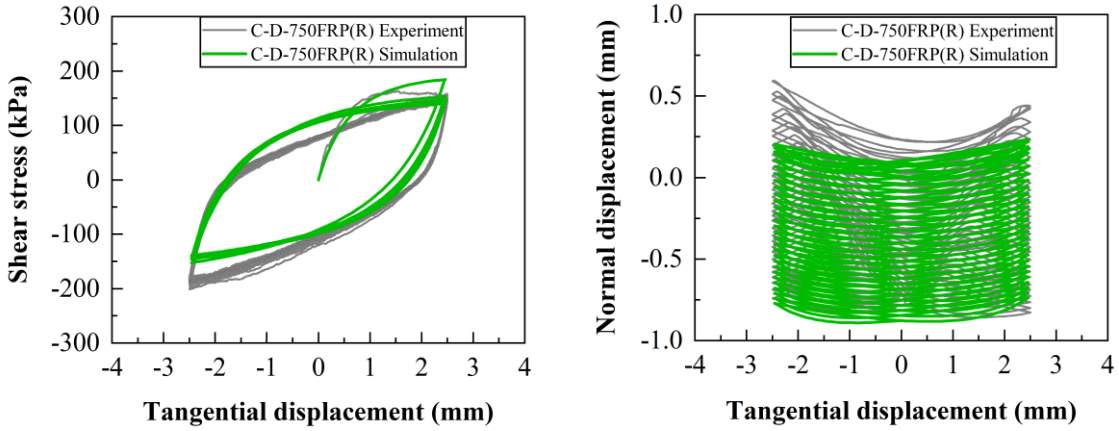

(c)

Figure 6-16 Comparison of plots on the effect of particle size (a) fine sand, (b) medium sand, and (c) coarse sand on 750FRP(R) under 200 kPa normal stress

Table 6-1 Properties of the hyperbolic constitutive model

S. N.	Categories	Symbol	Description
1	Basic	σ_{a}	Adhesive stress
2		G_0	Initial shear modulus
3		R	Ratio of elastic normal to elastic shear modulus
4		A_{d}	A dilatancy parameter
5		ϕ_{u}	Critical friction angle (degrees)
6		t_{s}/D_{50}	Ratio of shear zone thickness to mean particle size
7		D_{50}	Mean particle size
8		n_g	Exponent of the formula of shear modulus
9		e_0	Initial void ratio
10	Critical state	e_{ref0}	Virgin reference critical void ratio
11		λ	A parameter controls the shape of the CSL line
12		ξ	A parameter controls the nonlinearity of the CSL line
13		n_{p}	Exponent of the formula of the peak friction angle
14		n_{d}	Exponent that controls the mobilised-phase-transformation in hardening/softening
15	Particle breakage	e_{refu}	Ultimate reference critical void ratio
16		ρ	A constant controls the decreasing rate of CSL line due to particle breakage
17		b	A constant controls the evolution rate of CSL attributed to particle breakage
18		n_{w}	Exponent on energy effect during breakage

Table 6-2 Summary of the state variables for FRIC and VFRIC subroutines

State	Symbol	Description
1-3	γ	Tangential displacement
4-6	σ	Stress
7-9	ε	Strain
10-12	$\mathrm{d}\sigma$	Incremental stress
13-15	$\mathrm{d}\varepsilon$	Incremental strain
16-17	τ	Shear stress, $\sigma\,(2{:}3)$
18-20	σ_{R}	Reversal stress
21-23	ε_{R}	Reversal strain
24	DIR	Slip direction (1 for increase, -1 for decrease)
25	W	Total work
26	B_{R}	Breakage index
27	e_{ref}	Reference void ratio
28	e_{c}	Critical void ratio
29	e	Void ratio
30	$\tan\phi_{\mathrm{p}}$	Coefficient of mobilised peak friction angle
31	$\tan\phi_{\mathrm{pt}}$	Coefficient of mobilised phase-transformation angle
32	G	Shear modulus
33	A	Coefficient of hyperbolic formula
34-36	SLIP DIR	Direction of the slip (X, Y, Z)

Table 6-3 Summary of the simulation scheme

S.N.	Test type	Interface ID	Sand type [First item in ID]	Specimen type	Amplitude (mm)	Normal stress (kPa)
1	Monotonic	F-PFRP(S)	Fine	Loose (L) and dense (D)	n/a	50, 100, 200
2		F-1500FRP				
3		M-1500FRP	Medium			
4		S1-PFRP(R)	5% F + 95% M			
5		S4-PFRP(R)	30% F + 70% M			
6	Cyclic	M-D-HFRP(R)	Medium	Dense (D)	± 1.0, ± 2.5, ± 5.0	200
7		F-D-PFRP(S)	Fine		± 2.5	
8		M-D-PFRP(S)	Medium			
9		C-D-PFRP(S)	Coarse			
10		F-D-750FRP(R)	Fine			
11		M-D-750FRP(R)	Medium			
12		C-D-750FRP(R)	Coarse			

Note: n/a refers to not available.

Table 6-4 Identified model parameters for monotonic shearing

Parameters	F-PFRP(S)	F-1500FRP	M-1500FRP	S1-PFRP(R)	S4-PFRP(R)
σ_a	0	0	0	0	0
G_0	165	200	368	200	169
R	2.25	5.18	6.18	9.7	9.9
A_d	0.334	0.47	0.59	0.397	0.4
ϕ_μ	19.6	24.8	21.8	22.3	23.8
t_s/D_{50}	8	12	6	3	4
n_g	0.6	0.6	0.6	0.6	0.6
e_{ref0}	0.955	0.893	0.983	0.727	0.623
λ	0.042	0.057	0.267	0.02	0.012
ξ	1.498	0.011	0.011	1.48	1.48
n_p	0.75	1.07	1.35	1.27	0.47
n_d	0.71	2.24	1.52	1.84	1.25
e_{refu}	0.769	0.79	0.77	0.531	0.39
ρ	198	124.63	0.96	1.02	1.69
b	2237.55	3887	15.03	17.36	33.37
n_w	1	1	1	1	1
RMSE (%)	≤ 8.5%				

Note: RMSE refers to root mean square error.

Table 6-5 Parameters and their values for parametric study

Parameters	Parametric values
Dilatancy parameter, A_{d}	0.1, 0.25, 0.5, 0.75, 1.0, 1.5
Shape factor for CSL, λ	0.01, 0.05, 0.1, 0.25, 0.5, 1.0, 1.5
Nonlinearity factor of CSL, ξ	0.01, 0.05, 0.1, 0.25, 0.5, 1.0, 1.5
Exponent of peak friction angle, n_{p}	0.1, 0.5, 1.0, 1.5, 2.0, 5.0, 10.0
Exponent of mobilised phase transformation angle, n_{d}	0.1, 0.5, 1.0, 1.5, 2.0, 3.0, 5.0, 10.0
Breakage parameter for decreasing rate of CSL, ρ	0.1, 0.5, 1.0, 10, 50, 100, 150, 200
Constant for evolution rate of particle breakage, b	0.1, 1, 10, 100, 500, 1000, 2000, 4000

Table 6-6 Identified model parameters for cyclic shearing

Parameters	Interfaces				
	M-D-HFRP(R)			Smooth interface	
	(±1.0 mm)	(± 2.5 mm)	(± 5.0 mm)	F-D-PFRP(S)	M-D-PFRP(S)
σ_{a}	0	0	0	0	0
G_0	1180.0	1937.0	1977.4	1790.98	364.88
R	2.11	9.10	1.26	6.986	2.946
A_{d}	0.101	0.081	0.086	0.24	0.088
ϕ_{μ}	32.2	26.1	32.7	24.4	21.9
d_{t}/D_{50}	8.0	17.2	21.8	37.78	2.8
n_g	0.6	0.6	0.6	0.6	0.6
e_{ref0}	0.97	0.704	0.864	1.496	0.643
λ	0.217	0.013	0.084	0.662	0.048
ξ	0.27	0.859	0.081	0.0272	0.827
n_{p}	3.27	4.92	0.656	2.812	4.98
n_{d}	3.73	1.43	1.31	0.0027	0.423
e_{refu}	0.36	0.052	0.497	0.564	0.068
ρ	0.65	3.26	16.86	4.57	0.74
b	11780.5	26190.8	15520.4	5112.2	12918.6
n_{w}	1.22	0.96	0.835	1	0.97
RMSE (%)	9.02	7.21	6.14	10.2	9.91

(Continued)

Table 6-6 (Continued) Identified model parameters for cyclic shearing

Parameters	Interfaces			
	Smooth interface	Rough interface		
	C-D-PFRP(S)	F-D-750FRP(R)	M-D-750FRP(R)	C-D-750FRP(R)
σ_a	0	0	0	0
G_0	1165.3	1266.2	1315.0	1250.2
R	5.51	3.728	4.31	3.08
A_d	0.11	0.218	0.271	0.224
ϕ_μ	23.0	24.8	33.2	31.6
d_t/D_{50}	2.6	53.8	17.5	11.5
n_g	0.6	0.6	0.6	0.6
e_{ref0}	0.798	1.494	1.485	1.490
λ	0.18	0.234	0.54	0.758
ξ	0.338	0.587	0.425	0.011
n_p	2.864	1.669	4.96	4.96
n_d	0.002	0.004	4.98	4.98
e_{refu}	0.192	0.546	0.534	0.521
ρ	1.4	4.64	4.28	4.36
b	3949.2	4000.4	1990.8	1968.6
n_w	0.76	1.0	1.0	1.0
RMSE (%)	13.9%	9.15	8.45	8.61

CHAPTER 7: CONCLUSIONS AND RECOMMENDATIONS

7.1 Conclusions

Reduced surface hardness and lower friction properties at interfaces pose significant challenges to the practical application of fibre-reinforced polymer (FRP). This study addressed these limitations by employing a sand-epoxy coating technique, representing an advancement over the conventional direct sand-coating methods on GFRP laminates. The investigation employed two distinct types of GFRP composites: an industrially manufactured variant comprising ATLAC 430 epoxy with strand mat fibres, conferring moderate to high surface hardness and subjected exclusively to sand-epoxy coatings with multiple sand grades, and a laboratory-fabricated counterpart composed of GXA120 prepreg adhesive with prepreg glass fibres, yielding moderate hardness, with both composites subsequently assessed through sand-GFRP interface testing to facilitate systematic examination of shear behaviour under controlled laboratory conditions. The shear behaviour at the sand-GFRP interface was systematically examined and characterised using both monotonic and cyclic shearing within constant normal load (CNL) frameworks. The study focused exclusively on dry conditions, with interface behaviour assessed using standard silica sand of varying particle sizes and multiple grades of sand-epoxy coatings. A comprehensive evaluation combined experimental testing with numerical modelling approaches using the discrete element method (DEM) and the finite element method (FEM), to deepen the mechanistic understanding of interface performance. Surface roughness was also quantitatively analysed to elucidate its evolution and role in enhancing interface shear resistance. These findings are explicitly framed within the context of dry-state interface mechanics and provide a robust foundation for future studies incorporating environmental variability and

broader material typologies.

The sand-epoxy coating technique doubled the surface hardness of GFRP compared to uncoated specimens. Interface friction properties improved by over 40% at peak shear strength and by more than 25% at the ultimate state. Furthermore, interface particle slippage was significantly reduced from nearly 100% to 50-70%, demonstrating the effectiveness of the sand-epoxy coating in enhancing interfacial stability. Notably, the long-term degradation resistance of GFRP was markedly improved with the application of sand-epoxy coatings.

The findings underscore that shear strength and volumetric behaviour at the sand-GFRP interface are significantly influenced by sand gradation, particle shape, interface roughness, and normal stress levels. Fine sand specimens exhibited higher interface shear strength, particularly when combined with a moderate proportion of subangular to subrounded particles. However, excessive fine proportions resulted in a decline in interface strength due to reduced interlocking effects. These conclusions offer valuable insights into the contact mechanisms governing sand-GFRP interactions. Further experimental and micromechanical analyses in the following sections will provide a more detailed understanding of the underlying mechanisms.

7.1.1 Impact of sand-epoxy coating on friction

A total of 43 sets of monotonic interface shear tests were conducted, with each set comprising three tests under varying normal stresses (e.g., 50, 100, and 200 kPa; or 200, 400, and 800 kPa), covering a full range from 50 to 800 kPa. In addition, 101 cyclic interface shear tests were performed under normal stresses ranging from 200 to 800 kPa. Furthermore, multiple tests were performed to define internal friction properties and ensure repeatability validation. The findings demonstrate that applying sand-epoxy coatings on GFRP surfaces enhances surface roughness, which in turn influences interface shear strength. Increasing epoxied sand grades and concentrations improves the friction coefficient, whereas an increase in normal stress reduces the friction coefficient within the 50 kPa to 800 kPa range in monotonic interface shearing. In contrast,

under elevated normal stress and cyclic mobilisation, particle breakage of sand specimens and surface degradation of both uncoated and sand-epoxied GFRP intensify. The synergistic interplay of multiple factors reforming the localised shear zone at degraded surfaces enhances the mobilised friction coefficient, particularly at normal stresses exceeding 400 kPa. This distinction clarifies the critical role of high normal stress in frictional strengthening at the sand-GFRP interface under cyclic shearing.

This study further establishes that uniformly graded sand exhibits a linear increase in interface friction angle with increasing roughness, whereas sand mixtures follow a quadratic trend. The friction angle was significantly enhanced, approaching values closer to the internal friction angle at peak and ultimate states, particularly at intermediate to rough relative roughness levels. These findings provide a framework for optimising sand-epoxy coated GFRP design, where friction angle versus relative roughness plots can guide the selection of optimal epoxied sand concentration, grading, and surface roughness.

Furthermore, cyclic interface shear behaviour was influenced by cycle number, median particle size, roughness, and normal stress, leading to an increase in cyclic mobilised friction angle. Notably, the cyclic friction angle was observed to be several degrees higher than that of monotonic shearing, highlighting the progressive mobilisation of interface resistance under cyclic loading conditions.

Overall, this research advances the understanding of interface mechanics in GFRP applications by establishing a robust framework for designing and optimising sand-epoxy coatings under controlled dry laboratory conditions. The established correlations between relative roughness and friction angle serve as a practical tool for tailoring surface treatments to specific geotechnical and structural performance demands. This work contributes original data and interpretations to the interface mechanics literature, offering a scalable methodology for enhancing the performance of composite-ground systems under both monotonic and cyclic loading conditions. Although this study focused on air-dried standard silica sand and primarily utilised ATLAC 430 epoxies in pultruded industrial GFRP, the findings provide a foundation for broader

applications in other GFRP systems. Future studies will address the role of environmental loading conditions and additional GFRP types to expand and validate the proposed framework.

7.1.2 Surface roughness evolution on sand-epoxied GFRP

Both loose and dense sand conditions were utilised in monotonic shearing under 50 kPa to 200 kPa to assess the influence of relative density on roughness evolution. The findings indicate that dense specimens exhibited a more pronounced impact on roughness evolution. Consequently, the experimental scope was expanded to focus on dense specimens while incorporating enhanced GFRP surface hardness through fibre content of up to 50% by weight and various grades of epoxied sand. These modifications enabled an in-depth investigation of surface roughness evolution under moderate to large normal stresses (200 kPa to 800 kPa) in both monotonic and cyclic shearing under CNL conditions.

The study identifies optimal sand-epoxy coating concentrations that enhance interface performance while mitigating excessive roughness fluctuations. The evolution of surface roughness during cyclic shearing is highly dependent on interface characteristics. On smooth GFRP surfaces, surface roughness evolution is predominantly driven by mass sliding and particle rotation. In contrast, on rougher interfaces, roughness evolution is governed by rotational effects and the bonding-debonding of interlocking contact mechanisms.

Surface roughness degradation is more pronounced with increasing median particle size, higher cycle numbers, and elevated normal stresses. However, the application of sand-epoxy coatings significantly enhances long-term durability by improving surface hardness. Ultimately, an appropriate safety factor should be incorporated into design considerations to account for roughness degradation over time, ensuring structural reliability based on the presented findings.

The implications of these findings are twofold. First, they underscore the necessity of optimising coating parameters to achieve both initial performance and long-term durability. Second, they highlight the critical need to incorporate an appropriate safety factor in the design of GFRP-soil interfaces to account for

progressive roughness degradation over time. This research delivers a novel framework for understanding and predicting the evolution of surface characteristics in engineered composite interfaces, providing an essential design tool for the development of robust, reliable, and durable GFRP systems under realistic service conditions.

7.1.3 Micromechanical insights into the influence of sand-epoxy coating

A discrete element method (DEM) investigation was conducted, comprising 63 interface shear tests. The findings indicate that smoother surfaces increase particle slip, whereas rougher surfaces promote greater interlocking, altering the balance between sliding and rotational effects. While higher concentrations of sand-epoxied coatings improve interface shear strength, excessive roughness levels introduce significant roughness variations over prolonged shearing, which may compromise interface stability.

DEM simulations further underscore the influence of particle shape, revealing that ellipsoidal particles exhibit greater interlocking and higher force chain concentration at the interface compared to spherical counterparts. Additionally, force chain anisotropy and localised roughness variations were identified as key contributors to interface degradation during shearing, emphasising the complex interplay between micromechanical interactions and interface evolution.

Overall, the micromechanical insights obtained from this DEM investigation provide a novel, mechanistic framework for interpreting the observed macroscopic behaviours of sand-epoxied GFRP interfaces. By linking interfacial shear strength to particle kinematics, contact mechanics, and geometric anisotropy, this study delivers an original contribution to the field of composite interface engineering. These findings offer valuable guidance for tailoring surface treatments and material selection strategies that balance enhanced strength with long-term mechanical stability in geotechnical and structural applications.

7.1.4 FEM modelling of the sand-GFRP interface

The finite element method (FEM) successfully captured interface response, providing strong validation of experimental observations. The adopted hyperbolic model, comprising 18 model parameters, effectively incorporated a non-linear shear modulus to simulate incremental stress dilatancy while integrating critical state principles. Additionally, the model accounted for particle breakage and reversal effects in cyclic shearing. The model enables accurate predictions of hardening behaviour and contraction in monotonic shearing. However, limitations persist in capturing softening effects and dilation, particularly under large deformations. Further refinements are required to enhance the model's ability to simulate post-peak softening and dilative responses, ensuring greater accuracy in predicting complex interface behaviour.

Furthermore, cyclic shear simulations require refinement to improve the prediction of dilative behaviour. The findings suggest that incorporating evolving roughness parameters into constitutive models could significantly enhance the accuracy of numerical predictions, particularly in capturing complex interface mechanics under cyclic loading conditions.

In summary, this research advances the state-of-the-art in numerical modelling of soil-composite interfaces by delivering a robust FEM framework that captures the essential characteristics of sand-GFRP interaction while outlining clear pathways for enhancing its predictive capabilities. These findings establish a foundation for the improvement of constitutive models, thereby enabling more precise design and performance evaluation of geocomposite interfaces.

The research makes important contributions in the following key areas that align with the academic achievement requirements:

1) **Innovative experimental system development:** A comprehensive experimental framework is established, combining interface direct shear testing and surface topology characterisation under varying normal stress levels and prolonged cyclic loading. This system enables a detailed study

of the interface behaviour between granular materials and composite surfaces, providing data not previously available in the literature, and supports the development of the simplified and the generalised design charts, which enable frictional characterisation based on interface roughness and facilitate the configuration of sand-epoxy coatings for field applications.

2) **Significant computational advancements:** This study establishes a robust, multi-scale computational framework by employing complementary micromechanical and continuum-scale simulations to investigate sand-GFRP interface behaviour. By applying both DEM and FEM independently yet complementarily, this study offers a comprehensive multi-scale perspective on sand-GFRP interaction. The dual modelling approach significantly strengthens the generalisability, reliability, and depth of the findings, delivering a powerful computational foundation for future engineering design and analysis of composite interfaces under complex loading conditions.
3) **Systematic and innovative academic output:** The findings provide researchers with validated methodologies, critical data for model development, and practical insights for optimising interface design. Findings contribute not only to academic knowledge but also present direct implications for infrastructure durability and economic feasibility. The novelty and the systematic nature of the findings have been reflected in published/under review journal articles.

In conclusion, this thesis delivers critical advancements in geotechnical interface mechanics through novel experiments, innovative modelling, and robust computational tools. It sets a new benchmark in interface analysis by uniting theory and practice, offering a systematic, original, and publication-driven

contribution with direct relevance to durable and cost-effective infrastructure design.

7.2 Recommendations

Several aspects can be discussed for further investigations into experimental and computational sand-GFRP interface shear behaviour. Extension of the current framework to diverse sediment types for real-world validation can be considered as a future direction. While the present study on standard silica sand has largely addressed the relationship between particle morphology and crushing behaviour qualitatively, the findings suggest that establishing quantitative correlations between morphological indices and breakage indices could provide deeper insight into stress-dependent particle degradation. Future studies should explore extended cyclic shear tests beyond the current limits to further understand the degradation mechanisms of sand-epoxied GFRP surfaces under prolonged loading conditions, such as accelerated ageing tests. Exploring alternative epoxy formulations and application techniques may optimise the balance between interface strength enhancement and roughness stability over long-term shearing. Investigating a wider range of sand gradations and particle shapes could refine the understanding of interfacial mechanisms and expand the applicability of sand-epoxied GFRP systems.

Conducting large-scale or in situ tests would help validate laboratory findings, ensuring practical applicability in real-world infrastructure applications. Laboratory testing and in-situ validation under environmental loading (e.g., moisture, saline moisture, temperature, freeze-thaw cycles) can be considered in future studies. To achieve a more realistic representation of the microstructure at the GFRP interface, future research should incorporate CT scan data. This would improve the geometric accuracy of numerical models and enhance the engineering relevance of the simulations. Incorporating evolving roughness parameters into FEM simulations could improve the accuracy of softening and dilative behaviour predictions, providing more reliable numerical models. Integrating DEM-FEM/FDM hybrid models could provide deeper insights into

the micromechanical and macro-scale behaviour of sand-GFRP interfaces, enhancing predictive capabilities. Studying the influence of different epoxy coatings and surface treatments could expand the potential applications of GFRP in geotechnical, ocean, and structural engineering.

7.3 Environmental impact of the study

This study contributes to environmental sustainability by enhancing the durability and performance of GFRP structures through sand-epoxy coatings. The significant improvement in hardness, nearly doubling GFRP's resistance, significantly reduces material degradation and thereby extends the service life of GFRP applications in geotechnical engineering, such as sea walls, piles, and slope reinforcement. This increased longevity minimises the frequency of repairs and replacements, reducing material consumption and lowering carbon emissions associated with production, transportation, and construction activities.

Furthermore, the enhanced interface friction properties achieved through optimised sand-epoxy coatings reduce excessive material usage while maintaining structural integrity, promoting efficient resource utilisation. This improved surface treatment offers a sustainable alternative with minimal environmental impact. While the study was conducted under dry conditions, the findings support the potential for sand-epoxy coatings to complement GFRP's inherent durability in harsh environments, reducing waste through better surface retention under cyclic shear loading.

Overall, the findings of this research support the development of resilient, low-maintenance, and environmentally friendly geotechnical solutions through improved interface performance under dry conditions. The optimised sand-epoxy coating method aligns with sustainable engineering principles, contributing to the advancement of greener infrastructure with lower lifecycle environmental costs.

LIST OF SYMBOLS AND ACRONYMS

CNL	Constant Normal Load
CSL	Critical State Line
DEM	Discrete Element Method
FEM	Finite Element Method
FRP	Fibre-Reinforced Polymer
GFRP	Glass Fibre-Reinforced Polymer
A_c	Cyclic Tangential Displacement Semi-Amplitude
A_d	A Dilatancy Parameter
b	A Constant Controls the Evolution Rate of CSL (Breakage)
C_{irc}	Circularity
C_u	Coefficient of Uniformity
d	Particle Size in Diameter
D_r	Relative Density
D_{50}	Mean Particle Size
d_{50}	Median Particle Size
$D.R.$	Design Ratio
$E.F$	Efficiency Factor)
$E.F._{\text{s-e GFRP}}$	Efficiency Factor Based on Plain GFRP
G_s	Specific Gravity
G_0	Initial Shear Modulus
N	Cycle Number
$PFAR$	Peak Friction Angle Ratio
R_{rd}	Roundness
R	Relative Roughness
R_a	Average Centre Line Roughness of Evaluation Lengths
$R_{max,avg}$	Average of Maximum Roughness of Evaluation Lengths

R_{ra}	Representative Average Roughness
R. F.	Roughness Factor
S_{a}	Average Surface Roughness of Evaluation Areas
$S_{\mathrm{z,avg}}$	Average of Maximum Roughness of Evaluation Areas
t_{s}/D_{50}	Ratio of Shear Zone Thickness to Mean Particle Size
δ_{limit}	Mobilised Cyclic Interface Friction Angle at Limit State
δ_{p}	Peak Interface Friction Angle in Monotonic Tests
δ_{ult}	Ultimate Interface Friction Angle in Monotonic Tests
ΔS_{a}	Variation in Average Surface Roughness
$\Delta S_{\mathrm{z,avg}}$	Variation in Average of Maximum Roughness
e_0	Initial Void Ratio
e_{ref0}	Virgin Reference Critical Void Ratio
e_{refu}	Ultimate Reference Critical Void Ratio
ξ	A Parameter Controls the Nonlinearity of the CSL
λ	A Parameter Controls the Shape of the CSL
σ_{a}	Adhesive Stress
σ_{n}	Normal Stress
ρ	Constant Controls the Decreasing Rate of CSL
τ_{m}	Mobilised Cyclic Shear Stress
τ_{limit}	Mobilised Cyclic Shear Stress at the 50th Cycle (as Limit)
τ_{p}	Peak Shear Stress in Monotonic Tests
τ_{ult}	Ultimate Shear Stress in Monotonic Tests
ϕ_{limit}	Mobilised Cyclic Internal Friction Angle at Limit State
ϕ_{p}	Peak Internal Friction Angle
ϕ_{ult}	Ultimate Internal Friction Angle

REFERENCES

ABUEL-NAGA H M, SHAIA H A. Interface friction evolution of FRP tube confined concrete piles during the driving installation process[J]. Géotechnique Letters, 2014, 4(1):52-56.

AL-DOURI R H, POULOS H G. Static and cyclic direct shear tests on carbonate sands[J]. Geotechnical Testing Journal, 1992, 15(2):138-157.

ALI A A M, ESSA M J K, HASSAN A Q. Dynamic analysis of offshore piles embedded in elastoplastic soft clay[C]//LAU H H, TANG F E, NG C K, et al., eds. Proceedings of the Conference on Geotechnical Engineering. ISEC Press, 2016.

ALMALLAH A, SADEGHIAN P, EL NAGGAR H. Enhancing the interface friction between glass fiber-reinforced polymer sheets and sandy soils through sand coating[J]. Geomechanics and Geoengineering, 2020a, 15(3):186-202.

ALMALLAH A, EL NAGGAR H, SADEGHIAN P. Axial behavior of innovative sand-coated GFRP piles in cohesionless soil[J]. International Journal of Geomechanics, 2020b, 20: 04020179.

ALNATIT, N M E. Computational study on shear strengthening of RC continuous beams using CFRP sheet[D]. Batu Pahat: Universiti Tun Hussein Onn Malaysia, 2011.

ALTUHAFI F N, COOP M R, GEORGIANNOU V N. Effect of particle shape on the mechanical behavior of natural sands[J]. Journal of Geotechnical and Geoenvironmental Engineering, 2016, 142: 04016071.

ANGELIDAKIS V, NADIMI S, UTILI S. Elongation, flatness and compactness indices to characterise particle form[J]. Powder Technology, 2022, 396: 689-695.

ARAÚJO G L S, SÁNCHEZ N P, PALMEIRA E M, et al. Influence of micro and macroroughness of geomembrane surfaces on soil-geomembrane and geotextile-geomembrane interface strength[J]. Geotextiles and Geomembranes, 2022, 50(4):751-763.

ARCHARD J F. Contact and rubbing of flat surfaces[J]. Journal of Applied Physics, 1953, 24(8):981-988.

ARCHARD J F. Elastic deformation and the laws of friction[J]. Proceedings of the Royal Society of London. Series A. Mathematical and Physical Sciences, 1957,

243: 190-205.

ARI A, AKBULUT S. Effect of fractal dimension on sand-geosynthetic interface shear strength[J]. Powder Technology, 2022, 401:117349.

ASTM D2487-17e1. Standard practice for classification of soils for engineering purposes (Unified Soil Classification System)[S]. West Conshohocken: ASTM International, 2017.

ASTM D3080-11. Standard test method for direct shear test of soils under consolidated drained conditions[S]. West Conshohocken: ASTM International, 2011.

ASTM D4253-16a. Standard test methods for maximum index density and unit weight of soils using a vibratory table[S]. West Conshohocken: ASTM International, 2016.

ASTM D4254-16b. Standard test methods for minimum index density and unit weight of soils and calculation of relative density[S]. West Conshohocken: ASTM International, 2016.

ASTM E11-24. Standard specification for woven wire test sieve cloth and test sieves[S]. West Conshohocken: ASTM International, 2024.

ASTM E384-22. Standard test method for microindentation hardness of materials [S]. West Conshohocken: ASTM International, 2022.

BAI J. 1 - Introduction[M]//BAI J. Advanced fiber-Reinforced Polymer (FRP) Composites for Structural Applications. 2nd ed. Cambridge**:** Woodhead Publishing, 2023a: 1-6.

BAI J. 5 - Fiber-reinforced polymer types and properties[M]// BAI J. Advanced fiber-Reinforced Polymer (FRP) Composites for Structural Applications. 2nd ed. Cambridge**:** Woodhead Publishing, 2023b: 93-99.

BAKIS C E, BANK L C, BROWN V L, et al. Fiber-reinforced polymer composites for construction—state-of-the-art review[J]. Journal of Composites for Construction, 2002, 6(2):73-87.

BIAN S H, WU B, MA Y Z, et al. Development of an interface model based on hyperbolic hardening rule and contact effect analysis of earth rockfill dam[J]. European Journal of Environmental and Civil Engineering, 2020, 26(4):1581-1602.

BIAREZ J, HICHER P-Y. Elementary mechanics of soil behaviour: saturated remoulded soils[M]. Rotterdam: A.A. Balkema, 1994.

BISHOP A W. The strength of soils as engineering materials[J]. Géotechnique, 1966, 16(2):91-130.

BOULON M, FORAY P. Physical and numerical simulation of lateral shaft friction along offshore piles in sand[C]//Proceedings of the 3rd International Conference on Numerical Methods in Offshore Piling. Nantes, France: Editions Technip, 1986: 127-147.

BOULON M. Basic features of soil structure interface behaviour[J]. Computers and Geotechnics, 1989, 7(1):115-131.

BRINKGREVE R B J. Selection of soil models and parameters for geotechnical engineering application[C]//YAMAMURO J A, KALIAKIN V N, eds. Soil Constitutive Models: Evaluation, Selection, and Calibration. Reston, Virginia: American Society of Civil Engineers, 2005: 69-98.

BRUMUND W, LEONARDS G. Experimental study of static and dynamic friction between sand and typical constuction materials[J]. Journal of Testing and Evaluation, 1973, 1(2):162-165.

CABALAR A F. The effects of fines on the behaviour of a sand mixture[J]. Geotechnical and Geological Engineering, 2010, 29(1):91-100.

CAO Y, GAO G, WANG W, et al. Deterioration behaviors of phenolic amine/epoxy-based GFRP laminates exposed to aggressive environments[J]. Composites Part A: Applied Science and Manufacturing, 2025, 192.

CEN W J, WANG H, SUN Y J, et al. Monotonic and cyclic shear behaviour of geomembrane-sand interface[J]. Geosynthetics International, 2018, 25(4):369-377.

CERFONTAINE B, DIEUDONNÉ A C, RADU J P, et al. 3D zero-thickness coupled interface finite element: Formulation and application[J]. Computers and Geotechnics, 2015, 69: 124-140.

CHEN W-B, XU T, ZHOU W-H. Microanalysis of smooth geomembrane-sand interface using FDM-DEM coupling simulation[J]. Geotextiles and Geomembranes, 2021, 49(1):276-288.

CHEN W-B, ZHOU W-H, YIN Z-Y. Recent development on macro-micro mechanism of soil-structure interface shearing through DEM[J]. Archives of Computational Methods in Engineering, 2023, 30(3):1843-1862.

CHEN X, ZHANG J, XIAO Y, et al. Effect of roughness on shear behavior of red clay-concrete interface in large-scale direct shear tests[J]. Canadian Geotechnical Journal, 2015, 52(8):1122-1135.

CHIANG D-Y. The generalized masing models for deteriorating hysteresis and cyclic plasticity[J]. Applied Mathematical Modelling, 1999, 23(11):847-863.

CHOUDHRY J, ALMQVIST A, LARSSON R. Improving Archard's wear model: an energy-based approach[J]. Tribology Letters, 2024, 72(3):93.

CLOUGH G W, DUNCAN J M. Finite element analyses of retaining wall behavior[J]. Journal of the Soil Mechanics and Foundations Division, 1971, 97(12):1657-1673.

COETZEE C J. Edinburgh-Elasto-Plastic-Adhesion (EEPA) contact model-implementation in PFC [EB/OL]. ResearchGate, 2020[2025-03-08].

COOP M R, SORENSEN K K, FREITAS T B, et al. Particle breakage during shearing of a carbonate sand[J]. Géotechnique, 2004, 54(3):157-163.

CUNDALL P A, STRACK O D L 1979. A discrete numerical model for granular assemblies[J]. Géotechnique, 2004, 29(1):47-65.

D'AGUIAR S C, MODARESSI-FARAHMAND-RAZAVI A, DOS SANTOS J A, et al. Elastoplastic constitutive modelling of soil-structure interfaces under monotonic and cyclic loading[J]. Computers and Geotechnics, 2011, 38(4):430-447.

DANESH A, MIRGHASEMI A A, PALASSI M. Evaluation of particle shape on direct shear mechanical behavior of ballast assembly using discrete element method (DEM)[J]. Transportation Geotechnics, 2020, 23: 100357.

DAOUADJI A, HICHER P-Y. An enhanced constitutive model for crushable granular materials[J]. International Journal for Numerical and Analytical Methods in Geomechanics, 2010, 34(6):555-580.

DAOUADJI A, HICHER P-Y, RAHMA A. An elastoplastic model for granular materials taking into account grain breakage[J]. European Journal of Mechanics-A/Solids, 2001, 20(1):113-137.

DASSAULT SYSTÈMES. ABAQUS user subroutines reference guide[M/OL]. USA: Dassault Systèmes Simulia Corporation, 2020[2025-03-08].

DAVID SUITS L, SHEAHAN T C, PORCINO D, et al. Interface behavior of sands from constant normal stiffness direct shear tests[J]. Geotechnical Testing Journal, 2003, 26(3): 1-10.

DEJONG J T, RANDOLPH M F, WHITE D J. Interface load transfer degradation during cyclic loading: a microscale investigation[J]. Soils and Foundations, 2003, 43(4):81-93.

DEJONG J T, WESTGATE Z J. Role of initial state, material properties, and confinement condition on local and global soil-structure interface behavior[J]. Journal of Geotechnical and Geoenvironmental Engineering, 2009, 135(11):1646-1660.

DESAI C S, DRUMM E C, ZAMAN M M. Cyclic testing and modeling of interfaces[J]. Journal of Geotechnical Engineering, 1985, 111(6):793-815.

DESAI C S, MA Y. Modelling of joints and interfaces using the disturbed-state concept[J]. International Journal for Numerical and Analytical Methods in Geomechanics, 1992, 16(9):623-653.

DESAI C S, MUQTADIR A, SCHEELE F. Interaction analysis of anchor-soil systems[J]. Journal of Geotechnical Engineering, 1986, 112(5):537-553.

DESAI C S, ZAMAN M M, LIGHTNER J G, et al. Thin-layer element for interfaces and joints[J]. International Journal for Numerical and Analytical Methods in Geomechanics, 1984, 8(1):19-43.

DI DONNA A, FERRARI A, LALOUI L. Experimental investigations of the soil-concrete interface: physical mechanisms, cyclic mobilization, and behaviour at different temperatures[J]. Canadian Geotechnical Journal, 2015, 53:659-672.

DIETZ M S, LINGS M L. Postpeak strength of interfaces in a stress-dilatancy framework[J]. Journal of Geotechnical and Geoenvironmental Engineering, 2006 132(11):1474-1484.

DOVE J E, FROST J D. Peak friction behavior of smooth geomembrane-particle interfaces[J]. Journal of Geotechnical and Geoenvironmental Engineering, 1999, 125(7):544-555.

DUNCAN J M, CHANG C-Y. Nonlinear analysis of stress and strain in soils[J]. Journal of the Soil Mechanics and Foundations Division, 1970, 96: 1629-1653.

EVGIN E, FAKHARIAN K. Cyclic rotational simple-shear behaviour of sand-steel interfaces[J]. Soils and Foundations, 1998, 38(2):191-199.

FAKHARIAN K, EVGIN E. Elasto-plastic modelling of stress-path-dependent behaviour of interfaces[J]. International Journal for Numerical and Analytical

Methods in Geomechanics, 2000, 24(2):183-199.

FELIGHA M, HAMMOUD F, BELACHIA M, et al. Experimental investigation of frictional behavior between cohesive soils and solid materials using direct shear apparatus[J]. Geotechnical and Geological Engineering, 2015, 34(2):567-578.

FENG D-K, ZHANG J-M, DENG L-J. Three-dimensional monotonic and cyclic behavior of a gravel-steel interface from large-scale simple-shear tests[J]. Canadian Geotechnical Journal, 2018, 55(11):1657-1667.

FENG S-J, CHEN J-N, CHEN H-X, et al. Analysis of sand-woven geotextile interface shear behavior using discrete element method (DEM)[J]. Canadian Geotechnical Journal, 2020, 57(3):433-447.

FENG S-J, LIU X, CHEN H-X, et al. Micro-mechanical analysis of geomembrane-sand interactions using DEM[J]. Computers and Geotechnics, 2018, 94: 58-71

FENG S-J, WANG Y-Q, CHEN H-X. DEM simulation of geotextile-geomembrane interface direct shear test considering the interlocking and wearing processes[J]. Computers and Geotechnics, 2022, 148: 104805.

FENG W-Q, ZHANG T-Y, LI Y-X, et al. Experimental study of interface performance between calcareous sand and steel pile with different surface roughness and temperatures[J]. Ocean Engineering, 2024, 292: 116469.

FENG Y, WANG D. Shear behaviors and peak friction angle predictions of three critical geomembrane-soil interfaces[J]. Acta Geotechnica, 2023, 19: 3139-3160.

FIORAVANTE V, GHIONNA V N, PEDRONI S, et al. A constant normal stiffness direct shear box for soil-solid interface tests[C]//Proceedings of the 12th European Conference on Soil Mechanics and Geotechnical Engineering. Amsterdam, Netherlands, 1999:1167-1172.

FLEMING I R, SHARMA J S, JOGI M B. Shear strength of geomembrane-soil interface under unsaturated conditions[J]. Geotextiles and Geomembranes, 2006, 24(5):274-284.

FROST J D, DEJONG J T, RECALDE M. Shear failure behavior of granular-continuum interfaces[J]. Engineering Fracture Mechanics, 2002, 69(17):2029-2048.

FROST J D, HAN J. Behavior of interfaces between fiber-reinforced polymers and sands[J]. Journal of Geotechnical and Geoenvironmental Engineering, 1999, 125(8):633-640.

FROST J D, KIM D, LEE S-W. Microscale geomembrane-granular material interactions[J]. KSCE Journal of Civil Engineering, 2012, 16(1):79-92.

GENNARO V D, FRANK R. Elasto-plastic analysis of the interface behaviour between granular media and structure[J]. Computers and Geotechnics, 2002, 29(7):547-572.

GHIONNA V N, MORTARA G. An elastoplastic model for sand-structure interface behaviour[J]. Géotechnique, 2002, 52(1): 41-50.

GIRALDO J, RAYHANI M T. Influence of fiber-reinforced polymers on pile-soil interface strength in clays[J]. Advances in Civil Engineering Materials, 2013, 2(1): 534-550.

GIRALDO J, RAYHANI M T. Load transfer of hollow fiber-reinforced polymer (FRP) piles in soft clay[J]. Transportation Geotechnics, 2014, 1(2): 63-73.

GÓMEZ J E, FILZ G M, EBELING R M. Extended hyperbolic model for sand-to-concrete interfaces[J]. Journal of Geotechnical and Geoenvironmental Engineering, 2003, 129(11): 993-1000.

GOODMAN R E, TAYLOR R L, BREKKE T L. A model for the mechanics of jointed rock[J]. Journal of the Soil Mechanics and Foundations Division, 1968, 94(3): 637-659.

GRABOWSKI A, NITKA M, TEJCHMAN J. 3D DEM simulations of monotonic interface behaviour between cohesionless sand and rigid wall of different roughness[J]. Acta Geotechnica, 2021a, 16(4): 1001-1026.

GRABOWSKI A, NITKA M, TEJCHMAN J. Comparative 3D DEM simulations of sand-structure interfaces with similarly shaped clumps versus spheres with contact moments[J]. Acta Geotechnica, 2021b, 16(11): 3533-3554.

GU X, CHEN Y, HUANG M. Critical state shear behavior of the soil-structure interface determined by discrete element modeling[J]. Particuology, 2017, 35: 68-77.

HAN F, GANJU E, SALGADO R, et al. Effects of interface roughness, particle geometry, and gradation on the sand-steel interface friction angle[J]. Journal of Geotechnical and Geoenvironmental Engineering, 2018, 144(12): 04018096.

HAN J. An experimental and analytical study of the behavior of fiber-reinforced polymer piles and pile-sand interactions[D]. Atlanta: Georgia Institute of Technology, 1997.

HANSEN N. The CMA evolution strategy: a comparing review[C]//LOZANO J A, LARRAÑAGA P, INZA I, BENGOETXEA E, eds. Towards a New Evolutionary Computation: Advances in the Estimation of Distribution Algorithms. Berlin, Heidelberg: Springer, 2007: 75-102.

HE H, CHEN W, YIN Z-Y, et al. A micromechanical-based study on the tribological and creep-relaxation behavior of sand-FRP composite interfaces[J]. Composite Structures, 2021, 275: 114423.

HO T Y K, JARDINE R J, ANH-MINH N. Large-displacement interface shear between steel and granular media[J]. Géotechnique, 2011, 61(3):221-234.

HOU J, LI H, LIU L, et al. A DEM analysis of geomembrane-lined landfill subject to vertical loading[J]. Geotextiles and Geomembranes, 2021, 49(2): 369-375.

HU L, PU J. Testing and Modeling of Soil-Structure Interface[J]. Journal of Geotechnical and Geoenvironmental Engineering, 2004, 130(8): 851-860.

HU L P, JIA L. Application of damage model for soil-structure interface[J]. Computers and Geotechnics, 2003, 30(2): 165-183.

HU W, YIN Z, DANO C, et al. A constitutive model for granular materials considering grain breakage[J]. Science China Technological Sciences, 2011, 54(8): 2188-2196.

HUANG M, CHEN Y, GU X. Discrete element modeling of soil-structure interface behavior under cyclic loading[J]. Computers and Geotechnics, 2019, 107: 14-24.

HUANG X, HANLEY K J, O'SULLIVAN C, et al. Exploring the influence of interparticle friction on critical state behaviour using DEM[J]. International Journal for Numerical and Analytical Methods in Geomechanics, 2014, 38(12): 1276-1297.

ISKANDER M G, HASSAN M. State of the practice review in FRP composite piling[J]. Journal of Composites for Construction, 1998, 2(3): 116-120.

ISO 4287. Geometrical product specifications (GPS) — surface texture: profile method — terms, definitions, and surface texture parameters[S]. Geneva: International Organization for Standardization, 1997.

ISO 25178-2. Geometrical product specifications (GPS) — surface texture: areal — part 2: terms, definitions and surface texture parameters[S]. Geneva: International Organization for Standardization, 2012.

JACOBSON D, VALDES J, EVANS T. A numerical view into direct shear specimen size

effects[J]. Geotechnical Testing Journal, 2007, 30(6): 512-516.

JANOO V C. Quantification of shape, angularity, and surface texture of base course materials[R/OL]. 1998[2025-03-08]. https://rosap.ntl.bts.gov/view/dot/14065.

JEWELL R A. Direct shear tests on sand[J]. Géotechnique, 1989, 39(2):309-322.

JIA Y, ZHANG J, ZHENG Y. 3D DEM investigation of shear behavior and interaction mechanism of woven geotextile-sand interfaces[J]. Geotextiles and Geomembranes, 2024, 52(5): 1011-1023.

JIANG M, SHEN Z, WANG J. A novel three-dimensional contact model for granulates incorporating rolling and twisting resistances[J]. Computers and Geotechnics, 2015, 65: 147-163.

JING X-Y, ZHOU W-H, ZHU H-X, et al. Analysis of soil-structural interface behavior using three-dimensional DEM simulations[J]. International Journal for Numerical and Analytical Methods in Geomechanics, 2018, 42(2): 339-357.

JOHNSON K L, KENDALL K, ROBERTS A D. Surface energy and the contact of elastic solids[J]. Proceedings of the Royal Society of London. A. Mathematical and Physical Sciences, 1971, 324:301-313.

KHISHVAND M, NAZEM M. On application of the third medium contact method in analysis of geotechnical problems[J]. Applied Mechanics and Materials, 2016, 846:282-287.

KOK S, TI, HUAT B, et al. A review of basic soil constitutive models for geotechnical application[J]. Electronic Journal of Geotechnical Engineering, 2009, 14: 1-18.

LADE P V. Overview of constitutive models for soils[C]//Proceedings of the ASCE Geotechnical Special Publication No. 128: Soil Constitutive Models: Evaluation, Selection, and Calibration. Reston, VA: American Society of Civil Engineers, 2005a: 1-34.

LADE P V. Single hardening model for soils: parameter determination and typical values[C]//Proceedings of the ASCE Geotechnical Special Publication No. 128: Soil Constitutive Models: Evaluation, Selection, and Calibration. Reston, VA: American Society of Civil Engineers, 2005b: 290-309.

LASHKARI A. A critical state model for saturated and unsaturated interfaces[J]. Scientia Iranica, 2012, 19(5): 1147-1156.

LASHKARI A, JAMALI V. Global and local sand-geosynthetic interface behaviour[J].

Géotechnique, 2021, 71(4): 346-367.

LAVANYA I, PRABHA R, MURUGAN M. Behaviour of interfaces between carbon fibre reinforced polymer and gravel soils[J]. International Journal of Research in Engineering and Technology, 2014, 3(11): 4.

LE T M, FATAHI B, KHABBAZ H. Viscous behaviour of soft clay and inducing factors[J]. Geotechnical and Geological Engineering, 2012, 30(5): 1069-1083.

LIU F-Y, YING M-J, YUAN G-H, et al. Particle shape effects on the cyclic shear behaviour of the soil-geogrid interface[J]. Geotextiles and Geomembranes, 2021, 49(4): 991-1003.

LIU H, SONG E, LING H I. Constitutive modeling of soil-structure interface through the concept of critical state soil mechanics[J]. Mechanics Research Communications, 2006, 33(4): 515-531.

LIU J, WU L, YIN K, et al. Methods for solving finite element mesh-dependency problems in geotechnical engineering—a review[J]. Sustainability, 2022, 14: 2982.

LIU J, YIN Z-Y, WU L, et al. Finite element implementation and application of a sand model in micropolar theory[J]. SN Applied Sciences, 2021, 3: 725.

LIU J, ZOU D, KONG X. A three-dimensional state-dependent model of soil-structure interface for monotonic and cyclic loadings[J]. Computers and Geotechnics, 2014, 61: 166-177.

LIU J W, CUI L, ZHU N, et al. Investigation of cyclic pile-sand interface weakening mechanism based on large-scale CNS cyclic direct shear tests[J]. Ocean Engineering, 2019, 194: 106650.

LIU R, LI C, PENG B. Axial pipe-soil interaction during pipeline-walking analysis of pipelines placed on Bohai sand[J]. Applied Ocean Research, 2020, 99: 102133.

LIU Y, GAO R, CHEN J. Exploring the influence of sphericity on the mechanical behaviors of ballast particles subjected to direct shear[J]. Granular Matter, 2019, 21: 94.

MAGHSOODI S. Thermo-mechanical behavior of soil-structure interface under monotonic and cyclic loads in the context of energy geostructures[D]. Nancy: Université de Lorraine, 2020.

MAGHSOODI S, CUISINIER O, MASROURI F. Effect of temperature on the cyclic behavior of clay-structure interface[J]. Journal of Geotechnical and

Geoenvironmental Engineering, 2020a, 146(10): 04020103.

MAGHSOODI S, CUISINIER O, MASROURI F. Thermal effects on mechanical behaviour of soil-structure interface[J]. Canadian Geotechnical Journal, 2020b, 57(1): 32-47.

MARTINEZ A, FROST J. Particle-scale effects on global axial and torsional interface shear behavior[J]. International Journal for Numerical and Analytical Methods in Geomechanics, 2016, 41: 400-421.

MARTINEZ A, FROST J D. The influence of surface roughness form on the strength of sand-structure interfaces[J]. Géotechnique Letters, 2017, 7(1): 104-111.

MARTINEZ A, STUTZ H H. Rate effects on the interface shear behaviour of normally and overconsolidated clay[J]. Géotechnique, 2019, 69(9): 801-815.

MINH N H, CHENG Y P. On the contact force distributions of granular mixtures under 1D-compression[J]. Granular Matter, 2016, 18(2): 1-18.

MORALES ARIAS J P M, VAZQUEZ A, ESCOBAR M M. Use of sand coating to improve bonding between GFRP bars and concrete[J]. Journal of composite materials, 2012, 46: 2271-2278.

MORRISSEY J. Discrete element modelling of iron ore pellets to include the effects of moisture and fines[D]. Edinburgh: University of Edinburgh, 2013.

MORTARA G, MANGIOLA A, GHIONNA V N. Cyclic shear stress degradation and post-cyclic behaviour from sand-steel interface direct shear tests[J]. Canadian Geotechnical Journal, 2007, 44(7): 739-752.

NAMJOO A M, BANIASADI M, JAFARI K, et al. Studying effects of interface surface roughness, mean particle size, and particle shape on the shear behavior of sand-coated CFRP interface[J]. Transportation Geotechnics, 2022, 37: 100841.

NAMJOO A M, JAFARI K, TOUFIGH V. Effect of particle size of sand and surface properties of reinforcement on sand-geosynthetics and sand-carbon fiber polymer interface shear behavior[J]. Transportation Geotechnics, 2020, 24: 100403.

NECOCHEA J E, SÁEZ E, HANLEY K J. Effect of sand particle shape on micromechanical modeling in direct shear testing[J]. Computers and Geotechnics, 2024, 169: 106222.

NGUYEN H B K, RAHMAN M M, FOURIE A B. How particle shape affects the critical state, triggering of instability and dilatancy of granular materials – results from a

DEM study[J]. Géotechnique, 2021, 71(9): 749-764.

NITKA M, GRABOWSKI A. Shear band evolution phenomena in direct shear test modelled with DEM[J]. Powder Technology, 2021, 391: 369-384.

O'ROURKE T D, DRUSCHEL S J, NETRAVALI A N. Shear strength characteristics of sand-polymer interfaces[J]. Journal of Geotechnical Engineering, 1990, 116(3): 451-469.

OUMAROU T A, EVGIN E. Cyclic behaviour of a sand-steel plate interface [J]. Canadian Geotechnical Journal, 2005, 42(6): 1695-1704.

PAIKOWSKY S, PLAYER C, CONNORS P. A Dual interface apparatus for testing unrestricted friction of soil along solid surfaces[J]. Geotechnical Testing Journal, 1995, 18(2): 168-193.

PANDO A M, FILZ GEORGE M, DOVE JOSEPH E, et al. Interface shear tests on FRP composite piles[J]. Deep Foundations, 2002, 48: 1486-1500.

PONCE V M, BELL J M. Shear strength of sand at extremely low pressures[J]. Journal of the Soil Mechanics and Foundations Division, 1971, 97(4): 625-638.

PORCINO D, FIORAVANTE V, GHIONNA V, et al. Interface behavior of sands from constant normal stiffness direct shear tests[J]. Geotechnical Testing Journal, 2003, 26(3): 289-301.

POTYONDY J G. Skin friction between various soils and construction materials[J]. Géotechnique, 1961, 11(4): 339-353.

POULOS H G. Cyclic axial loading analysis of piles in sand[J]. Journal of Geotechnical Engineering, 1989, 115(6): 836-852.

POWELL M J D. An efficient method for finding the minimum of a function of several variables without calculating derivatives[J]. The Computer Journal, 1964, 7(2): 155-162.

PRA-AI S, BOULON M. Soil-structure cyclic direct shear tests: a new interpretation of the direct shear experiment and its application to a series of cyclic tests[J]. Acta Geotechnica, 2017, 12(1): 107-127.

QURESHI J. Fibre-reinforced polymer (FRP) in civil engineering[C]//L. LI, A. B. PEREIRA, A. L. PEREIRA. Next Generation Fiber-Reinforced Composites - New Insights. Rijeka:IntechOpen, 2022.

ROSCOE K H, BURLAND J. On the generalized stress-strain behaviour of wet

clay[M]//HEYMAN J, LECKIE F P, eds. Engineering Plasticity. Cambridge: Cambridge University Press, 1968: 535-609.

ROSCOE K H, SCHOFIELD A N, THURAIRAJAH A. Yielding of clays in states wetter than critical[J]. Géotechnique, 1963, 13(3): 211-240.

RUI S, WANG L, GUO Z, et al. 2021. Cyclic behavior of interface shear between carbonate sand and steel[J]. Acta Geotechnica, 16(1): 189-209.

SABERI M, ANNAN C-D, KONRAD J-M 2019. Implementation of a soil-structure interface constitutive model for application in geo-structures[J]. Soil dynamics and earthquake engineering, 116: 714-731.

SAKR M, NAGGAR M H E, NEHDI M. Interface characteristics and laboratory constructability tests of novel fiber-reinforced polymer/concrete piles[J]. Journal of Composites for Construction, 2005, 9(3): 274-283.

SAMANTA M, BHOWMIK R, KHANDERI H. Laboratory evaluation of dynamic shear response of sand-geomembrane interface[J]. Geosynthetics International, 2022, 29(1): 99-112.

SCHANZ T, VERMEER P A, BONNIER P G. The hardening soil model: Formulation and verification[C]//In: Proceedings plaxis symposium-beyond 2000 in computational geotechnics. Balkema, Amsterdam, 1999.

SCHANZ T, VERMEER P A, BONNIER P G. The hardening soil model: formulation and verification[M]. Beyond 2000 in Computational Geotechnics, 2019.

SCHELLEKENS J C J, DE BORST R. On the numerical integration of interface elements[J]. International Journal for Numerical Methods in Engineering, 1993, 36(1): 43-66.

SCHOFIELD A N, WROTH P. Critical state soil mechanics[M]. New York: McGraw-Hill London, 1968.

SHAHROUR I, REZAIE F. An elastoplastic constitutive relation for the soil-structure interface under cyclic loading[J]. Computers and Geotechnics, 1997, 21(1): 21-39.

SHAKIBA M, HOSSEINI S M, BAZLI M, et al. Enhancement of the bond behaviour between sand coated GFRP bar and normal concrete using innovative composite anchor heads[J]. Materials and Structures, 2022, 55: 236.

SHOOTER K V, TABOR D. The frictional properties of plastics[C]// Proceedings of the

Physical Society. Section B, 1952, 65(9): 661.

SMOLEŃ J, STĘPIEŃ K, MROWIEC A, et al. Study of resin coating adhesion on GFRP laminate surfaces after UV degradation[J]. International Journal of Adhesion and Adhesives, 2024, 135.

SONG S, WANG P, YIN Z, et al. Micromechanical modeling of hollow cylinder torsional shear test on sand using discrete element method[J]. Journal of Rock Mechanics and Geotechnical Engineering, 2024, 16(12): 5193-5208.

STARK T D, WILLIAMSON T A, EID H T. HDPE geomembrane/geotextile interface shear strength[J]. Journal of Geotechnical Engineering, 1996, 122(3): 197-203.

SU D, WU D, FAN M, et al. DEM investigation into the coupling effects of particle asphericity and interface roughness on shear behaviour of soil-structure interface[J]. Particuology, 2025, 97: 39-57.

SU L-J, ZHOU W-H, CHEN W-B, et al. Effects of relative roughness and mean particle size on the shear strength of sand-steel interface[J]. Measurement, 2018, 122: 339-346.

SUBBA RAO K S, RAO K S S, ALLAM M M, et al. Interfacial friction between sands and solid surfaces[J]. Proceedings of the Institution of Civil Engineers, Geotechnical Engineering, 1998, 131(2): 75-82.

TATSUOKA F, MASUDA T, SIDDIQUEE M S A, et al. Modeling the stress-strain relations of sand in cyclic plane strain loading[J]. Journal of Geotechnical and Geoenvironmental Engineering, 2003, 129(5): 450-467.

TENG J-C, YIN Z-Y, CHEN W-B, et al. Interface shear behavior of sandy soil-fRP with epoxy hardness effect and abrasion[J]. Journal of Composites for Construction, 2024, 28(6): 04024064.

THEVANAYAGAM S. Intergrain contact density indices for granular mixes—I: framework. Earthquake Engineering and Engineering Vibration [J], 2007, 6(2): 123-134.

THEVANAYAGAM S, SHENTHAN T, MOHAN S, et al. Undrained Fragility of Clean Sands, Silty Sands, and Sandy Silts[J]. Journal of Geotechnical and Geoenvironmental Engineering, 2002, 128: 849-859.

THOMAS T R. Rough surfaces[M]. London: Imperial College Press, 1998.

TIWARI B, AL-ADHADH A R. Influence of relative density on static soil-structure

frictional resistance of dry and saturated sand[J]. Geotechnical and Geological Engineering, 2013, 32(2): 411-427.

TOUFIGH V, OURIA A, DESAI C S, et al. Interface behavior between carbon-fiber polymer and sand[J]. Journal of Testing and Evaluation, 2016, 44(1): 385-390.

TSUBAKIHARA Y, KISHIDA H, NISHIYAMA T. Friction between cohesive soils and steel[J]. Soils and Foundations, 1993, 33(2): 145-156.

UESUGI M, KISHIDA H. Frictional resistance at yield between dry sand and mild steel[J]. Soils and Foundations, 1986a, 26(4): 139-149.

UESUGI M, KISHIDA H. Influential factors of friction between steel and dry sands[J]. Soils and Foundations, 1986b, 26(2): 33-46.

UESUGI M, KISHIDA H, TSUBAKIHARA Y. Behavior of sand particles in sand-steel friction[J]. Soils and Foundations, 1988, 28(1): 107-118.

UESUGI M, KISHIDA H, TSUBAKIHARA Y. Friction between sand and steel under repeated loading[J]. Soils and Foundations, 1989, 29(3): 127-137.

VANGLA P, GALI M L. Shear behavior of sand-smooth geomembrane interfaces through micro-topographical analysis[J]. Geotextiles and Geomembranes, 2016, 44(4): 592-603.

VANGLA P, LATHA G M. Influence of particle size on the friction and interfacial shear strength of sands of similar morphology[J]. International Journal of Geosynthetics and Ground Engineering, 2015, 1(1): 6.

VERMEER P, BAKKER K, BONNIER P. Plaxis; finite element code for soil and rock plasticity, version 4: general information and tutorial manual[M]. Rotterdam: Balkema, 1991.

VIEIRA C S, LOPES M L, CALDEIRA L M. Sand-geotextile interface characterisation through monotonic and cyclic direct shear tests[J]. Geosynthetics International, 2013, 20(1): 26-38.

WADELL H. Volume, shape, and roundness of rock particles[J]. Journal of Geology, 1932, 40(5): 443-451.

WALTON O R, BRAUN R L. Viscosity, granular-temperature, and stress calculations for shearing assemblies of inelastic, frictional disks[J]. Journal of Rheology, 1986, 30: 949-980.

WANG H-L, JIN Y-F, YIN Z-Y, et al. Uncertainty quantification of soil-structure

interface properties with an enhanced hypoplastic interface model[J]. International Journal of Geomechanics, 2024a, 24(6): 04024103.

WANG H-L, YIN Z-Y, GU X-Q, et al. Evaluation of soil-structure interface models considering cyclic loading effect[J]. International Journal for Numerical and Analytical Methods in Geomechanics, 2024b, 48(17): 4257-4273.

WANG H-L, YIN Z-Y, JIN Y-F, et al. Evaluation of soil-structure interface models[J]. Journal of Geotechnical and Geoenvironmental Engineering, 2024c, 150(7): 04024050.

WANG H-L, ZHANG Q-Y, YIN Z-Y, et al. Effect of sand particle size on interface shear behaviour between bio-cemented sand by MICP treatment and steel structure[J]. Canadian Geotechnical Journal, 2023, 60(3): 269-286.

WANG H-L, ZHOU W-H, YIN Z-Y, et al. Effect of grain size distribution of sandy soil on shearing behaviors at soil-structure interface[J]. Journal of Materials in Civil Engineering, 2019, 31(10): 04019238.

WANG J, GUTIERREZ M S, DOVE J E. Numerical studies of shear banding in interface shear tests using a new strain calculation method[J]. International Journal for Numerical and Analytical Methods in Geomechanics, 2007, 31(12): 1349-1366.

WANG J, LIU F Y, WANG P, et al. Particle size effects on coarse soil-geogrid interface response in cyclic and post-cyclic direct shear tests[J]. Geotextiles and Geomembranes, 2016, 44(6): 854-861.

WANG P, YIN Z-Y. Effect of particle breakage on the behavior of soil-structure interface under constant normal stiffness condition with DEM[J]. Computers and Geotechnics, 2022, 147: 104766.

WANG P, YIN Z-Y, WANG Z-Y. Micromechanical investigation of particle-size effect of granular materials in biaxial test with the role of particle breakage[J]. Journal of Engineering Mechanics, 2022a, 148(1): 04021133.

WANG P, YIN Z-Y, ZHOU W-H, et al. Micro-mechanical analysis of soil-structure interface behavior under constant normal stiffness condition with DEM[J]. Acta Geotechnica, 2022b, 17(7): 2711-2733.

WESTGATE Z J, DEJONG J T. Role of initial state, material properties, and confinement condition on local and global soil-structure interface behavior during cyclic shear[J]. Journal of Geotechnical and Geoenvironmental Engineering, 2023,

149(10).

WHITE D. An investigation into the behaviour of pressed-in piles [D]. Cambridge: University of Cambridge, 2002.

WHITE D, DIJKSTRA J, GAUDIN C. Comparison of failure modes below footings on carbonate and silica sands[J]. International Journal of Physical Modelling in Geotechnics, 2013, 13: 1-12.

WICHTMANN T. Soil behaviour under cyclic loading - experimental observations, constitutive description and applications [D]. Karlsruhe: Karlsruhe Institute of Technology, 2016.

WU Y, YAMAMOTO H, CUI J, et al. Influence of load mode on particle crushing characteristics of silica sand at high stresses[J]. International Journal of Geomechanics, 2020, 20: 04019194.

XIONG Z, LIU Y, ZUO Y, et al. Shear performance assessment of sand-coated GFRP perforated connectors embedded in concrete[J]. Materials, 2019, 12(12):1906.

XU G, SHI J, LI Y. Change pattern of geomembrane surface roughness for geotextile/textured geomembrane interfaces[J]. Geotextiles and Geomembranes, 2023, 51(1): 88-99.

YANG S, LACASSE S, SANDVEN R. Determination of the Transitional Fines Content of Mixtures of Sand and Non-plastic Fines[J]. Geotechnical Testing Journal, 2006, 29: 102-107.

YANG J, YIN Z Y. Soil-structure interface modeling with the nonlinear incremental approach[J]. International Journal for Numerical and Analytical Methods in Geomechanics, 2021, 45(10): 1381-1404.

YILMAZ Y, DENG Y, CHANG C S, et al. Strength–dilatancy and critical state behaviours of binary mixtures of graded sands influenced by particle size ratio and fines content[J]. Géotechnique, 2021, 73: 202-217.

YIN Z-Y, CHANG C S. Stress-dilatancy behavior for sand under loading and unloading conditions[J]. International Journal for Numerical and Analytical Methods in Geomechanics, 2013, 37(8): 855-870.

YIN Z-Y, HICHER P-Y, JIN Y-F. Practice of constitutive modelling for saturated soils[M]. Singapore: Springer Singapore, 2020.

YIN Z-Y, JIN Y-F, SHEN J S, et al. Optimization techniques for identifying soil

parameters in geotechnical engineering: Comparative study and enhancement[J]. International Journal for Numerical and Analytical Methods in Geomechanics, 2018a, 42(1): 70-94.

YIN Z-Y, WU Z-X, HICHER P-Y. Modeling monotonic and cyclic behavior of granular materials by exponential constitutive function[J]. Journal of Engineering Mechanics, 2018b, 144(4): 04018014.

YOSHIMI Y, KISHIDA T. A ring torsion apparatus for evaluating friction between soil and metal surfaces[J]. Geotechnical Testing Journal, 1981, 4(4): 145-152.

YUE Y, WANG W-W, ZHANG L, et al. Effect of sand coating on durability and micro-structural deterioration of GFRP rebar under alkaline environment attack[J]. Construction and Building Materials, 2024, 413.

ZAMAN M M U, DESAI C S, DRUMM E C. Interface model for dynamic soil-structure interaction[J]. Journal of Geotechnical Engineering, 1984a, 110(9): 1257-1273.

ZETTLER T E, FROST J D, DEJONG J T. Shear-induced changes in smooth HDPE geomembrane surface topography[J]. Geosynthetics International, 2000, 7(3): 243-267.

ZHANG B, HUANG Y. Impact behavior of superspeed granular flow: Insights from centrifuge modeling and DEM simulation[J]. Engineering Geology, 2022, 299: 106569.

ZHANG C-C, ZHU H-H, SHI B, et al. Experimental investigation of pullout behavior of fiber-reinforced polymer reinforcements in sand[J]. Journal of Composites for Construction, 2015, 19(3): 04014062.

ZHANG G, ZHANG J-M. Large-scale apparatus for monotonic and cyclic soil-structure interface test[J]. Geotechnical Testing Journal, 2006, 29(5): 401-408.

ZHANG G, ZHANG J. State of the art: mechanical behavior of soil-structure interface[J]. Progress in Natural Science, 2009, 19(10): 1187-1196.

ZHANG P, DING S, FEI K. Research on shear behavior of sand-structure interface based on monotonic and cyclic tests[J]. Applied Sciences, 2021, 11(24): 11837.

ZHAO C, ZHANG R, ZHAO C, et al. A three-dimensional evaluation of interface shear behavior between granular material and rough surface[J]. Journal of Testing and Evaluation, 2021, 49(2): 713-727.

ZHAO Q, ZHAO X-L, ZHANG D, et al. Degradation of GFRP bars with epoxy and

vinyl ester matrices in a marine concrete environment: an experimental study and theoretical modeling[J]. Journal of Composites for Construction, 2024, 28.

ZHAO S, ZHOU X, LIU W. Discrete element simulations of direct shear tests with particle angularity effect[J]. Granular Matter, 2015, 17(6): 793-806.

ZHOU W, GUO Z, WANG L, et al. Sand-steel interface behaviour under large-displacement and cyclic shear[J]. Soil Dynamics and Earthquake Engineering, 2020, 138: 106352.

ZHOU W, XU M. DEM analysis of the influence of particle shape on the small-strain stiffness of granular materials[J]. Computers and Geotechnics, 2025, 179: 106996.

ZOHRA B F, FOUAD B A, MOHAMED C. Soil-structure interaction interfaces: literature review[J]. Arabian Journal of Geosciences, 2022, 15(12): 1130.

ZUO L, BAUDET B A. Determination of the transitional fines content of sand-non plastic fines mixtures[J]. Soils and Foundations, 2015, 55: 213-219.

APPENDIX A: SUPPLIMENTARY FINDINGS FOR CHAPTER 3

Figure A-1 provides the supporting analysis of strength envelope and fitting demonstration, showing the coefficient of determination (R^2) for different interfaces for loose and dense specimen value in the linear fitting is closer to 1.

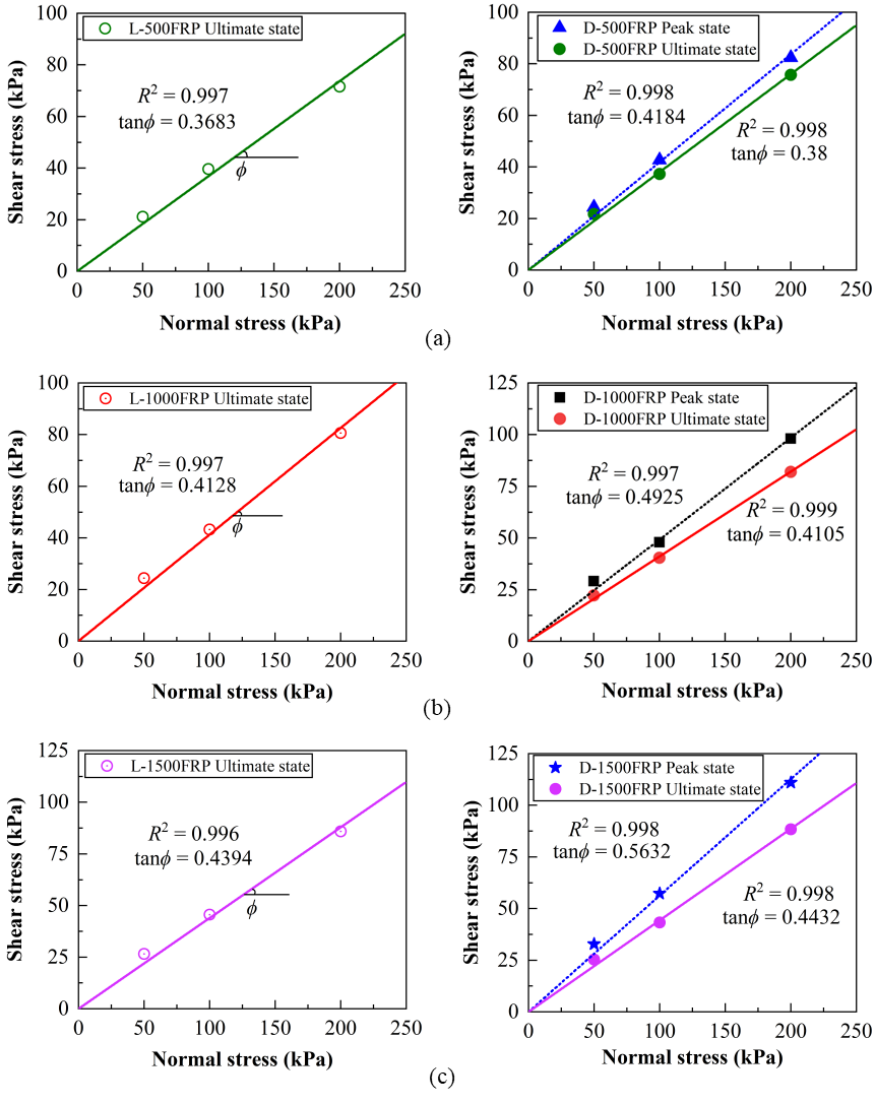

Figure A-1 Strength envelope and coefficient of determination for different interfaces for loose and dense specimens (a) F-500FRP, (b) F-1000FRP, and (c) F-1500FRP

Table A-1 Overview of materials and test setups used in present study and literature

Reference	Soil	d_{50} [size range] (mm)	Specimen type or D_r (%)	Particle morphology	Structure type	Shear rate (mm/min)	Normal stress (kPa)
Present study	Fujian sand	0.212, 1.001 [0.15–0.3, 0.85–1.18]	90±2	C_{irc}=0.726, 0.855 R_{rd}=0.596, 0.678	Pultruded GFRP (smooth and rough) and sand-epoxied GFRP with 0.1–0.8 mm grade and concentrations (500–1500 g/m^2)	0.6	50, 100, 200
Namjoo et al. (2022)	Sand	0.212, 0.841 [0.15–0.3, 0.6–1.18]	80	R_{rd}=0.68, 0.756 S=0.825, 0.869	Sand-coated CFRP sheets with four grain ranges: 0.15–0.3, 0.3–0.6, 0.6–1.18, and 1.18–2.0 mm	1.0	100
Almallah et al. (2020a)	Sand	0.6 [0.075–4.75]	33, 95	Subrounded to rounded	GFRP sheets and sand-coated GFRP sheets with 1.18–2.36 grade and concentrations (500–2500 g/m^2)	0.24	50, 100, 200
Toufigh et al. (2016)	Sand	~0.229*	92–99	n/a	Sand-coated CFRP sheets	0.47	31–196
Sakr et al. (2005)	Fanshawe brick-sand	0.26 [0.075–2.0]	90±2.5	Subrounded to rounded	Filament-wound smooth surface GFRP (fiber layup +55°/-55°) and rough surface GFRP (fiber layup 0°/90°)	0.25	25–200
Frost and Han (1999)	Blasting sand and Glass beads	~1.6* [0.075–2.36], ~0.55*	81–94, Dense sand	Subangular to angular, Rounded	Pultruded GFRP	0.25	27–206

Note: d_{50} refers to the median particle size, D_r refers to the relative density of the specimen, C_{irc} refers to the circularity, R_{rd} refers to the roundness, S refers to the particle sphericity, and n/a refers to not available. *Estimated from the provided graph or tabulated data.

APPENDIX B: SUPPLEMENTARY FINDINGS FOR CHAPTER 4

A quantitative comparison of the friction angle of sand-GFRP interfaces can be made with respect to the friction angle of pure sand shearing. These ratios at peak state and ultimate state can be obtained by peak friction angle ratio ($PFAR$), and ultimate friction angle ratio ($UFAR$), respectively, given by:

$$PFAR = \frac{\delta_{\mathrm{p}}}{\phi_{\mathrm{p}}} \tag{B-1a}$$

$$UFAR = \frac{\delta_{\mathrm{ult}}}{\phi_{\mathrm{ult}}} \tag{B-1b}$$

In engineering applications such as piles and anchors, the limit state design holds design ratio ($D.R.$) and efficiency factors ($E.F.$) for structural reinforcement purposes, which are estimated through (e.g., Namjoo et al., 2022):

$$D.R. = \frac{\tan(\delta_{\mathrm{ult}})}{\tan(\phi_{\mathrm{ult}})} \tag{B-2a}$$

$$E.F. = \frac{\tan(\delta_{\mathrm{p}})}{\tan(\phi_{\mathrm{p}})} \tag{B-2b}$$

Furthermore, to examine the effectiveness of sand-epoxied GFRP, the efficiency factor ($E.F._{\mathrm{s-e\,GFRP}}$) based on the tangent of the peak stress state envelope can be calculated through

$$E.F._{\mathrm{s-e\,GFRP}} = \frac{\tan(\delta_{\mathrm{p}})_{\mathrm{GFRP}}}{\tan(\phi_{\mathrm{p}})_{\mathrm{PFRP(S)}}} \tag{B-3}$$

Figure B-1 shows the mechanical response of pure sand shearing in direct shear tests. Increasing particle size and roundness prevailed for an increasing tendency towards dilation and strain softening, which diminished with the increasing normal stresses. The trends follow the expected theoretical trend in the mechanical responses of fine, medium, and coarse sand curves under 200,

400, and 800 kPa normal stress (Figures B-1(a) and B-1(b)).

Figure B-2 shows the cyclic shear response for pure sand (fine and coarse sand) shearing under 200 kPa normal stress, considering 100 cycles. It illustrates that around 50 cycle numbers are the appropriate number of cycles for the present configuration of the shearing system. After 50 cycles, excessive sand particles start to flow outward from the interface. Therefore, an effective maximum number of 50 cycles was performed in the entire study in the strain-dependent cyclic shearing mode.

Figure B-3 shows the cyclic shear stress and normal displacement versus tangential displacement of fine, medium, and coarse sand under 200 kPa normal stress for N = 1, 4, 15, 30, and 50 cycle numbers. Figure B-4 illustrates the mobilised friction angle at the limit state of cyclic shearing, along with the peak and ultimate friction angles from monotonic shearing with respect to median particle size. As the median particle size increases, the peak friction angle of pure sand in monotonic shearing also increases. A similar trend is observed for the limit state friction angle in cyclic shearing, which exhibits more than a 6% increase, as shown in Figure B-4.

Figure B-5 demonstrates that the repeatability test results closely match those with three consecutive test samples, indicating high precision. This trend confirms the accuracy of both sample preparation and testing. For the engineering design and application of sand-GFRP interfaces, parameters such as the friction angle ratio, efficiency factors, and design ratios play a critical role. These parameters are derived from monotonic testing and are summarised in Table B-1. The efficiency factors for sand-GFRP interfaces range from 0.72 to 0.98, with a mean of 0.86 and a standard deviation of 0.08. Similarly, the design ratios vary between 0.74 and 1.07, with a mean of 0.93 and a standard deviation of 0.09. Specifically, for sand-epoxied GFRPs, the mean efficiency factor and mean design ratio are 0.89 and 0.95, respectively.

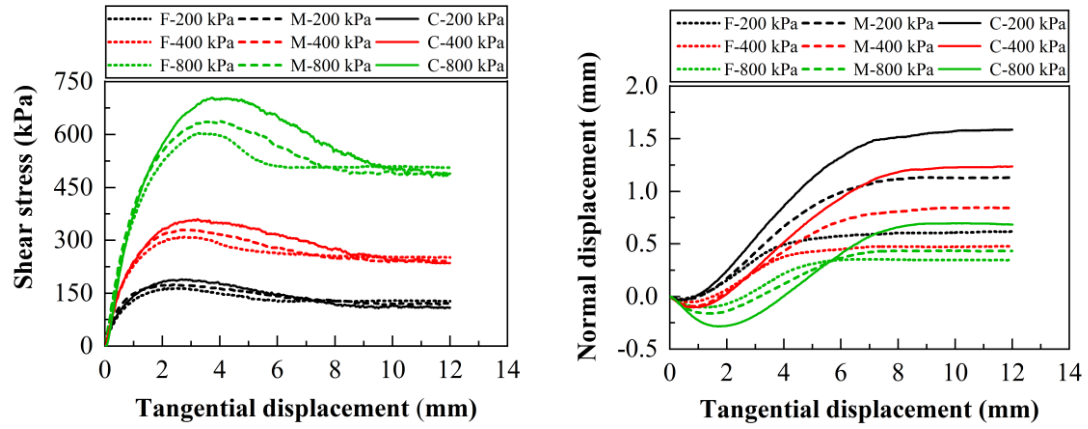

(a) (b)

Figure B-1 Mechanical responses of fine, medium, and coarse sand specimens in direct shear test at monotonic shearing: (a) shear stress versus tangential-displacement, (b) normal displacement versus tangential displacement under normal stresses of 200 kPa, 400 kPa, and 800 kPa

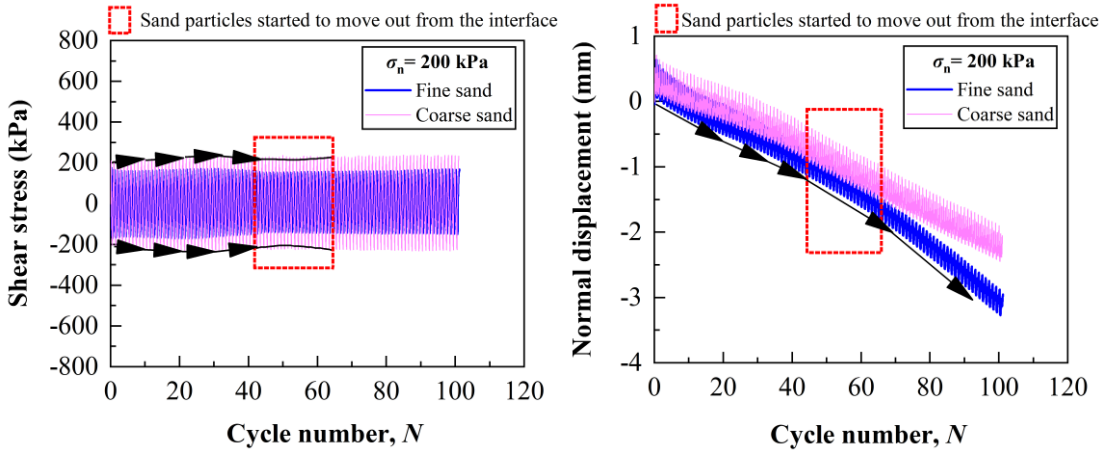

(a) (b)

Figure B-2 Identification of the effective maximum number of cycles in the current configuration of cyclic tests: (a) shear stress versus cycle number and (b) normal displacement versus cycle number for fine and coarse sand under 200 kPa normal stress at ± 2.5 mm of tangential displacement amplitude

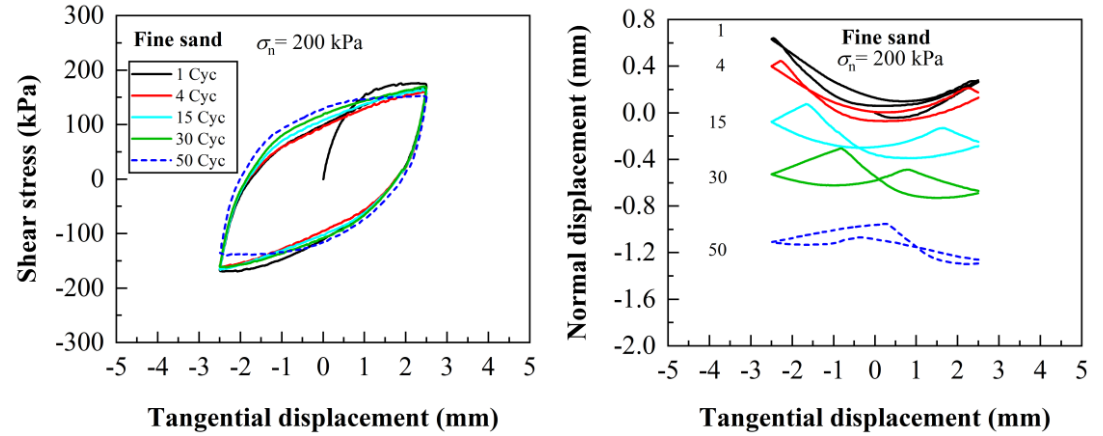

(a)

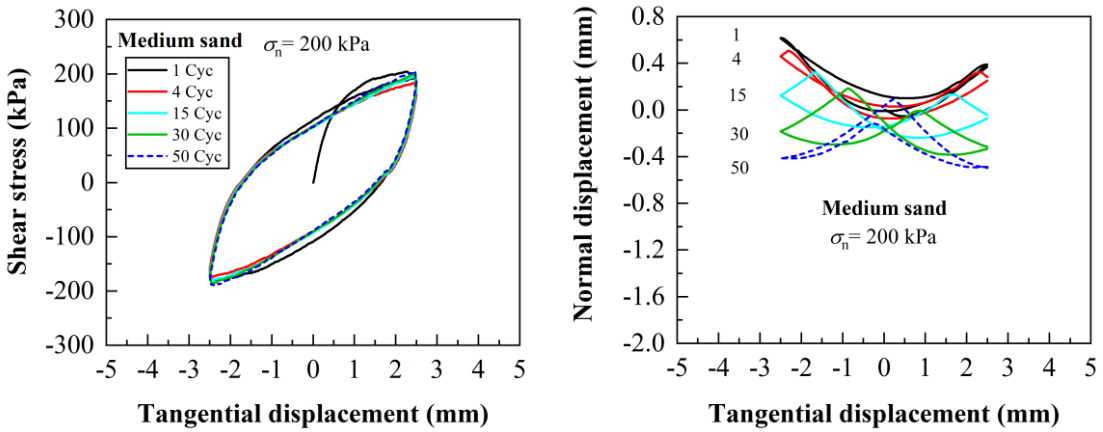

(b)

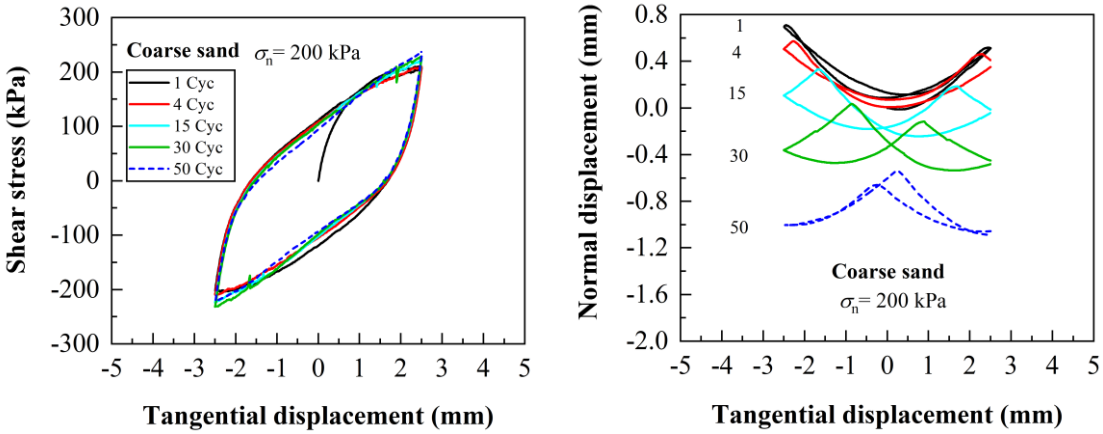

(c)

Figure B-3 Cyclic shear response of dense specimen of (a) fine sand, (b) medium sand, and (c) coarse sand under 200 kPa normal stress

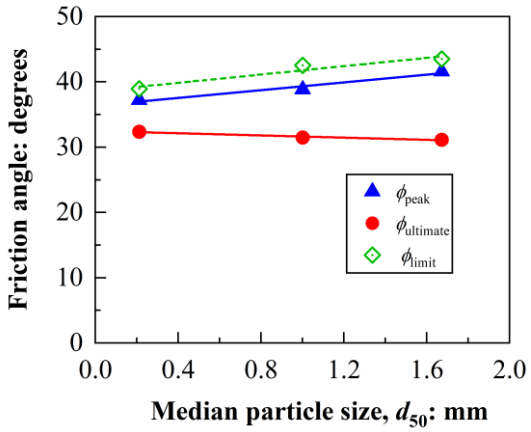

Figure B-4 Variation in friction angle of pure sand shearing in monotonic and cyclic conditions with respect to median particle size

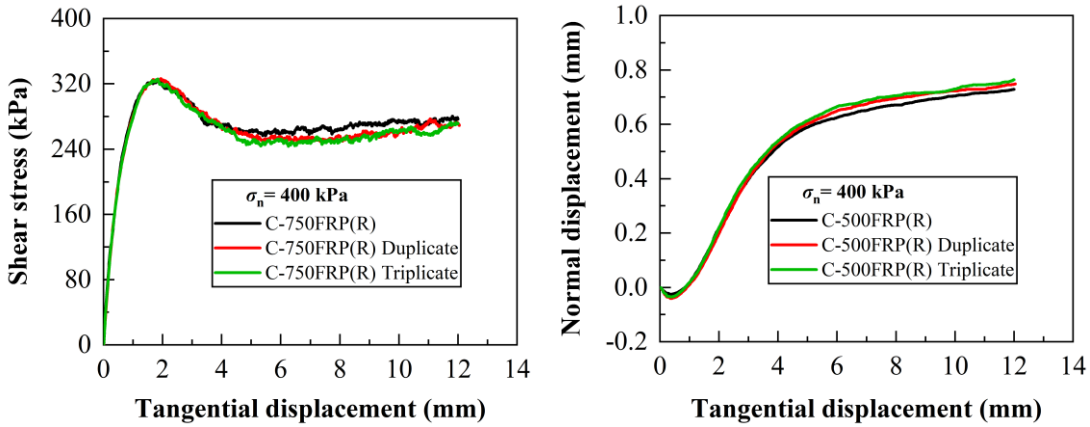

(a) (b)

Figure B-5 Repeatability of monotonic test results for the dense specimen of coarse sand against 750FRP(R): (a) shear stress and (b) normal displacement response with respect to tangential displacement under 400 kPa

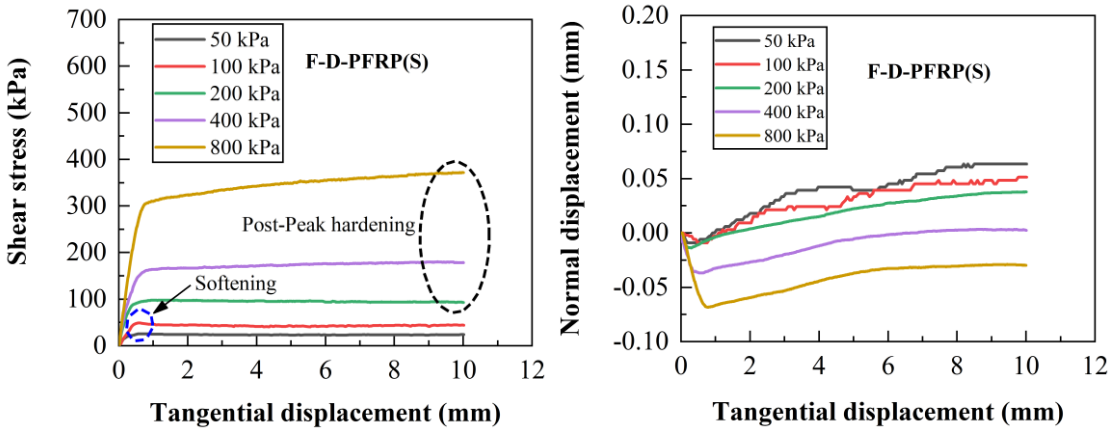

(a) (b)

Figure B-6 Confinement effect for the F-D-PFRP(S) interface: (a) shear stress and (b) normal displacement response with respect to tangential displacement under normal stresses ranging from 50 to 800 kPa (Note: mechanical responses of specimen types (Chapter 3, 50–100 kPa) plotted across the specimen types in Chapter 4 (200–800 kPa))

Table B-1 Summary of engineering design parameters of sand-GFRP interfaces

Interface materials	Normal stress (kPa)	Friction angle (degrees)		Friction angle ratio		Design factors	
		Peak	Ultimate	$PFAR$	$UFAR$	$E.F.$	$D.R.$
Fine sand (F)	200, 400, 800	37.20	32.35	1.0	1.0	1.0	1.0
F-PFRP(R)		29.78	27.58	0.8	0.85	0.75	0.82
F-HFRP(R)		30.01	28.22	0.81	0.87	0.76	0.85
ssF-750FRP(S)		n/a	27.30	n/a	0.84	n/a	0.81
F-1500FRP(MR)		34.72	28.73	0.93	0.89	0.91	0.87
F-750FRP(R)		35.73	31.10	0.96	0.96	0.94	0.95
F-1500FRP(R)		35.89	31.25	0.97	0.97	0.95	0.96
Medium sand (M)		38.83	31.47	1.0	1.0	1.0	1.0
M-PFRP(R)		n/a	30.80	n/a	0.97	n/a	0.97
M-HFRP(R)		n/a	25.92	n/a	0.82	n/a	0.79
M-750FRP(S)		n/a	24.29	n/a	0.77	n/a	0.74
M-750FRP(MR)		35.39	29.74	0.91	0.95	0.88	0.93
M-1500FRP(MR)		34.76	32.08	0.89	1.02	0.86	1.02
M-750FRP(R)		36.63	32.32	0.94	1.03	0.92	1.03
M-1500FRP(R)		38.13	33.10	0.98	1.05	0.98	1.07
Coarse sand (C)		41.58	31.13	1.0	1.0	1.0	1.0
C-PFRP(R)		n/a	31.01	n/a	0.99	n/a	0.99
C-HFRP(R)		n/a	29.25	n/a	0.93	n/a	0.93
C-750FRP(MR)		32.71	29.52	0.79	0.95	0.72	0.94
C-750FRP(R)		35.6	32.19	0.86	1.03	0.81	1.04
C-1500FRP(R)		38.33	32.68	0.92	1.05	0.89	1.06

Note: n/a refers to not available.

Table B-2 Interface materials and testing setup in literature

Reference	Soil	d_{50} (mm)	D_r (%)	Particle shape	Structure type	R_a (μm)	R
Wang et al. (2023)	Silica sand	0.252–1.514	90	C_{irc} = 0.7–0.872 R_{rd} = 0.55–0.627	Sawtooth steel	250*	0.165-0.993
Lashkari and Jamali (2021)	Crushed river sand, sea sand, glass beads	0.32, 0.65, 0.32, 0.65	61, 57, 77, 42	R_{rd} = 0.365, 0.444, 0.551, 0.912	Woven geotextile, geomembrane	3.65, 37.19	0.0056-0.116
Su et al. (2018)	Silica sand	1.001 1.536	90	Subrounded	Stainless steel Sawtooth steel	0.056** 100–795*	0.00003 -0.794
Han et al. (2018)	Silica sand	0.212, 1.001, 1.536	80 ±1	S = 0.78, 0.82, 0.83 R_{rd} = 0.4, 0.35, 0.44	Smooth steel Rusted steel	1.08 2.53–9.31	0.0007-0.044
DeJong and Westgate (2009)	Ottawa 20-30 silica, Q-Rok blasting sand, glass beads	0.714, 0.75, 0.95	95, 85	Subrounded, subangular, rounded	Smooth steel, sand-blasted steel, sand-epoxied steel	1.8, 6.2, 133	0.0025, 0.1863
Dietz and Lings (2006)	Silver fine sand	0.13	92–99	Subrounded	Machine and ground mild steel	0.147–9.4	0.00018-0.259
	Virgin Leighton Buzzard	0.78	83-94	Rounded	Sand-coated mild steel	33.7–180	
Sakr et al. (2005)	Fanshawe Bricksand	0.26	90 ±2.5	Subrounded	Smooth FRP, rough FRP, steel	1.66, 11.54, 1.05	0.004-0.044
Subba Rao et al. (1998)	Quartz sand	0.27, 0.42, 0.74, 1.10, 1.60	85	Well rounded	Stainless steel Mild steel Ferrocement	0.056 0.491, 2.49 8.85, 13.98	0.00005-0.0517

Note: d_{50} refers to median particle size, D_r refers to relative density, R_a refers to average roughness of literature, R refers to relative roughness, C_{irc} refers to circularity, R_{rd} refers to roundness, S refers to sphericity. 250* and 100-795* represent the average roughness value converted from the maximum roughness of isosceles groove. 0.056** represents the average roughness value supposed for smooth stainless steel identical to that of Subba Rao et al. (1998).

APPENDIX C: SUPPLIMENTARY FINDINGS FOR CHAPTER 5

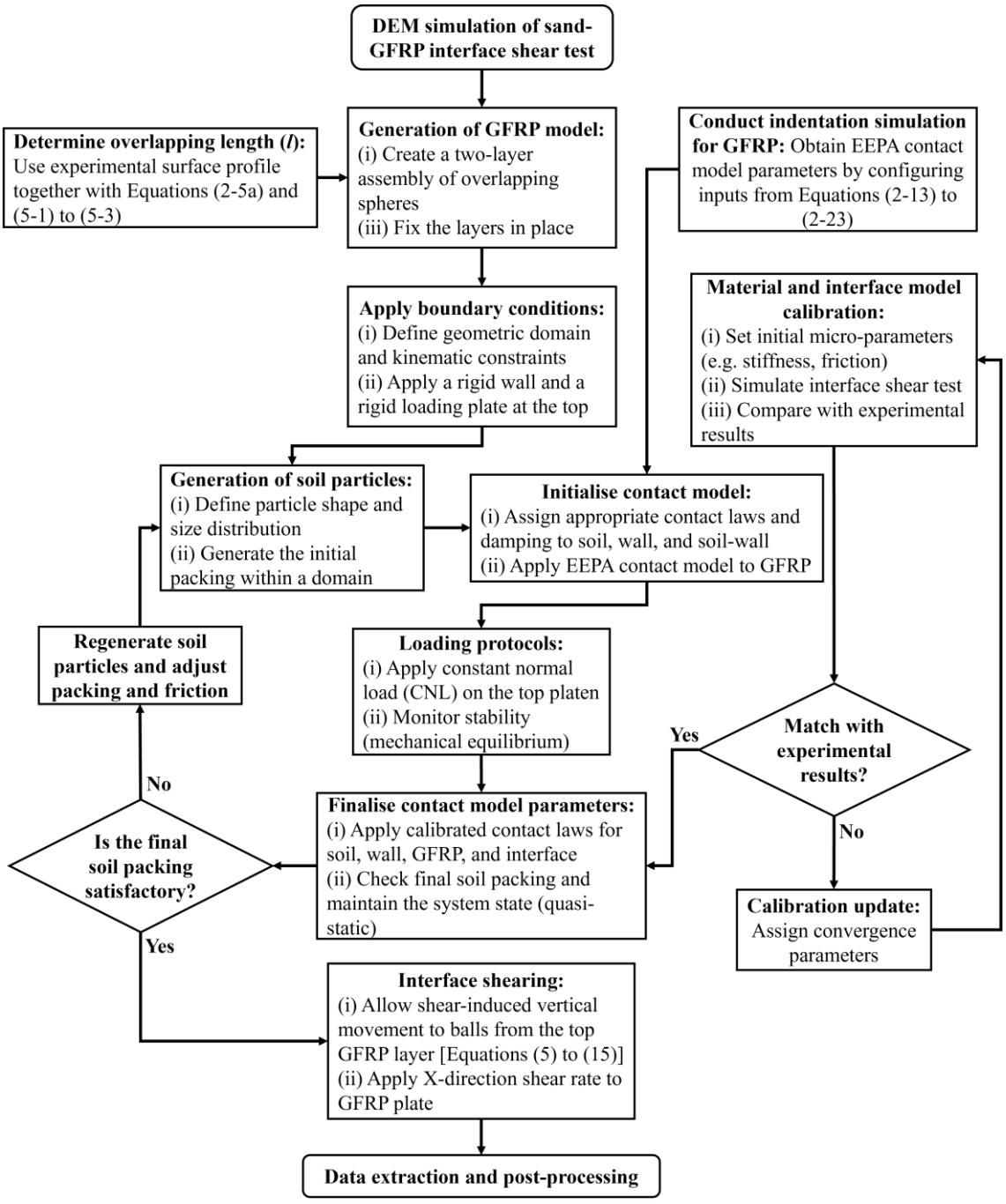

Figure C-1 Flowchart for the DEM simulation of sand-GFRP interface shear test

Table C-1 Summary of the simulation results of friction angles

S.N.	Interfaces	Particle shape	Normal stress (kPa)	Normalised roughness, R_n	Friction angle (degrees)			$E.F._{s-e\ GFRP}$
					Dense		Loose	
					δ_p	δ_{ult}	δ_{ult}	
1	F-PFRP(S)	Sphere	50, 100, 200	0.21	20.67	19.64	20.56	1.0
2	F-500FRP			0.49	22.65	20.63	20.74	1.1
3	F-1000FRP			0.85	24.94	20.72	21.50	1.2
4	F-1500FRP			1.32	28.32	23.53	22.92	1.37
5	M-PFRP(R)			0.11	20.76	18.72	17.95	n/a
6	M-1500FRP			0.19	24.59	20.92	20.70	1.79
7	F-1500FRP	Ellipsoid	50, 100, 200	1.32	28.01	24.68	23.77	1.36
8	M-1500FRP			0.19	25.26	22.74	22.43	1.84
9	M-1500FRP I	Sphere	50, 100, 200	0.04	13.72	13.6	n/a	1.0
10	M-1500FRP II			0.08	18.03	18.31	n/a	1.31
11	M-1500FRP III			0.16	23.03	19.8	n/a	1.68
12	M-1500FRP IV			0.23	26.15	20.56	n/a	1.91
13	M-1500FRP V			0.34	27.22	23.05	n/a	1.98

Note: n/a refers to not available; $E.F._{s-e\ GFRP}$ refers to efficiency factors of sand-epoxied GFRP based on plain GFRP(Smooth) or corresponding smooth interface at peak state.